Investigating the cellular role of the deubiquitylating enzyme ZUP1, a novel player in the DNA damage response

Matthew James Drake
Department of Biochemistry
Merton College
University of Oxford

A thesis submitted for the degree of
Doctor of Philosophy
Hilary Term 2023

To past and future Dr Drakes

" I am a part of all that I have met;
Yet all experience is an arch wherethro'
Gleams that untravell'd world whose margin fades
For ever and forever when I move.
How dull it is to pause, to make an end,
To rust unburnish'd, not to shine in use!
As tho' to breathe were life! Life piled on life
Were all too little, and of one to me
Little remains: but every hour is saved
From that eternal silence, something more,
A bringer of new things; and vile it were
For some three suns to store and hoard myself,
And this gray spirit yearning in desire
To follow knowledge like a sinking star,
Beyond the utmost bound of human thought." (18–32)

From *"Ulysses"* – Alfred, Lord Tennyson

Acknowledgements

I would firstly like to extend my sincerest thanks to **Dr Ian Gibbs-Seymour** for his supervision, guidance, and support throughout my DPhil. Your knowledge and advice have been invaluable resources, and it has been a pleasure being part of your lab these past 4 years.

I would additionally like to thank **Martin Attwood**, **Ben Foster**, **Kay Chong** and the other members of the Gibbs-Seymour lab. It has been an honour to chip away at the coal face of science with you.

I also extend my thanks to the members of the **Ebner lab** who provided help and guidance for the CRISPR screen that constitutes Chapter 5 of this thesis.

My thanks also to the denizens of 46 Chilswell Road and 7 Bartlemas Road whom I had the distinct honour of sharing a house and friendship with during my time in Oxford.

A mention also to the members of **Merton College Boat Club** who gave me a reason to see the world at 5:30 am on crisp Oxford mornings and without whom this thesis would likely have been finished years earlier! You are all gentlemen of ambition and character and I salute you.

A mention and thanks also to the siblings **Josh**, **Guy**, and **Gemma**. One of us had to do it… you're welcome!

My love and thanks also to my partner in crime **Issy**, with whom I've had the best time sharing this journey with. You and I *contra mundum*.

Lastly, a special thanks to my parents **Tony** and **Susie**, without whose support, love, and fine example none of this would be possible.

Declaration of authorship

I confirm that the work conducted for this thesis is entirely my own unless otherwise acknowledged and has not been submitted for any other degree.

Matthew Drake

April 2023

Abstract

The DNA damage response (DDR) is a network of interrelated signal transduction pathways that identify and repair DNA lesions to maintain genome integrity. To coordinate the DDR, cells use post-translational modifications (PTMs) such as ubiquitin to modify and control protein fate and function. Importantly, ubiquitin signalling is a dynamic modification that can be edited or removed from substrates by deubiquitylating enzymes (DUBs). ZUP1 was recently discovered as the founding member of a new DUB class with selectivity against long K63-linked ubiquitin chains and a putative, but poorly defined, role in the DDR. This thesis aimed to improve our understanding of the cellular role of ZUP1 and define which DDR pathway(s) it functions in. To this end, I generated monoclonal ZUP1 knockout (KO) cell lines using CRISPR-Cas9 gene editing and found that these cells were sensitive to genotoxins that induce replication-coupled DNA damage, with hypersensitivity to the interstrand crosslinking agent mitomycin C (MMC), and the PARP inhibitors olaparib and talazoparib. Using the high-content immunofluorescence microscopy technique of quantitative image-based cytometry (QIBC), I then analysed the dynamics of key factors at stressed DNA replication forks and demonstrated that excess generation of ssDNA and persistence of RPA and RAD51 foci underlie the sensitivity of ZUP1 KO cells to MMC. Lastly, I investigated the chemogenetic interactors of ZUP1 in response to MMC in an unbiased manner using genome-wide CRISPR-Cas9 screening and identified potential synergistic interactions between ZUP1 and the factors BRCA2 and HELQ. Collectively, my results suggest that ZUP1 is a novel player in the response to replication-coupled DNA damage and provides new insight into its cellular roles.

Table of Contents

List of Figures

List of Tables

List of Abbreviations

2′-OH	2′-hydroxyl
3′-OH	3′-hydroxyl
3′-P	3′-phosphate
3′-PG	3′-phosphoglycolate
5-aza-dC	5-aza-2′-deoxycytidine
5′-dRP	5′-deoxyribose phosphate
5′-AMP	5′-adenosine monophosphate
5′-P	5′-phosphate
53BP1	p53-binding protein 1
9-1-1	RAD9–RAD1–HUS1
AAD	ATR activating domain
ADP	Adenosine diphosphate
alt-NHEJ	Alternative non-homologous end joining
AMC	7-amino-4-methylcoumarin
AP	Apurinic or apyrimidinic/ abasic
APE1	AP-endonuclease 1
APE2	AP-endonuclease 2
APTX	Aprataxin
ARH3	(ADP-ribosyl) hydrolase 3
ATM	Ataxia-telangiectasia mutated
ATP	Adenosine triphosphate
ATR	Ataxia telangiectasia and Rad3-related
ATRIP	ATR interacting protein
BARD1	BRCA1-associated RING domain 1
BER	Base excision repair
BIR	Break-induced replication
BLM	Bloom Syndrome RecQ-like helicase
bp	Basepair
BRCA1	Breast cancer 1
BRCA2	Breast cancer 2
BRCT	BRCA1 C-terminal
BrdU	5-Bromo-2′-deoxyuridine
BUDR	BRCT-domain-associated ubiquitin-dependent recruitment motif
Cas	CRISPR associated
CDK	Cyclin-dependent kinase
CETN2	Centrin 2
CHK1	Checkpoint kinase 1
CIP2A	Cellular inhibitor of PP2A

CK2	Casein kinase 2
CldU	5-chloro-2′-deoxyuridine
CMG	CDC45, MCM2-7, GINS
CPDs	Cyclobutane–pyrimidine dimers
CRISPR	Clustered regularly interspaced short palindromic repeats
CRISPR-KO	CRISPR knockout
crRNA	CRISPR RNA
CHROMASS	Chromatin mass spectrometry
CSA	Cockayne Syndrome group A
CSB	Cockayne Syndrome group B
D-loop	Displacement loop
DAPI	4′,6-diamidino-2-phenylindole
DDR	DNA damage response
DDT	DNA damage tolerance
DMEM	Dulbecco's modified eagle medium
DMSO	Dimethyl sulfoxide
DNA-PK	DNA-dependent protein kinase
DNA-PKcs	DNA-dependent protein kinase catalytic subunit
DNMT1	DNA-methyltransferase 1
dNTP	Deoxyribonucleotide triphosphate
DPC	DNA–protein crosslink
DSB	Double strand break
dsDNA	Double-stranded DNA
DTT	Dithiothreitol
DUB	Deubiquitylating enzyme
ERCC1	Excision repair cross-complementation group 1
EV	Empty vector
EXO1	Exonuclease 1
FAN1	FANCD2/FANCI-associated nuclease 1
FBS	Foetal bovine serum
FEN1	Flap structure-specific endonuclease 1
FITC	Fluorescein isothiocyanate
gDNA	Genomic DNA
GG-NER	Global genome NER
GOI	Gene of interest
h	Hours
H2AK15	Histone H2A lysine 15
H3K4	Histone 3 lysine 4
H4K20	Histone H4 lysine 20
HELQ	POLQ-like helicase
HMCES	5-hydroxymethylcytosine binding, ES cell specific
HR	Homologous recombination

HROB	Homologous recombination factor with OB-fold
ICE	Interference of CRISPR edits
ICL	Interstrand crosslink
IdU	5-iodo-2′-deoxyuridine
Indel	Insertion or deletion
IR	Ionising radiation
KO	Knockout
LacO	Lac operator
LacR	Lac repressor
LD20	Lethal dose, 20%
LIG1	DNA ligase 1
LIG3	DNA ligase 3
LIG4	DNA ligase 4
LTGC	Long tract gene conversion
MaGECK	Model-based analysis of genome-wide CRISPR-Cas9 knockout
MCM	Minichromosome maintenance
MDC1	Mediator of DNA damage checkpoint 1
mins	Minutes
miRNA	MicroRNA
MIU	Motif interacting with ubiquitin
MMC	Mitomycin C
MMEJ	Microhomology-mediated end joining
MMR	Mismatch repair
MOI	Multiplicity of infection
MRN	MRE11, RAD50, NBS1
mRNA	Messenger RNA
NEIL3	Nei like DNA glycosylase 3
NELF	Negative elongation factor
NER	Nucleotide excision repair
NGS	Next-generation sequencing
NHEJ	Non-homologous end joining
NLS	Nuclear localisation signal
NZF	NPL4-type zinc finger
OB	Oligonucleotide/oligosaccharide binding
ORC	Origin recognition complex
p97i	p97 inhibitor
PALB2	Partner and localizer of BRCA2
PAM	Protospacer adjacent motif
PARG	Poly (ADP-ribose) glycohydrolase
PARP	Poly (ADP-ribose) polymerase
PARylation	Poly ADP-ribosylation
PAXX	Paralog of XRCC4 and XLF

PBS . . . . . Phosphate buffered saline
PCNA . . . . . Proliferating cell nuclear antigen
PCR . . . . . Polymerase chain reaction
PIKK . . . . . Phosphatidylinositol 3-kinase-related kinase
PIP . . . . . PCNA-interacting protein
PNKP . . . . . Polynucleotide kinase-phosphatase
POL . . . . . DNA polymerase
POLθ . . . . . DNA polymerase theta
pre-IC . . . . . Pre-initiation complex
pre-RC . . . . . Pre-replication complex
PRIMPOL . . . . . Primase and DNA directed polymerase
PRP19 . . . . . Pre-mRNA processing factor 19
pRPA . . . . . Phosphorylated RPA
PTM . . . . . Post-translational modification
QIBC . . . . . Quantitative image-based cytometry
RAD23B . . . . . RAD23 homolog B
RER . . . . . Ribonucleotide excision repair
RFC . . . . . Replication factor C
RFWD3 . . . . . Ring finger and WD repeat domain 3
RISC . . . . . RNA-induced silencing complex
RNAi . . . . . RNA interference
RNAPII . . . . . RNA polymerase II
rNTP . . . . . Ribonucleotide triphosphate
ROS . . . . . Reactive oxygen species
RPA . . . . . Replication protein A
RRM2 . . . . . Ribonucleoside-diphosphate reductase subunit M2
RT-PCR . . . . . Reverse transcriptase polymerase chain reaction
RTEL1 . . . . . Regulator of telomere elongation helicase 1
SDSA . . . . . Synthesis-dependent strand annealing
sgRNA . . . . . Single guide RNA
shRNA . . . . . Short-hairpin RNA
siRNA . . . . . Short interfering RNA
SSA . . . . . Single-strand annealing
SSB . . . . . Single strand break
ssDNA . . . . . Single-stranded DNA
SUMO . . . . . Small ubiquitin-like modifier
TALEN . . . . . Transcription activator-like effector nucleases
TBS . . . . . Tris-buffered saline
TC-NER . . . . . Transcription-coupled NER
TDP1 . . . . . Tyrosyl-DNA phosphodiesterase 1
TDP2 . . . . . Tyrosyl-DNA phosphodiesterase 2
TFIIH . . . . . Transcription factor IIH
TKOv3 . . . . . Toronto KnockOut version 3

TLS . . . . . Translesion DNA synthesis
TMEJ . . . . . Theta-mediated end joining
TOP1 . . . . . Topoisomerase 1
TOP1cc . . . . . TOP1 covalent complex
TOP2 . . . . . Topoisomerase 2
tracrRNA . . . . . Trans-activating crRNA
TRAIP . . . . . TRAF interacting protein
TS . . . . . Template switching
Ub . . . . . Ubiquitin
UBD . . . . . Ubiquitin binding domain
UBL . . . . . Ubiquitin-like modifier
UBZ . . . . . Ubiquitin binding zinc finger
UFM1 . . . . . Ubiquitin-fold modifier 1
UFSP . . . . . UFM1-specific protease
USP1 . . . . . Ubiquitin specific peptidase 1
USP7 . . . . . Ubiquitin specific peptidase 7
UV . . . . . Ultraviolet
UV-DDB . . . . . UV DNA damage binding
UVSSA . . . . . UV stimulated scaffold protein A
VCP . . . . . Vasolin-containing protein
WRN . . . . . Werner syndrome RecQ-like helicase
WT . . . . . Wild type
XLF . . . . . XRCC4-like factor
XPC . . . . . Xeroderma pigmentosum, complementation group C
XRCC1 . . . . . X-ray repair cross-complementing protein 1
ZFN . . . . . Zinc finger nuclease
ZHA . . . . . ZUP1 helical arm
ZnF . . . . . Zinc finger
ZUFSP . . . . . Zinc finger with UFM1-specific peptidase domain
ZUP1 . . . . . Zinc finger containing ubiquitin peptidase 1

1

Introduction

Contents

In the introductory sections below I outline the major pathways of the DNA damage response (DDR) (Figure 1), consider how its orchestration relies on dynamic post-translation modifications, and review how the powerful new technique of genome-wide clustered regularly interspaced short palindromic repeats (CRISPR) screening has allowed for a deeper understanding of the DDR. Lastly, I introduce the recently discovered deubiquitylating enzyme (DUB) zinc finger containing ubiquitin peptidase 1 (ZUP1), a novel player in the cellular response to replication-coupled DNA damage and the focus of this thesis.

1.1. Major pathways of the DNA damage response

1.1.1. Mismatch repair

During replication of the eukaryotic genome DNA polymerases occasionally incorporate an incorrect nucleotide that is not immediately repaired by the 3' to 5' exonuclease proofreading activity of DNA polymerase (POL) δ or POLε, resulting in a base mismatch (Kunkel, 2009). Larger insertion or deletion (indel) mutations can also be generated at repetitive genome sequences, such as microsatellite regions, that cause strand slippage due to the aberrant dissociation and reannealing of template and primer strands at the incorrect repeat (Kunkel, 1993). Cells have therefore evolved an efficient mismatch repair (MMR) pathway to restore instances of incorrectly paired DNA bases that counteracts mutagenesis and maintains sequence fidelity (Kunkel and Erie, 2015). In mammalian cells the MMR pathway is initiated by the recognition of a mismatched lesion by the MSH2–MSH6 (MutSα) or MSH2–MSH3 (MutSβ) heterodimer complexes which recognise 1–2 basepair (bp) mismatches or larger indels respectively (Acharya et al., 1996; Gradia et al., 1997; Palombo et al., 1996). MutSα or MutSβ complexes then

recruits the MLH1-PMS2 (MutLα) or MLH1–MLH3 (MutLβ) heterodimers which together form a sliding clamp structure that undergoes an adenosine triphosphate (ATP)-dependent conformational change allowing it to translocate away from the mismatch site (Li and Modrich, 1995; Lipkin et al., 2000). When a migrating MutS–MutL clamp encounters proliferating cell nuclear antigen (PCNA) and replication factor C (RFC) at a nearby replisome the endonucleoltyic activity of MutL is activated, and a nick is generated in the strand bearing the mismatch (Kadyrov et al., 2006; Pluciennik et al., 2010). The exonuclease 1 (EXO1) enzyme can then bind and degrade the strand in the 5' to 3' direction to remove the region containing a mismatch (Tran et al., 2004). POLδ then fills in the resulting gap with the correct nucleotides and the fragment is ligated to the rest of the DNA by DNA ligase 1 (LIG1), thereby restoring the accurate sequence (Longley et al., 1997).

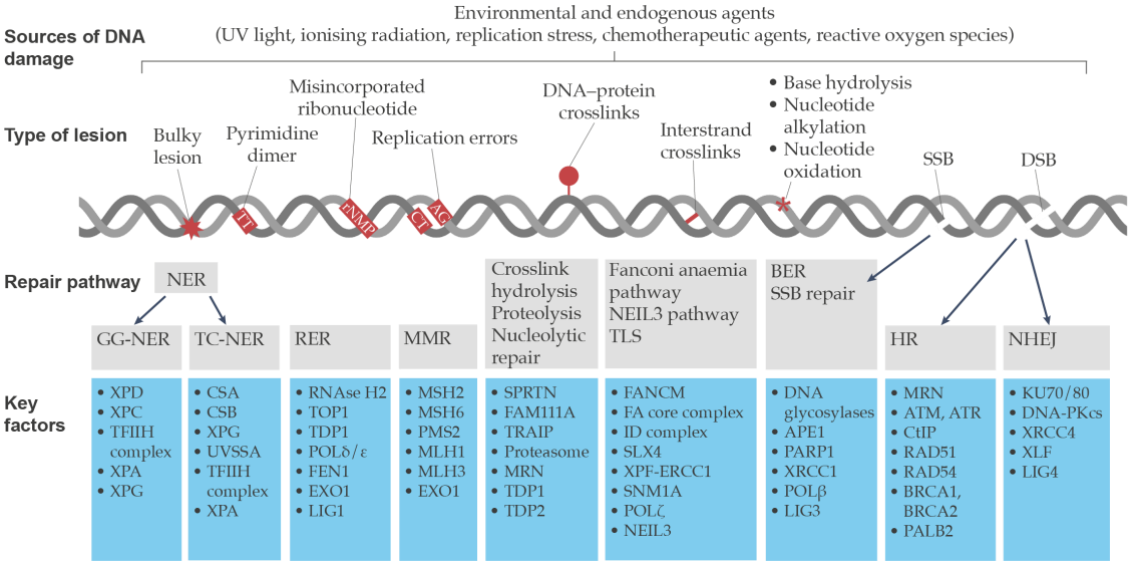

Figure 1. Sources of DNA damage and the major DNA repair pathways

Cells routinely encounter a wide range of DNA damage that is induced by a diverse array of endogenous and exogenous agents requiring dedicated pathways to repair specific lesion types. The major forms of DNA damage and the cellular pathways employed to combat each type of damage are depicted. Shown in blue boxes are the key factors that constitute each pathway. Figure created using BioRender.com with reference to (Awwad et al., 2023).

1.1.2. Base excision repair

In addition to the incorrect incorporation of nucleotides during replication, DNA bases can also sustain a wide array of damage from endogenous and exogenous sources, typically involving oxidation, alkylation, or deamination, that pose a threat to genome integrity (Hoeijmakers, 2009). Some forms of damage can be directly reversed by the action of a single enzyme such as the photolyase reversal of ultraviolet (UV) light-induced photolesions, alkyltransferase reversal of *O*-alkylated DNA damage, and the dioxygenase reversal of *N*-alkylated base adducts (Yi and He, 2013). However, some forms of damaged DNA bases are not amenable to direct chemical reversal and instead require removal and replacement with undamaged bases. The base excision repair (BER) pathway exists to combat this damage and can remove and replace small, non-helix-distorting lesions (Beard et al., 2019). Central to the BER pathway are a suite of DNA glycosylases that can recognise a diverse range of damaged bases and cleave the *N*-glycosidic bond connecting a base to the sugar-phosphate backbone of DNA, leaving an abasic (AP) site (Krokan and Bjoras, 2013). The DNA backbone located 5′ to the AP site is then incised by AP-endonuclease 1 (APE1) creating a single-strand break (SSB) with 3′-hydroxyl (3′-OH) and 5′-deoxyribose phosphate (5′-dRP) termini (Hegde et al., 2008). The BER pathway then proceeds with the steps of DNA end processing, gap filling synthesis, and end ligation which are discussed in further detail in section 1.1.5.3 on SSB repair. For SSBs arising as a result of BER**,** gap filling commonly involves the insertion of a single missing nucleotide in a process known as ‘short-patch repair’, but can involve the FEN1-mediated displacement of 5′-nucleotides and synthesis of a longer stretch of DNA in a process known as ‘long-patch repair’ (Caldecott, 2014; Klungland and Lindahl, 1997).

1.1.3. Ribonucleotide excision repair

To faithfully copy DNA templates, replicative DNA polymerases must distinguish between deoxyribonucleotide triphosphate (dNTP) and ribonucleotide triphosphate (rNTP) precursors that differ solely by the presence of a 2′-hydroxyl (2′-OH) moiety on the ribose of rNTPs (Klein, 2017). The problem is compounded by the presence of a much higher concentration of rNTPs relative to dNTPs in the available nuclear pool (Traut, 1994). While the replicative DNA polymerases (POLα, POLδ, POLε) display a relatively high fidelity for dNTPs due to a conserved tyrosine residue in their active site that acts as a steric block to the 2′-OH group of rNTPs, ribonucleotides are still misincorporated into replicating DNA at an estimated rate of approximately 1 in 1,000 (Nick McElhinny et al., 2010b). Misincorporated ribonucleotides have a significant impact on DNA's structure and stability and can interfere with the processes of transcription and replication (Jaishree et al., 1993; Nick McElhinny et al., 2010a). The inbuilt proofreading activity of replicative DNA polymerases is ineffective at removing aberrantly incorporated ribonucleotides, therefore cells have evolved dedicated molecular pathways known as ribonucleotide excision repair (RER) pathways to perform this function (Clausen et al., 2013; Kellner and Luke, 2020).

1.1.3.1. RNAse H2 pathway

The primary RER pathway utilises RNAse H2 to cleave and remove misincorporated ribonucleotides (Sparks et al., 2012). RNAse H2 makes an incision in the phosphodiester backbone at the 5′ junction of the RNA component of a DNA–RNA hybrid creating a nick with 3′-OH and 5′-phosphate (5′-P) termini. The 3′-OH then acts as a primer for POLδ or POLε which perform strand displacement synthesis that creates a 5′ flap structure containing the aberrant ribonucleotide. The flap is then cleaved by the

endonuclease activity of flap structure-specific endonuclease 1 (FEN1) or EXO1 and the remaining nick is sealed by LIG1 (Sparks et al., 2012).

1.1.3.2. TOP1 pathway

While the RNAse H2 pathway is an error-free mechanism for removing embedded ribonucleotides, a less common error-prone backup pathway involving topoisomerase 1 (TOP1) can be used in RNAse H2's absence (Williams et al., 2013). The TOP1 pathway involves the formation of a covalent complex (TOP1cc) between the active site tyrosine of TOP1 and the 3′-phosphate (3′-P) of an incorporated ribonucleotide in a manner analogous to its physiological role in nicking unmodified DNA to relieve torsional stress. While TOP1 can readily seal nicks when bound to normal DNA, the 2′-OH of a ribonucleotide is liable to attack the phospho-tryosyl bond of the TOP1cc forming a 2′,3′-cyclic phosphate moiety that is not amenable to ligation (Sekiguchi and Shuman, 1997). Repair of this intermediate can proceed via secondary engagement of TOP1 upstream of the nick and error-free proteolysis and end processing by tyrosyl-DNA phosphodiesterase 1 (TDP1) as discussed below in section 1.1.7.5; or may result in strand slippage realignment and re-ligation resulting in a 2–5 bp deletion (Sparks and Burgers, 2015). Interestingly, it was discovered in genome-wide CRISPR screens for sensitisers to the poly (ADP-ribose) polymerase (PARP) inhibitor olaparib that loss of genes encoding RNAse H2 resulted in increased sensitivity to PARP inhibition (Zimmermann et al., 2018). The author's demonstrated that the basis for this sensitivity was increased reliance on the TOP1 RER pathway in RNAse H2's absence, which yields a greater degree of PARP trapping lesions that interrupt DNA replication and cause genome instability.

1.1.4. Nucleotide excision repair

Nucleotide excision repair (NER) is a versatile repair pathway that counteracts a wide array of chemically and structurally diverse helix distorting lesions that are not readily repaired by BER (Scharer, 2013). Two broad subpathways of NER exist, termed global-genome NER (GG-NER) and transcription-coupled NER (TC-NER) that differ in their recognition of DNA damage but share common downstream processing steps (Figure 2) (Marteijn et al., 2014).

1.1.4.1. GG-NER

In the GG-NER pathway the damage sensor protein xeroderma pigmentosum (XP), complementation group C (XPC) in complex with RAD23 homolog B (RAD23B) and Centrin 2 (CETN2) probes the genome until it encounters a helix distorting lesion (Shell et al., 2013). Importantly, this recognition does not involve direct contact with the lesion and instead relies on sensing DNA structural destabilisation which allows the GG-NER system to identify a heterogenous set of chemically distinct lesion types (Chen et al., 2015). For certain lesion types that don't cause major helix distortion, however, recognition is aided by the UV DNA damage binding (UV-DDB) complex which makes direct contact with lesions (Sugasawa et al., 2005). Following damage recognition XPC then recruits the transcription factor II H (TFIIH) complex which mediates the downstream repair processes (Yokoi et al., 2000). TFIIH comprises a 7-subunit core complex two of which, XPB and XPD, possess helicase activity that unwinds the DNA duplex to create a repair bubble surrounding the lesion site (Fan et al., 2006). XPD together with the factor XPA, which binds altered nucleotides, plays an important role in lesion verification to ensure that the NER machinery is correctly targeted sites of damaged DNA (Mathieu et al., 2013). Replication protein A (RPA) is also recruited to

the repair bubble and binds single-stranded DNA (ssDNA) on the undamaged strand to protect it and direct incision to the opposite strand (de Laat et al., 1998). XPA plays an additional role in recruiting the XPF-excision repair cross-complementation group 1 (ERCC1) and XPG structure-specific nucleases that perform dual incision of the damaged strand 5′ and 3′ of the lesion site respectively to generate a ~24–32 nucleotide excised region (Tsodikov et al., 2007). The resulting gap is then filled in by POLδ, POLε, or POLκ and the nicks are finally sealed by either LIG1 or DNA ligase 3 (LIG3) (Ogi et al., 2010).

1.1.4.2. TC-NER

In the TC-NER subpathway, helix distorting damage is recognised when RNA polymerase II (RNAPII) stalls at a lesion site during transcription extension (Vermeulen and Fousteri, 2013). Stalling of RNAPII stabilises its interaction with Cockayne Syndrome group B (CSB) which in turn promotes the stepwise recruitment of Cockayne Syndrome group A (CSA) and the UV Stimulated Scaffold Protein A (UVSSA)/Ubiquitin Specific Peptidase 7 (USP7) complex (van den Heuvel et al., 2021). CSA forms the substrate recognition subunit of the $CLR4^{CSA}$ E3 ligase which contributes to the ubiquitylation of the largest RNAPII subunit RPB1 at K1268 and stimulates the binding of UVSSA (Nakazawa et al., 2020). UVSSA then recruits the TFIIH complex which facilitates the downstream repair steps as in GG-NER described above (van der Weegen et al., 2020). The $CLR4^{CSA}$ complex also orchestrates chromatin remodelling events that are thought to allow RNAPII to 'backtrack' from lesion sites and provide access to subsequent repair machinery (Fousteri and Mullenders, 2008).

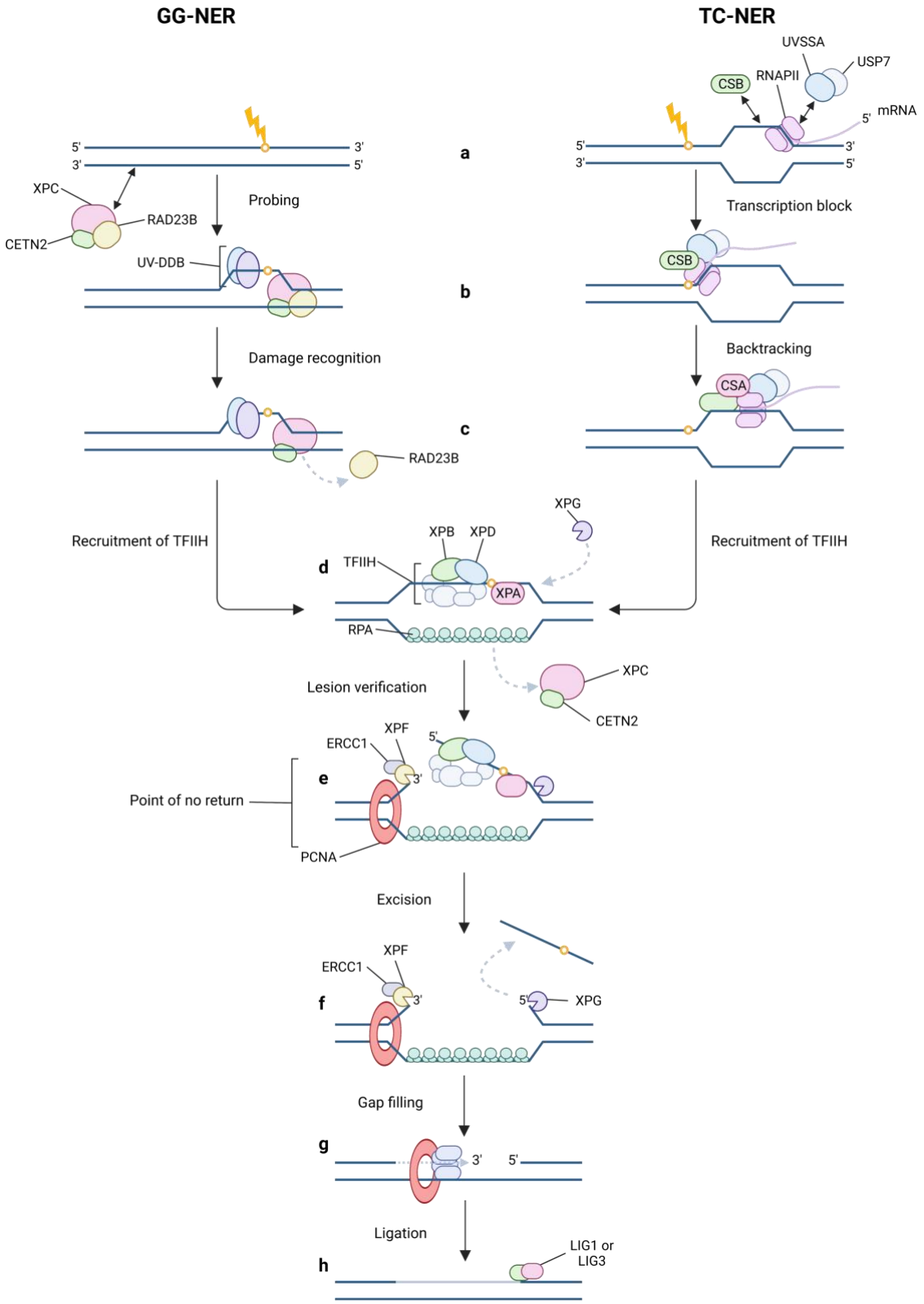
GG-NER
TC-NER
UVSSA
USP7
CSB
RNAPII
mRNA
5'
3'
XPC
RAD23B
CETN2
Probing
UV-DDB
a
b
c
d
e
f
g
h
Transcription block
Backtracking
CSA
Damage recognition
RAD23B
Recruitment of TFIIH
Recruitment of TFIIH
XPG
XPB
XPD
TFIIH
XPA
RPA
Lesion verification
XPC
CETN2
XPF
ERCC1
Point of no return
PCNA
Excision
Gap filling
Ligation
LIG1 or
LIG3

Figure 2. GG-NER and TC-NER nucleotide excision repair pathways

a, left) Lesion recognition in GG-NER relies on the damage sensor XPC in complex with CETN2 and RAD23B which continually probe the genome for helix-distorting lesions. **a, right)** TC-NER lesions are recognised when RNAPII stalls during transcription elongation at a distorting lesion. **b, left)** In GG-NER Damage recognition can be aided by UV-DDB at certain lesions that do not cause extensive helix distortion. **b, right)** RNAPII stalling increases its association with CSB and UVSSA-USP7. **c, right)** This in turn results in recruitment of CSA which mediates the processing steps required for backtracking of RNAPII and recruitment of TFIIH**. c, left)** In GG-NER recruitment of TFIIH is mediated by XPC following damage recognition. **d)** Both NER pathways then proceed according to the same steps of XPB and XPD helicase unwinding of a repair bubble surrounding the lesion site followed by XPA mediated lesion verification while the undamaged strand is stabilised by RPA binding. **e)** XPF-ERCC1 and XPG structure specific nucleases are then recruited marking a 'point of no return' and make incisions 5′ and 3′ to the lesion respectively. **f-h)** The resulting 24-32 nucleotide fragment is then excised, and the intervening gap is filled in and ligated by POLδ, POLε, or POLκ and LIG1 or LIG3 respectively. Figure created using BioRender.com with reference to (Marteijn et al., 2014).

1.1.5. Single strand break repair

Single-strand breaks (SSBs) are one of the most common DNA lesions experienced by cells (Lindahl, 1993). SSBs can arise spontaneously due to oxidative attack of the DNA sugar-phosphate backbone by reactive oxygen species (ROS), or as a reaction intermediate or product of certain DNA repair pathways or metabolic processes such as BER or topoisomerase processing respectively (Caldecott, 2020; Demple and Harrison, 1994; Pommier et al., 2016). SSBs that are not repaired pose a challenge to transcription by blocking RNA polymerases and can also stall DNA replication forks, which can lead to the generation of far more cytotoxic double-strand break (DSB) lesions (Caldecott, 2014; Caldecott, 2022). Cells have therefore evolved molecular pathways to rapidly detect and repair SSBs which proceed via the following steps.

1.1.5.1. SSB detection

PARP enzymes are the primary molecular sensors of SSBs which, when activated, catalyse the transfer of adenosine diphosphate (ADP)-ribose moieties from NAD^+ to target proteins (Eisemann and Pascal, 2020). PARP1 and PARP2 catalyse the addition of multiple ADP-ribose subunits in a process known as poly ADP-ribosylation (PARylation), while PARP3 commonly modifies target proteins with a mono-ADP-ribose group (Gibson and Kraus, 2012; Grundy et al., 2016). Synthesis of PAR chains is one of the earliest events in SSB repair that signals the presence of damage and acts as a platform for the recruitment of subsequent repair factors (Ciccia and Elledge, 2010). PARylation is a reversible and highly dynamic process due to the activities of poly (ADP-ribose) glycohydrolase (PARG), which degrades PAR chains, and ADP-ribosyl hydrolases such as (ADP-ribosyl) hydrolase 3 (ARH3), which removes residual mono-ADP-ribose modifications (Pascal and Ellenberger, 2015; Rack et al., 2020). Importantly,

rather than acting simply as a negative regulator of SSB repair the activity of PARG is thought to fully remove PAR chains and allow for subsequent rounds of synthesis to occur (Davidovic et al., 2001). PARP1 engagement at sites of DNA damage itself is regulated, with the E3 ligases CHFR and TRIP12 being suggested to bind auto-PARylated, and thus active, PARP1 and catalyse its polyubiquitylation leading to its proteasomal turnover (Gatti et al., 2020; Liu et al., 2013). X-ray repair cross-complementing protein 1 (XRCC1) has additionally been suggested to prevent excessive PARP1 engagement during DNA repair therefore mitigating the cytotoxic consequences of PARP trapping (Demin et al., 2021). Indeed, a key function of PARylation is to recruit the XRCC1 protein which acts as a scaffold to interact with and directly recruit most of the factors required for SSB repair (El-Khamisy et al., 2003). XRCC1 is recruited via a direct interaction of its BRCA1 C-terminal (BRCT) domain with PAR chains (Breslin et al., 2015).

1.1.5.2. Chromatin remodelling

One important consequence of PARP enzyme activity for SSB repair is the remodelling of the chromatin environment to facilitate repair (Ray Chaudhuri and Nussenzweig, 2017). PARylation of histones following PARP activation can directly reduce chromatin compaction as well as recruit various chromatin remodelling enzymes that lead to the relaxation of the local chromatin environment (de Murcia et al., 1986; Zong et al., 2022). It is thought that the loosening of the chromatin architecture surrounding a SSB facilitates the access of factors required for efficient repair (Caldecott, 2022). PARPs also play a role in transcription regulation through modification of chromatin compaction and by direct PARylation of factors that control RNA polymerase elongation, such as negative elongation factor (NELF) components. These modifications

lead to context-dependent impacts on transcription rates which may help to avoid conflicts between the SSB repair and transcription machineries (Gibson et al., 2016; Matveeva et al., 2019).

1.1.5.3. DNA end processing

The generation of SSBs by ROS can notably result in aberrant 3′-P or 3′-phosphoglycolate (3′-PG) termini which must be converted back to conventional 3′-OH and 5′-P moieties prior to gap filling and DNA ligation (Caldecott, 2008). 3′-P residues are dephosphorylated by polynucleotide kinase-phosphatase (PNKP) which is recruited and activated by interacting with XRCC1 (Breslin and Caldecott, 2009; Whitehouse et al., 2001). 3′-PG termini on the other hand are processed by APE1 (Parsons et al., 2004). SSBs that arise due to the abortive activity of TOP1 yield a 5′-OH moiety and 3′-phospho-tyrosyl covalently linked to TOP1 itself (Caldecott, 2022). Repair of these SSBs involves the proteasomal degradation of trapped TOP1 leaving a small residual peptide which is removed by TDP1 or AP-endonuclease 2 (APE2), followed by restoration of canonical 3′-OH and 5′-P groups by PNKP (Alvarez-Quilon et al., 2020; Kalasova et al., 2020; Plo et al., 2003; Sun et al., 2020b). The generation of SSBs during BER can also generate unproductive 5′-dRP termini as mentioned above, which are processed by the apurinic or apyrimidinic (AP) lyase activity of POLβ (Matsumoto and Kim, 1995). Finally, abortive attempts to re-ligate SSBs can yield 5′-adenosine monophosphate (5′-AMP) termini which are removed by the aprataxin (APTX) enzyme (Ahel et al., 2006).

1.1.5.4. DNA gap filling and ligation

Once normal DNA ends are restored, SSB repair proceeds with the filling of the intervening gap by DNA polymerases. POLβ is the polymerase primarily involved in gap filling during SSB repair (Prasad et al., 1998). The last step of SSB repair restores the

undamaged DNA sequence via the ligation of the remaining DNA nick by either LIG3 or LIG1 (Cappelli et al., 1997; Ho and Satoh, 2003).

1.1.6. Interstrand crosslink repair

The covalent linking of DNA bases on separate strands to form an interstrand crosslink (ICL) is a significant source of cytotoxicity due to the disruption of physiological DNA transactions such as transcription and DNA replication (Deans and West, 2011). A diverse set of bifunctional crosslinking agents with both endogenous and exogenous sources can result in ICL formation (Semlow and Walter, 2021). Reactive metabolites such as acetaldehyde, formaldehyde and nitric oxide can be endogenous sources of ICLs, while the ability to form ICLs is exploited by exogenous chemotherapeutic agents such as cisplatin and mitomycin C (MMC) (Semlow and Walter, 2021). ICLs can also form between the commonly occurring DNA lesion of an AP site and a reactive amine contained within a nucleobase on the opposing strand (Price et al., 2014). Two major pathways exist for replication-coupled ICL repair – a Nei like DNA glycosylase 3 (NEIL3) glycosylase dependent pathway and a canonical pathway dependent on 22 *FANC* gene products so called because mutations in these genes cause the genome instability syndrome Fanconi anaemia (FA) (Kottemann and Smogorzewska, 2013; Semlow et al., 2016). Four categories of FANC proteins have been proposed that classify them based on their functional characteristics as depicted in Table 1 (Semlow and Walter, 2021).

Table 1. List of FANC proteins

Number	Group	FANC protein	Alias	Function
1	1	M	-	DNA translocase
2	2	A	-	E3 ubiquitin ligase for ID complex
3		B	-	
4		C	-	
5		E	-	
6		F	-	
7		G	-	
8		L	-	
9		T	UBE2T	
10	3	D2	-	ID complex
11		I	-	
12	4	P	SLX4	XPF-binding protein
13		Q	XPF	Endonuclease (NER)
14		D1	BRCA2	Recombination
15		O	RAD51C	
16		R	RAD51	
17		U	XRCC2	
18		N	PALB2	
19		S	BRCA1	
20		J	BRIP1	DNA Helicase
21		W	RFWD3	E3 ubiquitin ligase
22		V	REV7	TLS polymerase

Adapted from (Semlow and Walter, 2021).

1.1.6.1. Fanconi anaemia pathway

The currently accepted model for FA pathway repair initially requires the convergence of two replication forks that stall at the site of an ICL (Figure 3) (Zhang et al., 2015). This model is preferred over a single fork mechanism as it allows cells to distinguish a permanent ICL lesion from a more transient replication block, such as a non-covalent stably bound protein that might temporarily arrest one fork but not ultimately require the engagement of FA repair factors (Semlow and Walter, 2021). The convergence of replication forks activates the E3 ubiquitin ligase TRAF interacting protein (TRAIP), which catalyses the polyubiquitylation of the replicative CMG helicase complex (comprising CDC45, MCM2-7, and GINS) (Wu et al., 2019). Long chain K48-linked polyubiquitylated CMG is then targeted for unloading from chromatin by the p97/vasolin-containing protein (VCP) 'segregase' complex (Fullbright et al., 2016). Unloading of CMG from chromatin also facilitates the reversal of one of the converged forks (Amunugama et al., 2018). Interestingly, it has also been shown that in some instances the CMG helicase is able to traverse an ICL blocking lesion rather than being unloaded, in a process dependent on the ATPase activity of FANCM and the repriming ability of primase and DNA directed polymerase (PRIMPOL) (Gonzalez-Acosta et al., 2021; Huang et al., 2013). Importantly, however, it has been suggested that the DNA structures resulting from either fork convergence or CMG traversal present a similar X-shaped structure that are both funnelled into the same downstream repair processes (Huang et al., 2013).

The initial stages of this pathway require FANCM which binds a diverse set of stressed replication fork structures and mediates the recruitment of the FA core complex (Deans and West, 2009). The FA core complex in turn recruits the FANCD2-FANCI (ID)

complex and acts as an E3 ligase through the catalytic domain contained in FANCL to promote ID ubiquitylation in conjunction with the E2 conjugating enzyme FANCT (UBE2T) (Alpi et al., 2008; Longerich et al., 2009). The unmodified ID complex is maintained as an open trough-like structure that requires conformational remodelling to reveal the lysine residues targeted for ubiquitylation which are buried in the N-terminal interface of the ID heterodimer (Alcon et al., 2020). Mechanistically this occurs when the ID complex binds the FA core complex which facilitates its partial closure around DNA by rotating the C-terminal domains of FANCD2 and FANCI towards each other (Wang et al., 2021). The phosphorylation of FANCI by the ataxia telangiectasia and Rad3 related (ATR) kinase has also been shown to be important for the conformational shift from open to closed structure of the ID complex that promotes it ubiquitylation (Sijacki et al., 2022). ATR phosphorylation and DNA binding leads to the full closure of the ID complex exposing K561 on the FANCD2 N-terminus which can now be ubiquitylated causing a subsequent conformational change that locks the ID complex in position around DNA (Wang et al., 2020). This conformational change additionally exposes K523 on FANCI allowing for its ubiquitylation which then prevents excessive deubiquitylation of FANCD2-Ub by the DUB Ubiquitin Specific Peptidase 1 (USP1) (Lemonidis et al., 2023; van Twest et al., 2017). The dynamic control of ID ubiquitylation is important for ICL repair as revealed by the fact that cells deficient for USP1 display sensitivity to crosslinking agents (Oestergaard et al., 2007). A key function of the ubiquitylated ID complex is to promote ICL unhooking from one of the DNA strands by recruiting endonucleases that make incisions in the phosphodiester DNA backbone either side of an ICL. This is achieved by recruiting the scaffolding protein FANCP (SLX4) which in turn contacts the structure specific flap nuclease XPF-ERCC1 that incises the DNA backbone upstream of an ICL (Klein Douwel et al., 2014). The candidate

nuclease proposed to make the 3′ incision the other side of the ICL is SNM1A, but there may be some functional redundancy with FAN1, SLX1, or MUS81 nucleases (Semlow and Walter, 2021).

Following ICL unhooking the FA pathway employs the translesion DNA synthesis (TLS) polymerases REV1 or POLζ to both insert a nucleotide opposite an unhooked ICL and to perform DNA synthesis to extend the leading strand past the ICL lesion (Budzowska et al., 2015; Roy and Scharer, 2016). Once extended, the lefthand leading strand is then ligated to an Okazaki fragment generated by the righthand converging fork (Roy and Scharer, 2016). The two-ended DSB on the opposite strand generated by ICL unhooking is then repaired by homologous recombination (HR) using the canonical molecular machinery (see section 1.1.8.4) (Long et al., 2011). TLS and HR restore intact DNA strands but leaves the unhooked ICL adduct attached to the DNA strand that was not incised. This monoadduct is therefore thought to be repaired by a downstream NER pathway (Muniandy et al., 2010).

1.1.6.2. NEIL3 pathway

An alternative ICL repair pathway that processes a subset of lesions is the NEIL3 pathway which, instead of incising the phosphodiester backbone of DNA, directly cleaves the *N*-glycosyl bond that constitutes the ICL itself (Figure 3) (Semlow et al., 2016). This pathway therefore circumvents the generation a potentially deleterious DSB but is precluded from acting on certain ICL lesions that significantly distort DNA, such as those induced by cisplatin, which must be repaired by the FA pathway (Huang et al., 1995). NEIL3 has therefore predominantly been seen to process the simpler ICLs arising from psoralen treatment or AP lesions (Semlow et al., 2016). The NEIL3 pathway is initiated upon replication fork convergence on an ICL in a similar manner to the FA

pathway. However, whereas the FA pathway requires p97/VCP-mediated CMG unloading triggered by extensive long chain polyubiquitylation, short ubiquitin (Ub) chains are sufficient to engage NEIL3 via its NPL4-type zinc finger (NZF) ubiquitin-binding domain (UBD) (Wu et al., 2019). NEIL3 catalysed cleavage of an ICL yields an AP site that is filled in by the action of a TLS polymerase such as REV1–POLζ (Budzowska et al., 2015). The relative simplicity of the NEIL3 pathway compared to the FA pathway and its requirement for shorter CMG polyUb chains means it is the initially prioritised ICL repair pathway. However, if NEIL3 cannot process an ICL lesion, Ub chains on CMG are extended by TRAIP and repair is directed to the FA pathway (Wu et al., 2019).

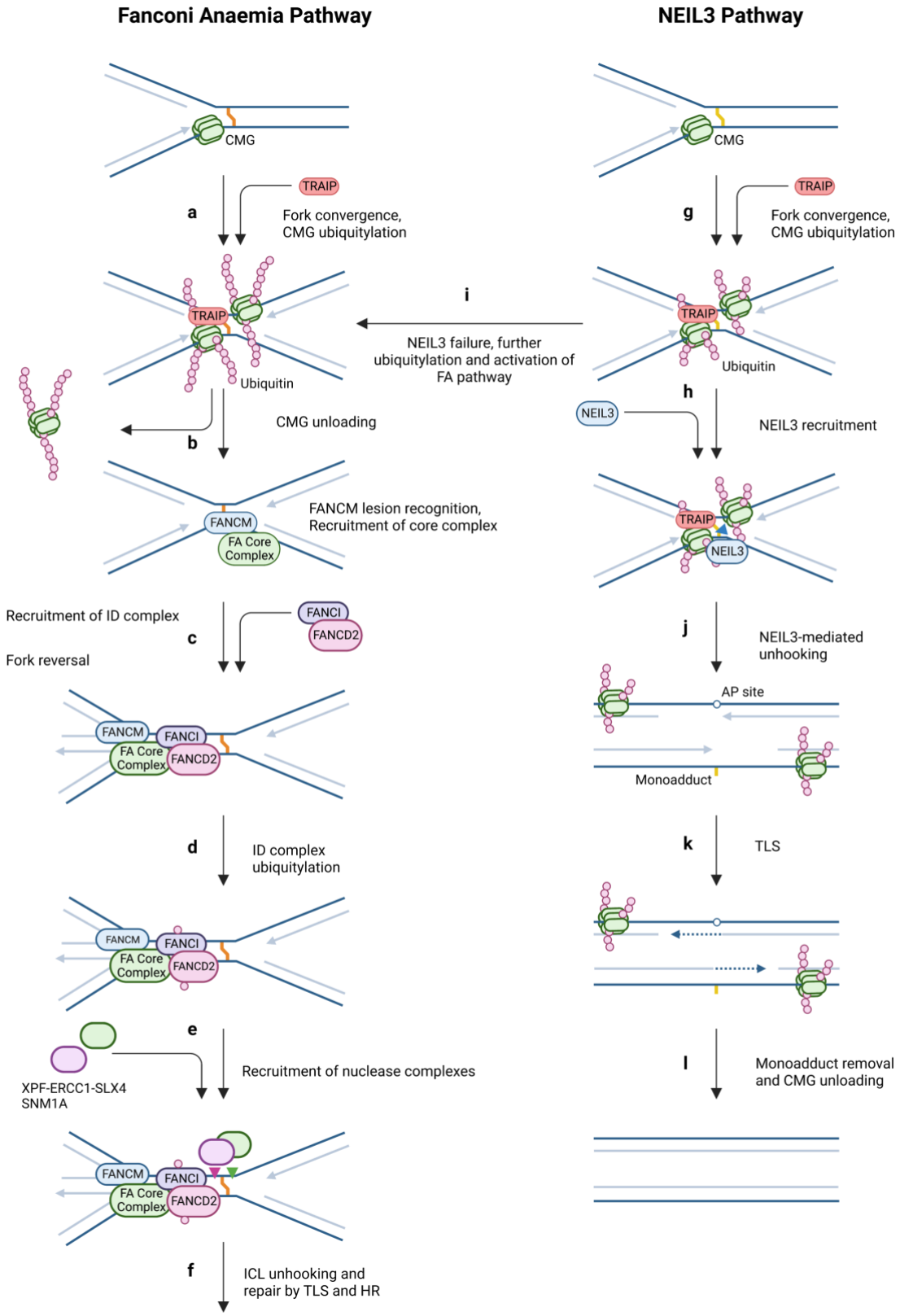
Fanconi Anaemia Pathway
NEIL3 Pathway
CMG
TRAIP
a
Fork convergence,
CMG ubiquitylation
Ubiquitin
b
CMG unloading
FANCM
FA Core Complex
FANCM lesion recognition,
Recruitment of core complex
Recruitment of ID complex
Fork reversal
c
FANCI
FANCD2
d
ID complex
ubiquitylation
e
XPF-ERCC1-SLX4
SNM1A
Recruitment of nuclease complexes
f
ICL unhooking and
repair by TLS and HR
i
NEIL3 failure, further
ubiquitylation and activation of
FA pathway
g
h
NEIL3
NEIL3 recruitment
j
NEIL3-mediated
unhooking
AP site
Monoadduct
k
TLS
l
Monoadduct removal
and CMG unloading

Figure 3. Fanconi anaemia and NEIL3-dependent ICL repair pathways

a-f) Depicts the fork convergence model of FA pathway repair of ICLs which is driven by the TRAIP-dependent ubiquitylation of the CMG helicase with long Ub chains. The pink and green arrowheads in panel **e)** indicate the location of the ICL unhooking incisions made in the phosphodiester backbone by XPF-ERCC1-SLX4 and SNM1A structure specific nucleases. **f)** following ICL unhooking the FA pathway proceeds with TLS and HR to repair the resulting ssDNA gap (downstream TLS and HR steps are not depicted here). **g-l)** Depicts the NEIL3 ICL repair pathway that is triggered by shorter chain ubiquitylation of CMG following replication fork convergence. In contrast to the FA pathway, NEIL3 directly cleaves the N-glycosl bond of an ICL itself depicted by the blue arrowhead in panel **h)**, preventing the need to generate a deleterious DSB. **i)** If NIEL3 is not able repair an ICL, ubiquitin accumulates on the CMG helicase and repair is channelled towards the FA pathway instead. Figure created using BioRender.com with reference to (Semlow and Walter, 2021).

1.1.7. DNA-protein crosslink repair

Covalent DNA-protein crosslinks (DPCs) are bulky lesions that pose a significant threat to genome integrity and cell viability as their size impairs processes that must traverse DNA such as transcription and DNA replication (Weickert and Stingele, 2022). Some DPCs can be adaptive, however, such as that formed between 5-hydroxymethylcytosine binding, ES cell specific (HMCES) and an AP site which shields it during DNA replication (Mohni et al., 2019). DPCs are heterogenous in nature but can be broadly classified into three categories based on the origin of their formation – enzymatic DPCs, non-enzymatic DPCs, and DPC-like trapped proteins – which are described in more detail below (Stingele et al., 2017).

1.1.7.1. Enzymatic DPCs

Enzymatic DPCs form when a covalent reaction intermediate is stabilised between DNA and a processing enzyme, prominent examples of which are TOP1, topoisomerase 2 (TOP2), and DNA-methyltransferase 1 (DNMT1) (Stingele and Jentsch, 2015). This can occur spontaneously or through the action of targeted therapeutic molecules.

TOP1 relieves the torsional stress in DNA molecules created during transcription or replication by generating a nick in one of the DNA strands allowing it to relax by freely rotating and then ligating the break together again (Pommier et al., 2016). TOP1 is covalently linked to the 3′ end of the nicked DNA strand via its active site tyrosine residue in a transient intermediate known as the TOP1cc that persists until the SSB is re-ligated, at which point TOP1 is released (Champoux, 2001). Any process that prevents re-ligation, however, traps TOP1 as a covalent DNA bound intermediate thereby generating a stable DPC. For example, the TOP1 inhibitor camptothecin and its derivatives topotecan and irinotecan stabilise the TOP1cc by intercalating at the TOP1-

DNA interface, while the release of TOP1 can also be prevented by naturally occurring DNA lesions that cause a distortion in the DNA molecular structure (Liu et al., 2000a; Pommier, 2006; Pourquier et al., 1997).

Stabilisation of TOP2's reaction intermediate similarly leads to the formation of a DPC. Conversely, however, TOP2 acts as a homodimer to create nicks in opposing DNA strands thereby generating a DSB with 5′ ends covalently bound by TOP2 (Chen et al., 2013). This allows superhelical tension to be relieved by passing another DNA strand through this gap. Several commonly used chemotherapeutic agents such as etoposide and doxorubicin can stabilise the transient TOP2 covalent complex thereby generating a DPC (Nitiss, 2009).

Cytotoxic DPCs can also be formed with the methyltransferase DNMT1 when cells are treated with the cytosine analogue 5-aza-2′-deoxycytidine (5-aza-dC), which acts as a pseudosubstrate for DNMT1 and traps its covalent reaction intermediate during methylation (Maslov et al., 2012).

1.1.7.2. Non-enzymatic DPCs

In addition to enzymatic sources of DPCs, potentially any protein in the vicinity of DNA can become covalently trapped due to the action of a crosslinking agent, which can have an endogenous or exogenous origin (Weickert and Stingele, 2022). Endogenous sources of crosslinking agents include acetaldehyde produced during ethanol metabolism, metabolically produced formaldehyde, and ROS which generate reactive free radical species (Barker et al., 2005; O'Brien et al., 2005). Exogenous crosslinkers include the commonly used platinum-based therapeutic agents cisplatin, carboplatin, and oxaliplatin, which in addition to ICL formation can generate DPCs (Chvalova et al.,

2007). Additionally, DPCs are formed by UV light and ionising radiation (IR) especially under hypoxic conditions (Zhang et al., 1995).

1.1.7.3. DPC-like trapped proteins

A final category of DPCs are those induced by PARP inhibitors (PARPi) such as olaparib, talazoparib, niraparib and rucaparib which trap PARP enzymes on DNA (Murai et al., 2012). While trapped PARP enzymes are not *bona fide* DPCs since they lack a covalent linkage to DNA, they nevertheless are bound tightly enough to be functionally equivalent and impose the same consequences on transcription and replication (Stingele et al., 2017). Significantly, trapping of PARP has been suggested to be a key mediator of PARPi efficacy with the cytotoxic effect of the different inhibitors correlating with their trapping efficiency (Hopkins et al., 2015).

Cells have evolved a wide range of repair pathways that target each of the three components of a DPC that allow them to respond to the diverse range of crosslinked proteins (Kuhbacher and Duxin, 2020). These broadly involve hydrolysis of the DNA–protein crosslink itself, nuclease-dependent repair, and protease-dependent repair described below.

1.1.7.4. Protease-mediated repair

The protease-mediated repair of DPCs is initiated when a translocating replicative CMG helicase encounters a trapped protein on the leading strand, causing it to stall (Fu et al., 2011). Stalling of CMG triggers the polyubiquitylation of the DPC by the E3 ligase TRAIP which promotes its bypass (Larsen et al., 2019). Bypass of the DPC by CMG is facilitated by the 5′ to 3′ helicase regulator of telomere elongation helicase 1 (RTEL1) which is thought to travel along the undamaged lagging strand and unwind DNA downstream of the DPC (Sparks et al., 2019). The precise molecular details of CMG

bypass are incompletely understood, but may involve the opening of a side channel in the hexameric ring structure of its minichromosome maintenance (MCM)2-7 subunit to allow the DPC to pass through. The bypass of CMG uncouples the replication machinery since replicative polymerases cannot bypass a DPC in the same fashion, resulting in extended ssDNA creation which is rapidly bound by RPA (Duxin et al., 2014). This ssDNA bound RPA then recruits the E3 ligase ring finger and WD repeat domain 3 (RFWD3) which further ubiquitylates the DPC stimulating its degradation (Gallina et al., 2021). RFWD3 also ubiquitylates surrounding factors which contributes to the recruitment of TLS polymerases required for the latter stages of DPC repair (Gallina et al., 2021). In order to facilitate downstream repair processes the trapped protein must be 'debulked' through proteolytic degradation carried out predominantly by the overlapping functions of the SPRTN protease and proteasome-mediated degradation (Larsen et al., 2019). Other proteases have also been implicated in DPC debulking such as the PCNA-interacting serine protease FAM111A, which has been shown to be important for removing trapped PARP1 and TOP1 enzymes (Kojima et al., 2020). SPRTN protease activity is promoted by the presence of a ssDNA-dsDNA junction provided by a stalled replication fork, while proteasomal degradation requires DPC polyubiquitylation (Reinking et al., 2020). More recently, it has been reported that the SPTRN-mediated cleavage of a DPC is facilitated by the unfolding of the protein adduct by the FANCJ helicase (also known as BRIP1) (Yaneva et al., 2023). Proteolysis reduces the size of a DPC allowing access by the TLS machinery to perform DNA synthesis across the remaining linked peptide. FANCJ has also been shown to facilitate TLS even when DPC degradation is blocked (Yaneva et al., 2023).

1.1.7.5. Repair by DPC hydrolysis

Two enzymes, TDP1 and TDP2, have evolved specifically to deal with the DPCs that form during the abortive action of TOP1 and TOP2 respectively, by cleaving the phosphodiester bond between a DNA terminus and the active site tyrosine residue of a TOP enzyme (Pommier et al., 2014). The tyrosyl-DNA linkage that TDP1 acts on is occluded by the bulk of the TOP1 enzyme and therefore requires processing to gain access (Lin et al., 2008). Degradation occurs by initial small ubiquitin-like modifier (SUMO)ylation followed by polyubiquitylation by a SUMO-targeted E3 ligase such as RNF4 which triggers proteasomal cleavage (Liu et al., 2021; Sun et al., 2020a). TDP1 then hydrolyses the tyrosyl-DNA phosphodiester bond creating a SSB whose repair occurs according to the pathway describe in section 1.1.5 above. The bonds between DNA and a trapped TOP2 dimer occur on the 5′ ends of DNA which are cleaved by TDP2 (Cortes Ledesma et al., 2009). Proteasomal degradation of TOP2 also occurs following SUMOylation and polyubiquitylation as for TOP1, but accessory factors such as the SUMO E3 ligase ZATT can also remodel the TOP2 DPC to allow access by TDP2 (Gao et al., 2014; Schellenberg et al., 2017). Cleavage by TDP2 generates a DSB with canonical 5′-P termini that can be ligated by the classical NHEJ repair pathway described in section 1.1.8.1 (Gomez-Herreros et al., 2013).

1.1.7.6. Nucleolytic repair

Classical DSB repair nucleases such as the MRN nuclease complex (composed of MRE11–RAD50–NBS1) can be repurposed for DPC repair (Neale et al., 2005). Protein adducts at the end of DNA stimulate the activity of MRN and this stimulation appears to be independent of the nature of the DPC (Deshpande et al., 2016). MRN activity is restricted to DNA ends by a ring-to-rod conformational transition whereby the MRE11

nuclease moves through the ring formed by two RAD50 subunit coiled coil domains which locks it in place next to a DPC and stimulates its nucleolytic activity (Kashammer et al., 2019). A nick is made on one DNA strand which is then resected in the 3′ to 5′ direction, at which point a second endonucleolytic incision is made to generate a DSB that frees the DPC adduct and allows for repair by canonical DSB repair mechanisms (Hoa et al., 2016).

1.1.8. Double strand break repair

While SSBs occur relatively commonly in cells, the generation of DSBs, while rarer, pose a far more cytotoxic threat (Tounekti et al., 2001). Indeed it is thought that a single unrepaired DSB is sufficient to lead to the death of a cell (Trenner and Sartori, 2019). Numerous repair pathways, therefore, have evolved to combat DSB formation and preserve genomic integrity which are reviewed below (Figure 4).

1.1.8.1. Non-homologous end joining

The two major pathways of DSB repair are classical non-homologous end joining (NHEJ) and HR. NHEJ repairs the majority of DSBs in mammalian cells and is the favoured repair pathway throughout G1 and G2 phase of the cell cycle, while HR is used in S and G2 phase when there is the presence of actively replicating chromosomes and sister chromatids (Beucher et al., 2009; Karanam et al., 2012). NHEJ is deprioritised during S phase as repair of one-ended DSBs, resulting from collapsed replication forks, can result in deleterious chromosomal rearrangements by ligating DNA ends from different chromosomes (Scully et al., 2019). NHEJ has traditionally been seen as an error prone repair mechanism that leads to the formation of indel mutations due to the lack of an intact homologous template, a fact that is exploited by CRISPR-Cas9 gene editing (Hsu et al., 2014; Nambiar et al., 2022). However, it has been suggested that NHEJ is actually a highly accurate and efficient process, with indel formation being accounted for by the requirement to process some chemically and structurally incompatible ends rather than an inherent feature of the NHEJ machinery (Betermier et al., 2014).

NHEJ is initiated by the binding of DSB ends by the Ku70/80 heterodimer, a toroidal ring-shaped structural complex that wraps around DNA (Mahaney et al., 2009; Walker et al., 2001). Ku70/80 predominantly provides a platform for the recruitment and

activation of downstream NHEJ repair factors, but also acts to protect DSB ends from unwinding and resection by helicases and nucleases respectively (Ciccia and Elledge, 2010). The Ku70/80 heterodimer loads and activates the catalytic subunit of the phosphatidylinositol 3-kinase-related kinase (PIKK) DNA-dependent protein kinase (DNA-PK) (DNA-PKcs) forming a large holoenzyme that tethers broken DNA ends and promotes synapse formation (Graham et al., 2016). DNA-PKcs is autophosphorylated following binding to DSB ends which promotes the formation of short-range synaptic complexes that allow for the re-ligation of DNA ends (Graham et al., 2016). Autophosphorylation has also been shown to promote DNA-PKcs dissociation from the Ku70/80 heterodimer and may serve as a way to promote DNA-PK complex disassembly from DNA ends to allow access by end processing factors such as ARTEMIS (Dobbs et al., 2010; Hammel et al., 2010). Autophosphorylation at different residue clusters on DNA-PKcs has also been suggested to control the extent of end processing at DSB ends and therefore the choice between NHEJ and HR pathways; with phosphorylation at the T2609 "ABCDE" cluster exerting a stimulatory effect while phosphorylation of the S2056 "PQR" cluster prevents excessive end processing (Jiang et al., 2015; Shrivastav et al., 2008).

Ligation of DNA ends is carried out by DNA ligase 4 (LIG4) in conjunction with its stable binding partner X-ray repair cross-complementing protein 4 (XRCC4) (Critchlow et al., 1997; Grawunder et al., 1997). Ligation is also promoted by the interactions of the core NHEJ factors XRCC4-like factor (XLF) and paralog of XRCC4 and XLF (PAXX), which play a partly redundant role as demonstrated by a synthetic lethal interaction between the two proteins (Ahnesorg et al., 2006; Balmus et al., 2016; Lescale et al., 2016; Ochi et al., 2015). DSB ends that are not immediately amenable to ligation can be processed by NHEJ accessory factors such the nuclease ARTEMIS to trim incompatible

ends, POLμ and POLλ to add nucleotides, and TDP1 and PNKP to process modified nucleotides that block ligation (Zhao et al., 2020).

1.1.8.2. Alternative end joining

Cells also employ an alternative form of NHEJ (alt-EJ) which utilises distinct molecular machinery (i.e. not requiring Ku, XRCC4, or LIG4) that can be used as a backup repair mechanism if classical NHEJ fails or in cells with an NHEJ deficiency (Sfeir and Symington, 2015). Alt-EJ also encompasses the pathways of microhomology-mediated end joining (MMEJ) and DNA polymerase-theta(POLθ)-mediated end joining (TMEJ), but in eukaryotic cells an overall definition has been suggested to satisfy the following criteria: end joining that is independent of classical NHEJ machinery, utilises resected 3′ overhangs, favours the presence of short microhomologies flanking the DSB site, and predominantly engages POLθ (Ramsden et al., 2022). The reliance of alt-EJ pathways on POLθ and the observed depletion of microhomology associated deletions that typically define MMEJ in POLθ-deficient cells has led to some authors arguing for these pathways to be subsumed under the TMEJ term (Wyatt et al., 2016). However, for clarity the process will be described as alt-EJ for the remainder of this section.

Repair of a DSB by alt-EJ proceeds according to the stages of DNA end recognition, end pairing and microhomology search, trimming of non-homologous tails, DNA synthesis from microhomology regions, and resolution. Processing of DSB ends by nucleases such as MRN or CtIP is required for the initiation of alt-EJ and is one of the factors that shifts pathway choice away from NHEJ and towards alt-EJ or HR repair (Truong et al., 2013; Xie et al., 2009). In mammals it has been suggested that resected overhangs of ~30–70 nucleotides promotes the choice of alt-EJ over NHEJ (Wyatt et al., 2016). ssDNA regions of resected ends are bound by the RPA complex which removes

secondary structure from ssDNA and prevents the annealing of homologous regions contained within overhangs themselves (Deng et al., 2015). RPA thus imposes an inhibitory barrier to alt-EJ progression which is overcome by the activity of the helicase-like HelD domain of POLθ which functions to displace RPA from ssDNA and allow for the subsequent stages of end pairing and microhomology search (Mateos-Gomez et al., 2017). Interestingly, HMCES may also play a role in the RPA removal stage as it was shown to bind to ssDNA overhangs and promote alt-EJ (Shukla et al., 2020). The activity of PARP1 has also been implicated in the recruitment of alt-EJ factors and synapse formation between DSB ends in experiments in mammalian cells deficient in classical NHEJ components (Audebert et al., 2004; Mansour et al., 2010; Wang et al., 2006). Interestingly, FANCD2 has also been shown to promote the recruitment of POLθ to sites of DSBs and repair via alt-EJ in a BRCA1/2 deficient, and therefore HR deficient, background (Kais et al., 2016).

Following displacement of RPA by POLθ HelD activity, 3′ overhangs are paired and if microhomology regions are present within the overhangs they are annealed. Studies *in vitro* and in mammalian cells have demonstrated that alt-EJ is completed efficiently when regions of microhomology are 3 bp or longer and are located within 15 nucleotides of the DSB end (Carvajal-Garcia et al., 2020; He and Yang, 2018). The incidence of such microhomologies is expected to be quite common, however, with a theoretical frequency of 93% in break site flanking regions comprised of random 15 bp sequences (Carvajal-Garcia et al., 2020). Since regions of microhomology are unlikely to be located at the proximal ends of 3′ overhangs their pairing often results in non-homologous overhanging flaps which must be removed for efficient alt-EJ (Ramsden et al., 2022). Candidate nucleases for this function include the 3′ nuclease contained in the PolD domain of POLθ which would allow spatiotemporal coupling of its nuclease activity to

its subsequent DNA synthesis activity, or the 3′ flap endonuclease complex XPF–ERCC1, deficiency of which has been seen to reduce alt-EJ in mammalian cells (Bennardo et al., 2008; Zahn et al., 2015).

The single-strand regions surrounding annealed microhomology regions are filled in by the action of POLθ's PolD domain which possesses template-dependent, low processivity, error-prone polymerase activity (Arana et al., 2008; Hogg et al., 2011). It is thought that POLθ activity alone is insufficient to complete the gap-filling synthesis required for alt-EJ and other more highly processive polymerases such as POLδ are therefore employed to complete this step (Layer et al., 2020). The final ligation step of alt-EJ that resolves the DSB is thought to predominantly be carried out by LIG3 with LIG1 functioning as a backup enzyme (Masani et al., 2016; Simsek et al., 2011).

1.1.8.3. Single strand annealing

An additional pathway for repairing DSBs is single-strand annealing (SSA) that, similarly to alt-EJ, involves the formation of a synapse between broken DNA ends via the annealing of homologous regions that flank the break site. Repair via SSA proceeds along broadly similar lines to alt-EJ involving the steps of DSB end resection, annealing of homologous regions flanking the break site, removal of 3′ flaps, gap filling DNA synthesis, and ligation to seal nicks (Bhargava et al., 2016). SSA differs from alt-EJ, however, in the extent of end resection that initiates the pathway, the nature of the homologous repeats used, and the factors that are engaged in the respective pathways. A key difference between the two pathways is the use of longer regions of homology in SSA compared to alt-EJ, with direct repeats of ~30-400 bp being using in SSA compared to just ~3 bp in alt-EJ (Lin et al., 1984; Sugawara et al., 2000). The choice of pathway between SSA and alt-EJ pathways is therefore partly driven by the extent of end resection

that occurs at a DSB, with SSA requiring a greater level of resection to reveal the larger homologous regions required for its annealing step (Symington, 2016). Interestingly, disruption of PARP signalling via inhibition with olaparib showed no effect on SSA, while a marked decrease in alt-EJ was observed, suggesting a distinct role for PARP in the latter pathway as discussed above (Howard et al., 2015). Conversely, a key mediator of homology annealing and synapse formation in SSA is RAD52, whose function is largely dispensable in alt-EJ (Bhargava et al., 2016; Van Dyck et al., 1999). RAD52 also stimulates the activity of the XPF-ERCC1 3′ flap nuclease complex, which functions to remove the unannealed, non-homologous sequences flanking the break site in a similar manner to alt-EJ and which is required for efficient completion of SSA (Al-Minawi et al., 2008; Motycka et al., 2004). After processing of 3′ flaps the SSA pathway completes by gap filling DNA synthesis and ligation of DNA ends to seal nicks. However, these stages remain less well characterised than the terminal stages of alt-EJ with the precise factors utilised currently unknown. Various authors have hypothesised that POLδ and LIG1 utilised in alt-EJ are potential candidates for the functions of gap filling and end ligation respectively in SSA (McVey et al., 2016; Vu et al., 2022).

A factor that exerts an inhibitory effect on the annealing of complementary ssDNA by RAD52 is RAD51 which thereby limits SSA and promotes repair via HR as described below (Wu et al., 2008). Like the HR pathway, SSA also requires the resection of DSB ends so it is likely that this pathway is restricted to S/G2 phase when the cyclin-dependent kinase (CDK) controlled nucleases responsible for end resection, such as CtIP, are active (Huertas and Jackson, 2009). It is possible that the SSA pathway therefore functions during S phase when there is active resection, but not always the presence of a sister chromatid required for efficient HR repair (Bhargava et al., 2016; Johnson and Jasin, 2000). Interestingly, while repair of replication-independent DSBs via SSA is

obligatorily error-prone due to the removal of the intervening sequence between homologous repeats, it has been suggested that SSA repair at stalled replication forks may in fact be error-free. This is proposed to be because stalled replication forks have a tendency to generate tandem duplications via the aberrant restart of replication which can result in the end-on-end joining of sequences duplicated by converging replication forks by NHEJ (Willis et al., 2017). Therefore, the action of SSA to anneal tandem duplications and remove the intervening sequence reverts aberrantly duplicated sequences to their original form and maintains genomic fidelity (Scully et al., 2019).

1.1.8.4. Homologous recombination repair

In contrast to the end joining pathways described above, repair of DSBs via HR involves the templated repair from an intact homologous DNA molecule allowing for the potentially error-free resolution of damage (Takata et al., 1998). In somatic cells the sister chromatid is preferentially used as the recombination template due to its close physical alignment and sequence identity, which prevents the loss of heterozygosity that would occur if the homologous chromosome of a diploid cell was used (Kadyk and Hartwell, 1992). The initial step of HR is the 5′ to 3′ resection of DSB ends to generate 3′ ssDNA overhangs that serve as a platform for the downstream formation of RAD51 nucleoprotein filaments that mediate the HR-defining features of template duplex DNA strand invasion and homology search (San Filippo et al., 2008). End resection is initiated in a 'short-range' process by the MRN complex which generates a nick on the 5′-terminated strand up to 300–400 bp away from the break site and then utilises 3′ to 5′ exonuclease activity to extend this resection back to the DSB site (Symington, 2016). Localisation of MRN to DSB sites also activates the ataxia-telangiectasia mutated (ATM) kinase which serves as an apical coordinator of the DSB repair response (Dupre et al.,

2006; Lee and Paull, 2004). A crucial cofactor of MRN, required for efficient 'short-range' resection, is CtIP which additionally tethers resection activity, and thus HR, to S/G2 phase of the cell cycle due to its requirement to be activated by phosphorylation by CDKs (Huertas and Jackson, 2009; Sartori et al., 2007). CtIP phosphorylation by ATM is also required for resection in human cells (Wang et al., 2013). A consequence of the 3′ to 5′ exonuclease activity of MRN is to strip bound proteins from 3′ ssDNA overhangs allowing for access by downstream HR factors. It is thought that MRN–CtIP mediated short-range resection also helps to remove the NHEJ factor Ku70/80 from DSB ends, thereby channelling repair towards the HR pathway (Chanut et al., 2016).

After initial short-range resection, longer-range unwinding and resection of the 5′ strand is carried out by the partially overlapping functions of the EXO1 and DNA2 nucleases and Bloom Syndrome RecQ-like helicase (BLM) and Werner Syndrome RecQ-like helicase (WRN) helicases to generate long 3′ ssDNA overhangs (Gravel et al., 2008; Mimitou and Symington, 2008; Nimonkar et al., 2011; Sturzenegger et al., 2014; Zhu et al., 2008). While not strictly necessary for the progression of HR, it is thought that long-range resection is important to ensure the accurate pairing of repetitive sequences to sister chromatid templates and to promote robust activation of ATR by regions of RPA-coated ssDNA that prevents premature entry into mitosis (Chung et al., 2010). Accordingly, the 3′ ssDNA tail generated by end resection is rapidly bound by the heterotrimeric RPA complex composed of RPA1, RPA2, and RPA3, which removes secondary structures from the ssDNA and prevents premature metabolism or off-target interactions with the resected end (Ciccia and Elledge, 2010; Wold, 1997).

The next stage of HR involves the displacement of RPA by RAD51 to form a dynamic nucleoprotein filament that subsequently mediates the homology search for an appropriate repair template (Benson et al., 1994; West, 2003). To overcome the barrier to

ssDNA access imposed by the higher affinity binding of RPA, RAD51 binding requires the concerted action of breast cancer 1 (BRCA1)–BRCA1-associated RING domain 1 (BARD1), partner and localizer of BRCA2 (PALB2), and breast cancer 2 (BRCA2) (Tarsounas and Sung, 2020). BRCA1–BARD1, through its interaction with PALB2, functions to recruit BRCA2 whose interaction with ssDNA and RAD51 monomers facilitates nucleofilament formation by competing with RPA for ssDNA binding (Jensen et al., 2010; Sy et al., 2009; Thorslund et al., 2010; Zhang et al., 2009). The BRCA2 associated factor DSS1 has also been shown to promote the exchange of RPA for RAD51 on ssDNA (Zhao et al., 2015). The dual roles of BRCA1 in promoting end resection (discussed below) and RAD51 nucleofilament assembly suggest that BRCA1 functionally couples these processes to ensure the timely loading of RAD51 (Chen et al., 2018). RAD51 nucleofilaments, also known as 'presynaptic complexes', perform the central functions of homology search and strand invasion in HR and their assembly is a dynamic process that is tightly regulated by the action of mediator proteins that promote nucleofilament assembly and anti-recombinogenic helicases that disrupt RAD51 binding (Heyer et al., 2010). While the precise mechanism of homology search is still uncharacterised it is thought that presynaptic complexes make multiple temporary contacts and randomly probe targets in the genome until a homologous region is identified (Renkawitz et al., 2014). This process is aided by the observed increase in mobility of broken DNA ends (Mine-Hattab and Rothstein, 2012). Once RAD51 nucleofilaments invade the duplex DNA of an homologous template they facilitate the base pairing to complimentary sequences forming a heteroduplex 'synaptic complex' in a process that is promoted by an additional function of BRCA1-BARD1 (Zhao et al., 2017). Stabilisation of the synaptic complex resulting from sufficient base pairing with the invading strand leads to the formation of a displacement loop (D-loop) in the

homologous template creating a heteroduplex region of DNA (San Filippo et al., 2008). D-loops are further stabilised by RPA binding to the displaced ssDNA and removal of RAD51 from heteroduplex DNA by the translocase RAD54 (Eggler et al., 2002; Wright and Heyer, 2014).

Following D-looop formation, the 3′ end of the invading strand can then act to prime DNA synthesis using the invaded sister chromatid DNA as a template in a process known as gene conversion, which allows for the maintenance of gene sequence fidelity (McVey et al., 2016). It is thought that POLδ is the key polymerase that carries out nascent strand synthesis during HR, but TLS polymerases such as POLη have also been implicated to a lesser degree (Sneeden et al., 2013). Experiments performed in Drosophilia and yeast suggest that DNA synthesis is regulated by multiple rounds of RAD51-mediated strand invasion, short DNA synthesis, and displacement of the D-loop, thereby limiting the extent of gene conversion (McVey et al., 2004; Smith et al., 2007). The resolution of D-loop structures can occur via various pathways that are considered below.

Synthesis-dependent strand annealing (SDSA) is the predominant repair pathway in somatic cells and occurs when the invading strand of a D-loop is displaced following synthesis and the nascent strand anneals with the second end of the DSB (Sung and Klein, 2006). Since no Holliday junction is formed, SDSA is therefore a conservative pathway that precludes the possibility of crossover events.

In contrast to SDSA, the canonical HR repair pathway, which functions chiefly during meiosis, involves the capture of the second DSB end by the D-loop and formation of a double Holliday junction (dHJ) structure, which can then be resolved by three distinct pathways that result in crossover or non-crossover events (Duckett et al., 1988; West et al., 2015). The first, preferentially utilised pathway, is a ‘dissolution’ mechanism

that utilises the BTR complex (comprising BLM, TOP3α, RMI1, and RMI2) that mediates the convergent branch migration of the two HJs and decatenation without the generation of crossover events (Bizard and Hickson, 2014; Wu and Hickson, 2003). The remaining two pathways are nucleolytic pathways that employ the structure specific nucleases SLX1–SLX4–MUS81–EME1 (SLX–MUS complex) or GEN1 to create asymmetric or symmetric incisions respectively in the dHJ structure and resolve breaks in a way that can either lead to crossover or non-crossover events (Rass et al., 2010; Sarbajna et al., 2014; Wyatt et al., 2013).

A third pathway for restoring DSBs is break-induced replication (BIR) which usually occurs when there is a lack of a second DSB end, such as that results from a collapsed and broken replication fork (Sakofsky and Malkova, 2017). BIR results in unrestrained nascent strand synthesis which proceeds via a migrating bubble mechanism resulting in conservative DNA synthesis that can run the whole length of the template to the telomere ends (Saini et al., 2013). BIR is a highly inaccurate and mutagenic process that can lead to the loss of heterozygosity of the regions downstream of a DSB and so is not favoured in most instances when there is a second DSB end present (Deem et al., 2011).

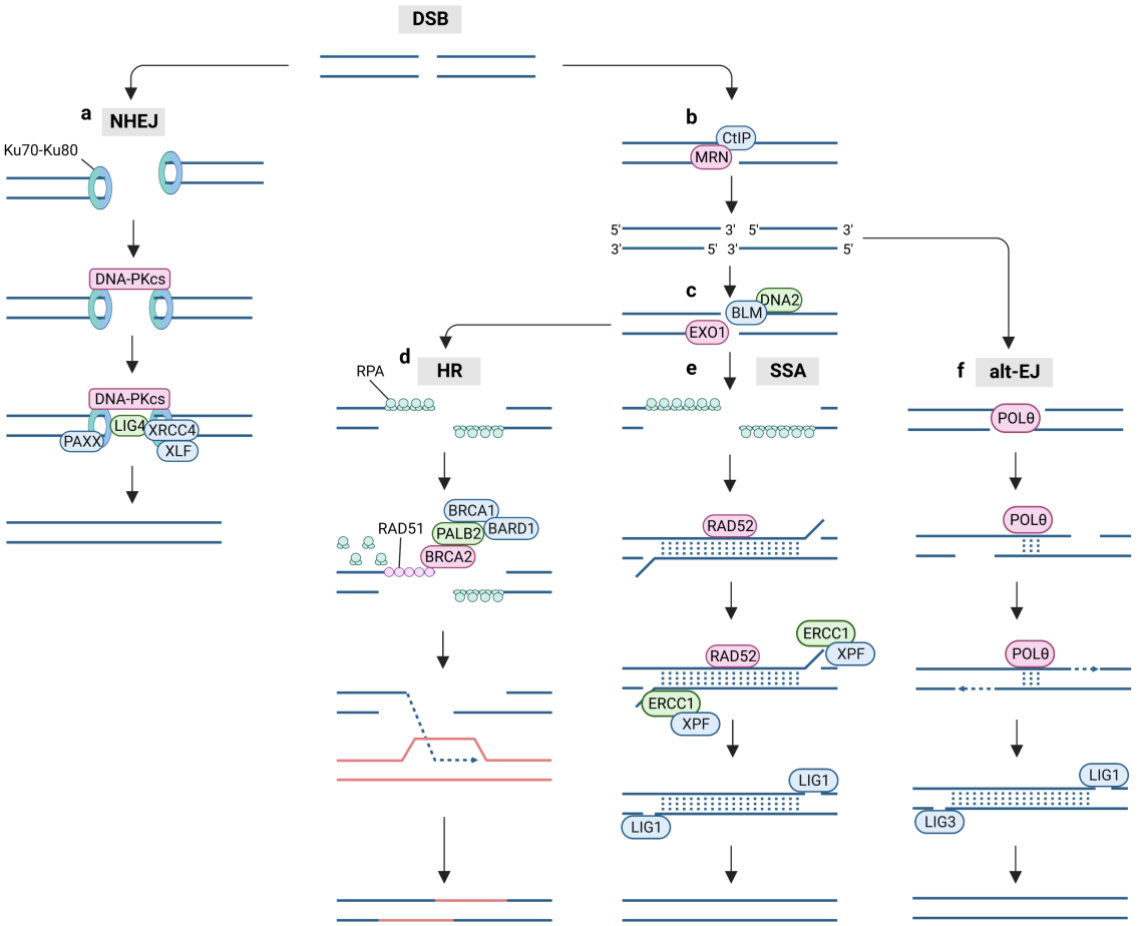

Figure 4. Double-strand break repair pathways

The choice of DSB repair pathway depends on cell cycle dependent factors and the extent of DNA end resection at a break site. **a)** The majority of DSBs are repaired by the NHEJ pathway, which is active throughout most of the cell cycle and involves the direct ligation of broken DNA ends by XRCC4–LIG4 together with XLF or PAXX following end recognition by the Ku70/80 heterodimer. **b)** DSB repair pathways dependent on homology-directed repair are initiated by MRN–CtIP resection which is restricted to S-

phase of the cell cycle. **f)** This short-range resection is sufficient to promote POLθ driven alt-NHEJ which relies on very small (~3 bp) regions of microhomology to facilitate strand annealing. **c)** Alternatively, BLM-DNA2 helicase-nuclease and EXO1 nuclease may promote longer range resection to generate ssDNA overhangs that are bound by RPA and facilitate **d)** HR repair and **e)** SSA that requires more extensive regions of homology. **d)** In HR repair the generation of RAD51 nucleofilaments, aided by the actions of BRCA1, PALB2, and BRCA2, facilitates strand invasion and homology search in a sister chromatid that can be utilises as a repair template to restore the accurate DNA sequence. **e)** RAD52 on other hand facilitates the pairing of homologous regions found near a break site on the same strand of DNA which restore integrity but results in the deletion of sequences that intervene regions of homology. Figure created using BioRender.com with reference to (Groelly et al., 2023).

1.1.8.5. Choice of repair pathway

A key determinant in the choice between NHEJ and HR pathways is the initiation of DNA end resection which is driven in part by the competing actions of BRCA1-BARD1 and p53-binding protein 1 (53BP1), which act to promote and antagonise DSB end resection respectively (Cejka and Symington, 2021; Scully et al., 2019). The engagement of these factors has been shown to depend on the chromatin context of a DSB with BARD1 and 53BP1 being readers of histone H2A lysine 15 (H2AK15) ubiquitylation and histone H4 lysine 20 (H4K20) methylation status. 53BP1 binds H2AK15Ub, laid down by RNF168, and H4K20me2 where it recruits RIF1 and REV7, SHLD1, SHLD2 and SHLD3 that make up the 'shieldin' complex which inhibits end resection by the binding of

SHLD2 to ssDNA via oligonucleotide/oligosaccharide binding (OB)-fold domains (Botuyan et al., 2006; Fradet-Turcotte et al., 2013; Noordermeer et al., 2018). Resection is also countered by the 53BP1-dependent fill-in DNA synthesis by POLα that limits the amount of ssDNA generated at a DSB and therefore inhibits RAD51 filament assembly (Mirman et al., 2022; Paiano et al., 2021). BRCA1 is similarly recruited to DSB sites through its binding partner BARD1 which binds to RNF168-dependent H2AK15Ub via a BRCT-domain-associated ubiquitin-dependent recruitment (BUDR) motif (Becker et al., 2021; Krais et al., 2021). Crucially, however, BARD1 recognises unmethylated H4K20 rather that its di-methylated counterpart found in mature chromatin, which restricts BRCA1-BARD1 recruitment to nascent chromatin in proximity to active replication forks (Nakamura et al., 2019). These chromatin marks together maintain NHEJ as the default repair pathway through most of interphase, but preference the use of HR in the repair of broken replication forks when the use of NHEJ to repair one-ended breaks would create toxic chromosomal translocations (Balmus et al., 2019). Interestingly, recruitment of both BRCA1-BARD1 and 53BP1 is inhibited during mitosis therefore requiring the engagement of other factors to safeguard DSBs during mitosis (Blackford and Stucki, 2020). Accordingly, it was discovered that TOPBP1 is recruited to DSB sites during mitosis by an interaction with casein kinase 2 (CK2) phosphorylated mediator of DNA damage checkpoint 1 (MDC1) and together with cellular inhibitor of PP2A (CIP2A) forms filamentous structures that bridge DSB sites to tether broken chromosomes together to ensure correct segregation until breaks can be repaired in the next G1 phase (Leimbacher et al., 2019). Since CK2 phosphorylation of MDC1 is not cell-cycle dependent, an additional function of CIP2A is to specifically enforce recruitment of TOPBP1 during mitosis (Adam et al., 2021; De Marco Zompit et al., 2022).

1.1.8.6. HELQ

A protein with an emerging role in the repair of DSBs is the ATP-dependent 5′ to 3′ helicase POLQ-like helicase (HELQ) (Takata et al., 2013). Loss of the *HELQ* gene results in ICL sensitivity and infertility in mice and predisposes cells to become cancerous (Adelman et al., 2013). HELQ was found to possess strand annealing capability in addition to its helicase activity that facilitates the pairing of complementary sequences and therefore promotes the processes of SSA, MMEJ, and the SDSA mode of HR (Kamp et al., 2021). Indeed, genetic perturbation of *HELQ* in cells led to the persistence of RAD51 foci following treatment with the ICL inducing agent MMC, and reduced repair via SSA and MMEJ in reporter assays (Adelman et al., 2013; Anand et al., 2022). The activity of HELQ was shown to be regulated by the contrasting actions of RPA and RAD51 which promote its strand annealing and helicase actions respectively (Anand et al., 2022). From a mechanistic point of view HELQ is thought to capture RPA coated ssDNA and displace RPA to facilitate its binding to complementary sequences (Jenkins et al., 2021). More recently HELQ was shown to physically interact with the POLD subunit of POLδ and restrain DNA synthesis during HR repair, thereby limiting the extent of long tract gene conversion (LTGC) and DNA duplication thus promoting genome stability (He et al., 2023). Interestingly, HELQ was identified as a synergistic interactor of the homologous recombination factor with OB-fold (HROB) which is proposed to act as a loader for the MCM8–MCM9 helicase complex that functions in a post-synaptic process during HR, possibly by facilitating D-loop migration (Hustedt et al., 2019). This positions HELQ as a mediator of strand annealing processes downstream of RAD51 nucleofilament formation that functions redundantly with the HROB–MCM8–MCM9 axis.

1.2. The replication stress response

One of the most significant threats to genome stability is posed by lesions that lead to the stalling of replication forks (Ciccia and Elledge, 2010). Replication fork stalling falls under the broader category of replication stress, which is defined as any process that causes a deviation from physiological replication fork progression and is caused by a wide range of genotoxic lesion types with endogenous and exogenous sources (Saxena and Zou, 2022). Endogenous sources of fork stalling lesions include the misincorporation of ribonucleotides into replicating DNA, ssDNA gaps, AP sites, transcription-replication conflicts, RNA-DNA hybrids, DPCs, presence of DNA secondary structures such as G-quadruplexes, depletion of dNTP nucleotide pools, oncogene driven increases in replication origin firing, and the presence of inherently hard-to-replicate regions within the genome (Zeman and Cimprich, 2014). Exogenous sources of fork stalling lesions include genotoxic chemotherapeutic agents that cause ICL formation such as cisplatin and MMC, topoisomerase inhibitors such as camptothecin or topotecan, alkylating agents, or antimetabolites (Ceccaldi et al., 2016; Kuhbacher and Duxin, 2020). Exogenous physical sources such as IR and UV light can also produce genotoxic insults which lead to SSB or DSBs, or pyrimidine dimers and 6-4 photoproducts respectively (Ciccia and Elledge, 2010). Altogether it is estimated that a typical cell may experience up to 10^5 spontaneous lesions a day, some of which impose replication stress inducing lesions (Hoeijmakers, 2009). Moreover, it has been shown that replication stress is higher in cancer and pre-cancer cells and is a leading cause of genomic instability and tumorigenesis (Gaillard et al., 2015). To combat replication stress, cells have evolved an intricate network of pathways known as DNA damage tolerance (DDT) pathways (Sale, 2012). Importantly, DDT pathways are regulated and dynamically controlled by post-

translational modifications (PTMs), with ubiquitylation and phosphorylation being central modifiers (Mirsanaye et al., 2021).

1.2.1. The role of ATR

ATR is the apical PIKK kinase which coordinates the response to replication stress in cells (Saldivar et al., 2017). In contrast to the ATM and DNA-PK kinases, loss of ATR is embryonic lethal reflecting its role in responding to a wider range of genotoxic stress (Brown and Baltimore, 2000). The response of ATR centres on processes that generate ssDNA (Zou and Elledge, 2003). The encounter of certain lesions by the replisome leads to replication fork stalling and can lead to the functional uncoupling of the CMG helicase and replicative DNA polymerases due to the discrepancy in the ability of the two machineries to bypass lesions (Figure 5) (Byun et al., 2005). While this imposes less of a burden for lagging strand synthesis due to the ability to reprime and synthesise Okazaki fragments when a fork stalls; on the leading strand the continued procession of the CMG helicase without the concomitant activity of DNA polymerases leads to the generation of large sections of ssDNA (Taylor and Yeeles, 2019). It is thought, however, that certain lesion types such as ICLs may not lead to significant replisome uncoupling if they stall both the helicase and polymerase functions. Rather ssDNA may be generated following fork reversal, a process when nascent DNA strands anneal together to form a four-way junction, which is susceptible to nucleolytic resection (Neelsen and Lopes, 2015; Thangavel et al., 2015). In either case, the ssDNA generated is rapidly bound by the RPA complex which possesses multiple OB-fold domains that allow it to make high-affinity ($K_a \approx 10^{-10}$) contacts with ssDNA (Fanning et al., 2006; Kim et al., 1994). RPA bound ssDNA then acts as a platform to recruit ATR via its obligate binding partner ATR

interacting protein (ATRIP) (Zou and Elledge, 2003). ATR activity at sites of DNA damage is then stimulated by two separate factors, TOPBP1 and ETAA1. TOPBP1 is recruited to ssDNA-dsDNA junctions via an interaction with the RAD9–RAD1–HUS1 (9-1-1) clamp complex and contacts ATR–ATRIP via an ATR activating domain (AAD) to stimulate its activity (Delacroix et al., 2007; Kumagai et al., 2006). ETAA1, on the other hand, is recruited via a direct interaction with RPA and similarly activates ATR via an AAD domain (Bass et al., 2016; Haahr et al., 2016). Once activated, ATR phosphorylates a multitude of targets to promote cell cycle arrest, suppress global origin firing while promoting local dormant origin firing, stimulate dNTP synthesis, and stabilise and facilitate repair and restart of damaged replication forks (Saldivar et al., 2017).

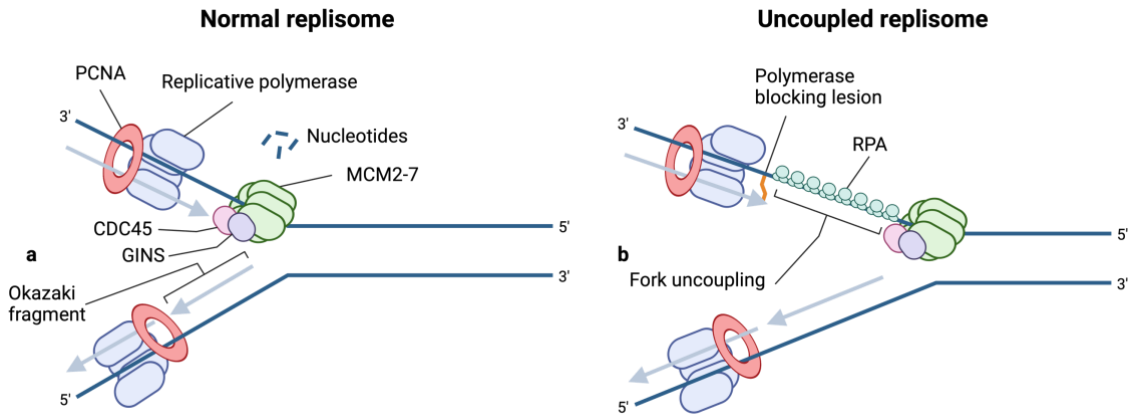

Figure 5. Uncoupling of replication forks

a) During normal replication in eukaryotic cells the parental template DNA is unwound by the CMG helicase complex, and DNA is replicated by the coupled action of a replicative polymerase (POLδ or POLε). This occurs continuously on the leading strand through the action of POLε but requires repeated priming and engagement of POLδ to generate discontinuous Okazaki fragments on the lagging strand. **b)** When a replisome encounters certain types of DNA lesions (indicated by the red triangle) it can result in the selective stalling of the replicative polymerase, while the CMG helicase is able to traverse the lesion and continue unwinding the DNA. Whilst on the lagging strand the inherently discontinuous nature of DNA synthesis can circumvent a polymerase stalling lesion, on the leading strand this often leads to the aberrant generation of long stretches of ssDNA that is bound and protected by RPA. Figure created using BioRender.com with reference to (Cybulla and Vindigni, 2023).

1.2.1.1. Cell cycle arrest

A central target of ATR phosphorylation is the protein checkpoint kinase 1 (CHK1) which promotes its activation. Activated CHK1 in turn phosphorylates the CDC25A phosphatase, promoting its proteasomal degradation, and thereby preventing its removal of inhibitory phosphorylation marks from CDK1 and CDK2 (Liu et al., 2000b; Mailand et al., 2000). CHK1 also exerts its cell cycle arrest function by activating the WEE1 kinase which promotes the inhibitory phosphorylation of CDK1 (Harvey et al., 2005; Lee et al., 2001).The inhibition of CDK1 and CDK2 prevents cells from passing the G2–M and S–G2 cell cycle checkpoints, respectively, resulting in cell cycle arrest and allowing time for DNA repair before entry into mitosis (Boutros et al., 2006; Zhao et al., 2002).

1.2.1.2. Regulation of origin firing and dNTP pools

Another central function of the ATR–CHK1 axis in response to replication stress is to suppress the firing of replication origins (Saldivar et al., 2017). Origin firing is a two-step process that involves the licencing of origins in G1 by the loading of the pre-replication complex (pre-RC) followed by activation of replicative helicase function in S-phase by loading of the pre-initiation complex (pre-IC) (Fragkos et al., 2015). The pre-RC is partly made up by the origin recognition complex (ORC), the licencing factor CDT1, and the hexameric replicative helicase MCM2-7; while the pre-IC complex includes CDC45, Treslin, the GINS complex, TOPBP1, DDK kinase (also known as DBF4-CDC7), CDKs, and a replicative polymerase (Fragkos et al., 2015). Importantly, the recruitment of the pre-IC is dependent on phosphorylation events carried out by DDK and CDK kinases, while helicase activation requires CDC45 binding. The CHK1-mediated cascade leading to CDK1 inhibition described above therefore is one way that ATR activation

suppresses origin firing (Katsuno et al., 2009). CHK1 has also been shown to directly phosphorylate Treslin, which disrupts its recruitment of CDC45 and thereby limits origin firing (Guo et al., 2015). An additional mechanism whereby ATR suppresses origin firing is its phosphorylation of the MLL methyltransferase which promotes its stabilisation leading to methylation of histone H3 Lys 4 (H3K4me), which is inhibitory to CDC45 loading at nearby replication origins (Liu et al., 2010).

A notable feature of ATR's control of origin firing during replication stress is its inhibition of origin firing globally, while facilitating local dormant origin firing (Ge and Blow, 2010). Replication in eukaryotes occurs in clusters of licenced origins termed 'replication factories' where only a fraction of origins will fire at one time while the others remain dormant (Hozak and Cook, 1994). It is thought therefore that ATR's promotion of dormant origin firing at sites close to a stalled fork allows completion of replication within these regions, while suppression of global dormant origin firing ensures that further fork stalling is prevented (Yekezare et al., 2013). The key role of ATR was demonstrated in experiments where ATR was inhibited in conditions of replication stress, which was shown to lead to excess ssDNA formation due to unscheduled origin firing resulting in depletion of the nuclear pool of RPA and ultimately leading to 'replication catastrophe' and loss of cell viability (Toledo et al., 2013). Another important function of ATR in response to DNA damage is to upregulate ribonucleoside-diphosphate reductase subunit M2 (RRM2), which is responsible for the production of dNTPs from ribonucleotides, thereby maintaining a sufficient nuclear pool of dNTPs for use in replication and repair (D'Angiolella et al., 2012).

1.2.2. Lesion bypass by TLS or TS

One process that cells employ to bypass fork stalling lesions is to use low fidelity TLS polymerases (REV1, POLζ, POLκ, POLη, and POLι) that are permissive to damaged templates and allow DNA synthesis to traverse a blocking lesion (Waters et al., 2009). While this allows DNA replication to proceed, TLS polymerases are inherently mutagenic and lack 3′ to 5′ proofreading activity, which leads to the accumulation of mutations that can drive tumorigenesis (Sale, 2013). Regulation of TLS is achieved by monoubiquitylation of PCNA by RAD18 following DNA damage, which specifically recruits TLS polymerases since they mostly possess both PCNA-interacting protein (PIP) box and UBD motifs (Choe and Moldovan, 2017). Recruitment of RAD18 to lesion sites has also been shown to depend on an interaction with RPA (Huttner and Ulrich, 2008). Interestingly, a more recent study using *Xenopus* egg extracts has implicated RFWD3 in the K63-linked polyubiquitylation of PCNA at stalled forks and shown that this activity promotes TLS (Gallina et al., 2021). This stands in contrast to the previously accepted model based on experiments performed in yeast cells whereby K63-linked polyubiquitylation of PCNA drives lesion bypass via an alternative template switching (TS) mechanism (Chiu et al., 2006). In TS the stalled nascent strand is thought to utilise the newly generated sister chromatid as a repair template in a manner akin to HR repair (Branzei and Szakal, 2016). In yeast K63-linked polyubiquitylation of PCNA is catalysed by the E3 ligase Rad5 (Giannattasio et al., 2014; Hoege et al., 2002). However, the human orthologues of Rad5, HLTF and SHPRH, have only been shown to polyubiquitylate PCNA *in vitro,* and residual PCNA polyubiquitylation is observed in HLTF and SHPRH null cells which are also not sensitive to DNA damage (Krijger et al., 2011; Motegi et al.,

2008). TS may therefore be more complex in higher eukaryotes, and further research is required to identify the factors involved in PCNA polyubiquitylation.

1.2.3. Fork reversal and restart

A widespread response to replication stress is the re-annealing of nascent daughter strands to form a four-way fork structure in a process known as fork reversal (Zellweger et al., 2015). Initially regarded as a pathological consequence of replication fork destabilisation, fork reversal is now thought to be an important mechanism to promote genome stability by slowing down replication progression under conditions of replication stress and potentially promoting error-free repair pathways such as TS (Qiu et al., 2021). Fork reversal in human cells is mediated by three main translocase enzymes: SMARCAL1, HLTF, and ZRANB3, which possess distinct functional domains and have been shown to be exhibit different DNA substrate preferences (Berti et al., 2020; Bhat and Cortez, 2018). ZRANB3 is recruited to stalled forks by an interaction with K63-polyubiquitylated PCNA through bivalent PIP box and UBD domains in a manner analogous to the recruitment of TLS polymerases (Ciccia et al., 2012; Vujanovic et al., 2017). HLTF, conversely, is recruited via a direct interaction of its HIRAN domain with the free 3′-OH of a reversed fork (Kile et al., 2015). SMARCAL, meanwhile, is localised to reversed forks by an interaction with RPA (Bhat et al., 2015). Another central player in the formation of reversed forks is the RAD51 recombinase. RAD51 is proposed to promote the initial stages of fork reversal independent of BRCA2 strand exchange activity, while a second step involving the formation of 'metastable' nucleofilaments (i.e. discontinuous, interspersed with RPA) that protects reversed forks from nucleolytic attack requires BRCA2 (Kolinjivadi et al., 2017; Mijic et al., 2017; Quinet et al., 2017b).

BRCA2 activity has been shown to limit the excessive nucleolytic degradation of reversed forks by MRE11 and EXO1 (Schlacher et al., 2011). Interestingly, in BRCA2 deficient cells reversed forks can still be rescued through a BIR-like mechanism that relies on processing by the MUS81 nuclease and DNA synthesis by POLD3 (Lemacon et al., 2017). RAD51 filament loading is also balanced by several accessory factors including FBH1, RECQ5 and RADX (Berti et al., 2020; Fugger et al., 2015). Fork reversal is further regulated by ATR which catalyses the inhibitory phosphorylation of SMARCAL1 thereby preventing excessive fork reversal (Couch et al., 2013).

Once a lesion has been repaired at least two distinct pathways can restart replication from reversed forks. The first involves RECQ1 which restores an active three-way fork structure through branch migration. Importantly, this process is transiently inhibited by PARP1 catalysed PARylation which signals the presence of DNA damage and allows fork restart to occur only in the context of a repaired template (Berti et al., 2013). A second fork restart pathway utilises unwinding and control nucleolytic processing by WRN and DNA2 to restore the classical thee-way fork architecture (Thangavel et al., 2015).

1.2.4. Repriming

An additional mechanism employed by cells to counteract fork stalling lesions on the leading strand is to restart DNA synthesis by repriming downstream of the damaged site. PRIMPOL catalyses the repriming of DNA synthesis downstream of a lesion site on the leading strand in a manner analogous to the formation of Okazaki fragments on the lagging strand; a function previously thought to be exclusive to prokaryotes and lower eukaryotes (Bianchi et al., 2013; Mouron et al., 2013). PRIMPOL is recruited to stalled forks via an interaction with RPA, which also serves to stimulate its primase activity

(Guilliam et al., 2017). CHK1 has also recently been shown to phosphorylate PRIMPOL to promote its repriming activity in a further example of the ATR axis' coordination of the replication stress response (Mehta et al., 2022). PRIMPOL repriming has been suggested to compete with fork reversal and is activated under conditions when fork reversal is impaired, such as cells depleted of fork reversal factors (e.g. RAD51, SMARCAL1, HTLF) or with BRCA1/2 deficiency (Bai et al., 2020; Quinet et al., 2020; Vallerga et al., 2015). The repriming process leaves ssDNA gaps that must be filled in by TLS or TS mechanisms with these repair processes being carried out in G2 and S-phase respectively (Tirman et al., 2021). Deficiency in gap filling mechanisms leads to the accumulation of ssDNA gaps that are susceptible to nucleolytic cleavage and conversion to DSBs (Cong et al., 2021). Interestingly, the accumulation of ssDNA gaps following REV1-Polζ- mediated TLS inhibition has been shown to mediate the sensitivity to PARPi in BRCA1/2 deficient cells defective for HR repair (Panzarino et al., 2021; Taglialatela et al., 2021). Similarly, loss of LIG3 in a BRCA1-deficient background has been shown to result in MRE11-mediated ssDNA gaps that enhance the sensitivity to PARPi (Paes Dias et al., 2021).

1.2.5. RPA phosphorylation

As seen above, a central factor in the cellular response to replication stress is the RPA complex. Importantly, coordination of RPA's function is dependent on its PTM by modifications such as phosphorylation, SUMOylation, and ubiquitylation (Marechal and Zou, 2015). RPA is subject to extensive phosphorylation at multiple serine/threonine residues throughout the complex (Marechal and Zou, 2015). While the RPA1 subunit has also been seen to be phosphorylated, most phosphorylation events occur on the N-

terminus of RPA2 (Byrne and Oakley, 2019). During a normal, unperturbed cell cycle RPA2 is phosphorylated at S23 and S29 by CDKs in S-phase and mitosis respectively, which is thought to promote cell cycle progression (Din et al., 1990; Stephan et al., 2009). In response to DNA damage RPA2 is hyperphosphorylated on four key residues located in its N-terminus: S4/S8, S33, and T21 (Liu et al., 2012). This phosphorylation is carried out by the three apical DDR PIKK kinases: ATM, ATR, and DNA-PK. While there is substantial crosstalk between their kinase activities, S33 is thought to be primarily phosphorylated by ATR, while S4/S8 phosphorylation is mostly catalysed by DNA-PK with some input from ATM (Liu et al., 2012). The exact phosphorylation patterns appear to be genotoxin specific, however, with T21 phosphorylation seen to be dependent on all three PIKKs in turn, contingent on which DNA damaging agent was used to induce damage (Block et al., 2004). RPA2 phosphorylation following DNA damage has also been suggested to be sequential and synergistic with modification of S23 and S29 'priming' cells for phosphorylation of S33, which facilitates the subsequent phosphorylation of S4/8 and T21 only in the hyperphosphorylated state (Anantha et al., 2007). While the role of RPA phosphorylation in the DNA damage response is complex and multifaceted, a few key functions are considered below.

Firstly, it was found using phospho-mimetic RPA mutants that phosphorylated RPA's (pRPA) interaction with active replication centres was impaired (Vassin et al., 2004). Phosphorylation of RPA therefore potentially mediates a shift away from replicative processes to DNA repair processes to allow lesions to be fixed before DNA is duplicated. To this end pRPA has also been implicated in replication stress checkpoint activation, which may additionally be potentiated by the Ub-mediated 'feedforward' loop described in section 1.3.2. (Ashley et al., 2014; Olson et al., 2006). Consistent with pRPA's role in shifting cellular processes from replication to repair, it has also been

directly implicated in numerous repair processes. For example, pRPA was shown to aid the recruitment of PALB2, and by extension BRCA2, to sites of replication stress and therefore mediate their replication fork protection functions (Murphy et al., 2014). The phosphorylation status of RPA has also been suggested to play a role in HR repair with context dependent effects on the promotion of RAD51 nucleofilament assembly and progression of HR (Marechal and Zou, 2015). Notably, the dynamics of RPA phosphorylation are important since a dephosphorylation step by the PP4 or PP2A phosphatases was shown to be required for efficient HR repair following replication stress (Feng et al., 2009; Lee et al., 2010). Interestingly, it was recently demonstrated in BRCA-deficient cells that RPA phosphorylation facilitates the alternative RAD52-mediated loading of RAD51 on ssDNA to form nucleofilaments, a function usually carried out by BRCA2 (Carley et al., 2022). The mechanistic basis for exchange of RPA by RAD51 may also be explained by the finding in a recent single-molecule imaging study that the coordination of RPA for ssDNA is reduced by phosphorylation at S33, therefore potentially facilitating its displacement (Yin et al., 2021). A separate single-molecule imaging study also proposed that RPA phosphorylation inhibits DNA end resection by altering its interaction with BLM helicase, which usually stimulates resection by EXO1 or DNA2 (Soniat et al., 2019). Phosphorylation of RPA was seen to stimulate BLM's intrinsic strand-switching activity which reduces its helicase activity and thereby limits end resection (Soniat et al., 2019). Taken together, the data considered above suggests a wide range of roles for RPA phosphorylation in the cell's response to replication stress that is reflective of RPAs role as a signalling and recruitment platform on ssDNA.

1.3. Ubiquitylation in the DDR

The coordination and regulation of DDR pathways is driven by the PTM of protein factors with modifications such as phosphorylation, PARylation, SUMOylation, and ubiquitylation as seen in the examples given in the sections above (Dantuma and van Attikum, 2016). Ubiquitylation in particular has emerged as a key post-translational mediator of the replication stress response (Yates and Marechal, 2018). Ub is a 76-amino-acid polypeptide that can be covalently appended to target proteins via a sequential enzymatic cascade involving E1 ubiquitin-activating enzymes, E2 Ub conjugating enzymes, and E3 Ub ligases (Figure 6) (Oh et al., 2018). Classically, Ub is added to a target protein via an isopeptide bond formed between the ε amino group of a lysine residue within the substrate and the C-terminal glycine carboxy group of ubiquitin. However, ubiquitylation targeted to non-canonical residues such as cysteine, serine, threonine, and methionine has also been reported in more recent studies (Kelsall, 2022). Ub can be appended to a target either as a single moiety in a process known as monoubiquitylation, or via repeated conjugation at seven internal lysine residues or its N-terminal methionine can form polyUb chains of different length and linkage type which drive distinct signalling outcomes (Swatek and Komander, 2016). In addition to homotypic polyUb chains formed of Ub subunits linked by the same internal residue, heterotypic chains can also be formed where linkage types are either 'mixed' but still form a linear chain, or 'branched' whereby additional side chains are formed on pre-existing chains (French et al., 2021; Yau and Rape, 2016).

The complexity of Ub signalling is further compounded by PTM of Ub subunits themselves with modifications such as phosphorylation, acetylation or ADP-ribosylation (Song and Luo, 2019). The astonishing variety of Ub chain architecture

constitutes a 'ubiquitin code' that can be read by hundreds of proteins possessing UBDs which drive a diverse range of functional outcomes (Komander and Rape, 2012; Rahighi and Dikic, 2012). Classical examples of the divergent functional outcomes driven by distinct Ub chain architecture is the targeting for 26S proteasomal degradation by K11, K48, or K11/K48 branched chains, and the non-proteolytic regulation of protein-protein interaction driven by K63-linked polyubiquitylation (Oh et al., 2018). A key feature of ubiquitylation is that it is a reversible and highly dynamic modification. This is enforced by the class of proteases known as DUBs which catalyse the cleavage and disassembly of Ub chains, and also process Ub precursors to maintain a sufficient pool of free Ub (Clague et al., 2019; Grou et al., 2015). The ubiquitin code is thus coordinated by a set of 'writer' E1, E2, and E3 ligase proteins, 'reader' UBD-containing effector proteins, and 'eraser' DUB proteins prominent examples of which that function in the replication stress response are given in Table 2 adapted from (Mirsanaye et al., 2021).

1.3.1. PCNA and CMG ubiquitylation

As discussed in section 1.2.2 and 1.2.3 the ubiquitylation of PCNA is one of the central coordinators of the replication stress response. Classically, E3 ligase RAD18-dependent monoubiquitylation is thought to drive TLS factor recruitment, while K63-linked polyubiquitylation by HLTF or SHPRH is thought to promote TS; although K63-linked polyubiquitylation by RFWD3 has more recently been shown to promote TLS as well (Choe and Moldovan, 2017; Gallina et al., 2021). As mentioned, K63-linked polyubiquitylation of PCNA also promotes the recruitment of the translocase ZRANB3 which stabilises stalled forks, facilitates fork reversal and limits excessive HR (Vujanovic et al., 2017). The Werner helicase interacting protein 1 (WRNIP1) has also been shown to

be recruited to sites of replication stress by ubiquitylated PCNA and play a role in fork stabilisation and restart by stabilising RAD51 nucleofilaments (Kanu et al., 2016; Leuzzi et al., 2016). Additionally, the FANCD2/FANCI-associated nuclease 1 (FAN1) has also been demonstrated to be recruited to stalled forks via RAD18-mediated PCNA-Ub via a previously uncharacterised PIP motif together with its ubiquitin binding zinc finger (UBZ) domain (Porro et al., 2017). FAN1 was shown to promote fork stability in a BRCA2-independent manner. Importantly, PCNA monoubiquitylation is maintained as a reversible modification by the DUB USP1 which intriguingly was found to be autocleaved upon UV damage to allow PCNA-Ub to accumulate and promote repair (Huang et al., 2006). Notably, however, there has not been a DUB reported in the literature that cleaves K63-linked polyubiquitin on PCNA.

In addition to the TRAIP-mediated ubiquitylation of CMG during DPC and ICL repair as discussed above in sections 1.1.6 and 1.1.7.4, CMG is also polyubiquitylated with K48-linked chains during replication termination to promote its unloading from chromatin. In higher eukaryotes, upon replication fork convergence, the MCM7 subunit of CMG is modified with K48-linked Ub chains by the E3 ligase $CRL2^{LRR1}$ which targets it for removal by the p97/VCP 'segregase' complex (Dewar et al., 2017). Interestingly, a backup TRAIP-dependent pathway also mediates the ubiquitylation and p97/VCP-mediated disassembly of CMG complexes that have not been removed during mitosis (Sonneville et al., 2019).

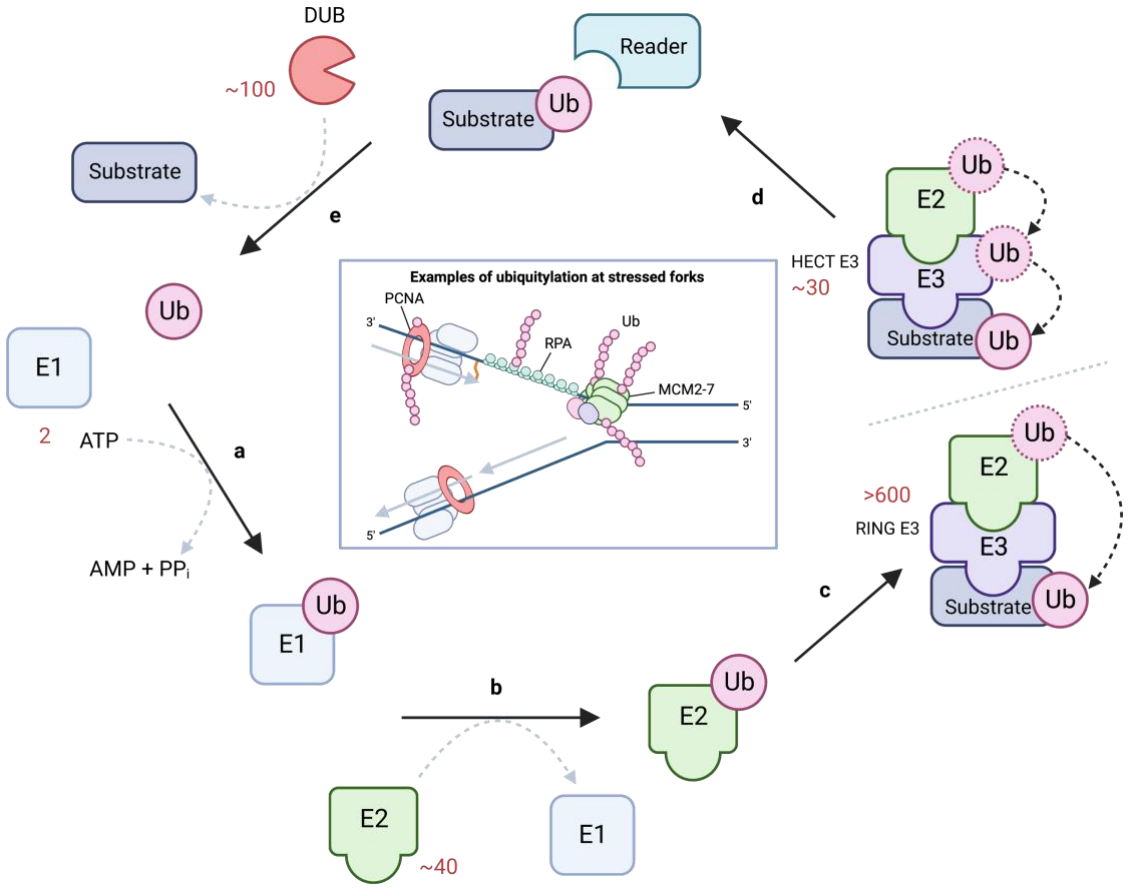

Figure 6. The ubiquitylation cascade

Dynamic ubiquitylation signalling is mediated through the actions of so-called writer, reader, and eraser classes of proteins. The writer class comprises the enzymes that perform the ubiquitylation cascade that transfers Ub to a target protein. **a)** First, a Ub molecule is attached to an E1 ubiquitin-activating enzyme in an ATP-dependent manner. **b)** The Ub is then transferred to an E2 ubiquitin-conjugating enzyme. **c)** Transfer to a target protein is then catalysed by E3 Ub ligase enzymes which can either facilitate the direct transfer of Ub from E2 enzyme to a target in the case of the RING E3 class of ligases or form a transient thioester linkage before transferring Ub in the case of HECT E3

ligases. **d)** The vast number of E3 ligases allows for a wide range of targets to be modified with many different Ub linkage architectures which can be decoded by a diverse set of proteins containing UBDs to drive distinct functional outcomes. The three main proteins (PCNA, RPA, and CMG) that Ub is articulated on during replication stress are depicted in the central box. **e)** Importantly, ubiquitylation is maintained as a reversible and highly dynamic modification through the action of DUB enzymes. The relative number of members of each class of protein is shown in red. Figure created using BioRender.com with reference to (Mirsanaye et al., 2021).

1.3.2. RPA ubiquitylation

The ubiquitylation of RPA has emerged as an important regulator of its function during the replication stress response (Davies et al., 2008; Mirsanaye et al., 2021). Two candidate E3 ligases, RFWD3 and pre-mRNA processing factor 19 (PRP19), have been proposed to be predominantly responsible for RPA ubiquitylation. RFWD3 was initially reported to be recruited to sites of DNA damage and make direct physical contact with RPA (Gong and Chen, 2011; Liu et al., 2011). A quantitative proteomics approach by the Elledge lab then demonstrated that the chromatin-bound RPA complex was ubiquitylated at multiple sites in an RFWD3 dependent manner (Elia et al., 2015). This ubiquitylation was induced by UV radiation, camptothecin, hydroxyurea, and aphidicolin, but not IR treatment, suggesting that RFWD3 ubiquitylation activity is stimulated by stalled replication forks. RFWD3 catalysed ubiquitylation was found to be non-proteolytic but was important for promoting HR and replication fork restart (Elia et al., 2015). A subsequent study by Inano *et al.*, demonstrated RFWD3 polyubiquitylates

both RPA and RAD51 and that knockout (KO) of RFWD3 leads to the persistence of RPA2 and RAD51 foci following MMC-induced DNA damage (Inano et al., 2017). Mechanistically it was shown that RFWD3 may promote chromatin extraction of RPA2 and RAD51 by the p97/VCP 'segregase' complex as protein turnover was drastically impaired following siRNA knockdown of RFWD3 or p97/VCP; or by expression of a ubiquitylation deficient RPA2–5KR substitute. The impairment of RPA and RAD51 turnover following RFWD3 depletion was suggested to impair the loading of downstream HR factors (Inano et al., 2017). From a clinical point of view RFWD3 has also been shown to be important for the repair of ICLs and mutations that disrupt its interaction with RPA have been found in patients with Fanconi anaemia, thereby leading to its annotation as the FA gene *FANCW* (Feeney et al., 2017; Knies et al., 2017). More recently, RFWD3 has been shown to promote more promiscuous ubiquitylation of ssDNA associated proteins at fork stalling lesions (Gallina et al., 2021). This includes the polyubiquitylation of PCNA that promotes gap filling TLS across a fork stalling lesion as discussed in sections 1.1.8.4 and 1.2.2.

In contrast to RFWD3, K63-linked polyubiquitylation of RPA2 by PRP19 is proposed to function in a 'feedforward' loop whereby ubiquitylation promotes the phosphorylation of RPA2 by recruiting ATRIP, the obligate binding partner of the ATR kinase (Marechal et al., 2014). This in turn drives further PRP19 recruitment to phosphorylated RPA through an interaction via a positively charged binding pocket in PRP19, which thereby reinforces the ATR activation cycle (Dubois et al., 2017). The ubiquitylation of RPA by PRP19 remains less well characterised than RFWD3's activity, however, and is brought into question by the finding that siRNAs used to knockdown PRP19 expression concomitantly impair the expression of His-tagged Ub constructs used to immunoprecipitate ubiquitylated RPA from cells (Elia et al., 2015). A third E3 ligase,

HERC2, has also been reported to influence RPA2 ubiquitylation and phosphorylation at S33, however the mechanistic details of this interaction await a more comprehensive elucidation (Lai et al., 2019).

Table 2. Writers, readers, and erasers of ubiquitylation at stressed replication forks

Factor	Function
Writers	
TRAIP	Ubiquitylates stalled CMG at helicase-blocking lesions to coordinate repair pathway choice between FA and NEIL3 pathways
RFWD3	Ubiquitylates ssDNA-bound RPA complexes in a non-proteolytic manner to promote DNA damage bypass and fork restart; polyubiquitylates PCNA to promote TLS
RAD18	Monoubiquitylates PCNA to stimulate TLS
HLTF	Promotes PCNA polyubiquitylation to promote error-free fork restart. Recognizes free 3′-OH ends in DNA and catalyses fork reversal
SHPRH	Promotes PCNA polyubiquitylation
$CRL2^{LRR1}$	Ubiquitylates MCM7 to promote p97/VCP-dependent CMG unloading upon fork convergence during replication termination
FANCL	Component of the FA core complex that monoubiquitylates FANCD2 and FANCI in conjunction with the E2 enzyme UBE2T
RNF168	Ubiquitylates H2A-type histones on K13 and K15 to promote recruitment of 53BP1, RNF169, and the BRCA1–A complex
FBH1	Accumulates at stalled forks and functions as a negative regulator of HR by disrupting RAD51 nucleofilaments
PRP19	Contributes to RPA ubiquitylation upon DNA damage
HERC2	May also contribute to RPA ubiquitylation
Readers	
TLS polymerases	Interacts with monoubiquitylated PCNA and enable error-prone replication past DNA lesions due to their permissive active sites
ZRANB3	Translocase that recognizes K63-polyubiquitylated PCNA and promotes fork reversal
p97/VCP	Recognize ubiquitylated client proteins to promote their displacement from replication forks
WRNIP	Accumulates at stalled forks via binding to ubiquitylated PCNA and stabilizes RAD51 nucleofilaments
SPRTN	Promotes replication-coupled DPC proteolysis by recognizing ubiquitylated factors at DPC sites
26S proteasome	Recognizes and proteolytically degrades ubiquitylated DPCs

Factor	Function
53BP1	Reader of RNF168-dependent H2A(X) ubiquitylation that protects stalled or reversed forks from nucleolytic degradation by MRE11
NEIL3	Glycosylase that recognizes short Ub chains on CMG and directly cleaves ICLs
FAN1	Recruited to monoubiquitylated PCNA to prevent replication fork collapse in a BRCA2-independent manner
Erasers	
USP7	Deubiquitylates SUMOylated proteins at unstressed forks to prevent their displacement from the replisome. Deubiquitylates SPRTN
USP1	Deubiquitylates monoubiquitylated FANCD2 and PCNA
VCPIP1	Reverses SPRTN monoubiquitylation to promote its chromatin access
ZUP1	Recognizes and deubiquitylates long K63-linked Ub chains at replication stress sites

Adapted from (Mirsanaye et al., 2021).

1.4. Genome-wide CRISPR screening

1.4.1. CRISPR-Cas9 gene editing

The advent of CRISPR-based gene editing technologies has proved to be a watershed moment for the field of functional genomics and has greatly enhanced the ability to efficiently modify and study gene function (Cong et al., 2013; Jinek et al., 2012; Mali et al., 2013). Prior to the development of CRISPR-based systems, targeted gene editing was performed using engineered programmable zinc finger nucleases (ZFNs) or transcription activator-like effector nucleases (TALENs) that make contact to specific DNA sequences through modular DNA-binding domains (Carroll, 2011; Joung and Sander, 2013). While these approaches marked a significant advance in site-specific genome editing capability, the requirement for customised protein engineering to target each new genetic locus severely hampered their versatility and throughput (Gaj et al., 2013). In contrast, the CRISPR system utilizes an RNA-guided CRISPR associated (Cas) DNA endonuclease allowing for exact modulation of targeting sequences making it a highly programmable and efficient gene editing technology (Doudna and Charpentier, 2014). The CRISPR-Cas components are derived from the prokaryotic adaptive immune system where they normally bind and cleave foreign nucleic acid sequences (from viruses or mobile genetic elements) and encode fragments of those sequences in their native genome as a form of immune 'memory' (Makarova et al., 2006). The components that make up the most widely adopted CRISPR-Cas9 system are a CRISPR RNA (crRNA) that is complementary in sequence to the target DNA, and a *trans*-activating crRNA (tracrRNA) that acts as a scaffold for a Cas9 nuclease which contains two nuclease domains that make incisions in opposing DNA strands at a target site to yield a DSB (Barrangou et al., 2007). In engineered CRISPR-Cas9 systems for use in eukaryotic cells

the crRNA and tracrRNA are artificially fused to yield a single guide RNA (sgRNA), enhancing its ease of use and efficiency (Jinek et al., 2012). Importantly, CRISPR-Cas9 can be targeted to any 20-nucleotide sequence that precedes a defined 3-nucleotide protospacer adjacent motif (PAM) ('NGG' for the commonly used *Streptococcus pyogenes* derived Cas9), meaning a vast genomic sequence space can be queried (Doudna and Charpentier, 2014). Moreover, rationally engineered Cas9 variants have been developed with altered or reduced requirements for a PAM sequence, thereby virtually removing the constraint on possible target sequences (Walton et al., 2020).

1.4.2. RNAi screens

Prior to the advent of CRISPR-based technologies, genome-scale functional genomic screens in mammalian cells were enabled by the use of RNA interference (RNAi) approaches (Boutros and Ahringer, 2008). Genome-wide RNAi screens utilise a library of encoded short-hairpin RNA (shRNA) or short interfering RNA (siRNA) sequences that direct the cell's endogenous RNA-induced silencing complex (RISC) to degrade a target messenger RNA (mRNA) and prevent its translation (Dykxhoorn et al., 2003). While multiple siRNA and shRNA libraries have been developed that allow the parallel targeting of many thousands of genes, their use has largely been superseded by CRISPR-based approaches due to several key limitations (Boettcher and McManus, 2015). Firstly, since RNAi functions at the transcript level, the knockdown of gene expression can be incomplete in some instances and result in confounding hypomorphic phenotypes that do not reflect full KO at the gene level (Boettcher and McManus, 2015). Secondly, RNAi suffers from off-target effects partly driven by the microRNA (miRNA)-like targeting of 3′-untranslated regions through partial sequence complementarity to these regions (Jackson et al., 2003). Additionally, expression of exogenous siRNAs and shRNAs can

overwhelm the endogenous miRNA system, leading to unintended perturbation of gene expression on a broader scale (Khan et al., 2009). A prominent example of RNAi's off-target effects came from a genome-wide RNAi screen designed to identify regulators of HR repair which found off-target depletion of RAD51 to be a commonly occurring false positive hit (Adamson et al., 2012). Nonetheless, RNAi screens have provided major advances in the DNA repair field and have helped to identify factors such as USP1 that deubiquitylates the FANCI-FANCD2 complex, and RNF168 which ubiquitylates histones to drive the recruitment of BRCA1-BARD1 and 53BP1 as discussed in sections 1.1.6.1 and 1.1.8.5 respectively (Doil et al., 2009; Nijman et al., 2005).

1.4.3. CRISPR knockout screens

The ease of specifying CRISPR target sites solely by changing the sequence of sgRNAs, coupled with the efficiency and specificity of Cas nucleases, led to the development of genome-scale sgRNA libraries which allow every gene in the genome to be targeted in parallel (Shalem et al., 2014). Genome-wide CRISPR screens are therefore a powerful new way to unbiasedly interrogate gene function at the genome scale and have proved a fruitful way to discover previously unknown pathways and molecular mechanisms that drive a given biological process or phenotype (Bock et al., 2022). CRISPR screens can be performed in arrayed format whereby guides targeting individual genes are physically separated by treating them in different wells of a multi-well plate (Metzakopian et al., 2017). This format is useful when coupling gene perturbations to direct phenotypic read-outs such as those monitored via microscopy or proteomic profiling. However, the scale and throughput of screens can be enhanced by performing genome-wide screens in pooled format whereby an sgRNA library is used to transduce cells in bulk at a low multiplicity of infection (MOI) such that individual

cells receive a single sgRNA vector targeting a particular gene (Aregger et al., 2019). Since sgRNA libraries are typically introduced via lentiviral transduction, the vectors integrate into the host genome and the identity of the targeting sequence can be distinguished in individual cells by high-throughput next-generation sequencing (NGS) (Aregger et al., 2019). This, moreover, provides a method to quantify the fitness impacts of a particular gene KO in a population of cells as NGS read counts are directly proportional to the abundance of integrated sgRNA cassettes, which will increase or decrease depending on whether the gene they target confers a selective advantage or disadvantage (Bodapati et al., 2020).

A widely used sgRNA library in genome-wide CRISPR KO screens is the Toronto KnockOut version 3 (TKOv3) library. The TKOv3 library is a one-component lentiviral encoded library that expresses Cas9 concomitantly with four sequence-optimised sgRNAs for each of the 18,053 protein-coding genes in the genome for a total of 71,090 guides (Hart et al., 2017). The library was designed by analysing sgRNAs targeting core essential genes from six previously conducted CRISPR KO screens to generate a 'sequence score' metric by comparing the incidence of nucleotides at each position in the sgRNA's 20-nucleotide sequence between the three best performing guides and three worst performing guides for a given gene (Hart et al., 2017). This metric was then used to score all possible Cas9 guides for protein-coding genes, with the four highest scoring guides for each gene being chosen. Smaller-scale targeted libraries have also been developed to perturb a set of functionally-linked genes such as those developed to specifically target known DDR genes (Su et al., 2020).

A notable achievement of pooled CRISPR KO screens has been the identification of a consensus set of 1,580 core essential genes across multiple cell lines that are required for cell viability (Hart et al., 2015). This represents a roughly 4-fold increase in the

number of essential genes discovered relative to similarly conceived RNAi screens (Vizeacoumar et al., 2013). CRISPR screens have also been indispensable to elucidate the response of cancer cells to genotoxic insults (Awwad et al., 2023). The format of these screens can either involve treating cells with a low dose of genotoxin to identify gene KOs that further sensitise cells, or a high dose to determine which genes mediate resistance to a particular genotoxin (MacLeod et al., 2022). The power of this approach was demonstrated in a recent study that catalogued 31 genome-scale CRISPR chemogenetic screens using 27 different genotoxic agents to identify a set of 890 genes that mediate cancer cell vulnerabilities to DNA damaging drugs (Olivieri et al., 2020).

1.4.4. Synthetic lethality

While great strides have been made to understand the response of cancer cells to monogenic perturbation, significant promise is also held by exploiting pairwise or combinatorial approaches to uncover interactions of multiple genes (Awwad et al., 2023). The DDR is a highly interrelated network of pathways with often redundant backup mechanisms to repair the same type of damage to ensure genomic stability is maintained (Ciccia and Elledge, 2010). However, genomic instability is one of the hallmarks of cancer cells and is often caused by a deficiency in one or more DNA repair pathways in these cells (Hanahan and Weinberg, 2011). The increased reliance on the remaining repair pathways for cell viability offers an exciting opportunity to specifically target cancer cells while preserving healthy cells possessing the full complement of DNA repair pathways (Curtin, 2012). This approach underlies the concept of synthetic lethality whereby targeting genes in redundant pathways individually does not impact viability, while concomitant targeting of both pathways results in cell death (Figure 7). The classical example of a synthetic lethal interaction is between PARP enzymes and

BRCA1 and BRCA2 (Lord and Ashworth, 2017). As described in the sections above, BRCA1 and BRCA2 function to promote error-free repair via HR but are often mutated in breast and ovarian cancers. Inhibition of PARP enzymes by small molecule inhibitors causes trapping of PARP proteins on DNA which results in replication fork stalling and collapse when these lesions are encountered. In normal cells collapsed replication forks can be repaired by HR, while in BRCA1/2 deficient backgrounds this option is not open leading to cell death. Interestingly, emerging evidence also points to a role for excessive ssDNA gap generation resulting from defective Okazaki fragment processing in BRCA deficient cells as a mediator of PARPi synthetic lethality (Cong et al., 2021). Many other synthetic lethal interactions to genotoxic agents have now been defined including the RNAse H2 synthetic lethality with PARPi and HROB synthetic lethality with HELQ discussed earlier in this introduction. Indeed, the concept of synthetic lethality holds great clinical promise to target genes that confer resistance to existing therapies and to personalise drugs based on specific vulnerabilities in each patient's tumour cells (O'Neil et al., 2017).

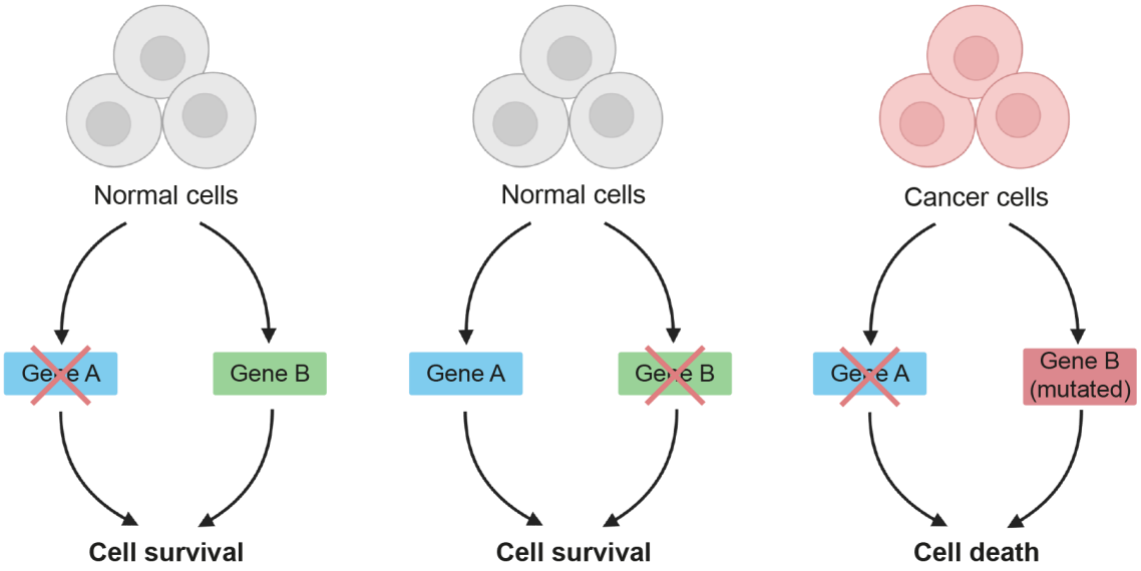

Figure 7. Synthetic lethality

In healthy cells perturbation of individual genes in parallel redundant pathways by mutation or small molecule inhibition does not affect cell viability. However, in cancer cells mutations in one of the pathways makes the cells reliant on the remaining gene and therefore perturbation of that gene function by chemical or genetic means results in loss of viability. Figure created using BioRender.com with reference to (Rehman et al., 2010).

1.5. Discovery of ZUP1

The discovery of ZUP1 was reported in 2018 by four independent groups who found it to constitute a novel class of DUB that lacks sequence homology to any existing class of enzyme (Haahr et al., 2018; Hermanns et al., 2018; Hewings et al., 2018; Kwasna et al., 2018). ZUP1 was discovered concomitantly using activity-based probes, which bind to the active site of DUBs via a thiol moiety, and by *in silico* bioinformatic searches for uncharacterized proteins bearing conserved UBD motifs. The ZUP1 peptidase domain was originally annotated as zinc finger with UFM1-specific peptidase domain (ZUFSP), due to its adoption of a similar fold structure to the ubiquitin-fold modifier 1 (UFM1)-specific protease (UFSP) class of proteins. However, sequence and structural analysis found that ZUP1 lacked the traditional catalytic histidine residue of UFSP family proteins, and furthermore could not react with a propargylated UFM1 probe, while readily being able to react with a propargylated Ub probe (Hermanns et al., 2018; Hewings et al., 2018). ZUP1 was also shown to specifically liberate the fluorophore 7-amino-4-methylcoumarin (AMC) from Ub-AMC fusions, but not other ubiquitin-like modifier (UBL) proteins such as SUMO1, SUMO2, NEDD8, ISG15 or LC3A (Hermanns et al., 2018). These data therefore reclassified ZUP1 as a DUB rather than a UFSP enzyme. Interestingly, in contrast to most existing DUBs, which display little Ub chain specificity, ZUP1 was shown *in vitro* to selectively cleave long K63-linked Ub chains (Haahr et al., 2018). This chain architecture predominantly drives non-proteolytic signalling and protein–protein interactions (Chen and Sun, 2009).

ZUP1 is a multidomain protein with a C-terminal peptidase domain responsible for its catalytic function (Figure 8) (Kwasna et al., 2018). However, this domain alone cannot cleave Ub chains and requires several additional domains for optimal function. These

include a helix-turn-helix motif denoted as the α2/3 domain which the Gibbs-Seymour lab has demonstrated to be required for both ZUP1's DUB activity and for its interaction with the RPA complex (Foster et al., 2023). Several UBDs are also required for optimal Ub cleavage. Directly adjacent to the α2/3 domain is a UBD termed the ZUP1 helical arm (ZHA), which provides the distal S1 binding site for Ub by interacting with its Ile44 patch. This is followed by a motif interacting with ubiquitin (MIU) domain that is proposed to constitute the S2 binding site for K63-linked polyUb chains. ZUP1 also contains four zinc finger domains (ZnFs), the fourth of which is termed the ubiquitin binding zinc finger (UBZ) domain and plays a significant role in overall polyUb binding by ZUP1.

Excitingly, preliminary mass-spectrometry interaction studies showed ZUP1 to interact with several DDR-related proteins, intimating a role in this process (Hermanns et al., 2018). Most notably an association with RPA was reported. Indeed, the Gibbs-Seymour lab has demonstrated a direct interaction of ZUP1 with RPA *in vitro* and *in vivo* with a stimulatory effect on its DUB activity upon binding (Foster et al., 2023). ZUP1 was also shown to localise to sites of DNA damage induced by laser micro-irradiation or site-specific FokI nuclease induced double strand breaks (Haahr et al., 2018; Kwasna et al., 2018). Unpublished work from the Gibbs-Seymour lab has also shown that ZUP1 localises to a DNA replication block formed by tamoxifen-induced lac repressor (LacR) binding to chromosomally integrated lac operator (*LacO*) repeats (I.G.-S. personal communication; unpublished). Hewings *et al.* additionally reported that levels of K63-linked ubiquitylated RPA1 and RPA2 were enriched in ZUP1 siRNA knockdown cell extracts immunoprecipitated with a linkage-specific Ub antibody (Hewings et al., 2018). Notably, K63-linked Ub chains were also significantly enriched in ZUP1 knockdown cells at *LacO*/LacR array replication blocks, suggesting the presence of ZUP1 specific

substrates at sites of replication stress (Haahr et al., 2018). Our lab has also demonstrated an interaction of ZUP1 with PCNA and shown that ubiquitylation of PCNA is consistently elevated in cells lacking ZUP1 following DNA damage (I.G.-S. personal communication; unpublished). Many aspects of ZUP1 function, however, remain uncharacterised with some of the outstanding questions that have yet to be addressed including:

1) What are the consequences of permanent ablation of the *ZUP1* gene using CRISPR-Cas9 gene editing?

2) Which DNA repair pathway(s) does ZUP1 function in?

3) How is ZUP1 recruited to sites of DNA damage?

4) What is the complement of ZUP1 binding partners and how is its activity regulated?

5) Finally, while RPA and PCNA are implicated as targets of ZUP1 DUB activity, the *bona fide* substrate(s) of ZUP1 have yet to be conclusively determined.

This DPhil project therefore seeks to build on the early work presented above to elucidate the cellular function of ZUP1 and characterise its role in promoting genome stability.

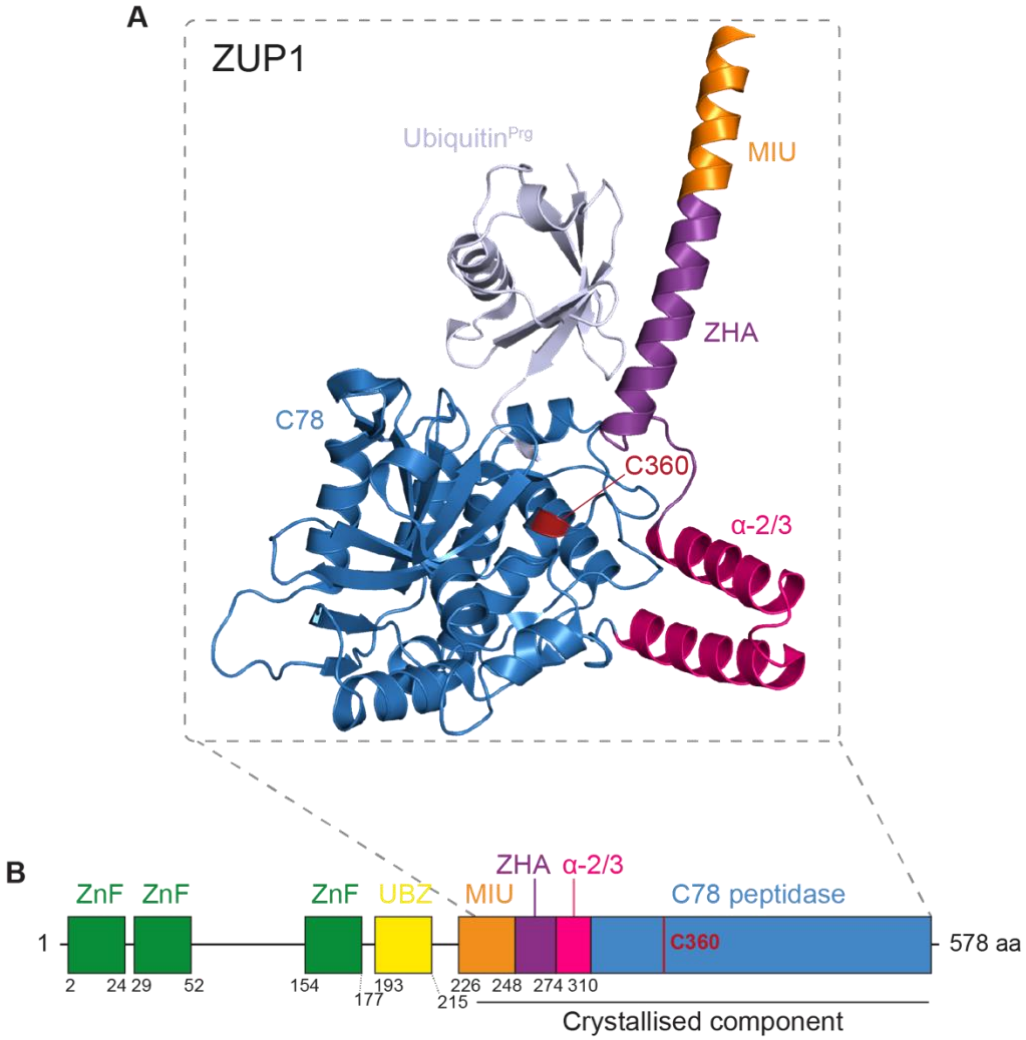

Figure 8. Crystal structure and domain architecture of ZUP1

(A) Structure of crystallisable portion of ZUP1 (amino acid residues 236-578) in complex with propargylated ubiquitin (PDB ID = 6FGE). Crystal structure was generated in PyMol.

(B) Schematic domain boundary for ZUP1 with amino acid demarcations. The location of the catalytic cysteine (C360) within the C78 peptidase domain shown in red.

1.6. Structure of thesis

1) In Chapter 3 of this thesis, I describe the generation of ZUP1 KO clones using CRISPR-Cas9 gene editing and demonstrate that these clones are complete KOs at the gene and protein level. I then use a semiquantitative RT-PCR approach to investigate the expression of previously poorly characterised ZUP1 isoforms and show that no residual splice variants are expressed in ZUP1 KO cells. I then define the sensitivity of ZUP1 KO clones to a range of genotoxic agents to identify the DNA repair pathway(s) that ZUP1 functions in. I also perform an initial characterisation of DDR marker activation in ZUP1 KO cells in response to DNA damage using immunoblotting. Finally, I describe the generation of ZUP1 complemented rescue cell lines and assess the extent to which they can reverse the phenotypic defects observed in ZUP1 KO cells.

2) In Chapter 4, I perform experiments using a high-content immunofluorescence imaging technique known as quantitative image-based cytometry (QIBC) to characterise the chromatin-loading dynamics of important DNA repair factors that are ubiquitylated in response to DNA damage. Using QIBC I demonstrate that ZUP1 KO cells display persistent chromatin-bound RPA2 and RAD51 in response to MMC-induced ICL lesions and reveal the underlying basis for this phenotype is the excessive generation of ssDNA in the absence of ZUP1. I also use QIBC to characterise the hyperphosphorylation of RPA2 in ZUP1 KO cells in response to MMC and use an siRNA screen to investigate potential factors that mediate this effect.

3) In Chapter 5, I conduct parallel genome-wide CRISPR-Cas9 dropout screens in wild type (WT) and ZUP1 KO cells to identify factors that mediate sensitivity to MMC. This data set identifies putative synergistic and suppressor interactors of ZUP1 and sheds light on the pathways that function in parallel to ZUP1. In this Chapter I additionally utilise two-colour competitive growth assays to validate selected hits from the CRISPR screen which suggest *bona fide* synergistic interactions between ZUP1 and HELQ and BRCA2 in response to MMC.

2

Materials and Methods

Contents

2.1. Materials

See Appendix A – Appendix H for a full list of reagents and resources used in this study.

2.2. Cell culture

Parental human osteosarcoma U-2 OS (U2OS; ATCC HTB-96) and embryonic kidney 293T (ATCC CRL-3216) cell lines were acquired from ATCC. U2OS ZUP1 KO cells were generated using CRISPR-Cas9 genome editing as part of this study (see below). U2OS pLenti-PGK-Hygro-Empty vector (EV), U2OS pLenti-PGK-Hygro-ZUP1(WT), U2OS ZUP1 KO pLenti-PGK-Hygro-EV, U2OS ZUP1 KO pLenti-PGK-Hygro-ZUP1(WT), U2OS ZUP1 KO pLenti-PGK-Hygro-ZUP1(C360R), and U2OS ZUP1 KO pLenti-PGK-Hygro-ZUP1(Δα2/3) complementation cell lines were generated as part of this study (see below). U2OS LentiCas9-Blast and U2OS ZUP1 KO LentiCas9-Blast stably expressing FLAG-Cas9 were additionally created as part of this study (see below). Cells were cultured in Dulbecco's Modified Eagle Medium (DMEM; Gibco) with high glucose, GlutaMax supplement, pyruvate, and supplemented with 10% foetal bovine serum (FBS; Gibco) filtered through a 0.45 μm Millex-HP syringe filter (Merck-Millipore). Cells were grown under standard conditions of 37°C and 5% CO_2 with passaging performed by detaching cells using TrypLE (Gibco). All cell lines were mycoplasma negative and were tested every 3–4 months using the MycoAlert detection kit (Lonza).

2.3. Molecular cloning

Cloning of sgRNA constructs for CRISPR-Cas9 gene editing of the *ZUP1* locus was performed based on the Zhang Lab protocol (Ran et al., 2013). sgRNA sequences were designed using the CHOPCHOP and CRISPOR online tools to target exon 2 and exon 6 of *ZUP1* respectively (Concordet and Haeussler, 2018; Labun et al., 2019). sgRNA sequences were inserted into the pSpCas9(BB)-2A-Puro (PX459) V2.0 vector expressing WT SpCas9 via restriction cloning with BbsI digestion and transformation of One Shot Stbl3 Chemically Competent *E. coli* (Thermo Fisher). Plasmid DNA was extracted from bacteria using a PureLink HiPure Plasmid Filter Maxiprep Kit (Thermo Fisher). Correct cloning and integration into parental vectors were confirmed by analytic gel electrophoresis and Sanger sequencing.

Cloning of lentiGuide-Puro parental vector constructs bearing GFP and mCherry sequences for use in two-colour competitive growth assays was carried out using HiFi DNA assembly. GFP and mCherry inserts were designed with a 3x SV40 nuclear localisation signal (NLS) tag and a P2A protease site for cleavage of the GFP/mCherry-3xNLS from the downstream puromycin N-acetyltransferase protein. GFP/mCherry-3xNLS-P2A vector inserts were ordered as synthetic oligonucleotide constructs. The lentiGuide-Puro target vector was linearised via PCR using lentiGuide-Puro_FWD and lentiGuide-Puro_REV primers. GFP/mCherry-3xNLS-P2A synthetic oligonucleotide inserts were linearised with GFP-3xNLS-P2A_FWD + GFP-3xNLS-P2A_REV and mCherry-3xNLS-P2A_FWD + mCherry-3xNLS-P2A_REV primers respectively. HiFi assembly was then performed using NEBuilder HiFi DNA Assembly Master Mix (New England Biolabs) with 100 ng of vector mass and a 2:1 insert:vector ratio. Assembled products were then used to transform One Shot Stbl3 Chemically Competent *E. coli*

(Thermo Fisher) and plasmid DNA was extracted from bacteria using a PureLink HiPure Plasmid Filter Maxiprep Kit (Thermo Fisher). Correct cloning and integration into parental vectors were confirmed by analytic gel electrophoresis and Sanger sequencing.

Cloning of lentiGuide-Puro-EGFP/mCherry-NLS constructs bearing sgRNA sequences targeting genes of interest (GOI) from the genome-wide CRISPR-Cas9 screen was performed using restriction digest with BsmBI according to the Zhang Lab protocol (Sanjana et al., 2014). sgRNAs targeting HELQ, NEIL3, BRCA2, BRIP1/FANCJ and LacZ non-targeting control were designed with the CRISPick online tool (Doench et al., 2016). Assembled vectors were used to transform Stbl3 cells and plasmid DNA extracted via Maxiprep as above with correct cloning and integration into parental vectors confirmed by analytic gel electrophoresis and Sanger sequencing.

Generation of untagged, constitutively expressed ZUP1 constructs for use in complementation assays was achieved via the Gateway LR recombination reaction of pDONR221 entry clones bearing ZUP1(WT), ZUP1(C360R), and ZUP1(Δα2/3) sequences into a pLenti-PGK-Hygro DEST destination vector. LR reactions were performed using Gateway LR Clonase II Enzyme Mix (Thermo Fisher) according to the manufacturer's instructions. Stbl3 cells were transformed, Maxipreps performed, and correct cloning confirmed by analytic gel electrophoresis and Sanger sequencing as described above. See Appendix F for primer sequences.

2.4. Generation of ZUP1 CRISPR-Cas9 knockout cells

Knockout of the *ZUP1* gene in U2OS cells was achieved by transfection with single guide RNA (sgRNA) (sgZUP1_Ex2_1; targeting exon 2) and (sgZUP1_Ex6_2 + sgZUP1_Ex6_3; flanking exon 6) cloned into the pSpCas9(BB)-2A-Puro (PX459) V2.0 vector using BbsI restriction digestion. Cells were plated in 60 mm dishes at a density of

2.5 x 10^5 cells per dish and allowed to settle overnight. Cells were then transfected using the TransIT-LT1 reagent (Mirus) according to the manufacturer's protocol with the volume of reagents listed in the table below. A 30-minute (mins) incubation time was used for the DNA-lipid particle formation step.

Table 3. TransIT-LT1 transfection reagent volumes

Reagent	Volume
DMEM media	5.0 ml
OptiME	500 µl
Plasmid DNA (1 µg/µl)	2.5 µl each
TransIT-LT1 Reagent	15 µl

After 24 hours (h) cells were split into 10 cm dishes. After a further 24 h cells were then selected using 2 µg/ml puromycin (Gibco). Puromycin selection was limited to 24 h to minimise the chance of PX459 vector integration into the genome. 5 days after selection cells were plated as single cells in 96-well plates via the limiting dilution method. After ~7 days plate wells were scored for the presence of single colonies via manual visual assessment with a light microscope. Approximately 18 days after plating, wells with single colonies were split into corresponding wells of two 24-well plates for screening via PCR and immunoblot and for the generation of cryopreserved stocks. Individual clones were then screened via PCR (described below), immunoblotting, and ICE analysis (Synthego) of Sanger sequencing traces from sgRNA targeting sites. Clones with successful KO of ZUP1 were selected for further characterisation with 3x independent clones for each sgRNA targeting strategy (exon 2 alone, exon 6 alone, and both exon 2/6) being represented in this study. Most experiments were performed using ZUP1 exon2/6 KO clones 38 and 62 (referred to as C38 and C62).

2.5. Immunoblotting

Cells were lysed on ice with Triton-X100 lysis buffer (50 mM Tris-HCl pH 8.0, 100 mM NaCl, 1% Triton X-100) supplemented with DTT (Thermo Fisher; 1 mM), protease inhibitor cocktail (Sigma-Aldrich; 1 mM), sodium orthovanadate (Sigma-Aldrich; 0.1 mM), N-Ethylmaleimide (Sigma-Aldrich; 5 mM), sodium fluoride (Sigma-Aldrich; 1 mM), β-Glycerophosphate (Sigma-Aldrich; 10 mM), and 5 mM $MgCl_2$. The lysates were incubated with 0.2% Benzonase nuclease (Sigma-Aldrich) for 20 mins at 4°C with rotation, centrifuged at 13,000 x g for 10 mins at 4°C, and then the supernatants were collected to fresh tubes. Protein concentrations were then determined using the Bradford Protein Assay (Bio-Rad). A normalised quantity of each sample was made up in 1x NuPAGE LDS sample buffer (Thermo Fisher) and samples were heated to 95°C for 5 min. Proteins were then resolved on appropriate NuPAGE Bis-Tris gels (6%, 8%, or 4–12%) run in NuPAGE MOPS SDS running buffer (Thermo Fisher), and transferred onto nitrocellulose or PVDF membranes (Bio-Rad) using the 30 mins setting on the Trans-Blot Turbo Transfer System (Bio-Rad). The membranes were blocked in 5% non-fat dried milk (Marvel) in Tris-buffered saline (TBS) with 0.1% Tween 20 for 1 h at room temperature with shaking. Membranes were then incubated overnight with primary antibodies at 4°C with gentle shaking followed by 1 h incubation with HRP-conjugated secondary anti-mouse or anti-rabbit antibodies at room temperature with gentle shaking. Blots were developed by incubating membranes with freshly reconstituted ECL substrate (Clarity, Bio-Rad; or Pierce, Thermo Fisher) and exposing to Amersham hyperfilm ECL films (GE Healthcare). Where indicated blots were stripped with ReBlot Plus solution (Sigma-Aldrich) and re-probed with a loading control antibody.

2.6. PCR screening of ZUP1 KO clones

A polymerase chain reaction (PCR) screening strategy was devised to identify successful ZUP1 exon 6 KO clones as described in Figure 9 using the following method. Genomic DNA (gDNA) was extracted from potential KO clones by the addition of QuickExtract DNA Solution (Lucigen) directly to plate wells that had been rinsed twice with phosphate buffered saline (PBS). Lysates were transferred to Eppendorf tubes, vortexed for 15 s, heated to 65°C for 6 min, vortexed for a further 15 s, then heated to 95°C for 2 min. Two separate PCRs were performed to amplify so called long and short fragment regions surrounding exon 6 of ZUP1 using the conditions listed in Table 4 and Table 5 below. The primers ZUP1_Ex6_FWD_1 + ZUP1_Ex6_REV_1 and ZUP1_Ex6_FWD_1 + ZUP1_Ex6_REV_2 were used to amplify long and short fragments respectively. 5 µl of each PCR product was run on a 1.2% agarose gel and visualised using the ChemiDoc XRS+ system (Bio-Rad) with Image Lab software v6.1. See Appendix F for primer sequences.

Table 4. PCR reaction components for KO screen

Component	25 µl Reaction	Final Concentration
Q5 High-Fidelity 2X Master Mix (NEB)	12.5 µl	1X
10 µM Forward Primer	1.25 µl	0.5 µM
10 µM Reverse Primer	1.25 µl	0.5 µM
Template DNA (100 ng/µl)	1 µl	100 ng
Nuclease-Free Water	to 25 µl	-

Table 5. PCR cycling conditions for KO screen

Step	Temperature	Time
Initial Denaturation	98°C	30 seconds
35 Cycles	98°C	10 seconds
	64 or 63°C[1]	30 seconds
	72°C	30 seconds/kb
Final Extension	72°C	2 mins
Hold	4°C	∞

[1]64°C for long fragment 63°C for short fragment

2.7. Sanger sequencing

gDNA extracted from putative ZUP1 KO clones were amplified using primers spanning the exon 2 and exon 6 regions using the conditions described above using ZUP1_Ex2_FWD_1 + ZUP1_Ex2_REV_1 and ZUP1_Ex6_FWD_1 + ZUP1_Ex6_REV_1 primers. Samples were then submitted for Sanger sequencing by Source BioScience using forward primers from each respective PCR reaction. See Appendix F for primer sequences.

2.8. Semi-quantitative RT-PCR

Total RNA was extracted from U2OS WT and ZUP1 KO cells using the Purelink RNA mini kit (Thermo Fisher) according to the manufacturer's protocol. gDNA was then digested using the ezDNase kit (Thermo Fisher) according to the manufacturer's protocol. mRNA was then converted to cDNA using the SuperScript IV first-strand synthesis system (Thermo Fisher) with oligo $d(T)_{20}$ primer according to the manufacturer's protocol using 2.5 μg of RNA as input for each reaction. Positive and negative (no reverse transcription) reactions from the kit were also performed for quality control. Cleavage of specific ZUP1 isoforms was then performed by splitting the sample into separate reactions and incubating with a synthetic deoxyoligonucleotide complementary to the intended exon containing a unique restriction site (ZUP1_Ex2_Cleavage + ScaI, ZUP1_Ex3_Cleavage + NdeI, ZUP1_Ex7_Cleavage + NsiI). The mixture was heated at 94°C for 2 min, 85°C for 15 min, 70°C for 15 min, 55°C for 15 min, and room temperature for 15 min. 1 μl of appropriate restriction endonuclease was then added, and samples were incubated at 37°C for 30 mins. Samples were then

amplified via PCR using ZUP1_Ex1_FWD_1 + ZUP1_Ex6_REV_3 primers and 10 µl of each product run on a 1.2% agarose gel and visualised using the ChemiDoc XRS+ system (Bio-Rad) with Image Lab software v6.1. See Appendix F for primer sequences.

2.9. Serial passage proliferation analysis

U2OS WT and three independent ZUP1 KO clones were seeded into 10 cm dishes at a density of 200,000 cells with two technical replicate dishes per cell line. Cells were collected, counted, and re-plated at 200,000 cells per well at 72 h intervals. Cell counting was performing using a CellDrop Automated Cell Counter (DeNovix) with triplicate readings being taken and averaged for each sample. The doubling time for each cell line was calculated using the formulae below:

$$Number\ of\ generations = \frac{\log_{10}(Final\ cell\ number) - \log_{10}(Cell\ number\ plated)}{\log_{10}(2)}$$

$$Doubling\ time = \frac{Time\ elapsed}{number\ of\ generations}$$

Calculation of doubling time was performed for cell numbers at each interval and the values were averaged to generate a mean doubling time for each cell line.

2.10. Drugs used in clonogenic survival assays

The following drugs were used in clonogenic survival assays: cisplatin (Sigma-Aldrich; Made up as a 1mg/ml stock in 0.9% NaCl), formaldehyde (Thermo Fisher; 16% methanol-free stock), mitomycin C (MMC) (Sigma-Aldrich; made up as a 1 mM stock in DMSO), olaparib (Enzo Life Sciences; made up as a 10 mM stock in DMSO), talazoparib

(Selleck Chemicals; made up as a 10 mM stock in DMSO), hydroxurea (Sigma-Aldrich; made up as a 1 M stock in RNAse free water), topotecan (Tocris; made up as a 10 mM stock in nuclease-free water), AZD6738 (ApexBio; made up as a 10 mM stock in DMSO).

2.11. Clonogenic survival assay

Clonogenic survival assays were performed according to a modified version of the Franken *et al.* protocol (Franken et al., 2006). Cells were seeded in triplicate into 6-well plates at an empirically determined density to yield ~150 colonies per well in an untreated condition (180–310 cells depending on cell line) in drug-free medium or medium containing an appropriate concentration of drug. Cells were either treated continuously without media change for 14 d (cisplatin, formaldehyde), for 24 h followed by growth in drug free media for 13 d (MMC, hydroxyurea, topotecan), or continuously with drug replacement every 3 d for 14 d (olaparib, talazoparib, ATRi). Cells were grown under standard conditions of 5% CO_2 and 37°C. At the experimental endpoint media was removed from plates, cells were washed twice with PBS with excess PBS removed by an aspirator, and ~2 ml of 0.5% crystal violet solution in 25% methanol was added to each well and incubated at room temperature for ~30 min. Crystal violet solution was then removed using a strippette and plates were washed by submerging in water and inverting three times, and then left to dry on Whatman paper. Plates were then imaged and counted manually using a Counter-Pen (VWR). The surviving fraction (SF) of cells was calculated using the formulae below where PE is the plating efficiency of untreated cells.

$$PE = \frac{no.of\ colonies\ formed}{no.of\ cells\ seeded} \times 100\%$$

$$SF = \frac{no.of\ colonies\ formed\ after\ treatment}{no.of\ cells\ seeded \times PE}$$

2.12. Packaging of lentiviral vectors

Lentiviral vectors used to generate ZUP1 complementation cell lines (pLenti-PGK-Hygro_ZUP1, pLenti-PGK-Hygro_ZUP1 (C360R), pLenti-PGK-Hygro_ZUP1 (Δα2/3)) and Cas9 stable cells (lentiCas9-Blast and pKLV2-BFP/GFP reporter) were packaged using pMD2.G envelope and psPAX2 packaging plasmids according to the following protocol. HEK293T cells were plated in 10 cm dishes at a density of 6 x 10^6 cells per dish. The following day the appropriate lentiviral vector was transfected together with packaging and envelope plasmids using the TransIT-LT1 transfection reagent (Mirus) according to the manufacturer's instructions. Media was replaced with fresh DMEM 24 h post-transfection. After a further 24 h lentivirus containing media was collected from dishes, centrifuged at 200 x g for 5 mins at 4°C, and filtered through a 0.45 μM Millex-HP syringe filter (Merck-Millipore). Lentivirus was then aliquoted and stored at -80°C until use.

2.13. Generation of rescue cell lines

For complementation assays U2OS WT and ZUP1 KO cell lines were transduced with pLenti-PGK-Hygro vectors bearing the following ZUP1 variants: ZUP1 WT, ZUP1(C360R), ZUP1(Δα2/3). Parental cell lines (WT or ZUP1 KO) were plated in 6-well plates at a density of 2 x 10^4 cells per well. 24 h later cells were transduced with the appropriate packaged lentiviral vector at an empirically determined MOI of 1.0. After 24 h lentivirus containing media was removed and replaced with fresh DMEM and cells were cultured for a further 24 h. Cells were then selected with 500 μg/ml hygromycin

(Thermo Fisher) for 72 h until all untransduced cells had died. Cells were maintained as a pool in the presence of 150 μg/ml hygromycin. Expression of ZUP1 and ZUP1 variants was verified by immunoblotting.

2.14. Quantitative image-based cytometry (QIBC)

Cells were seeded coverslips in 35 mm dishes at an appropriate density and allowed to settle overnight. The following day coverslips were moved into individual wells of 6-well plates and treated according to the treatment scheme indicated. At the relevant endpoint growth medium was removed and coverslips were rinsed with PBS. A pre-extraction step was performed by incubated coverslips in PBS 0.2% Triton X-100 on ice for 3 mins. Coverslips were then rinsed twice with PBS and cells were fixed using 4% formaldehyde in PBS for 15 mins at room temperature followed by a further three wash steps with PBS. Coverslips were then blocked in 1% BSA in PBS for 45 min. Coverslips were then incubated with the appropriate dilution of primary antibody in 1% BSA/PBS for 2 h at room temperature, washed three times with PBS 0.01% Tween 20 for 5 mins each, and incubated with the appropriate secondary antibody in 1% BSA/PBS buffer containing 4',6-Diamidino-2-Phenylindole Dihydrochloride (DAPI, 0.5 μg/mL; Thermo Fisher) for 1 hour at room temperature protected from light. Coverslips were then washed a final three times with PBS 0.01% Tween 20 for 5 mins each followed by two wash steps in distilled water and then dried on Whatman paper. When coverslips were completely dry, they were mounted on glass slides using 8 μl Mowiol (Sigma-Aldrich).

Images were captured using an Olympus ScanR inverted microscope system equipped with an IX83 inverted motorized frame with Z-drift control, Semrock DAPI/FITC/Cy3/Cy5 Quad LED filter set, sCMOS Hamamatsu Orca Fusion B Camera (Pixel size on chip 6.5 μm, Array size, 2304 x 2304 pixels or 5.3M pixels, FOV 14.976 mm

x 14.976 mm). An Olympus 20x UPLXAPO Air/Dry objective was used (NA 0.80, WD 0.6 mm, CC 0.17 mm). The light sources were Lumencor SPECTRA X Light Engine Independent LEDs (Violet 395/25 295 mW, Yellow 575/25 310 mW, Red 640/30 231 mW) used at 100% power. Identical exposure times were used for all samples within one experiment. For each sample, a grid of 7x7 fields of view were captured using the SCANR Acquisition Software (v3.2.0) under non-saturating conditions yielding a total of 3,000–7,000 nuclei per condition.

Images were analysed using the Olympus ScanR Image Analysis Software (v3.2.0). An automated background correction was performed for each colour channel separately. Segmentation of nuclei and foci was performed using the in-built object detection module based on intensity and size inclusion criteria with nuclei treated as the primary object and foci as the secondary object. Analysis results tables with parameters of interest (mean and total intensities of fluorescence channels, object area, foci counts etc.) were then exported and analysed and visualised using TIBCO Spotfire Software (v12.2.0).

2.15. Native-BrdU assay

Cells were seeded onto coverslips in growth medium containing 15 μM 5-Bromo-2′-deoxyuridine (BrdU) in 35 mm dishes and allowed to settle overnight. The following morning coverslips were transferred to individual wells of a 6-well plate and either left untreated or treated with 50 nM MMC. All cells were maintained in media containing 15 μM BrdU for the duration of the experiment. Media in MMC treated wells was rinsed out and replaced with fresh drug-free media after 24 h. Coverslips were then pre-extracted, fixed, and stained with relevant antibodies according to the identical procedure laid out in section 2.14 except the primary antibody incubation was

performed overnight at 4°C. Images and analysis were also carried out in the same fashion as for QIBC experiments described above.

2.16. siRNA knockdown

Gene knockdown with siRNA was achieved via reverse transfection with SMARTpool ON-TARGETplus siRNAs (Dharmacon) using Lipofectamine RNAiMAX transfection reagent (Thermo Fisher). For time course experiments siRNA transfection was performed 24 h prior to the addition of MMC. The following siRNAs were used at a concentration of 20 nM: siTOPBP1, siETAA1, siRFWD3. ON-TARGETplus Non-targeting Control Pool siRNA was used as a negative control.

2.17. Genome-wide CRISPR-Cas9 screen

The genome-wide CRISPR-Cas9 MMC sensitivity screen was performed using a modified version of the Olivieri and Durocher protocol (Olivieri and Durocher, 2021). U2OS WT and U2OS ZUP1 KO cells were plated in 33x T175 flasks each at a density of 3 x 10^6 cells per flask to yield a 422-fold library coverage. The following day cells were transduced with the LCV2::TKOv3 single-component lentiviral library at a low MOI of 0.3 determined empirically for each cell line with 8 μg/ml polybrene used to aid transduction efficiency. Growth media was replaced 24 h after transduction and after a further 24 h cells were selected by the addition of 2 μg/ml puromycin. Puromycin selection was continued for 72 h whereupon cells were passaged, and 30 x 10^6 cells were replated per condition to maintain 422x library coverage. Additionally, a cell pellet of 30 x 10^6 cells was collected for each cell line and considered as the day 0 (T0) initial time point. Cells were then subcultured in drug-free media on days 3 and 6 (T3 and T6) at which point they were split into technical duplicate populations that were either left

untreated or treated with an empirically determined lethal dose, 20% (LD20) of MMC (10 nM for WT; 2.5 nM for ZUP1 KO). Cells were then subcultured every 3 days (at T9, T12, and T15) with or without MMC with 30 x 10^6 cells replated for each condition until the experimental endpoint at day 18 (T18). At this stage cell pellets of 30 x 10^6 cells were collected and frozen at -80°C for each replicate.

Genomic DNA was extracted from pellets collected at T0 and T18 using the Wizard Genomic DNA Purification Kit (Promega) with RNA digestion performed using PureLink RNase A (Thermo Fisher). Genome-integrated sgRNA sequences were amplified from gDNA by PCR using NEBNext Ultra II Q5 Master Mix (New England Biolabs) with PCR1_LCV2_FWD and PCR1_LCV2_REV primers. A second PCR reaction was then performed to attach Illumina TruSeq adapters and i7 multiplexing barcodes using a pool of 9 staggered forward primers (PCR2_FWD_01–09) and a unique reverse primer for each sample containing the i7 barcode (PCR2_REV_01-13; primers 4, 10, and 11 were not used). PCR2 products were gel purified using a QIAquick Gel Extraction Kit (QIAGEN) and run through a QIAquick PCR purification column (QIAGEN) before being pooled and sequenced via next-generation sequencing (NGS) on an Illumina NovaSeq 6000. See Appendix F for primer sequences.

The raw FASTQ NGS output files were trimmed using the Cutadapt v4.1 script to leave the 20 bp regions corresponding to integrated sgRNA sequences (Martin, 2011). The trimmed products from each flow cell corresponding to the same sample were concatenated using the 'cat' zsh shell command on a mac terminal. Trimmed reads were then assigned to the relevant sgRNA in the TKOv3 library and a read count matrix generated using the MAGeCK v0.5.9 algorithm (Li et al., 2014). To identify genes required for survival in the presence of MMC in each cell line, normalised gene fold change scores (NormZ) were calculated from the read count matrix using the DrugZ

algorithm (Colic et al., 2019). A NormZ value of < -3.0 was applied as a cut-off for significant hits as had been used previously in a published genome-wide MMC sensitivity screen (Schubert et al., 2022).

2.18. Gene ontology enrichment and network interaction analysis

Gene ontology (GO) enrichment analysis was performed for the top hits from U2OS WT and ZUP1 KO cells (NormZ <-3.0) using the PANTHER v17.0 statistical overrepresentation test for Biological Process Complete annotated terms using Fisher's Exact test with Bonferroni correction for multiple testing (Mi et al., 2019).

Gene network analysis was performed using STRINGdb v11.5 with a full STRING network analysis (both functional and physical interactions) performed with an interaction threshold score of 0.400 (Szklarczyk et al., 2019). Networks were exported as a vector graphic image and figures edited in Adobe Illustrator.

2.19. Generation of Cas9 stable cell lines

U2OS WT and ZUP1 KO cells were plated in 6-well plates at a density of $2x10^4$ cell per plate. 24 h later cells were transduced with packaged lentiCas9-Blast lentiviral vector at an empirically determined MOI of 1.0. After 24 h lentivirus containing media was removed and replaced with fresh DMEM and cells were cultured for a further 24 h. Cells were selected with 15 μg/ml blasticidin (Thermo Fisher) for 7 days until all untransduced cells had died and maintained in 3 μg/ml blasticidin thereafter. Cells were then separated into single cell clones via the limiting dilution method described above for KO cell generation. Once single colonies were obtained, they were screened for FLAG-Cas9 by immunoblotting and clones with roughly equal expression levels were chosen for WT

and ZUP1 KO cells. Cas9 activity was assessed by transducing Cas9 stable cells and parental controls with the pKLV2-BFP/GFP reporter and measuring the GFP:BFP fluorescence ratio. The pKLV2 reporter bears an sgRNA targeting GFP while BFP acts as an internal control so by measuring the GFP:BFP fluorescence ratio a measure of Cas9's activity is obtained. U2OS lentiCas9 C4 and ZUP1 KO lentiCas9 C5 were chosen to perform two-colour competitive growth assays with as they had very similar FLAG-Cas9 expression and displayed a lack of GFP fluorescence when transduced with the pKLV2 reporter.

2.20. Two-colour competitive growth assay

Two-colour competitive growth assays were performed with sgRNA targeting the following GOIs: HELQ, NEIL3, BRCA2, and BRIP1/FANCJ with LacZ serving as a negative control. U2OS WT and ZUP1 KO cells stably expressing Cas9 were transduced with either lentiGuide-Puro-mCherry-NLS-sgLacZ or lentiGuide-Puro-GFP-NLS-sgGOI at an empirically determined MOI of 1.0. 24 h after transduction growth media was replaced with fresh media and cells were cultured for a further 24 h. Cells were then selected with 2 μg/ml puromycin (Gibco) for 72 h. At this stage mCherry-sgLacZ control and GFP-sgGOI cells were mixed in a 1:1 ratio (10,000 cells each) and plated in 12-well plate format in drug-free media or in media containing 2.5 nM MMC (i.e., the LD20 dose for ZUP1 KO cells). Live cell fluorescence imaging of GFP and mCherry signals was carried out ~6 h after initial plating to generate baseline t=0 readings. Cells were then imaged and passaged every 3 days for 18 days. Images were captured using an Olympus ScanR inverted microscope system (see section 2.14 for detail) equipped with a 4x UPLXAPO Air/Dry objective (NA 0.16, WD 13 mm) and a temperature, CO_2, and humidity environmental control chamber set to 37°C and 5% CO_2. For each sample, a

grid of 2x2 fields of view were captured using the SCANR Acquisition Software (v3.2.0). The focal plane was determined with the software autofocus tool using the transmission light channel, while GFP and mCherry fluorescence was captured using the FITC and Cy3 colour channels respectively. The number of GFP and mCherry positive nuclei was calculated by running sequential pipelines in the Olympus ScanR Image Analysis Software (v3.2.0) to segment nuclei as the main object in the FITC channel followed by the mCherry channel.

3

Generation and characterisation of ZUP1 CRISPR-Cas9 knockouts

Contents

3.1. Introduction

The initial investigations of ZUP1 cellular function utilised siRNA knockdown to study the phenotypic consequences of its depletion (Haahr et al., 2018; Hewings et al., 2018; Kwasna et al., 2018). A clonogenic survival assay using a single ZUP1 targeting siRNA showed that these cells were sensitive to IR and camptothecin treatment (Kwasna et al., 2018). Additionally, in unchallenged cells depleted of ZUP1 levels of chromatin-bound 53BP1 and γH2AX were observed to be higher than in WT cells, suggesting a higher rate of spontaneous DNA damage (Kwasna et al., 2018). The elevated number of 53BP1 foci could also be rescued by doxycline inducible expression of siRNA-resistant WT ZUP1 but not ZUP1 with a catalytic inactivating C360S mutation. Haahr *et al.* demonstrated that ZUP1 siRNA knockdown cells had an increased number of micronuclei when treated with aphidicolin, hydroxyurea, or camptothecin and showed that a greater proportion of micronuclei resulting from camptothecin treatment were positive for RPA2 foci relative to cells stably expressing siRNA-resistant GFP-tagged ZUP1 (Haahr et al., 2018). The same study also used a cell line bearing a single artificial lac operator (*LacO*) array bound by mCherry-tagged lac repressor (LacR) to induce a site-specific replication block. Using this model system, the authors demonstrated that levels of K63-linked Ub were elevated at this site-specific replication block when ZUP1 was depleted with siRNA. This finding was extended by the Hewings *et al.* study which found K63-linked ubiquitylated RPA1 and RPA2 to be substantially enriched following

K63-linked Ub immunoprecipitation in HEK293T cells treated with hydroxurea and depleted of ZUP1 using siRNA knockdown (Hewings et al., 2018).

Taken together, these preliminary findings strongly suggest a role for ZUP1 in regulating K63-linked ubiquitin dynamics at stressed replication forks. However, a caveat to these studies is that they all relied on siRNA knockdown to study the consequences of ZUP loss which, as detailed in Chapter 1, can suffer from off-target effects and incomplete depletion of the target protein. Based on these initial findings, the initial aim of my DPhil project was to generate ZUP1 KO cell lines using CRISPR-Cas9 gene editing to allow the first detailed analysis of the cellular phenotypes associated with complete ZUP1 loss.

3.2. Results

3.2.1. Generation of isoform-specific and catalytically inactive ZUP1 knockouts

The *ZUP1* gene sequence is made up of ten exons with the contribution of each to the protein sequence depicted in Figure 9A. ZUP1's catalytic cysteine C360 is encoded by exon 6 of its gene sequence, while the remaining two residues (H491 and D512) that make up its catalytic triad are encoded by exon 9. There are additionally five distinct predicted ZUP1 isoforms expressed within cells (isoforms A, B, C, D, and E) whose individual functions are unknown and have not been characterised. Importantly, the major bioinformatics databases give disparate predictions for functional ZUP1 isoforms with Ensembl predicting only two protein coding isoforms, while the NCBI AceView and NIH RefSeq databases predict four; potentially suggesting the presence of five sperate isoforms between them (Cunningham et al., 2022; O'Leary et al., 2016; Thierry-Mieg and Thierry-Mieg, 2006). Different sgRNA targeting strategies were therefore tested to determine the most effective approach to generate complete ZUP1 KOs that lack expression of all known isoforms (Figure 9C). The U2OS cell line was chosen to generate KOs in as it is a well-established, genetically tractable model cancer cell line used in the DNA repair field and is amenable to microscopic analysis due to its cellular morphology. After transfection of Cas9-sgRNA plasmids and brief puromycin selection, single-cell cloning was performed to yield monoclonal cell lines for each targeting approach. KO clones were screened by immunoblotting using a custom anti-ZUP1 antibody generated by the Gibbs-Seymour lab, which demonstrated far greater specificity than commercially available antibodies and with which I was able to identify the major isoforms of the protein. The antibody was generated by immunising mice with

full-length human ZUP1, and the epitope was mapped to the α2/3 domain by screening a deletion series of recombinant ZUP1 fragments by immunoblotting, which showed a loss of signal for the delta-α2/3 ZUP1 construct (data not shown). See Appendix A for antibody details.

The initial KO approach involved targeting *ZUP1* exon 2 with a single sgRNA to generate a frameshift indel mutation early in the gene sequence leading to nonsense mediated decay of the resulting transcripts. This approach resulted in the almost complete loss of the two main isoforms of the protein (denoted as A and B), but an immunoreactive band corresponding to the predicted size of ZUP1 isoform C was still observed by immunoblotting (Figure 9B; lanes 3-5). This is likely because exon 2 is not included in isoform C's spliced mRNA sequence and can still form functional protein when exon 2 is disrupted via a frameshift mutation.

As an alternative approach, the catalytic cysteine-containing exon 6 was therefore targeted since all predicted isoforms contain this exon and any residual protein would, by definition, not retain catalytic function. Exon 6 was targeted using a dual guide approach with intronic sgRNAs flanking the entire exon region so that this sequence would be entirely excised from the *ZUP1* gene sequence (Figure 9C; middle panel). While this approach abolished all bands corresponding to predicted ZUP1 isoforms on an immunoblot (Figure 9B; lanes 7-9), a band corresponding to the truncated form of isoform A (i.e. missing exon 6) was observed in all three representative KO clones tested (indicated by red arrowhead in Figure 9B). While this truncated protein would not carry any DUB catalytic function due to the absence of its catalytic cysteine, it is possible that it could carry out a scaffolding or protein-protein interaction function within cells and maintain some, perhaps dominant negative, physiological function. Additionally, a very faint band, possibly corresponding to the predicted size of isoform A, was still observed.

Therefore, a multi-guide approach was ultimately taken to target both exon 2 and exon 6 to cause a frameshift early in the gene sequence as well as excise the entire region conveying ZUP1's catalytic function (Figure 9C; bottom panel). Double exon 2/6 KOs were generated sequentially by targeting exon 6 in the pre-existing ZUP1 KO Exon 2 Clone 2 background. As shown in Figure 9B lanes 11-13, this approach yielded KO clones completely lacking any observable ZUP1 protein expression for isoforms A, B, or C. The absence of isoform D/E, however, could not be conclusively shown via immunoblotting leading to the subsequent sequence validation presented below. The independent double exon 2/6 KO clones C38 and C62 are predominantly used throughout this thesis to characterise the cellular effects of ZUP1's absence.

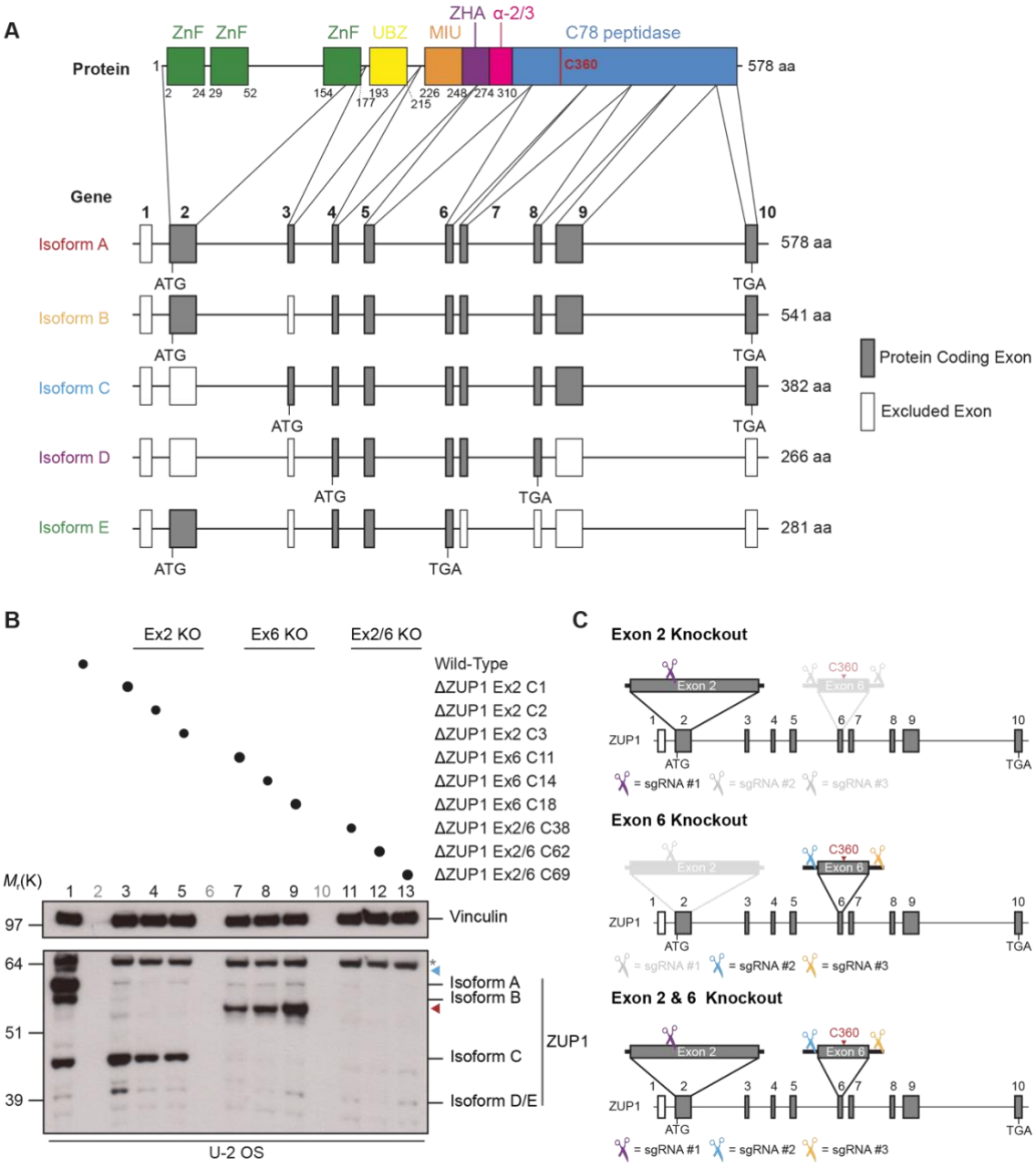
A
Protein
ZnF ZnF ZnF UBZ MIU ZHA α-2/3 C78 peptidase
C360
578 aa
Gene
Isoform A
Isoform B
Isoform C
Isoform D
Isoform E
ATG
TGA
578 aa
541 aa
382 aa
266 aa
281 aa
Protein Coding Exon
Excluded Exon
B
Ex2 KO
Ex6 KO
Ex2/6 KO
Wild-Type
ΔZUP1 Ex2 C1
ΔZUP1 Ex2 C2
ΔZUP1 Ex2 C3
ΔZUP1 Ex6 C11
ΔZUP1 Ex6 C14
ΔZUP1 Ex6 C18
ΔZUP1 Ex2/6 C38
ΔZUP1 Ex2/6 C62
ΔZUP1 Ex2/6 C69
Vinculin
Isoform A
Isoform B
Isoform C
Isoform D/E
ZUP1
U-2 OS
C
Exon 2 Knockout
Exon 6 Knockout
Exon 2 & 6 Knockout
= sgRNA #1
= sgRNA #2
= sgRNA #3

Figure 9. Generation of ZUP1 CRISPR-Cas9 knockout cell lines

(A) Schematic representation of ZUP1's gene and protein domain architecture and predicted isoform variants. Exons that contribute to the protein sequence of each isoform are highlighted in grey. The catalytic cysteine (C360) is shown in red within the C78 peptidase domain.

(B) Anti-ZUP1 immunoblot showing U2OS WT and representative clonal ZUP1 CRISPR-Cas9 KO cell lines for each of the sgRNA targeting strategies depicted in panel C. Blue arrowhead (➤) indicates possible monoubiquitinated ZUP1 species. Red arrowhead (➤) indicates truncated ZUP1 species resulting from deletion of exon 6. Grey asterisk (*) Indicates non-specific band.

(C) Schematic showing multi-guide approach to generate full CRISPR-Cas9 ZUP1 Kos. (Upper panel) Depicts the initial single guide approach taken to target exon 2 to generate a frameshift mutation disrupting the downstream gene sequence. (Middle panel) Shows a dual guide approach with sgRNAs flanking exon 6 of ZUP1 containing its catalytic cysteine residue. (Lower panel) Outlines the approach taken to target both exon 2 and exon 6 of ZUP1 to yield a complete KO with no residual protein expression.

3.2.2. Sequence confirmation of ZUP1 knockout

To confirm ZUP1 KO at the gene level the relevant regions surrounding exon 2 and 6 were amplified by PCR and sequenced via Sanger sequencing. Sequence traces for the exon 2 region revealed the presence of indels dependent on the identity of the sgRNA used to generate the KO (Figure 10A). Various sgRNAs were tested with resulting indels ranging from a small deletion to a single nucleotide insertion (Figure 10A). Exon 2 KO clones were additionally screened using the interference of CRISPR edits (ICE) algorithm and cell lines demonstrating the presence of a frameshift mutation in 100% of the monoclonal population were selected, as shown for the representative clones depicted in Figure 10B. Exon 6 KO clones were all screened via a PCR strategy using primers flanking the exon 6 region as shown in Figure 10D. Representative WT (+/+), heterozygous KO (+/-), and homozygous KO (-/-) cells screened via this approach are shown in Figure 10C. It should be noted that U2OS cells are karyotypically abnormal with chromosome counts in the hypertriploid range, so the notation used here may not reflect the true copy number of alleles present in cells. Rather they reflect the presence or absence of WT or truncated alleles amplified by the PCR strategy depicted in Figure 10D. Clonal cells selected for being homozygous exon 6 KOs via the PCR screening strategy were then sequenced via Sanger sequencing and the resulting traces aligned to the ZUP1 genome sequence (Figure 10E). These alignments confirmed that ZUP1 KO cells created using the dual-guide approach to excise exon 6 completely lacked this gene region, while retaining the rest of the gene sequence.

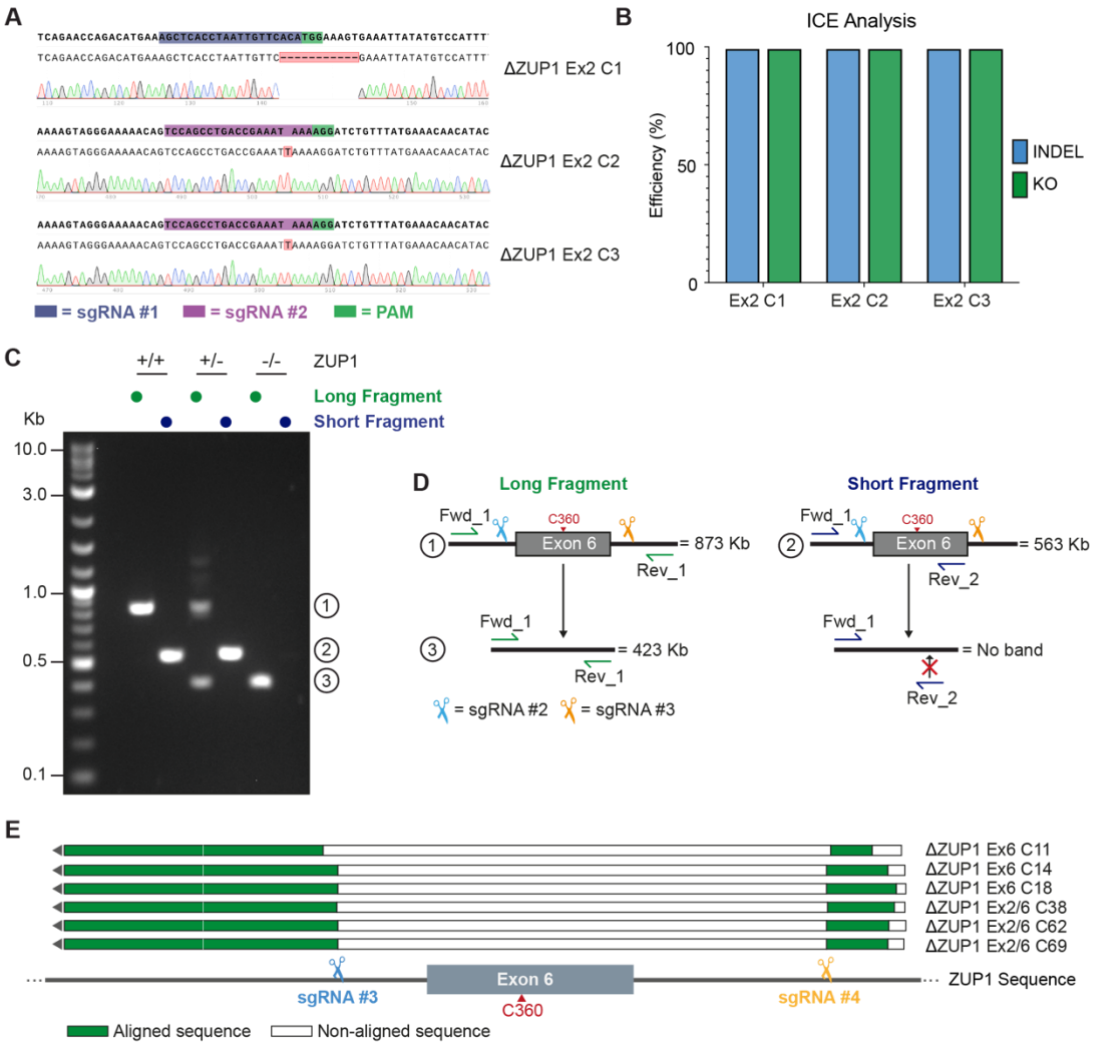
A
ΔZUP1 Ex2 C1
ΔZUP1 Ex2 C2
ΔZUP1 Ex2 C3
= sgRNA #1
= sgRNA #2
= PAM
B
ICE Analysis
Efficiency (%)
100
50
0
Ex2 C1
Ex2 C2
Ex2 C3
INDEL
KO
C
+/+
+/-
-/-
ZUP1
Long Fragment
Short Fragment
Kb
10.0
3.0
1.0
0.5
0.1
D
Long Fragment
Short Fragment
Fwd_1
C360
Exon 6
= 873 Kb
Rev_1
= 423 Kb
= 563 Kb
Rev_2
= No band
= sgRNA #2
= sgRNA #3
E
ΔZUP1 Ex6 C11
ΔZUP1 Ex6 C14
ΔZUP1 Ex6 C18
ΔZUP1 Ex2/6 C38
ΔZUP1 Ex2/6 C62
ΔZUP1 Ex2/6 C69
sgRNA #3
Exon 6
C360
sgRNA #4
ZUP1 Sequence
Aligned sequence
Non-aligned sequence

Figure 10. Sequence confirmation of ZUP1 knockout

(A) Alignment of Sanger sequencing traces from representative exon 2 KO clones showing the position of the sgRNA binding site and PAM sequence. The resulting indel is highlighted in red in the aligned sequence.

(B) ICE analysis of three representative exon 2 KO clones indicating the prevalence of indel mutations within the clonal population and the proportion of indels resulting in a frameshift mutation denoted as KO.

(C) Agarose gel showing PCR screening using exon 6 flanking primers described in panel D. Representative WT (+/+), heterozygous deletion (+/-) and homozygous deletion (-/-) mutants are shown.

(D) Schematic of PCR strategy used to screen ZUP1 exon 6 KO clones. Genomic DNA was isolated from clones and two PCR reactions were performed for each designated as long-fragment and short-fragment reactions. The long-fragment PCR used primers flanking the exon 6 region which results in a band of 873 kb (1) for an intact ZUP1 sequence or a band of 423 kb (3) if the region between the two sgRNAs has been excised. The short fragment reaction utilised a forward primer preceding exon 6 and a reverse primer internal to exon 6. For intact gene sequences this yields a band of 563 kb (2) or no product in the case of CRISPR edited sequences.

(E) Sequence alignment of the *ZUP1* exon 6 region for representative KO clones edited with sgRNAs targeting exon 6 alone or in conjunction with an sgRNA targeting exon 2.

3.2.3. Analysis of ZUP1 mRNA expression

The Ensembl and NCBI AceView databases were searched to identify predicted isoforms for ZUP1. This revealed four predicted protein coding isoforms from NCBI Aceview (A, B, C and D) and two from Ensembl (A and E) (Figure 11). The expected sizes for the given isoforms are as follows: isoform A = 66.0 kDa, isoform B = 61.6 kDa, isoform C = 43.8 kDa, isoform D = 30.5 kDa, isoform E = 32.3 kDa. However, the observed size of each isoform appears slightly differently when resolved by SDS-PAGE as seen in Figure 9B, as ZUP1 migrates a bit faster than expected on the gel. Nevertheless, bands clearly corresponding to the size of isoforms A, B, and C can be seen via immunoblot using the Gibbs-Seymour lab's custom mouse monoclonal ZUP1 antibody, while a very faint band similar in size to the predicted weights of isoform D or E may also be present (Figure 9B). Given that residual isoform expression was observed following CRISPR-Cas9 KO of exon 2 and 6 individually, I developed a semiquantitative RT-PCR strategy to identify which isoforms are expressed at transcript level in cells and to confirm that all predicted isoforms are absent in double exon 2/6 KOs (Figure 11). This strategy was based on a previously published RT-PCR method that demonstrated the amplification of low-abundance alternatively spliced mRNA variants by incorporating a cleavage step with exon-specific primers containing a restriction endonuclease site to degrade more highly expressed isoforms prior to PCR amplification (Wang et al., 2008). The workflow for this strategy is outlined in Figure 11B. Briefly, RNA was extracted from cells and total mRNA converted to cDNA using oligo dT primers that bind the poly-A tail of mature mRNA molecules. In separate reactions, specific ZUP1 isoforms were then degraded via restriction digestion using exon-specific primers containing a unique restriction site. By targeting exons unique to specific isoforms these transcripts could be depleted allowing

for the amplification of specific lower abundance isoforms. PCR was then performed using a forward primer contained in exon 1 and a reverse primer in exon 6 which are found in all predicted transcript variants. The expected pattern of bands for this semiquantitative RT-PCR approach with cDNA extracted from WT cells is shown with a simulated gel in Figure 11C. With no cleavage of specific isoform transcripts RT-PCR products for isoform A and C should be distinguishable at 1211 bp and 637 bp respectively, while the products for isoform B, D and E run at a similar size of 1042–1100 bp.

The actual resulting pattern from WT cDNA, seen in Figure 11D lane 3, shows bands corresponding to isoform A and isoforms B, D or E, but not isoform C. This may be due to the low abundance of isoform C transcript its PCR amplification is outcompeted by higher abundance transcripts. By targeting all other isoforms with an exon 2 specific cleavage primer, a product corresponding to the expected size of isoform C could indeed be observed (Figure 11D; lane 4). A faint residual band corresponding to isoform A is still present in lane 4 possibly reflecting incomplete digestion of the isoform A transcript. A specific product corresponding to the expected size of isoform B could also be observed when all other transcripts were depleted with a cleavage primer targeting exon 3 (Figure 11D; lane 5). To distinguish between isoform D and E, predicted by the NCBI AceView and Ensembl databases respectively, a cleavage primer was used to target exon 7 that is found in all transcripts except isoform E. Therefore, if a PCR product was obtained this should correspond to isoform E. Products were indeed observed from this amplification (Figure 11D; lane 4), however, the banding pattern resembled that of un-cleaved templates, possibly suggesting incomplete digestion of transcripts. Importantly, however, no products are observed when amplifying cDNA extracted from ZUP1 KO cells suggesting that these are complete KOs at the transcript level. While not

conclusively ruling out the presence of low abundance expression of isoform D or E at the transcript level, the semiquantitative RT-PCR data together with immunoblot and sequence data robustly characterise CRISPR-Cas9 cell lines as ZUP1 null at transcript and protein level.

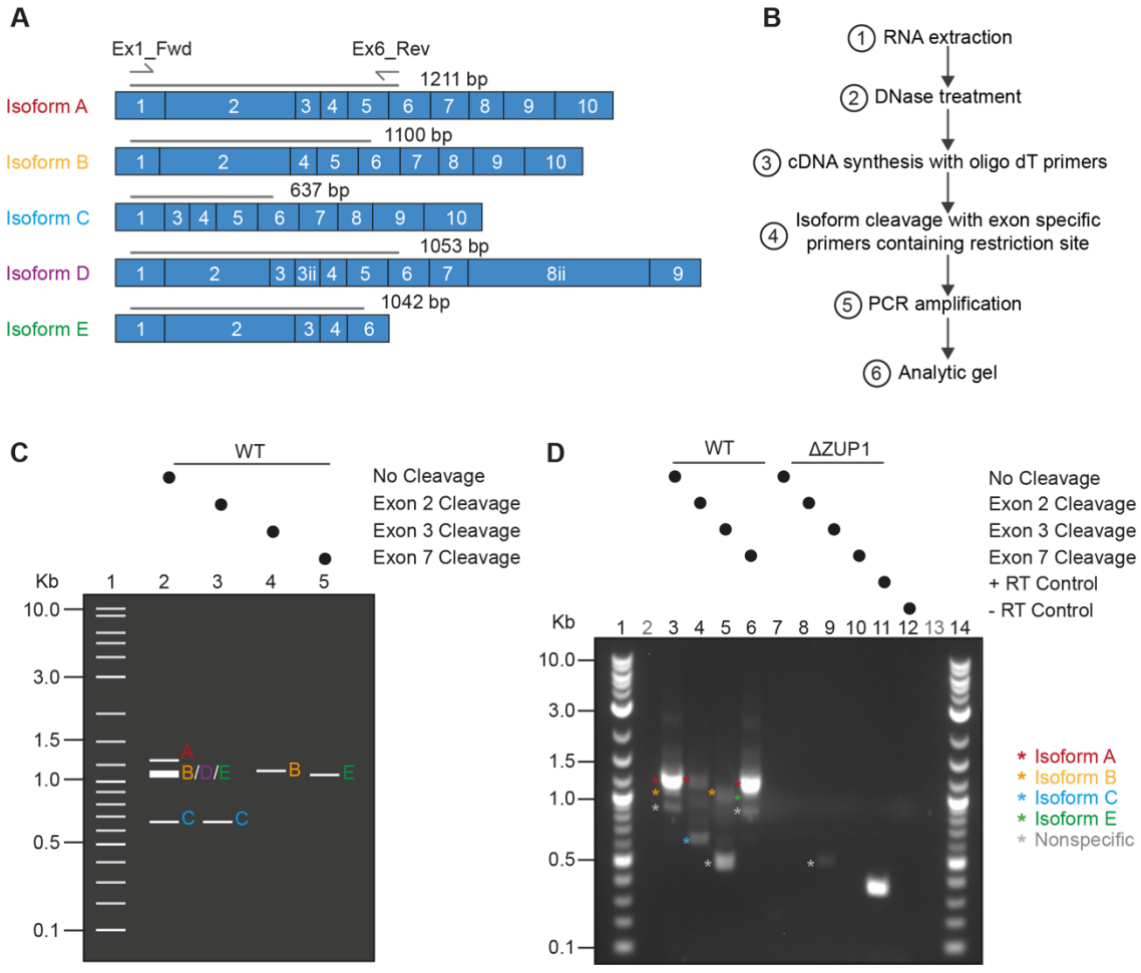

Figure 11. Identification of ZUP1 isoforms by semiquantitative RT-PCR

(A) Schematic diagram of the ZUP1 gene sequence with predicted ZUP1 isoforms. Exons that contribute to the protein sequence of each isoform is highlighted in blue.

(B) Schematic of ZUP1 isoform mRNA sequences with predicted size of PCR products resulting from amplification with a forward primer within exon 1 and reverse primer within exon 6.

(C) Simulated agarose gel showing expected band pattern resulting from the PCR amplification described in panel B. The expected band pattern for PCRs pre-treated with a restriction enzyme and oligonucleotide primer specific to exon 2, 3, or 7 and containing a unique restriction site are shown. The resulting PCR amplification should amplify only those isoforms that do not contain the exon targeted by the relevant cleavage primer.

(D) Actual band pattern observed from PCRs performed on cDNA derived from representative U2OS WT and ZUP1 KO Exon2/6 cells. The coloured asterisks indicate the relevant ZUP1 isoform. Grey asterisks indicate the presence of a non-specific band not correlated to any expected band sizes. A positive and negative control reaction with and without the addition of reverse transcriptase on a model substrate are included in lanes 11 and 12. Data presented here for C38 ZUP1 KO cells, but additionally performed for C62 clone used throughout this thesis.

3.2.4. ZUP1 is not required for unperturbed cell proliferation

Given that ZUP1 KO cells are viable and don't display any gross morphological abnormalities, an assessment of their proliferation rates was undertaken to generate a first approximation of the impact of ZUP1 loss on cellular fitness. This was achieved by a serial passage proliferation assay under standard conditions to compare the unchallenged growth rate of three independent U2OS ZUP1 KO clones to their WT counterparts (Figure 12). Cells were grown under normal conditions and were counted and passaged every 3 days. This analysis revealed that ZUP1 KO cells are fully viable but display a moderately impaired proliferation rate compared to WT cells. The doubling time for WT U2OS cells was calculated to be 25.7 h while the doubling time for ZUP1 KO clones ranged from 29.2–32.2 h. These data confirm that under standard conditions *ZUP1* is a non-essential gene as has been reported previously (Tsherniak et al., 2017). However, given the indications from the initial publications that ZUP1 plays a role in the DNA damage response, more severe phenotypic defects of ZUP1 KO cells may only be revealed following damage to their DNA.

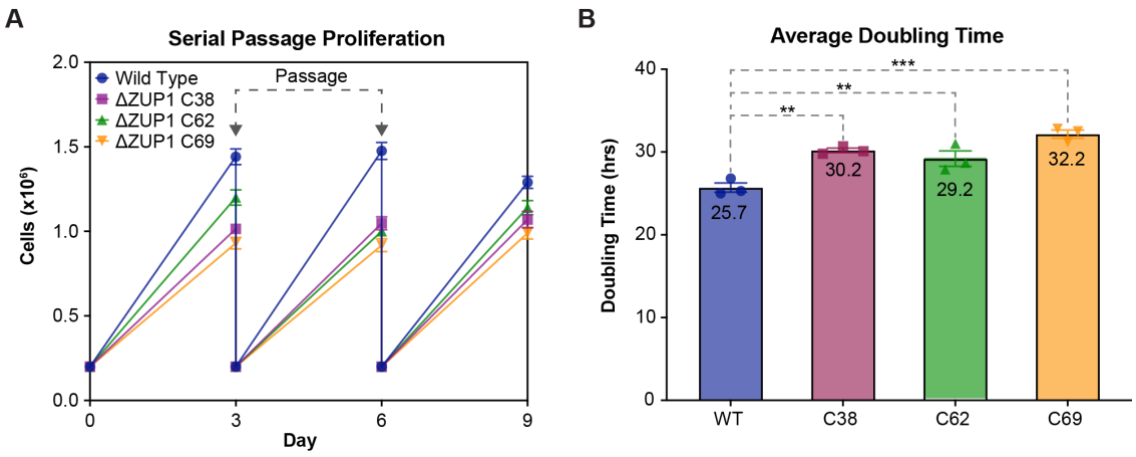

Figure 12. Serial passage growth rate analysis of U2OS ZUP1 KO cells

(A) Serial passage proliferation analysis of untreated U2OS ZUP1 KO cell lines in comparison to WT cells. Every 3 days cells were passaged and counted and replated at a density of 200,000 cells per dish. Each data point is representative of n=2 biological replicates with each repeat consisting of 3 technical replicates. Error bars indicate SEM. **(B)** Average double times for each indicated cell line. Doubling times were calculated for each passage and averaged across the three passages performed. Error bars indicate SEM. Asterisks indicate significance as calculated by one-way ANOVA with Dunnett's multiple comparisons test (** $p \leq 0.005$; *** $p \leq 0.0005$).

3.2.5. ZUP1 is required for cellular resistance to replication-coupled DNA damage

To determine whether ZUP1 plays a role in the DDR and to identify which DNA repair pathway(s) it functions in, the viability of KO cells was assessed in response to a suite of genotoxic agents that cause a wide range of distinct types of DNA damage. Hypersensitivity of ZUP1 KO cells to a particular lesion type would therefore suggest a dysfunction in a specific repair pathway of the DDR. The clonogenic survival assay is the gold standard used to assess the viability of cultured cells following insult to their genomic integrity (Franken et al., 2006). It assesses the ability of cells to grow from single cells to form a colony of many cells and is a measure of the proportion of cells that retain the ability to divide indefinitely following genotoxic insult. Clonogenic survival assays were therefore performed to assess the sensitivity of ZUP1 KO clones relative to their WT counterparts in response to cisplatin, formaldehyde, MMC, olaparip, talazoparib, hydroxyurea, topotecan, and the ATR inhibitor AZD6738. The mode of action and DNA lesion type induced by these agents are summarised in Table 6. The results of these clonogenic survival assays revealed ZUP1 KO clones to be significantly hypersensitive to genotoxic agents that cause replication-coupled DNA damage (Figure 13). ZUP1 KO cells were seen to be particularly hypersensitive to the interstrand crosslinking agent MMC and the PARP inhibitors talazoparib and olaparib, while some degree of sensitivity was seen against all agents tested except hydroxyurea (Table 6). It is interesting to note that cell death following talazoparib treatment was achieved at lower molarity than for olaparib treatment. Talazoparib has been shown to possess stronger PARP trapping activity than olaparib while inhibiting PARP catalytic activity to a similar extent, which suggests that PARP trapping may be a key mediator of cytotoxicity in

U2OS cells (Hopkins et al., 2015). However, ZUP1 KO cells showed similar sensitivity relative to WT cells when treated with talazoparib or olaparib. This could suggest that the additional hypersensitivity of ZUP1 KO cells to PARPi is mediated by an effect distinct from their PARP trapping activity, such as the recently described correlation of PARPi lethality with excessive ssDNA generation resulting from defective Okazaki fragment processing (Cong et al., 2021). Therefore, if ZUP1 loss leads to excessive ssDNA generation this could confer the observed sensitivity to PARPi.

Notably, no significant hypersensitivity of ZUP1 KO cells relative to WT cells was observed following treatment with hydroxurea. This may suggest that ZUP1 responds to fork blocking lesions rather than just fork stalling, or that the cytotoxicity of hydroxyurea is mediated by a mechanism of action distinct from its canonical fork stalling effect at the concentrations used in this assay (Figure 13F). It should also be noted that although the ZUP1 KO clones tested showed a broadly similar pattern of sensitivity to the same agents, variability was observed between the clones in response to some DNA damaging drugs. For the purposes of this DPhil thesis MMC was chosen for further investigation as ZUP1 KO cells displayed the greatest sensitivity to this agent. Further studies investigating the response to PARPi and ATRi treatment, however, would undoubtedly be of interest.

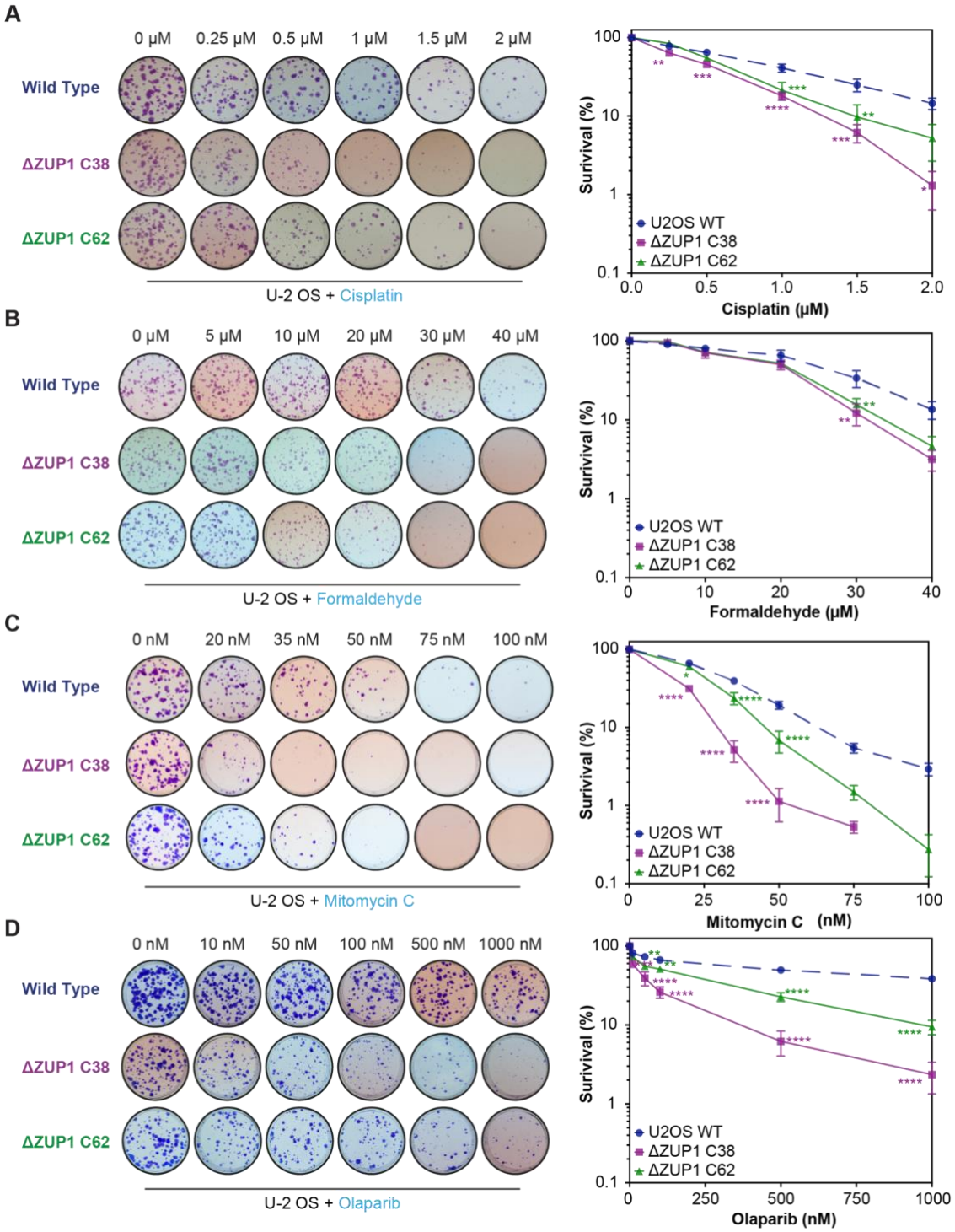

Figure continues on the next page.

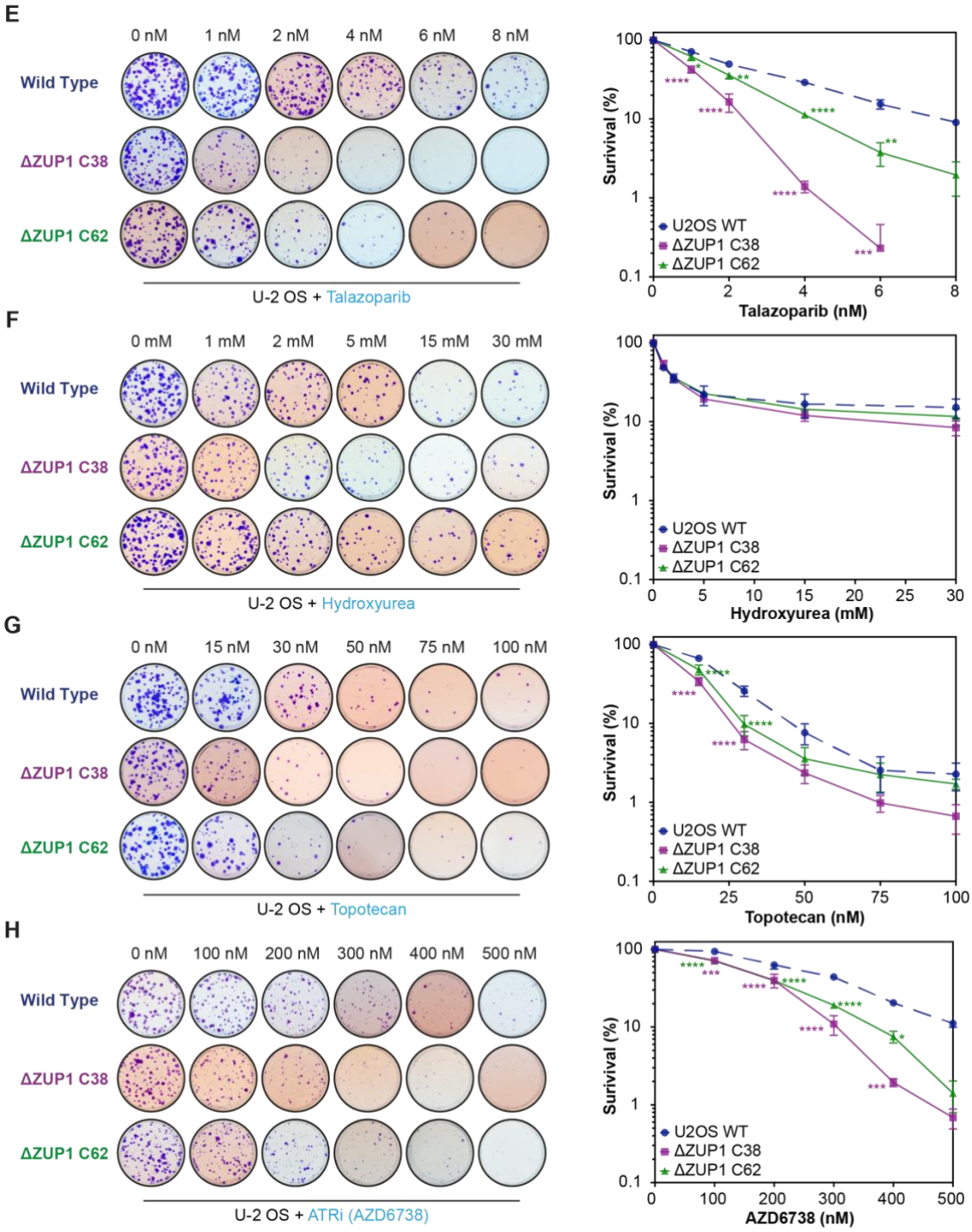
E
0 nM
1 nM
2 nM
4 nM
6 nM
8 nM
Wild Type
ΔZUP1 C38
ΔZUP1 C62
U-2 OS + Talazoparib
Survival (%)
U2OS WT
ΔZUP1 C38
ΔZUP1 C62
Talazoparib (nM)
F
0 mM
1 mM
2 mM
5 mM
15 mM
30 mM
U-2 OS + Hydroxyurea
Hydroxyurea (mM)
G
0 nM
15 nM
30 nM
50 nM
75 nM
100 nM
U-2 OS + Topotecan
Topotecan (nM)
H
0 nM
100 nM
200 nM
300 nM
400 nM
500 nM
U-2 OS + ATRi (AZD6738)
AZD6738 (nM)

Figure 13. Assessment of U2OS ZUP1 KO DNA damage sensitivities by clonogenic survival assay

Quantification and representative well images of clonogenic survival assays of U2OS WT and two independent ZUP1 KO cell lines performed with the indicated DNA damaging agents and treatment schedule. **(A)** Cisplatin chronic treatment. **(B)** Formaldehyde chronic treatment. **(C)** MMC acute treatment for 24 h. **(D)** Olaparib chronic treatment with drug change every 3 days. **(E)** Talazoparib chronic treatment with drug change every 3 days. **(F)** Hydroxyurea acute treatment for 24 h. **(G)** Topotecan acute treatment for 24 h. **(H)** ATRi (AZD6738) chronic treatment with drug change every 3 days. Each data point is representative of n=3 biological replicates with each replicate comprising 3 x technical replicate wells for each drug concentration. Clonogenic survival assays were carried out in conjunction with Kay Chong from the Gibbs-Seymour lab. Asterisks indicate significance as calculated by a two-way ANOVA with Dunnett's multiple comparisons test (* $p \leq 0.05$; ** $p \leq 0.005$; *** $p \leq 0.0005$; *** $p \leq 0.00005$). Error bars indicate SEM.

Table 6. Summary of sensitivities to DNA damaging agents

Drug	Treatment scheme	Mode of action	Sensitivity
MMC	24 h acute	DNA interstrand crosslinks	+++
Talazoparib	Continuous with replacement every 3 d	PARP inhibition/Increased trapping on DNA	+++
Olaparib	Continuous with replacement every 3 d	PARP inhibition/trapping on DNA	+++
Cisplatin	Continuous	DNA interstrand/intrastrand crosslinks	++
ATRi (AZD6738)	Continuous with replacement every 3 d	ATR inhibition → unscheduled origin firing, loss of replication fork protection	++
Formaldehyde	Continuous	DNA protein crosslinks	+
Toptotecan	24 h acute	Topoisomerase I inhibitor/ trapping on DNA	+
Hydroxyurea	24 h acute	dNTP synthesis inhibition → fork stalling	-

3.2.6. ZUP1 suppresses RPA hyperphosphorylation in response to ICLs

To further investigate the basis for ZUP1 KO cell's hypersensitivity to MMC, an immunoblot assay was carried out to monitor the activation of key DNA damage response markers following treatment with a sublethal dose of MMC (Figure 14). Cells were treated for a period of 24 h with 50 nM MMC to allow for all cells to enter S-phase so that the replication machinery of all cells would encounter ICL lesions introduced by MMC DNA damage. MMC was then washed out and fresh media supplied to cells and timepoints were taken to monitor the recovery of cells (Figure 14A). These data indicate that there is no apparent defect in the activation of FANCD2 or CHK1 by ubiquitylation or phosphorylation respectively in ZUP1 KO cells. No major alteration in the levels of unmodified FANCD2 or CHK1 markers was observed in ZUP1 KO cells either. There was, however, a substantially marked increase in RPA2 phosphorylation at S4/8, S33, and T21 in ZUP1 KO cells that persisted for a longer duration relative to their WT counterparts. RPA2 phosphorylation in WT cells peaked at 32 h after addition of MMC and began to recover towards baseline after this time. In ZUP1 KO cells, however, RPA2 phosphorylation continued to accumulate up to 48 h following MMC treatment and remained substantially elevated relative to WT at 72 h. These results suggest ICL repair is defective in cells following ZUP1 loss, and indicate that ZUP1 may function downstream, or parallel to, the activation of FANCD2 and CHK1.

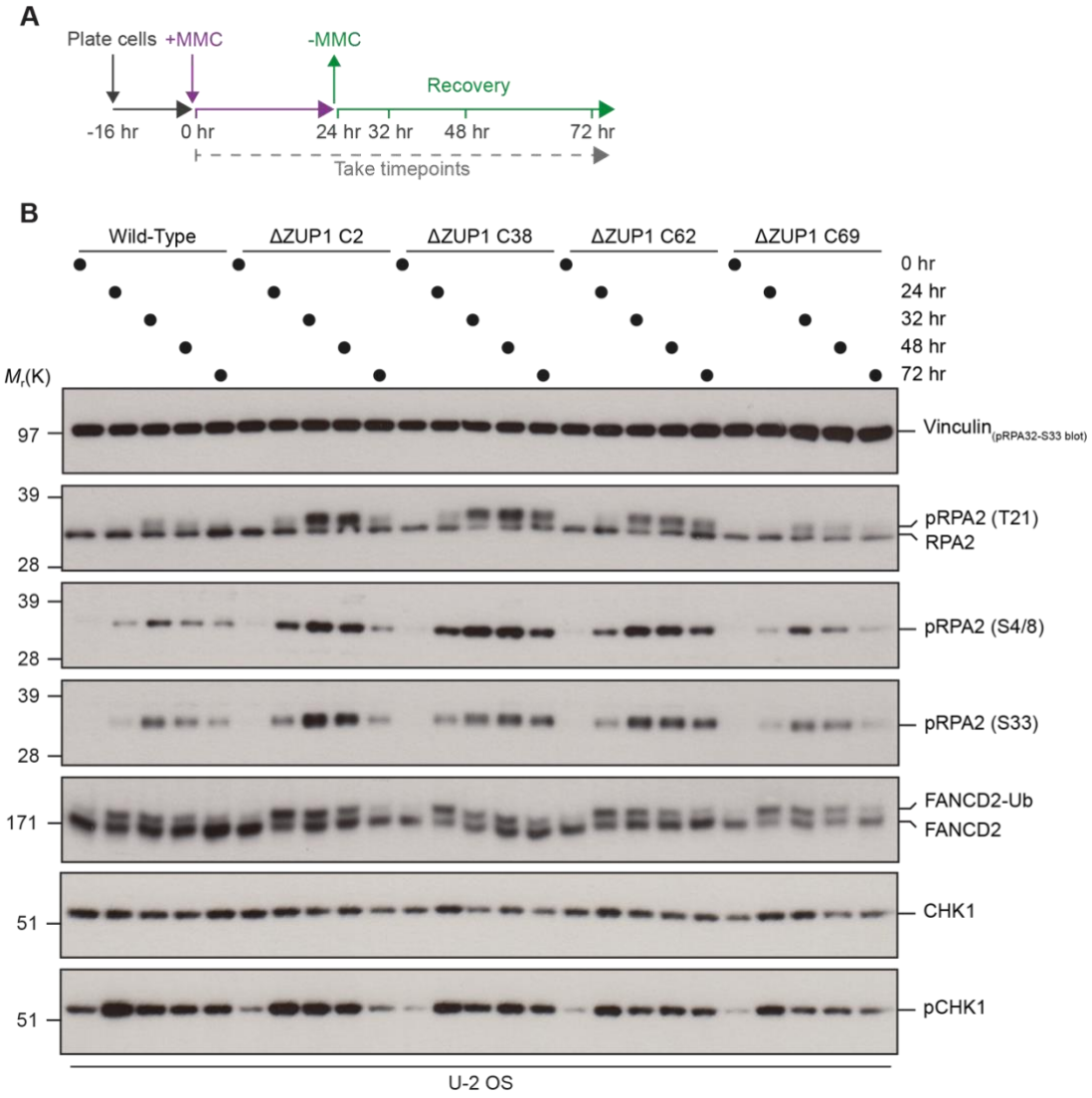

Figure 14. Immunoblot analysis of key DNA damage response factors in response to ICLs

(A) Schematic of MMC treatment time course and timepoint collection. Cells were treated with 50 nM MMC. Protein lysates were generated fresh at each timepoint and kept at -80°C until sample preparation.

(B) Immunoblot analysis of ZUP1 KO cells following recovery from MMC treatment using the indicated antibodies.

3.2.7. ZUP1 complemented cells show a trend towards rescue of RPA hyperphosphorylation and MMC sensitivity

Following the discovery of genotoxin hypersensitivity and hyperphosphorylation of RPA following MMC treatment in ZUP1 KO cells, my next aim was to determine whether these effects were mediated specifically by loss of ZUP1 by performing complementation experiments with exogenously expressed ZUP1. Rescue cell lines stably expressing exogenous ZUP1 constructs were therefore generated by transducing cells with lentiviral vectors expressing ZUP1 via promoters of different strength (PGK or CMV). The lentiviral vector utilising a PGK promotor was ultimately chosen as this resulted in ZUP1 expression most closely matching endogenous expression, whereas CMV promoter vectors greatly overexpressed ZUP1 (data not shown). Rescue cell lines were tested as pools and were not separated into monoclonal populations since it was reasoned that a distribution of ZUP1 expression levels among clones would be observed. Therefore, bias could be introduced by selecting clones that showed a desired phenotype. Looking at the whole pooled population would therefore give a less biased, more robust indication of whether re-expression of ZUP1 was able to rescue phenotypic defects. Initial rescue cells lines were created in a WT or ZUP1 KO background via transduction with a lentiviral vector expressing WT ZUP1 or an EV control (Figure 15). This ensured that rescue cells were compared to cell lines that underwent the same selection process for stable integration of the pLenti-PGK-Hygro vector.

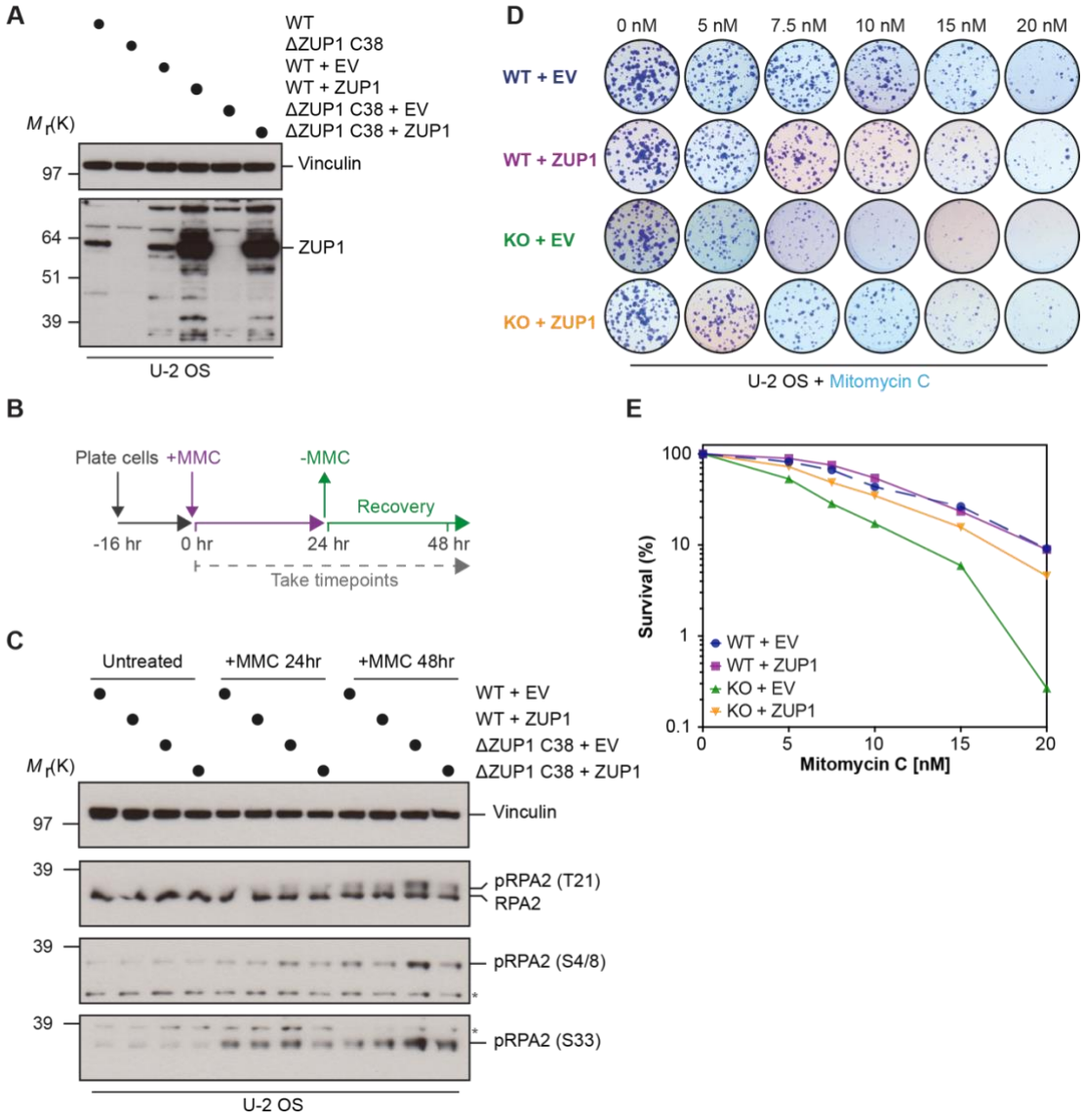

Figure 15. Initial rescue of RPA hyperphosphorylation and MMC sensitivity in ZUP1 KO cells

(A) Immunoblot to show rescue of ZUP1 expression in pooled ZUP1 KO U2OS cells using lentiviral encoded constructs expressed via a PGK promoter.

(B) MMC treatment schematic to test for rescue of RPA hyperphosphorylation.

(C) Immunoblot analysis of RPA phosphorylation following the MMC time course depicted in panel B.

(D) Representative well images from MMC clonogenic survival assay. Cells were treated with MMC chronically for 14 days.

(E) Quantification of colony survival following MMC treatment. Data points are from a single biological replicate with 3x technical repeat wells used for each concentration.

Although the pLenti-PGK-Hygro vector was chosen as expression construct due to most closely matching endogenous levels of ZUP1, immunoblot confirmation still revealed ZUP1 to be expressed ~5-fold higher than endogenous levels (Figure 15A). An initial immunoblot assay to monitor RPA2 phosphorylation at S4/8, S33, and T21 following recovery from MMC-induced damage revealed ZUP1 rescue cells to show a reduced level of phosphorylation of all three residues compared to their matched EV counterparts (Figure 15C). There was no apparent additional effect on RPA phosphorylation of ZUP1 expression in a WT background. ZUP1 rescue cells also showed almost complete rescue of sensitivity to MMC assessed by clonogenic survival assay (Figure 15D-E). However, these findings are caveated by the fact that these experiments constituted a single biological replicate as they were intended as an initial characterisation before generating re-expression cells lines using ZUP1 mutants for comparison. Following the initial promise of phenotypic rescue by WT ZUP1 complementation, cell lines were cryogenically stored, and additional rescue cell lines were generated bearing mutations in ZUP1 to determine the molecular basis for ZUP1's physiological function. These included variants bearing a mutation in the catalytic cysteine (C360R) and a deletion of the α2/3 region responsible for ZUP1's interaction with the RPA complex as well as for binding Ub chains (Figure 16A). Full-scale (n=3) immunoblot and clonogenic survival rescue experiments were then performed using

these cell lines as well as thawed stocks of cryopreserved WT and EV recues cell lines (Figure 16). These experiments, however, did not show a significant rescue of RPA hyperphosphorylation or reduction in sensitivity to MMC in ZUP1 KO complemented with WT ZUP1. However, a trend towards reduction in MMC sensitivity was observed in ZUP1 KO complemented with WT ZUP1 cells relative to KO cells complemented with EV, C360R or Δα2/3 protein. No additional increased viability or reduction in RPA phosphorylation was observed in WT cells complemented with ZUP1 protein.

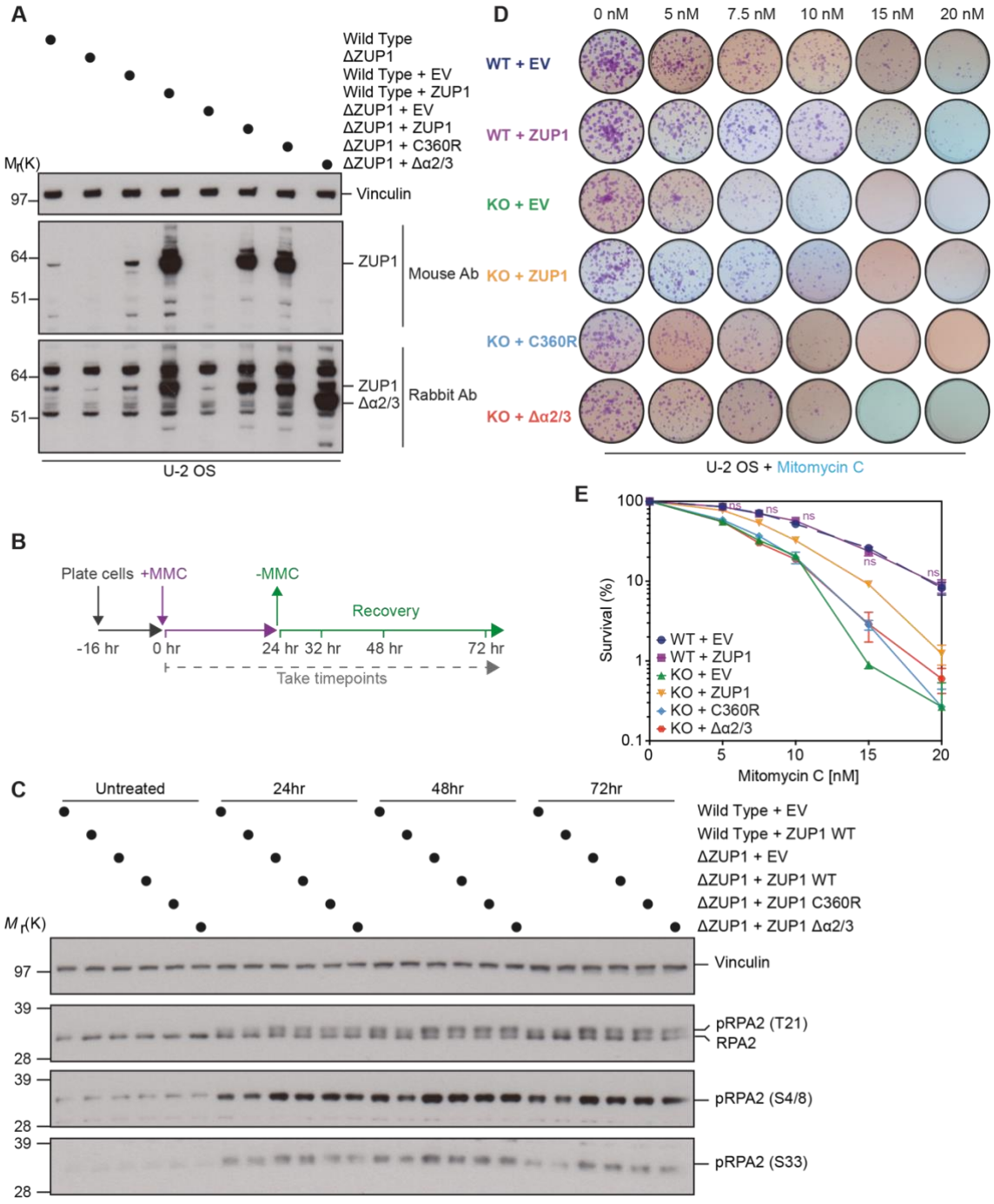
A
Wild Type
ΔZUP1
Wild Type + EV
Wild Type + ZUP1
ΔZUP1 + EV
ΔZUP1 + ZUP1
ΔZUP1 + C360R
ΔZUP1 + Δα2/3
Mr(K)
97
Vinculin
64
51
ZUP1
Mouse Ab
64
51
ZUP1
Δα2/3
Rabbit Ab
U-2 OS
B
Plate cells
+MMC
-MMC
Recovery
-16 hr
0 hr
24 hr
32 hr
48 hr
72 hr
Take timepoints
C
Untreated
24hr
48hr
72hr
Wild Type + EV
Wild Type + ZUP1 WT
ΔZUP1 + EV
ΔZUP1 + ZUP1 WT
ΔZUP1 + ZUP1 C360R
ΔZUP1 + ZUP1 Δα2/3
Mr(K)
97
Vinculin
39
28
pRPA2 (T21)
RPA2
39
28
pRPA2 (S4/8)
39
28
pRPA2 (S33)
D
0 nM
5 nM
7.5 nM
10 nM
15 nM
20 nM
WT + EV
WT + ZUP1
KO + EV
KO + ZUP1
KO + C360R
KO + Δα2/3
U-2 OS + Mitomycin C
E
Survival (%)
100
10
1
0.1
ns
WT + EV
WT + ZUP1
KO + EV
KO + ZUP1
KO + C360R
KO + Δα2/3
0
5
10
15
20
Mitomycin C [nM]

Figure 16. Second round rescue of RPA hyperphosphorylation and MMC sensitivity in ZUP1 KO cells

(A) Immunoblot to show rescue of ZUP1 expression in pooled ZUP1 KO U2OS cells using lentiviral encoded constructs expressed via a PGK promoter. Pooled cell lines re-expressing WT ZUP1 and ZUP1 containing C360R, and Δα2/3 mutations were generated as indicated. Rabbit polyclonal anti-ZUP1 antibody is used to visualise re-expression of the Δα2/3-ZUP1 construct as the binding site for the monoclonal mouse antibody is located in the α2/3 region.

(B) MMC treatment schematic. Cells were treated with 50 nM MMC.

(C) Immunoblot analysis of RPA phosphorylation following MMC time course depicted in panel B.

(D) Representative well images from MMC clonogenic survival assay. Cells were treated with MMC chronically for 14 days.

(E) Quantification of colony survival following MMC treatment. Data points are from n=3 biological replicates with 3x technical repeat wells used for each concentration. Error bars indicate SEM. Statistical difference was calculated using a two-way ANOVA with Dunnett's multiple comparison test. Cell lines and treatment timepoints without a significant difference relative to WT are denoted as 'ns' while all other data points showed a significant difference.

3.3. Discussion

3.3.1. Challenges of creating full ZUP1 knockouts

This chapter describes the successful generation of complete ZUP1 KO U2OS cell lines at the transcript and protein level using a multi-guide CRISPR–Cas9 approach. The process of creating these cell lines highlights the importance of robustly validating KOs and empirically determining the expression of splice variants for less well characterised genes such as *ZUP1*. I used immunoblotting and a PCR amplification strategy to demonstrate that ZUP1 KO cells completely lacked protein expression and used a semiquantitative RT-PCR approach to investigate the expression of alternative ZUP1 splice isoforms. Using this approach, I was able to show that the three main predicted protein coding isoforms (A, B, and C) are expressed in WT cells but are completely absent in ZUP1 KO cells. While the identification of a band corresponding to the smaller isoforms of D or E was less conclusive in WT cells, there was importantly no RT-PCR product obtained for either of these isoforms in ZUP1 KO cells. Additionally, no bands are observed on an immunoblot that correlate perfectly to the predicted size of isoform D or E (a faint band is seen at ~39 kDa while the predicted size is ~30 and ~32 kDa respectively), perhaps suggesting that these are non-translated isoforms or extremely low abundance. In future it will be interesting to investigate whether the different ZUP1 splice isoforms perform distinct functions in cells. This could be addressed by using selectively targeted KOs, for example by comparing the phenotypes of exon 2 targeted KOs, which still express isoform C, with full exon 2/6 KOs. It would also be important to create ZUP1 KOs in a more karyotypically normal cell line such as RPE1 to determine if the phenotypic consequences of ZUP1 absence are context-dependent on aneuploidy.

3.3.2. Significance of observed genotoxin sensitivities

In unchallenged conditions U2OS ZUP1 KO cells were found to be fully viable whilst displaying a modestly increased doubling time. This is in accordance with the suggestion from the papers describing ZUP1's discovery that it is a regulatory protein that functions in the DNA damage response but is not required for normal physiological function. The slightly increased doubling time in unchallenged conditions could reflect the higher rate of spontaneous DNA damage that was previously reported for ZUP1 siRNA knockdown cells (Kwasna et al., 2018). Here, I have additionally demonstrated that ZUP1 KO are hypersensitive to a broad array of genotoxic agents with significant sensitivity seen against MMC, talazoparib, cisplatin, olaparib, ATRi (AZD6738), formaldehyde, and topotecan for at least some drug concentrations. The only agent to which ZUP1 KO cells showed no significant hypersensitivity relative to WT cells was hydroxyurea. Given the overlapping function of DNA repair factors involved in the DDR and the crosstalk and redundancy between pathways it may be expected that ZUP1 KO cells would be sensitive to multiple DNA damaging agents. This is compounded by the fact that DNA damaging agents can generate heterogenous DNA lesion types. For example formaldehyde causes DNA protein crosslinks as well as DNA interstrand crosslinks (Grafstrom et al., 1983). These considerations suggest that ZUP1 may function in a downstream repair process common to multiple repair pathways that respond to distinct lesion types. Notably, all the genotoxins that ZUP1 KO cells are sensitive to cause replication stress; MMC and cisplatin by generating ICLs that impede replication forks; formaldehyde, topotecan, talazoparib, and olaparib by generating DPCs or DPC-like lesions which similarly block replication fork progression; and ATRi by causing unscheduled origin firing leading to excessive ssDNA generation and RPA exhaustion.

ZUP1 may therefore function in a repair process common to multiple sources of replication stress such as lesion bypass and fork reversal, or may be involved in the downstream repair of DSBs that result from extended replication fork stalling (Cortez, 2019).

Given ZUP1 KO cells hypersensitivity to replication stress inducing agents it is surprising that no sensitivity was observed to hydroxyurea. Lack of sensitivity, however, may be due to hydroxyurea's cytotoxic activity being mediated through its reported generation of ROS rather than its canonical function as an antimetabolite that inhibits ribonucleotide reductase leading to replication fork stalling (Kapor et al., 2021). The relatively high dose of HU used to induce cell death (30 mM highest dose) suggests significant ROS species would be generated which would likely generate DNA base damage and require BER or NER repair pathways to ameliorate this damage. The similar levels of sensitivity seen between WT and ZUP1 KO cells may therefore suggest that ZUP1 is not required for the BER or NER pathways. This, however, remains speculative and would require further experiments to elucidate. It will additionally be important in future to define ZUP1 KO cell sensitivity to replication-independent sources of DNA damage such as IR or UV light-induced damage to comprehensively demonstrate whether the repair defect in the absence of ZUP1 is specific for replication-coupled DNA repair.

An additional aspect of ZUP1 KO cell lines that should be considered is the clonal variability seen between independent KO clones. This clonal variation in genotoxin sensitivities could indicate a lack of a true isogenic background between clones, possibly due to compensatory mutations that arise following CRISPR-Cas9 editing. Despite this clonal variability, however, the data presented in this section robustly identify ZUP1 as a factor contributing to the efficient response to DNA damage. To address the problem

of clonal variability possible future targeting strategies could include the CRISPR-mediated knock-in of a degron tag at the *ZUP1* locus that would allow for inducible targeted protein degradation of ZUP1 and possibly circumvent issues of compensatory mutations that arise when knocking out the gene itself (Bondeson et al., 2022).

3.3.3. Speculation on RPA hyperphosphorylation phenotype

A major finding of this chapter was the observation of hyperphosphorylation of RPA2 following MMC-induced DNA damage in ZUP1 KO cells. This observation, coupled with the apparently normal CHK1 phosphorylation and FANCD2 ubiquitylation relative to WT cells may suggest that ZUP1 functions downstream, or parallel to, CHK1 and FANCD2–FANCI activation pathways. Importantly, the substrates of ZUP1 have yet to be conclusively verified, although an initial publication showed increased RPA polyubiquitylation upon ZUP1 siRNA depletion following DNA damage, and the Gibbs-Seymour lab has demonstrated increased PCNA polyubiquitylation in ZUP1 KO cells following damage (Hewings et al., 2018). It can be speculated that failure to de-modify K63-linked Ub on one of these substrates may interfere with ICL repair such that increased ssDNA is generated which is bound by RPA and phosphorylated. Alternatively, if RPA is a true substrate of ZUP1 the hyperphosphorylation observed following ZUP1 loss may predominantly be driven by the consequences of excess RPA ubiquitylation. As discussed in the introduction RPA ubiquitylation has been proposed to promote a feedforward loop driving further ATR-mediated phosphorylation of RPA (see sections 1.2.5 and 1.3.2). RPA ubiquitylation and phosphorylation have also been suggested to promote the timely removal of RPA from ssDNA to allow for downstream repair processes to occur (Feeney et al., 2017). If ZUP1 impacts the dynamics of RPA ubiquitylation and phosphorylation at stalled replication

forks this may interfere with its timely extraction from chromatin and thereby disrupt downstream repair processes such as HR. In Chapter 4, I build on these observations and utilise a high-content immunofluorescence imaging approach to analyse the chromatin-loading dynamics of RPA and other important repair factors at ICL lesions induced by MMC treatment.

3.3.4. Rescue of ZUP1 KO phenotypes and issues with partial rescue

The complementation of ZUP1 KO with exogenous WT ZUP1 presented in this chapter showed initial promise of rescue of MMC hypersensitivity and reverse of RPA hyperphosphorylation in proof-of-concept experiments. However, a larger-scale experiment comparing additional ZUP1 variants, failed to demonstrate significant rescue of these phenotypes. The following possible reasons could account for the lack of phenotypic rescue observed in full-scale experiments. Firstly, silencing of ZUP1 expression following cryopreservation and thawing of cells may have occurred, although immunoblot verification of ZUP1 expression was performed immediately prior to starting the first full-scale rescue experiments (Figure 16A). The long timescale of clonogenic survival assays and the time needed to perform biological repeats, however, could mean that ZUP1 expression is lost over time. Secondly, it may be that exogenous ZUP1 expression does not match endogenous levels sufficiently closely to preserve physiological function. Rescue of phenotypes may, therefore, not be a binary that merely requires the presence of ZUP1 protein, but rather requires a specific level of DUB activity to perform its physiological function. A third consideration is that the balance between the different isoforms of ZUP1 may also be important which would not be recapitulated by exogenous expression of ZUP1 via a plasmid construct bearing only

the full-length form of the protein. Additionally, the correct post-translational modifications regulating ZUP1 function may not be correctly appended when not expressed at endogenous levels. Our lab has demonstrated that ZUP1 itself is ubiquitylated in response to DNA damage, which may be important for its physiological function (I.G.-S. personal communication; unpublished). Finally, the rescue experiments performed as part of this thesis cannot rule out the possibility of additional off-target mutations created during CRISPR-Cas9 editing of the ZUP1 locus. Nevertheless, the use of multiple monoclonal ZUP1 KO cell lines in the experiments performed in this chapter still strongly suggest a role for ZUP1 in the repair of replication-coupled DNA damage.

4

ZUP1 limits ssDNA-dependent signalling during ICL repair

Contents

4.1. Introduction

In this chapter, I further characterise the phenotypic defects seen in ZUP1 KO cells using quantitative image-based cytometry (QIBC) to analyse the dynamics of key DDR factors following MMC-induced damage. QIBC utilises automated, multichannel, high-content, widefield immunofluorescence microscopy to generate cytometry-like outputs from fixed samples (Toledo et al., 2017; Toledo et al., 2013). This approach allows the visualisation of an entire population of cells with single-cell resolution and permits the multiplexing of antibodies in different fluorescent colour channels to simultaneously monitor the dynamics of multiple targets of interest. A key consideration for antibody multiplexing is that primary antibodies must be raised in different species to allow specific binding by secondary antibodies, but otherwise essentially any factor for which suitable antibodies exist can be studied. The ScanR software used to perform QIBC segments individual nuclei based on a DAPI nuclear counterstain channel and can associate sub-objects, based on multiplexed antibodies in different colour channels, to each parental nucleus. By using appropriate markers, a population of cells can therefore be stratified into different subpopulations, such as cell cycle phase, and the temporal and spatial dynamics of factors of interest can be tracked. Since QIBC uses fixed samples, processing steps can also be utilised to specifically visualise chromatin-bound

substrates. This involves a pre-extraction step prior to fixation whereby nuclei are permeabilised with 0.2% Triton X-100 buffer and soluble, non-chromatin-bound proteins are washed away leaving only insoluble cellular components such as chromatin. The visualisation of DNA repair factors with fluorescently tagged antibodies under these conditions reveals discrete subnuclear foci, which represent specific sites of DNA damage that can be used to monitor the recruitment of different repair factors (Rothkamm et al., 2015).

The aim of this chapter was to use QIBC analysis to characterise the impact of ZUP1 loss on the major ubiquitylation targets at stressed replication forks: PCNA, RPA, RAD51, and the MCM helicase complex. Ubiquitylation of these factors at stressed replication forks have previously been shown to be important for distinct repair outcomes as covered in the Introduction. Monoubiquitylation of PCNA by RAD18 is important for recruiting TLS polymerases (Choe and Moldovan, 2017). Polyubiquitylation of PCNA by RFWD3 has also been proposed to be important for lesion bypass by TLS as this process is impaired in the absence of RFWD3 (Gallina et al., 2021). RFWD3-mediated ubiquitylation of RPA and RAD51 has also been suggested to facilitate their extraction from chromatin by p97/VCP and allow efficient HR repair to proceed (Feeney et al., 2017). Polyubiquitylation of MCM by TRAIP has been shown to be important drive the ICL repair pathway decision tree between the NEIL3 pathway and the FA pathway, depending on the length of ubiquitylation. Long Ub chains on MCM drives its p97/VCP-mediated disassembly from chromatin allowing for engagement of FA pathway factors, whilst short Ub chains are sufficient for NEIL3 recruitment without the need for removal of MCM (Wu et al., 2019). The Gibbs-Seymour lab has demonstrated that ZUP1 interacts directly with the RPA complex both *in vitro* and *in vivo*, which functions to activate ZUP1 DUB activity (Foster et al., 2023).

Furthermore, FLAG–ZUP1 is able to co-immunoprecipitate the MCM complex and PCNA from cells, as demonstrated by mass spectrometry and immunoblotting (I.G.-S. personal communication; unpublished). Importantly, the Gibbs-Seymour lab have found that PCNA polyubiquitylation is increased after MMC treatment in ZUP1 KO cells, suggesting that ZUP1 is the first cellular DUB for PCNA polyubiquitylation (I.G.-S. personal communication; unpublished). There is, therefore, an emerging role for ZUP1 in mediating ubiquitylation dynamics at stressed replication forks through key factors that mediate DNA repair. This chapter seeks to investigate the consequences of disrupting these dynamics by studying the recruitment of the aforementioned factors to sites of MMC-induced ICL lesions using QIBC in WT and ZUP1 KO cells.

4.2. Results

4.2.1. ZUP1 prevents G2 phase arrest following MMC-induced DNA damage

The first QIBC experiment I conducted utilised multiplexed co-immunostaining for PCNA and RPA2 with a DAPI nuclear counterstain to monitor their dynamics following recovery from MMC-induced DNA damage over a 72 h treatment time course in U2OS WT cells and two independent ZUP1 KO clones (Figure 17A). DAPI nuclear staining and PCNA immunostaining allowed cells to be stratified by cell cycle phase (Figure 17C). PCNA acts as the sliding clamp during DNA replication and therefore cells positive for chromatin-bound PCNA can be assumed to be in S-phase as previously reported (Schonenberger et al., 2015). The intensity of DAPI nuclear staining is directly correlated to a cell's DNA content and therefore can be used to determine which cells are in G1-phase (2n DNA content) or G2-phase (4n DNA content) (Figure 17D). This experiment revealed that the distribution of untreated cells across the cell cycle was similar for U2OS WT and ZUP1 KO cells (Figure 17E; first column). Following treatment with MMC both WT and ZUP1 KO cells stalled in G2-phase of the cell cycle as has been well established for MMC treated cells in the existing literature (Kang et al., 2001). After release into untreated growth medium WT cells began to recover and start cycling through the cell cycle. By 72 h the peak associated with G1-phase cells increased substantially relative to G2-phase suggesting a more cells were actively dividing (Figure 17E; last column). A greater proportion of ZUP1 KO cells, however, remained stalled in G2-phase implying a defect in DNA repair (Figure 17E).

The Spotfire analysis software was then used to gate cells according to their cell cycle phase as shown in the representative example in Figure 17D. This allowed the precise

proportion of cells in each cell cycle phase to be quantified across the MMC treatment time course (Figure 17F). These data confirm that a greater proportion of cells remained stalled in G2 phase in ZUP1 KO cells compared to WT cells (62.6% and 48.0% in clone 38 and 62 respectively compared to 35.7% in WT at 72 h post MMC treatment). Additionally, fewer cells entered S-phase in ZUP1 KO cells compared to WT cells (13.4% and 17.9% in clone 38 and 62 respectively compared to 35.0% in WT at 72 h post MMC treatment). The activity of ZUP1 is therefore revealed to be important to prevent cells from arresting in G2 phase following DNA damage.

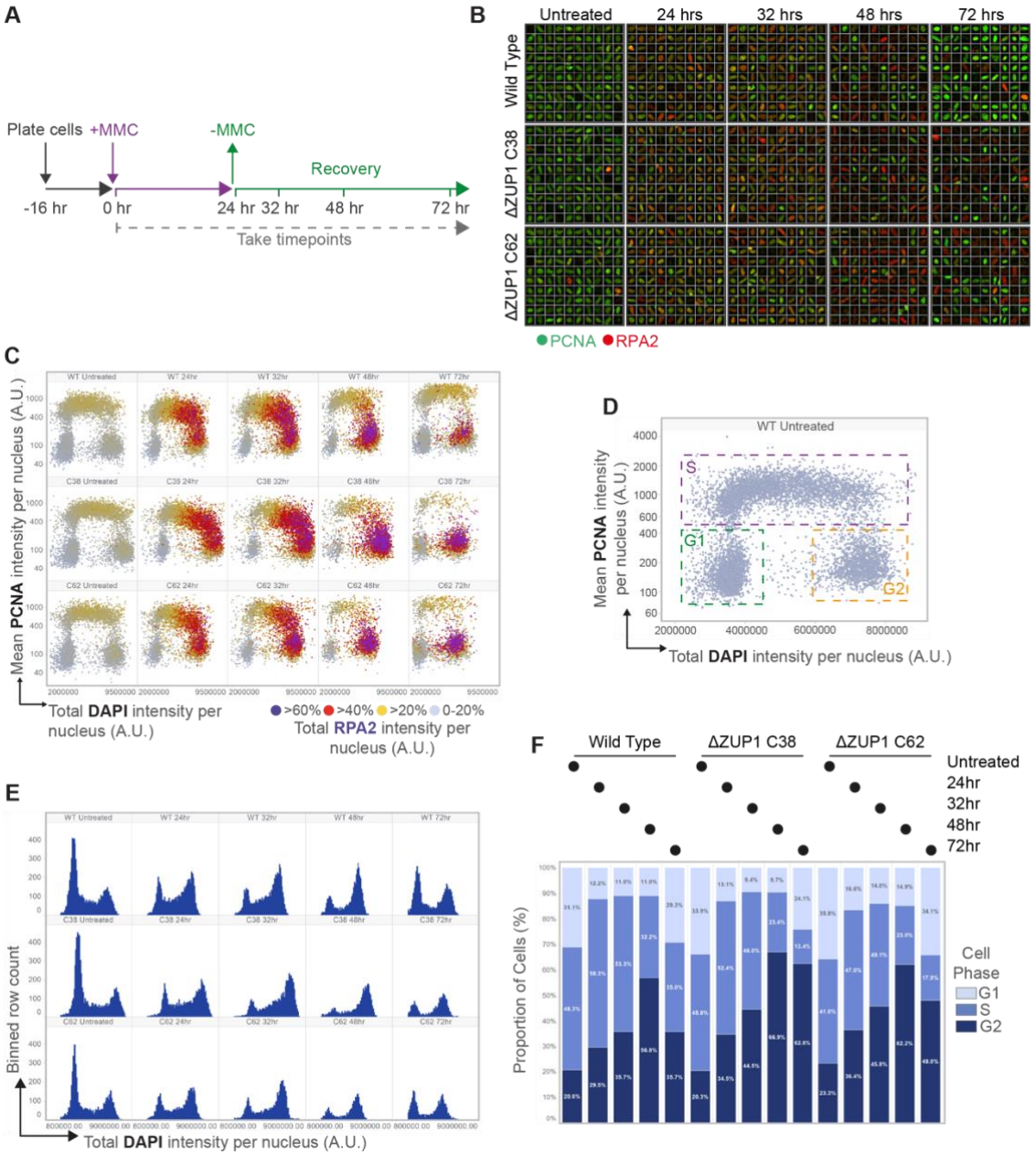
A
Plate cells
+MMC
-MMC
Recovery
-16 hr
0 hr
24 hr
32 hr
48 hr
72 hr
Take timepoints
B
Untreated
24 hrs
32 hrs
48 hrs
72 hrs
Wild Type
ΔZUP1 C38
ΔZUP1 C62
PCNA
RPA2
C
Mean PCNA intensity per nucleus (A.U.)
Total DAPI intensity per nucleus (A.U.)
>60%
>40%
>20%
0-20%
Total RPA2 intensity per nucleus (A.U.)
D
WT Untreated
S
G1
G2
Mean PCNA intensity per nucleus (A.U.)
Total DAPI intensity per nucleus (A.U.)
E
Binned row count
Total DAPI intensity per nucleus (A.U.)
F
Wild Type
ΔZUP1 C38
ΔZUP1 C62
Untreated
24hr
32hr
48hr
72hr
Proportion of Cells (%)
Cell Phase
G1
S
G2

Figure 17. QIBC analysis of PCNA and RPA2 chromatin loading dynamics over an MMC treatment time course

(A) MMC treatment schematic. Cells were treated with 50 nM MMC.

(B) Representative immunofluorescence images from QIBC assay with PCNA and RPA2 co-immunostain. Images show a random selection of nuclei chosen automatically using the ScanR software.

(C) QIBC plot of U2OS WT and ZUP1 KO cells immunostained for chromatin-bound PCNA and RPA2 following treatment with MMC. DNA was counterstained with DAPI. Soluble non-chromatin-bound proteins were removed prior to immunostaining via a pre-extraction step with 0.2% Triton X-100 buffer. A.U. arbitrary units. Approximately 5,000 cells were imaged per condition. Data is representative of n=2 biological replicates.

(D) Example PCNA vs DAPI QIBC plot showing segmentation strategy to stratify cells based on cell cycle phase. DAPI content was used to determine cells in G1 (2n) or G2 (4n) phase of the cell cycle, while cells that were positive for PCNA had active replication complexes and were cycling through S-phase of the cell cycle.

(E) Histogram showing distribution throughout the cell cycle of U2OS WT and ZUP1 KO cells treated with MMC. Graph plots total DAPI as a proxy for DNA content vs the binned count. Data is representative of n=2 biological replicates.

(F) Quantification of proportion of cells in each phase of the cell cycle from QIBC assay using gating strategy outlined in panel D. Data is representative of n=2 biological replicates.

4.2.2. ZUP1 KO cells accumulate chromatin-bound RPA2 in S/G2 phase

The multiplexed PCNA and RPA2 experiment described above also allowed for the dynamics of RPA2 chromatin loading to be studied across the cell cycle in response to MMC treatment. These data revealed that RPA2 was loaded onto chromatin in late S-phase and G2-phase (Figure 17B-C). The ScanR analysis software was then used to quantify the total fluorescence intensity of immunostained chromatin-bound RPA2, and the number of discrete RPA2 foci in S/G2 phase nuclei (Figure 18). These data revealed that both total intensity and number of foci were substantially elevated in ZUP1 KO cells relative to WT cells following MMC treatment and persisted for a longer duration (Figure 18). The baseline mean total intensity and number of RPA2 foci in untreated WT and ZUP1 KO cells were, however, very similar suggesting that no additional spontaneous DNA damage is generated in the absence of ZUP1 under unchallenged conditions. Mirroring the dynamics of RPA2 phosphorylation observed in immunoblot experiments, RPA2 loading in WT cells peaked at 32 h following MMC treatment and decreased towards baseline thereafter. In ZUP1 KO cells, however, RPA2 loading peaked at 48 h and remained elevated compared to WT at 72 h. These data suggest that they hyperphosphorylation of RPA2 in ZUP1 KO cells reflects an increase in chromatin-loaded RPA following DNA damage rather than merely an increase in phosphorylation of an existing chromatin-bound fraction.

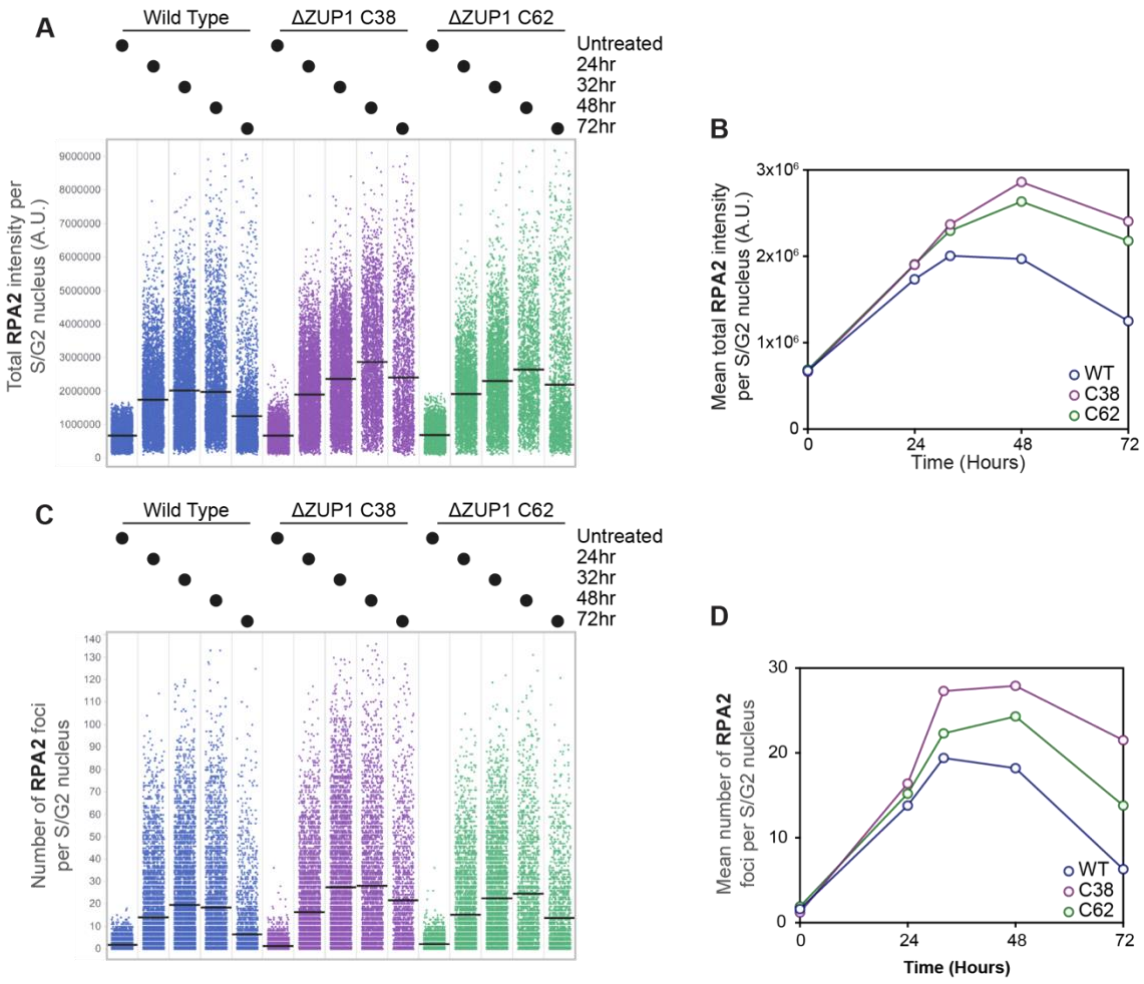

Figure 18. Quantification of QIBC analysis of PCNA and RPA2 chromatin loading dynamics over MMC treatment time course

(A) Plot of total RPA2 intensity per nucleus in S- or G2-phase of the cell cycle over MMC treatment time course. Cells were gated to include only those in 2/G2 phase according to the example in Figure 17D. Horizontal black lines indicate the mean across all included cells for a given treatment. Data is representative of n=2 biological replicates.

(B) Quantification of mean total RPA2 intensity across all included cells for a given treatment in panel A. Calculation of SEM yield error bars too small to be visualized on this scale for all data points.

(C) Plot of number of RPA2 foci per nucleus in S- or G2-phase of the cell cycle over MMC treatment time course. Foci were segmented as secondary objects using a ScanR analysis pipeline and then associated with their parental nucleus following segmentation using the DAPI channel as the primary object. Horizontal black lines indicate the mean across all included cells for a given treatment. Data is representative of n=2 biological replicates. **(D)** Quantification of mean number of RPA2 foci across all included cells for a given treatment in panel C. Calculation of SEM yield error bars too small to be visualized on this scale for all data points.

4.2.3. Chromatin-bound RPA2 is hyperphosphorylated in S/G2 phase in ZUP1 KO cells

QIBC assays were next used to assess the dynamics of RPA2 phosphorylation following MMC-induced damage. Antibodies against pRPA2 T21, S4/8 and S33 were first tested for use in QIBC assays (data not shown). The anti-pRPA2-T21 antibody was found to be not suitable for immunofluorescence experiments since it also binds to the unmodified version of RPA2 (observed as a lower band at 32 kDa on immunoblots), and therefore could not distinguish between the species via immunofluorescence microscopy. The anti-pRPA2-S4/8 antibody yielded phospho-specific labelling but displayed a poor dynamic range of signal intensity. pRPA2-S33 was therefore chosen as the phosphorylation marker as this antibody showed specific labelling and resulted in the best dynamic range out of the antibodies tested. It additionally can be used as a proxy for other pRPA2 markers as they were all observed to increase following MMC-induced damage via immunoblot (Figure 14). pRPA2-S33 is also reported to be predominantly phosphorylated by ATR and is therefore a key marker for replication stress as discussed in section 1.2.5. QIBC experiments were performed with multiplexed RPA2 and pRPA2-S33 antibodies to determine which sub-population of chromatin-bound RPA2 is phosphorylated in response to MMC. Cells were treated according to the same MMC time course used in the above experiment (Figure 19A). QIBC plots revealed that pRPA2-S33 accumulated in S/G2-phase cells following MMC damage and both total intensity and number of foci were elevated and persisted for longer in ZUP1 KO cells compared to WT counterparts, commensurate with the immunoblot data presented in Chapter 3 (Figure 19). Baseline phosphorylation levels and number of foci were again seen to be similar in untreated WT and ZUP1 KO cells. It additionally doesn't appear that pRPA2-

S33 are inherited by daughter cells as phosphorylation is restricted to S/G2 phase cells, suggesting that the ICL lesion site must be repaired before cells enter mitosis.

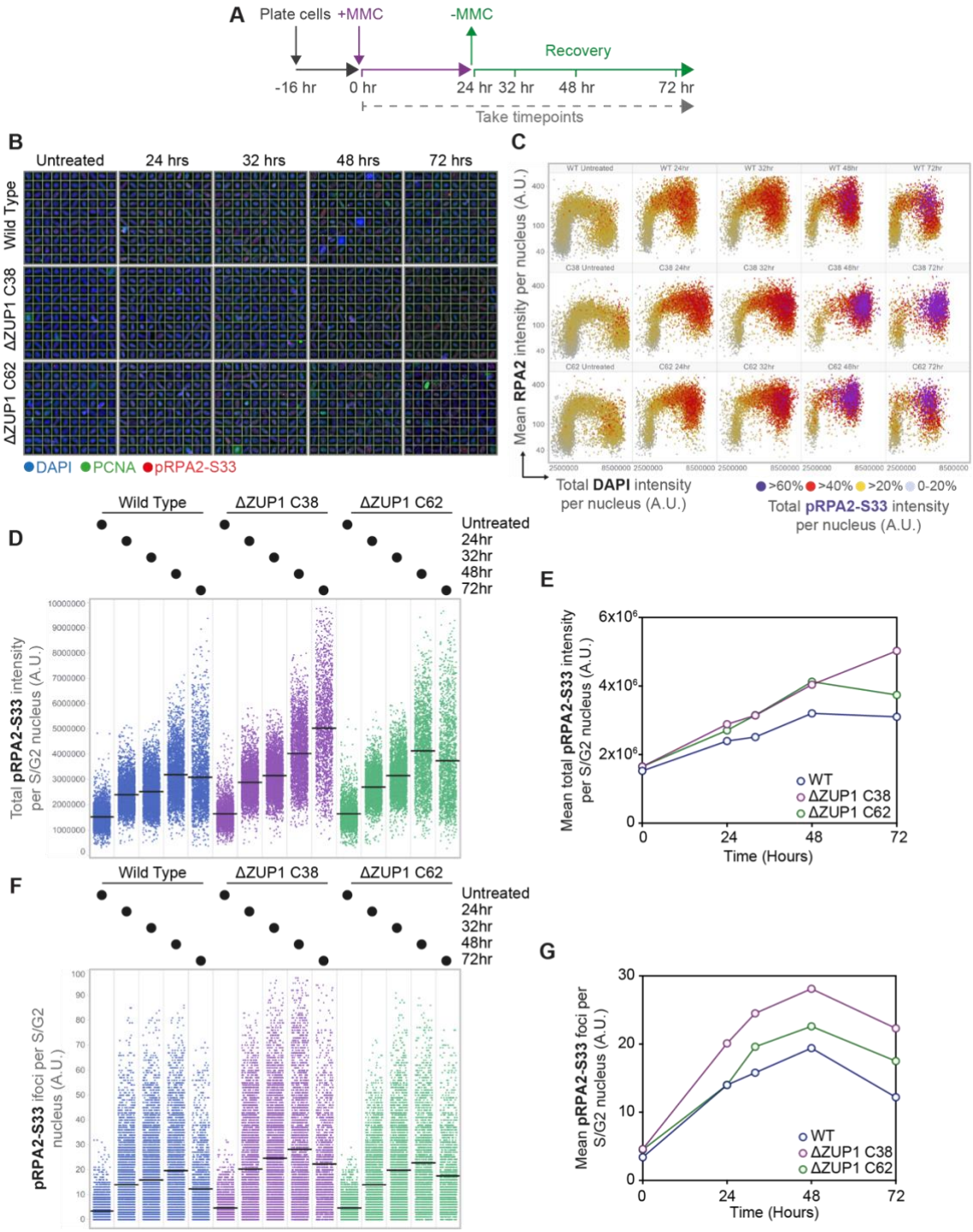

Figure 19. QIBC analysis of RPA2 and pRPA2-S33 chromatin loading dynamics over a time course following MMC-induced DNA damage

(A) MMC treatment schematic. Cells were treated with 50 nM MMC.

(B) Representative immunofluorescence images from QIBC assay with RPA2 and pRPA2-S33 co-immunostain. Images show a random selection of nuclei chosen automatically using the ScanR software.

(C) QIBC plot of U2OS WT and ZUP1 KO cells immunostained for chromatin-bound RPA2 and pRPA2-S33 following treatment with MMC. DNA was counterstained with DAPI. Soluble non-chromatin-bound proteins were removed prior to immunostaining via a pre-extraction step with 0.2% Triton X-100 buffer. A.U. arbitrary units. Roughly 5,000 cells were imaged per condition. Data is representative of n=2 biological replicates.

(D) Plot of total pRPA2-S33 intensity per nucleus in S- or G2-phase of the cell cycle over MMC treatment time course. Cells were gated to include only those in 2/G2 phase. Horizontal black lines indicate the mean across all included cells for a given treatment. Data is representative of n=2 biological replicates.

(E) Quantification of mean total pRPA2-S33 intensity across all included cells for a given treatment in panel D.

(F) Plot of number of pRPA2-S33 foci per nucleus in S- or G2-phase of the cell cycle over MMC treatment time course. Foci were segmented as secondary objects using a ScanR analysis pipeline and then associated with their parental nucleus following segmentation using the DAPI channel as the primary object. Horizontal black lines indicate the mean across all included cells for a given treatment. Data is representative of n=2 biological replicates.

(G) Quantification of mean number of pRPA2-S33 foci across all included cells for a given treatment in panel F. Calculation of SEM yield error bars too small to be visualized on this scale for all data points.

4.2.4. A synergistic effect on RPA phosphorylation is observed upon siRNA depletion of the E3 ligase RFWD3 in ZUP1 KO cells

I next used a QIBC assay to perform an siRNA screen of potential factors responsible for RPA hyperphosphorylation after MMC damage in ZUP1 KO cells (Figure 20). It was reasoned that ZUP1 may function in a pathway that regulates the factors responsible for ATR kinase activation, and hence result in hyperphosphorylation of ATR when absent. To this end the MMC-induced phosphorylation of RPA2 at S33 was monitored in U2OS WT and ZUP1 KO cells in which TOPBP1, ETAA1, and RFWD3 were knocked down using siRNA (Figure 20A). As mentioned in introduction section 1.2.1, TOPBP1 and ETAA1 are the co-factors that activate the ATR kinase. TOPBP1 binds RPA coated ssDNA at ssDNA–dsDNA junctions together with the 9-1-1 clamp which then recruits and activates ATR–ATRIP, whilst ETAA1 interacts directly with RPA and stimulates ATR activity (Delacroix et al., 2007; Haahr et al., 2016). The E3 ligase RFWD3 was also targeted as the ubiquitylation of RPA2 has been proposed to drive a feedforward loop resulting in its increased phosphorylation as described in section 1.3.2. Therefore, reduction in RPA2 Ub by knocking down RFWD3 may limit the excess RPA2 phosphorylation observed in ZUP1 KO cells.

This experiment revealed that knockdown of RFWD3, TOPBP1 and ETAA1 do not cause significant spontaneous RPA2 phosphorylation at S33 in the absence of DNA damage. The established pattern of hyperphosphorylation of RPA2-S33 was also observed in ZUP1 KO relative to WT cells transfected with non-targeting siRNA (siNT) following MMC-induced DNA damage (Figure 20A; column 3+4). This pattern was also broadly similar for cells in which ETAA1 is knocked down, with a slight additional increase in RPA2 phosphorylation observed in ZUP1 KO cells (Figure 20A; column

15+16). This may suggest that ATR activation by ETAA1 does not play a significant role in RPA2 phosphorylation following MMC damage and ATR is instead activated by TOPBP1. Surprisingly, however, the knockdown of TOPBP1 greatly increased pRPA2-S33 following MMC treatment to a similar extent in both WT and ZUP1 KO cells. This may be explained by the fact that TOPBP1 is an essential gene and plays multifaceted cellular roles ranging from ATR activation, replication origin licencing, HR repair, and protection of DNA damage during mitosis. It may be therefore that its knockdown leads to indirect pleiotropic consequences that lead to increased replication stress and RPA phosphorylation by other pathways (Wardlaw et al., 2014). Indeed, a similar increase in RPA2 phosphorylation has previously been reported in response to cisplatin treatment in TOPBP1 deficient cells (Obayashi et al., 2021). It should also be noted that although phosphorylation of RPA at S33 has been reported to be predominantly driven by ATR, the impact of ATM or DNA-PK was not directly assessed in this experiment and therefore could be contributing to the observed hyperphosphorylation in response to MMC (Liu et al., 2012).

Interestingly, the knockdown of RFWD3 also greatly increased RPA phosphorylation in ZUP1 KO cells following MMC damage, while RFWD3 knockdown in WT cells only led to a level of RPA phosphorylation comparable to that observed in ZUP1 KO cells treated with non-targeting siRNA. This finding seems to disconfirm the proposed feedforward loop model between RPA ubiquitylation and phosphorylation. While the model is consistent with ZUP1 KO leading to greater RPA2 phosphorylation if RPA-Ub is a substrate for ZUP1, it does not account for the synergistic effect seen with RFWD3 knockdown. This finding could instead reflect that RFWD3 and ZUP1 function in parallel pathways to repair ICLs and the absence of both leads to increased replication stress and elevated DDR kinase activation to signal the presence of DNA damage.

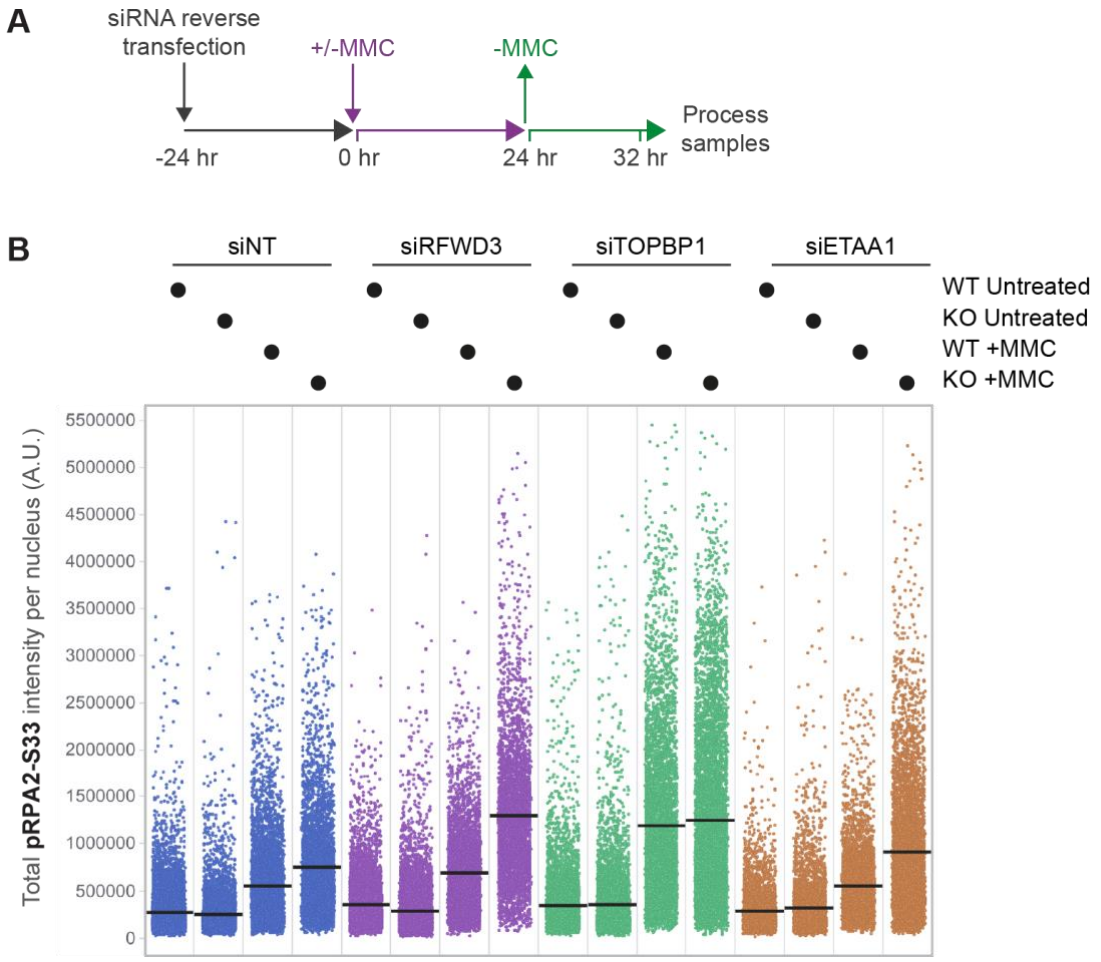

Figure 20. siRNA screen of factors affecting RPA phosphorylation following MMC-induced DNA damage

(A) siRNA treatment schematic. The indicated siRNAs were used to reverse transfect U2OS WT or ZUP1 KO cells at a concentration of 20 nM. 24 h later 50 nM MMC was added to relevant wells and cells were cultured for a further 24 h. Growth media was then replaced, and cells allowed to recover for 8 hrs. Coverslips were then fixed with a pre-extraction step using 0.2% Triton X-100 buffer to remove soluble non-chromatin-bound proteins.

(B) QIBC plot of total pRPA2-S33 foci intensity for each given treatment. Horizontal black lines indicate the mean across all included cells for a given treatment. Data is representative of a single biological replicate.

4.2.5. RPA hyperphosphorylation at S33 in ZUP1 KO cells following RFWD3 knockdown is predominantly driven by ATR

The surprising finding that siRNA knockdown of TOPBP1 and RFWD3 cause greatly elevated MMC-induced RPA2 phosphorylation led to the further investigation for the basis of this effect. As described in the introduction the three DDR PIKK kinases ATR, ATM, and DNA-PK all mediate RPA2 phosphorylation in response to DNA damage with significant interplay and crosstalk reported between their kinase activities (section 1.2.5). Since the hypothesis that knockdown of TOPBP1 and RFWD3 would reverse the ATR mediated hyperphosphorylation of RPA2 in ZUP1 KO cells was disconfirmed by the above experiment, a QIBC experiment was performed to investigate whether the excessive phosphorylation observed following their knockdown was due to the compensatory activity of one of the other PIKK kinases (Figure 21). This experiment utilised kinase-specific small molecule inhibitors of ATR, ATM, and DNA-PK to assess their individual contributions to the MMC-induced hyperphosphorylation or RPA2 observed in ZUP1 KO cells following knockdown of RFWD3 and TOPBP1 (Figure 21A). Inhibition of the ATR kinase led to the greatest decrease in RPA2-S33 phosphorylation following MMC-induced DNA damage in RFWD3 knockdown ZUP1 KO cells. ATRi reduced phosphorylation levels close to levels observed in siNT MMC treated cells. A small impact on phosphorylation levels was also observed in cells treated with ATMi, while DNA-PKi had no discernible impact on RPA2-S33 phosphorylation. Conversely, TOPBP1 knockdown cells showed a much greater impact of ATMi on phosphorylation levels following MMC damage, while a substantial decrease was still observed following ATRi treatment. A small reduction in phosphorylation was also observed following DNA-PKi treatment. This shift to ATM and DNA-PK driven phosphorylation is

consistent with a pleiotropic effect of TOPBP1 knockdown resulting in additional DDR pathway activation. These data suggest that in TOPBP1 knockdown cells, while ATR still carries out some RPA phosphorylation (possibly via the ETAA1 activation axis), ATM and DNA-PK compensate to perform RPA phosphorylation.

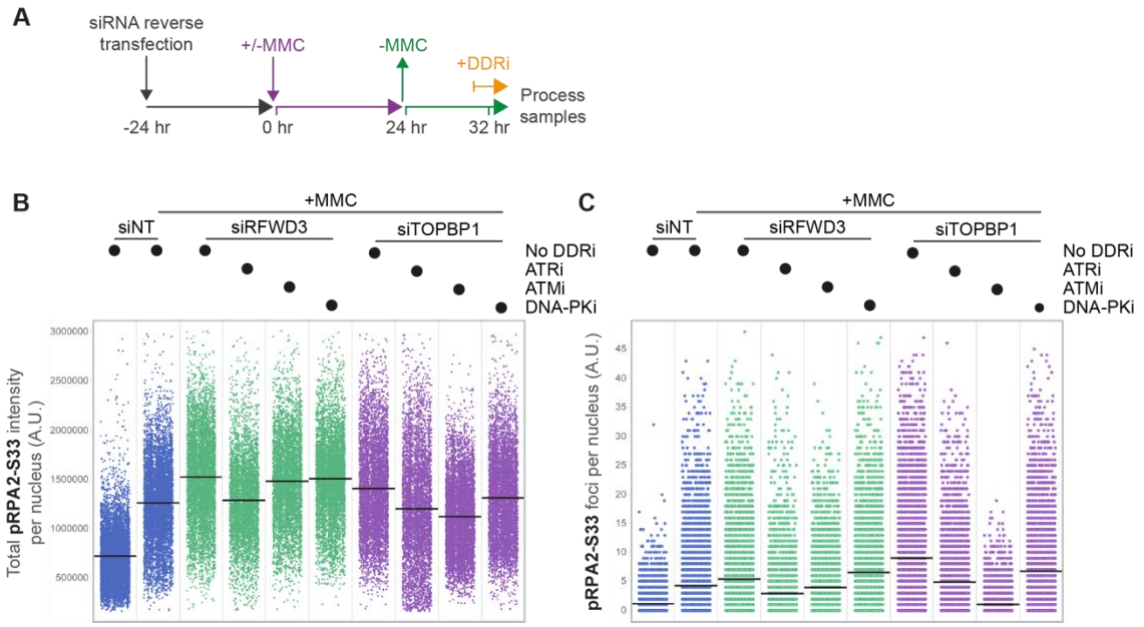

Figure 21. Assessment of DDR kinase inhibition of RPA phosphorylation following depletion of factors with siRNA

(A) siRNA and DDRi treatment schematic. The indicated siRNAs were used to reverse transfect U2OS ZUP1 KO cells at a concentration of 20 nM. 24 h later 50 nM MMC was added to relevant wells and cells were cultured for a further 24 h. Growth media was then replaced, and cells allowed to recover for 8 hrs. For the final hour the indicated kinase inhibitors were added to the growth media (5 μM ATRi, 10 μM ATMi or DNA-PKi). Coverslips were then fixed with a pre-extraction step using 0.2% Triton X-100 buffer to remove soluble non-chromatin-bound proteins.

(B) QIBC plot of total pRPA2-S33 foci intensity for each given treatment. Horizontal black lines indicate the mean across all included cells for a given treatment. Data is representative of a single biological replicate.

(C) QIBC plot of number of pRPA2-S33 foci for each given treatment. Horizontal black lines indicate the mean across all included cells for a given treatment. Data is representative of a single biological replicate.

4.2.6. RAD51 accumulates on chromatin to a greater degree in ZUP1 KO cells following MMC DNA damage

Following the finding that excessive RPA2 loading and phosphorylation occurs in ZUP1 KO cells treated with MMC, I next investigated if this defect had an impact on RAD51 recombinase loading. Given that RPA must be displaced from ssDNA to allow RAD51 binding it was hypothesised that the defective removal of RPA2 in ZUP1 KO cells may impact the ability of RAD51 to bind ssDNA and form nucleofilaments. Alternatively, it has previously been reported that cells in which RPA and RAD51 ubiquitylation is disrupted by knocking out the E3 ligase RFWD3 show persistent RPA and RAD51 foci following MMC damage (Inano et al., 2017). Loss of ZUP1 may therefore similarly impede the clearance of both markers following MMC damage by disrupting ubiquitylation dynamics at ICL lesions. A QIBC assay using multiplexed antibodies against RAD51 and RPA2 was therefore performed to study their chromatin loading dynamics following MMC-induced damage (Figure 22). The resolution of RAD51 immunostaining did not allow for discrete foci to be resolved and segmented using the ScanR software, but the levels of chromatin-loaded RAD51 could be monitored by the total fluorescence intensity in pre-extracted cells. In U2OS WT cells RAD51 was found to accumulate on chromatin following MMC DNA damage (Figure 22). The dynamics of RAD51 chromatin loading, however, differed from RPA2 with peak RAD51 loaded in WT cells 48 h after DNA damage was induced rather than at 32 h observed for RPA2. This aligns with the known function of RAD51 replacing the RPA complex on ssDNA to facilitate strand invasion and repair via HR as discussed in the Introduction (West, 2003). Interestingly, ZUP1 KO cells showed elevated and persistent RAD51 chromatin loading relative to WT cells, while loading also peaked later relative to RPA2. Notably, while

chromatin-bound RAD51 had begun to decrease at 72 h in WT cells, in ZUP1 KO cells RAD51 loading continued to increase at 72 h. Interestingly, these data reflect the same clearance defects of RPA2 and RAD51 observed in RFWD3 KO cells (Inano et al., 2017). An additional intriguing observation was that the baseline levels of RAD51 were elevated in ZUP1 KO cells relative to WT cells, which was consistent across n=2 biological replicates (Figure 22D-E). Finally, the relative levels between ZUP1 KO and WT cells of RPA2 loading in RAD51 co-immunostain experiments were consistent with the pattern observed with PCNA co-immunostain demonstrating that this is a robust and reproducible phenotype (Figure 22F-G).

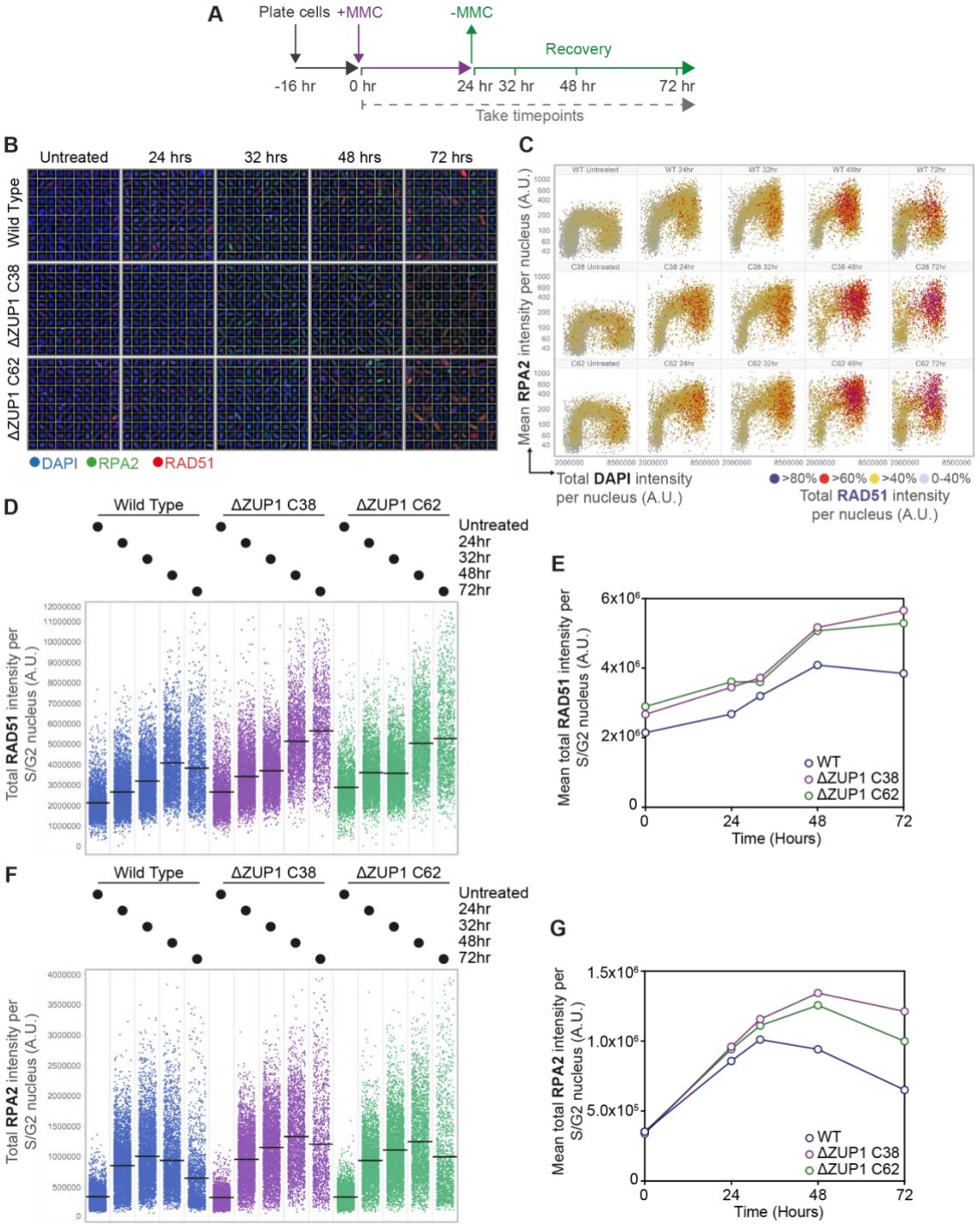
A
Plate cells
+MMC
-MMC
Recovery
-16 hr
0 hr
24 hr
32 hr
48 hr
72 hr
Take timepoints
B
Untreated
24 hrs
32 hrs
48 hrs
72 hrs
Wild Type
ΔZUP1 C38
ΔZUP1 C62
DAPI
RPA2
RAD51
C
Mean RPA2 intensity per nucleus (A.U.)
Total DAPI intensity per nucleus (A.U.)
>80%
>60%
>40%
0-40%
Total RAD51 intensity per nucleus (A.U.)
D
Wild Type
ΔZUP1 C38
ΔZUP1 C62
Untreated
24hr
32hr
48hr
72hr
Total RAD51 intensity per S/G2 nucleus (A.U.)
E
Mean total RAD51 intensity per S/G2 nucleus (A.U.)
6x10⁶
4x10⁶
2x10⁶
0
WT
ΔZUP1 C38
ΔZUP1 C62
0
24
48
72
Time (Hours)
F
Wild Type
ΔZUP1 C38
ΔZUP1 C62
Untreated
24hr
32hr
48hr
72hr
Total RPA2 intensity per S/G2 nucleus (A.U.)
G
Mean total RPA2 intensity per S/G2 nucleus (A.U.)
1.5x10⁶
1.0x10⁶
5.0x10⁵
0
WT
ΔZUP1 C38
ΔZUP1 C62
0
24
48
72
Time (Hours)

Figure 22. QIBC analysis of RPA2 and RAD51 chromatin loading dynamics over a time course following MMC-induced DNA damage

(A) MMC treatment schematic. Cells were treated with 50 nM MMC.

(B) Representative immunofluorescence images from QIBC assay with RPA2 and RAD51 co-immunostain. Images show a random selection of nuclei chosen automatically using the ScanR software.

(C) QIBC plot of U2OS WT and ZUP1 KO cells immunostained for chromatin-bound RPA2 and RAD51 following treatment with MMC. DNA was counterstained with DAPI. Soluble non-chromatin-bound proteins were removed prior to immunostaining via a pre-extraction step with 0.2% Triton X-100 buffer. A.U. arbitrary units. Roughly 5,000 cells were imaged per condition. Data is representative of n=2 biological replicates.

(D) Plot of total RAD51 intensity per nucleus in S- or G2-phase of the cell cycle over MMC treatment time course. Cells were gated to include only those in 2/G2 phase. Horizontal black lines indicate the mean across all included cells for a given treatment. Data is representative of n=2 biological replicates.

(E) Quantification of mean total RAD51 intensity across all included cells for a given treatment in panel D.

(F) Plot of total RPA2 intensity per nucleus in S- or G2-phase of the cell cycle over MMC treatment time course. Horizontal black lines indicate the mean across all included cells for a given treatment. Data is representative of n=2 biological replicates.

(G) Quantification of mean total RPA2 intensity across all included cells for a given treatment in panel A. Calculation of SEM yield error bars too small to be visualized on this scale for all data points.

4.2.7. Mean MCM3 loading is not substantially altered in ZUP1 KO cells

QIBC experiments were next performed to determine the chromatin loading dynamics of the MCM2-7 helicase in response to MMC DNA damage in WT and ZUP1 KO cells (Figure 23). A primary antibody against the MCM3 subunit of the MCM2-7 helicase was used as initial labelling tests with various MCM subunit specific antibodies revealed it to have the best dynamic range of fluorescence intensity in QIBC experiments (data not shown). Experiments were performed using the same MMC treatment timecourse as above with an MCM3 and PCNA co-immunostain (Figure 23A). Interestingly, in both WT and ZUP1 KO cells the loading of MCM3 was seen to increase following MMC damage and remain elevated for the duration of the time course (Figure 24A-B). This increase in MCM loading following DNA damage could potentially reflect the licencing of new origins in response to DNA damage. The total intensity of MCM3 staining per nucleus was the highest in G2-phase cells with moderately increased levels seen in ZUP1 KO cells relative to WT cells (Figure 23C and Figure 24A-B). However, it was also observed that the average area of nuclei was substantially elevated in MMC treated ZUP1 KO cells, reflective of their increased stalling in G2 phase and failure to divide and cycle through S-phase as quickly as WT cells following DNA damage (Figure 24E-F). Therefore, the increased total fluorescence intensity of MCM3 per nucleus of ZUP1 KO cells, which integrates the intensity over the whole nucleus, is likely a reflection of this larger nuclear area. By comparing the mean fluorescence intensity on the other hand, which averages the intensity over a nucleus, the values are in fact seen to be very similar between WT and ZUP1 KO cells (Figure 24C-D). The mean fluorescence intensity per nucleus was greatest in G1 and early S-phase following MMC

damage reflecting the role of the MCM helicase in licencing new replication origins in theses phases (Figure 23D). These data, therefore, suggest that ZUP1 DUB activity does not play a major role in regulating the chromatin loading dynamics of the MCM helicase.

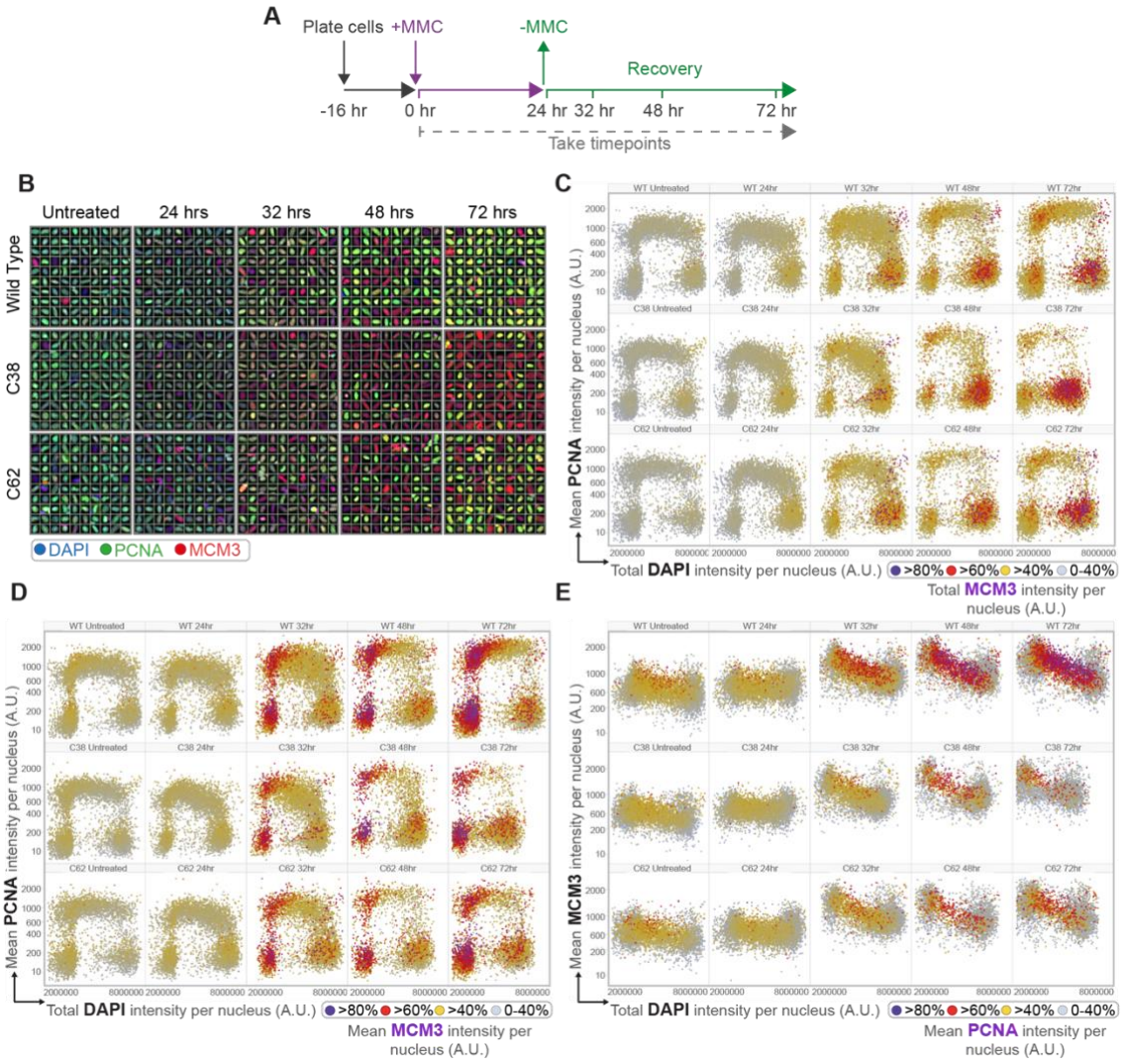

Figure 23. QIBC analysis of PCNA and MCM3 chromatin loading dynamics over a time course following MMC-induced DNA damage

(A) MMC treatment schematic. Cells were treated with 50 nM MMC.

(B) Representative immunofluorescence images from QIBC assay with PCNA and MCM3 co-immunostain. Images show a random selection of nuclei chosen automatically using the ScanR software.

(C) QIBC plot of U2OS WT and ZUP1 KO cells immunostained for chromatin-bound PCNA and MCM3 following treatment with MMC. DNA was counterstained with DAPI. The total fluorescence intensity of MCM3 bound antibodies is shown using the colour scale indicated. Soluble non-chromatin-bound proteins were removed prior to immunostaining via a pre-extraction step with 0.2% Triton X-100 buffer. A.U. arbitrary units. Roughly 5,000 cells were imaged per condition. Data is representative of n=2 biological replicates.

(D) QIBC plot of mean PCNA intensity vs total DAPI intensity per nucleus with mean fluorescence intensity of MCM3 shown using the colour scale indicated.

(E) QIBC plot of mean MCM3 intensity vs total DAPI intensity per nucleus with mean fluorescence intensity of PCNA shown using the colour scale indicated.

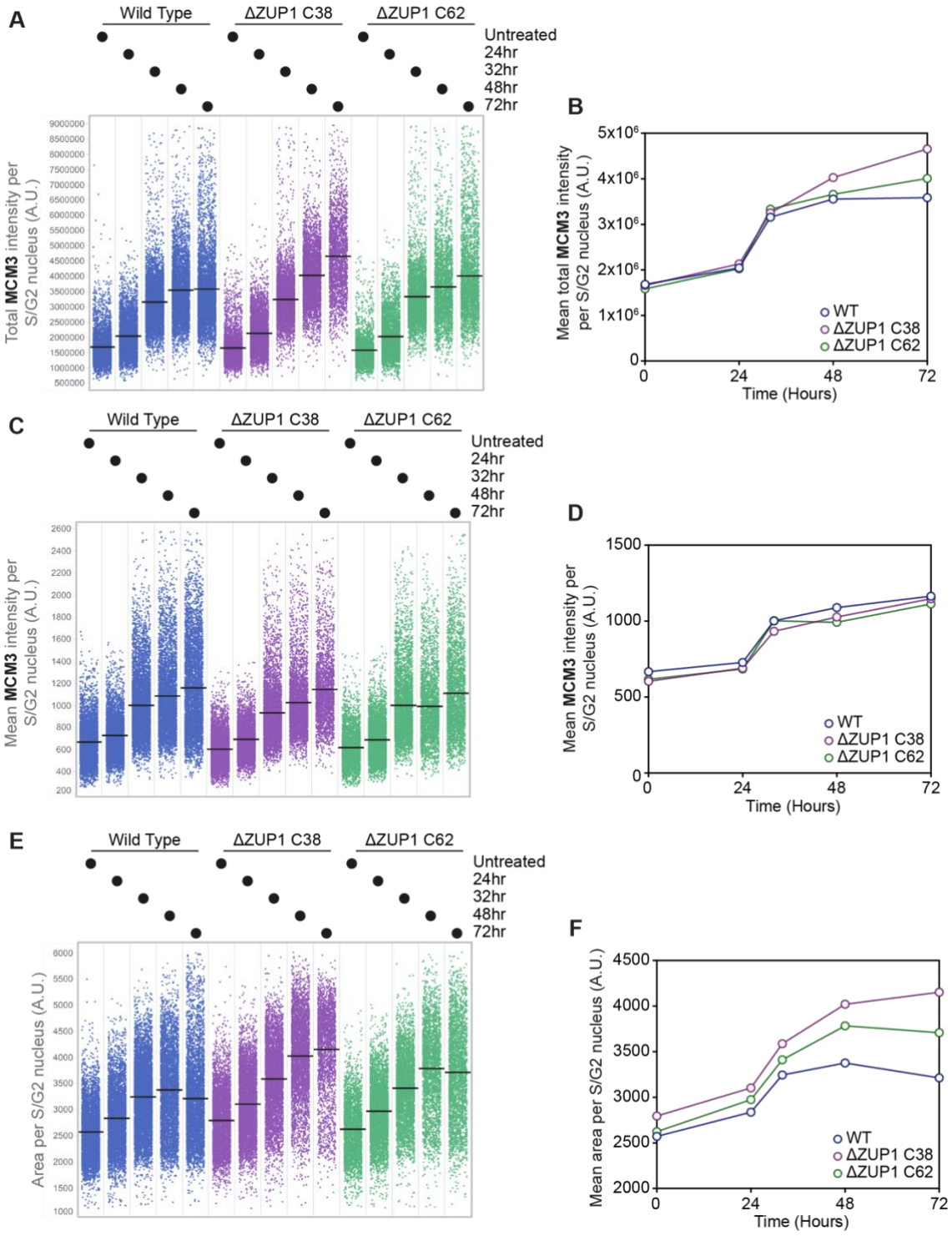
A
Wild Type
ΔZUP1 C38
ΔZUP1 C62
Untreated
24hr
32hr
48hr
72hr
Total MCM3 intensity per S/G2 nucleus (A.U.)
B
Mean total MCM3 intensity per S/G2 nucleus (A.U.)
WT
ΔZUP1 C38
ΔZUP1 C62
Time (Hours)
C
Mean MCM3 intensity per S/G2 nucleus (A.U.)
D
Mean MCM3 intensity per S/G2 nucleus (A.U.)
E
Area per S/G2 nucleus (A.U.)
F
Mean area per S/G2 nucleus (A.U.)

Figure 24. Quantification of QIBC analysis of PCNA and MCM3 chromatin loading dynamics over a time course following MMC-induced DNA damage

(A) Plot of total MCM3 intensity per nucleus in S- or G2-phase of the cell cycle over MMC treatment time course. Horizontal black lines indicate the mean across all included cells for a given treatment. Data is representative of n=2 biological replicates.

(B) Quantification of mean total MCM3 intensity across all included cells for a given treatment in panel A. Calculation of SEM yield error bars too small to be visualized on this scale for all data points.

(C) Plot of mean MCM3 intensity per nucleus in S- or G2-phase of the cell cycle over MMC treatment time course. Horizontal black lines indicate the mean across all included cells for a given treatment. Data is representative of n=2 biological replicates.

(D) Quantification of mean total MCM3 intensity across all included cells for a given treatment in panel **(C).** Calculation of SEM yield error bars too small to be visualized on this scale for all data points.

(E) Plot of area per nucleus in S- or G2-phase of the cell cycle over MMC treatment time course. Horizontal black lines indicate the mean across all included cells for a given treatment. Data is representative of n=2 biological replicates.

(F) Quantification of mean area per cell for a given treatment in panel E. Calculation of SEM yield error bars too small to be visualized on this scale for all data points.

4.2.8. Excessive ssDNA is generated in ZUP1 KO cells following MMC DNA damage

It was hypothesised that the increased loading of RPA2 and RAD51 onto chromatin in ZUP1 KO cells could either be a result of an increased number of molecules loaded at existing ssDNA or could reflect the underlying generation of excess ssDNA itself. To determine whether the underlying basis for increased loading of RPA2 and RAD51 was due to the increased formation of ssDNA, a QIBC experiment was performed using the native BrdU assay (Figure 25). The native BrdU assay utilises an antibody specific to the thymidine analogue BrdU. BrdU is incorporated into the DNA of replicating cells and fixed samples are then immunostained using an anti-BrdU antibody. This antibody can only access incorporated BrdU in single strand regions of DNA and is occluded from binding BrdU in dsDNA (Figure 25B). The assay is carried out under non-denaturing conditions to preserve the native structure of DNA and only reveal ssDNA regions that result from endogenous cellular processes such as the response to DNA damage. A native BrdU assay was carried out according to the schematic depicted in Figure 25A. Cells were co-immunostained with anti-BrdU and RPA1 antibodies to determine if chromatin-bound RPA corresponds to regions of ssDNA. This assay revealed that the baseline amount of ssDNA in WT and ZUP1 KO cells were similar, as evidenced by the native BrdU staining (Figure 25C-H; first column). Total intensity and number of BrdU positive foci, however, were substantially increased in ZUP1 KO cells relative to WT cells following MMC-induced DNA damage (Figure 25E-H). The intensity of BrdU staining also correlated to the intensity of RPA1 staining (Figure 25D**)**. These data strongly suggest that the basis for the observed phenotype of elevated chromatin-loaded

RPA and RAD51 is due to excessive generation of ssDNA in ZUP1 KO cells following MMC damage.

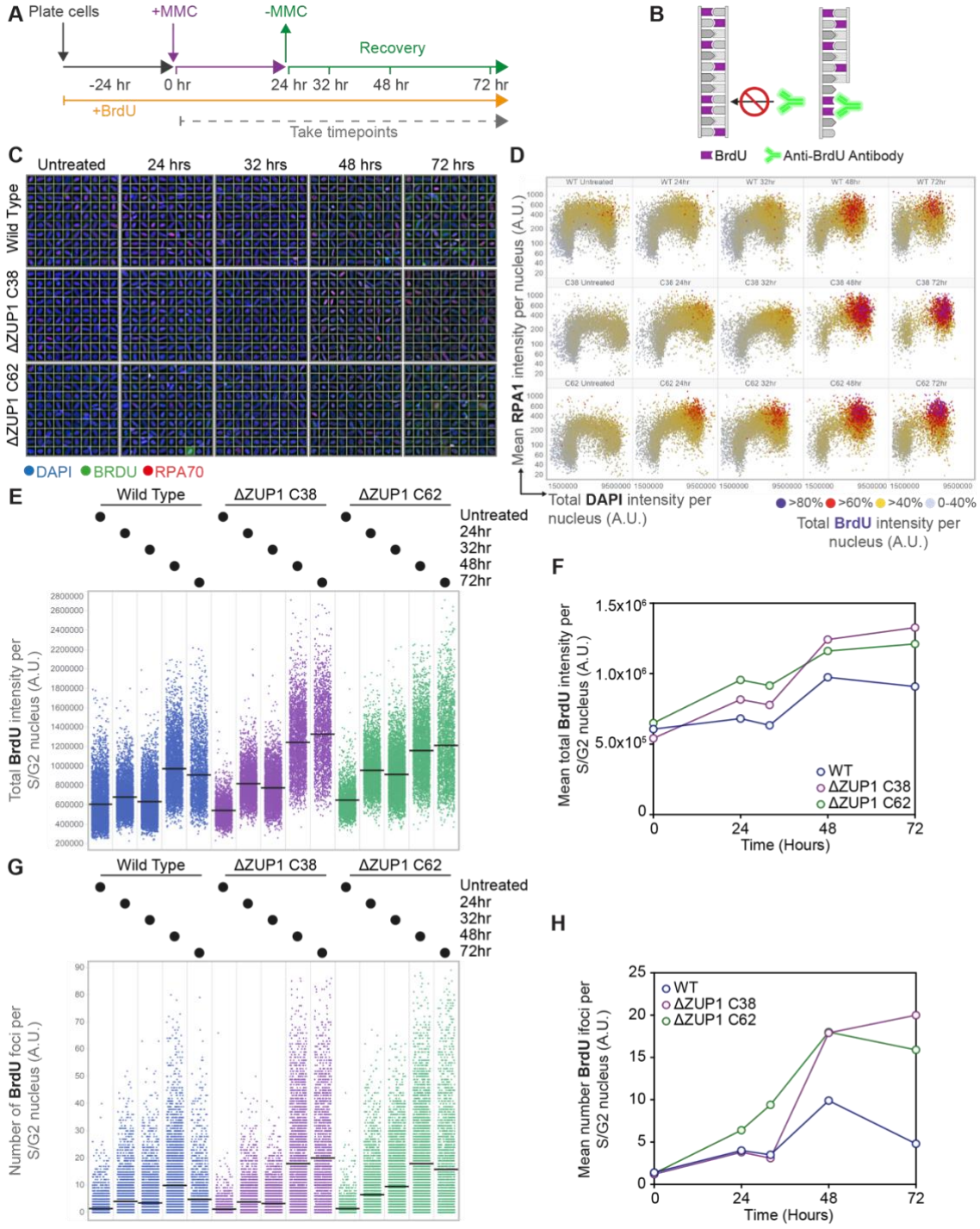

Figure 25. QIBC native BrdU assay for ssDNA identification over time course following MMC-induced DNA damage

(A) Native BrdU assay and MMC treatment schematic. Cells were plated on coverslips in media containing 15 μM BrdU and cultured with BrdU for the duration of the experiment. 24 h later cells were treated with 50 nM MMC. MMC was washed out and replaced with fresh media containing BrdU 24 h following MMC treatment. Coverslips were fixed with a pre-extraction step at the timepoints indicated. Following immunostaining with relevant antibodies cells were imaged with an Olympus ScanR widefield immunofluorescence microscope. Antibodies were incubated under non-denaturing conditions to visualize native regions of ssDNA formed due to MMC-induced DNA damage.

(B) Native BrdU assay schematic. The assay utilises an antibody specific to the thymidine analogue BrdU. BrdUis supplied in the growth media and is incorporated into cell's replicating DNA. The anti-BrdU antibody can only access and bind incorporated BrdU in single strand regions of DNA such as those generated following DNA damage.

(C) Representative immunofluorescence images from native BrdU QIBC assay with RPA1 and BrdU co-immunostain. Images show a random selection of nuclei chosen automatically using the ScanR software.

(D) QIBC plot of U2OS WT and ZUP1 KO cells immunostained for chromatin-bound RPA1 and ssDNA regions incorporating BrdU following treatment with MMC. DNA was counterstained with DAPI. Soluble non-chromatin-bound proteins were removed prior to immunostaining via a pre-extraction step with 0.2% Triton X-100 buffer. A.U. arbitrary units. Roughly 5,000 cells were imaged per condition. Data is representative of n=2 biological replicates.

(E) Plot of total BrdU intensity per nucleus in S- or G2-phase of the cell cycle over MMC treatment time course. Cells were gated to include only those in 2/G2 phase. Horizontal black lines indicate the mean across all included cells for a given treatment. Data is representative of n=2 biological replicates.

(F) Quantification of mean total BrdU intensity across all included cells for a given treatment in panel D.

(G) Plot of number of BrdU foci per nucleus in S- or G2-phase of the cell cycle over MMC treatment time course. Cells were gated to include only those in 2/G2 phase according to the example in Figure 17D. Horizontal black lines indicate the mean across all included cells for a given treatment. Data is representative of n=2 biological replicates.

(H) Quantification of mean number of BrdU foci across all included cells for a given treatment in panel A. Calculation of SEM yield error bars too small to be visualized on this scale for all data points.

4.2.9. No additive effect on RPA loading is observed following p97 inhibitor treatment in ZUP1 KO cells

A final aspect of excess RPA loading that I investigated was whether the p97/VCP ATPase plays a role in extracting RPA from chromatin following MMC damage, as has been reported for RFWD3 KO cells (Inano et al., 2017). ZUP1 has been shown by the Gibbs-Seymour lab to interact with the p97/VCP ATPase which acts as a 'segregase' to remove ubiquitylated substrates from chromatin as discussed in the introduction (I.G.-S. personal communication; unpublished). Therefore, a possible hypothesis for the excess loading of RPA onto chromatin in ZUP1 KO cells could be that ZUP1 has some role in directing the removal of RPA from chromatin by p97/VCP. In the absence of ZUP1 this function may be impaired and RPA not as efficiently removed from ssDNA. An exploratory QIBC experiment was performed to test this hypothesis by inhibiting p97 in WT and ZUP1 KO cells after inducing DNA damage with MMC as described in the schematic in Figure 26A. Cells were then co-immunostained for PCNA and RPA2 markers to allow the visualisation of RPA2 chromatin loading throughout the cell cycle. These data revealed that no substantial increase in RPA2 loading was observed following p97 inhibitor (p97i) treatment without prior induction of DNA damage by MMC in both WT and ZUP1 KO cells (Figure 26D-E). However, in WT cells the loading of RPA2 on chromatin was substantially increased by p97i treatment during an 8-hour recovery following 24-hour treatment with MMC (Figure 26). This is consistent with an impaired ability to extract chromatin-bound RPA loaded at sites of DNA damage. It should be caveated that while the concentration of p97 inhibitor used (NMS873) was in line with previous publications, this experiment lacked a true positive control for inhibitor activity.

Interestingly, while the number of discrete RPA2 foci did increase slightly following p97i treatment, the proportionate increase relative to sole MMC treatment was observed to be smaller than the increase in total RPA2 fluorescence intensity (~10% increase vs ~23% increase; Figure 26D-E; compare column means for column 2 and 4 between subpanels D and E). This may suggest that p97i leads to only a modest increase in new discrete sites of DNA damage, while the removal of RPA2 already bound at lesion sites is impaired, accounting for the proportionally larger increase in total fluorescence intensity observed. Notably, in contrast to WT cells, there was no additional increase in chromatin-loaded RPA2 in MMC and p97i treated ZUP1 KO cells. This could suggest that ZUP1 and p97/VCP do indeed function in an epistatic pathway(s) that facilitates the removal of RPA2 from chromatin. It should be noted, however, that this is a preliminary n=1 experiment as time constraints limited additional biological repeats, so drawing robust conclusions is difficult from this data. Nevertheless, the data presented suggests an interesting future avenue of research.

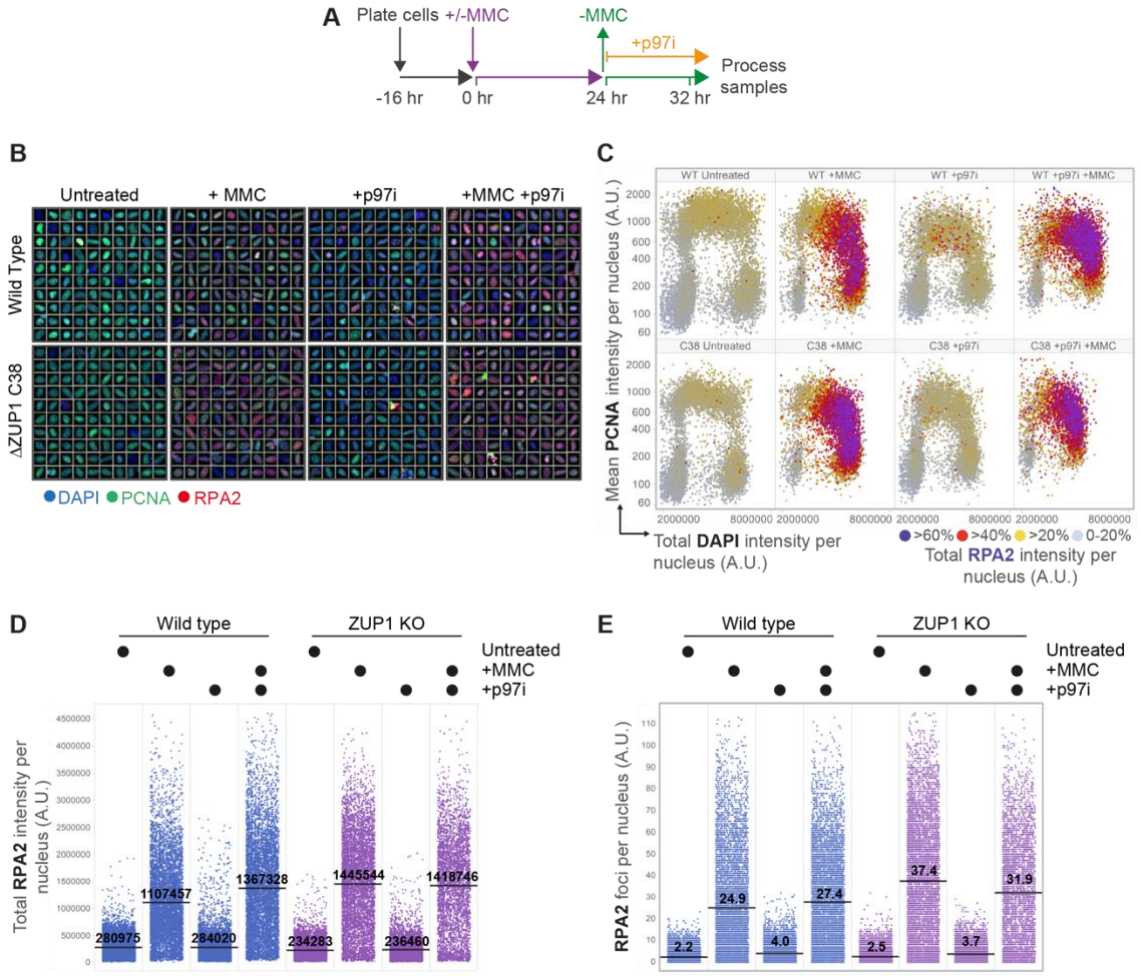

Figure 26. QIBC assessment of p97i on RPA2 chromatin loading following MMC-induced DNA damage

(A) p97i and MMC treatment schematic. Cells were plated on coverslips and allowed to settle overnight. Cells were then either treated with 50 nM MMC or left untreated for 24 h. MMC containing media was then removed and replaced with fresh media or media containing 5 μM p97i (NMS873) as appropriate. Cells were then cultured for a further 8 h and then coverslips were fixed with a pre-extraction step.

(B) Representative immunofluorescence images from MMC/p97i QIBC assay with PCNA and RPA2 co-immunostain. Images show a random selection of nuclei chosen automatically using the ScanR software.

(C) QIBC plot of U2OS WT and ZUP1 KO cells immunostained for chromatin-bound PCNA and RPA2 following treatment with MMC and/or p97i. A.U. arbitrary units. Approximately 5,000 cells were imaged per condition. Data is representative of a single biological replicate.

(D) QIBC plot of total RPA2 intensity per nucleus. Horizontal black lines indicate the mean across all included cells for a given treatment. Data is representative of a single biological replicate.

(E) QIBC plot of number of RPA2 foci per nucleus. Horizontal black lines indicate the mean across all included cells for a given treatment. Data is representative of a single biological replicate.

4.3. Discussion

4.3.1. Significance of RPA2 and RAD51 persistence following MMC damage

This chapter sought to elucidate the impact of ZUP1 loss on the chromatin recruitment dynamics of the major DNA repair factors that are ubiquitylated in the replication stress response. This investigation was greatly assisted using the high-content immunofluorescence imaging approach of QIBC which allowed for the data-rich monitoring of repair factors with single-cell resolution. The first major finding of this chapter was that chromatin-bound RPA2 and RAD51 are substantially elevated and persistent in ZUP1 KO cells relative to WT cells in response to MMC. Interestingly, more discrete RPA2 foci as well as higher fluorescence intensity were observed in ZUP1 KO cells following DNA damage suggesting that additional sites of DNA damage occurred. The increased total intensity of factors is partly driven by increased arrest in G2 phase of ZUP1 KO cells leading to larger nuclear morphology compared to WT, but foci segmentation of RPA2 and pRPA2-S33 markers also demonstrate that cells also have an increased and sustained number of foci following MMC damage. This finding could be explained by the following reasons. Firstly, sites of MMC-induced damage may be repaired less efficiently in ZUP1 KO cells resulting in greater accumulation of ssDNA and RPA2 binding. Secondly, a dysfunction in repair signalling or regulation of factors could result in increased generation of ssDNA during the repair process. For example, dysfunction of the ATR signalling axis could lead to increased unscheduled origin firing resulting in more replication forks running into ICLs imposed by MMC-induced damage. Alternatively, ZUP1 could regulate a nuclease or helicase involved in DNA

repair which could aberrantly lead to increased ssDNA generation in its absence as discussed below.

Notably, the phenotypic consequences of ZUP1 absence are reminiscent of the reported effects of MMC treatment in RFWD3 KO cells, which also display persistence of RPA2 and RAD51 foci (Inano et al., 2017). The RFWD3 mediated ubiquitylation of RPA2 and RAD51 has been suggested to target it for removal by p97/VCP. In this chapter I presented similar proof-of-concept data that demonstrated an impairment of RPA2 extraction from chromatin following p97i in WT cells, but no additional defect on extraction in ZUP1 KO cells. It is therefore tempting to speculate that the ubiquitylation dynamics of RPA2 are disrupted when ZUP1 is lost and RPA2 is not as efficiently targeted for extraction from chromatin by p97/VCP. This, however, will require further investigation and it will be important to confirm whether ubiquitylated RPA2 is a substrate for ZUP1, which has not yet been conclusively shown despite early suggestions in the initial publications describing ZUP1's discovery (Hewings et al., 2018). Turnover of RPA2 and RAD51 proteins themselves could be monitored in future experiments using fluorescence recovery after photobleaching by transiently transfecting fluorescently tagged RPA2 or RAD51 proteins in a WT or ZUP1 KO background and monitoring their recruitment to chromatin. This technique was previously used to demonstrate that knockdown of RFWD3 resulted in reduced turnover of RPA2 and RAD51 at photobleached sites, so it would therefore be interesting to see if ZUP1 loss recapitulated this phenotype (Inano et al., 2017).

A potential caveat to the above experiments was the use of PCNA to stratify cell cycle phase in response to ICL lesions, as it is itself modified and acts as a signalling platform following DNA damage. Although a robust pattern of excessive RPA and RAD51 loading was established in ZUP1 KO cells, future experiments could utilise EdU

incorporation and Cyclin A immunostaining to stratify cells in S or G2/M phase respectively to independently confirm the cell cycle distribution observed in PCNA stained experiments above.

4.3.2. Significance of RPA2 hyperphosphorylation in ZUP1 KO cells

In this chapter I uncovered a synergistic effect on MMC-induced RPA2 phosphorylation when both ZUP1 and RFWD3 are absent. Interestingly, it has previously been reported that RPA2 phosphorylation in RFWD3 KO cells is increased after MMC treatment, but decreased after hydroxyurea treatment relative to WT cells (Inano et al., 2017). This is suggestive of RFWD3's specific role in ICL repair and the synergistic effect on RPA2 phosphorylation in ZUP1 KO cells shown in this chapter may therefore suggest that ZUP1 and RFWD3 function is parallel pathways during ICL repair, rather than an epistatic pathway. This chapter also investigated the impact of knocking down the ATR activating proteins TOPBP1 and ETAA1 on MMC-induced RPA2 phosphorylation in ZUP1 KO cells. Whilst knockdown of ETAA1 did not result in a significant impact on phosphorylation levels, the knockdown of TOPBP1 surprisingly led to greatly elevated RPA2 phosphorylation, which was epistatic with ZUP1. This experiment therefore could not reveal if ZUP1 mediates RPA2 phosphorylation via regulation of TOPBP1 as the phosphorylation phenotype was confounded by the pleiotropic consequences of knocking down TOPBP1. Additionally, the significant impact on cell viability as a result of TOPBP1 knockdown precluded an assessment of the redundancy between TOPBP1 and ETAA1 activation of ATR, as double knockdown of these factors was not feasible in ZUP1 KO cells. In future the generation of a separation of function mutants of TOPBP1 and ETAA1 in which the ATR activating

domain (AAD) is mutated, but other functional domains are kept intact, could be used to determine whether their ATR activating function is important for the excess RPA2 phosphorylation observed in ZUP1 KO cells (Kumagai et al., 2006).

A possible alternative hypothesis that could account for the elevated RPA2 phosphorylation is that it arises as a secondary concentration-dependent consequence of excess ssDNA in ZUP1 KO cells. A recent single-molecule imaging study proposed a diffusion driven model for ATR activation whereby DNA damage that causes excessive ssDNA bound by RPA increases the local concentration of RPA–ATR interactions leading to a higher probability of ATR activation and subsequent phosphorylation of RPA (Yin et al., 2021). This model therefore can explain increased RPA phosphorylation in ZUP1 KO cells without necessitating any alteration of the intrinsic activity of ATR. If ZUP1 activity prevents excess generation of ssDNA, as I have demonstrated in this chapter using the native BrdU assay, loss of ZUP1 may therefore result in increased concentration dependent activation of ATR. Interestingly, the aforementioned study also demonstrated that the local activity of ATR driven by diffusion mediated contacts with RPA was independent of the global activation of the CHK1 axis, which may explain why CHK1 phosphorylation was not found to be substantially different between WT and ZUP1 KO cells as shown in Figure 14.

4.3.3. Possible mechanistic basis for excess ssDNA generation in ZUP1 KO cells

The use of the native BrdU assay demonstrated that the underlying basis for elevated RPA2 and RAD51 loading in ZUP1 KO cells is due to the excess generation of ssDNA following MMC damage. This, coupled with the possible defect in p97/VCP-mediated extraction of these factors, may explain their persistence on chromatin following DNA

damage. Increased ssDNA generation could perhaps reflect a defect in gap filling by TLS polymerases in ZUP1 KO cells during ICL repair. This possibility is suggested by the fact that ubiquitylation of PCNA directs the recruitment of TLS polymerases and the Gibbs-Seymour lab's finding that PCNA polyubiquitylation is elevated in ZUP1 KO cells (Choe and Moldovan, 2017). Moreover, disruption of PCNA ubiquitylation by depleting RFWD3 has been shown to drastically impair TLS at ICL lesions (Gallina et al., 2021). Given the similarity in RPA2 and RAD51 persistence phenotypes between RFWD3 and ZUP1 KO cells it would therefore be interesting to investigate if excess ssDNA in ZUP1 KO cells is a result of a TLS defect. This would help address whether excessive ubiquitylation during replication-coupled DNA repair is a loss-of-function (e.g. reduced access to specific TLS polymerases at DNA lesions that causes persistent ssDNA gaps) or gain-of-function effect (e.g. inappropriate use of certain TLS polymerases that creates ssDNA). To test this, future experiments could use a genetic approach to deplete or knockout the TLS polymerases and associated factors (e.g. POLκ, POLη, POLι, REV1–POLζ), as well as the RPA-interacting primase PRIMPOL in WT or ZUP1 KO backgrounds and repeat the QIBC analyses above (Mouron et al., 2013; Waters et al., 2009). Alternatively, the recently available REV1 inhibitor JH-RE-06 could be used to inhibit TLS (Wojtaszek et al., 2019). If appropriate antibodies are available, the dynamics of these factors themselves could be monitored using QIBC. If the data identifies a clear candidate(s) that produces the hyper ssDNA in ZUP1 KO cells, it would then be appropriate to reconstitute the bypass step *in vitro* to allow a more detailed mechanistic investigation of this Ub-dependent reaction in light of ZUP1 regulation.

Increased ssDNA could also result from altered regulation of specific replication fork structures such as reversed replication forks. There are limited proposed readers of PCNA polyUb including ZRANB3, WRNIP1, and potentially FAN1 (Ciccia et al., 2012;

Leuzzi et al., 2016; Porro et al., 2017). ZRANB3 is recruited to K63-linked PCNA polyUb and mediates fork reversal to confer a protective function at stalled replication forks and thereby limits the accumulation of ssDNA (Neelsen and Lopes, 2015). More recently, it has been demonstrated that RFWD3-dependent PCNA ubiquitylation is responsible for ZRANB3 recruitment to stalled forks and subsequent fork reversal (Moore et al., 2023). If PCNA deubiquitylation is disrupted by loss of ZUP1, as the Gibbs-Seymour lab have demonstrated, ZRANB3 fork reversal activity may be hyper-activated and reversed fork structures may then be more vulnerable to the generation of excessive ssDNA. Indeed, collaborators of our lab have utilised the ZUP1 KO cells I generated in this study in DNA fiber assays to reveal that cells possess a fork degradation phenotype that is rescued by loss of ZRANB3 (I.G-S. personal communication; unpublished). Interestingly, it has previously been shown that in BRCA2 deficient cells, reversed fork structures are targets of nucleolytic degradation due to the lack of stable RAD51 nucleofilament formation in BRCA2's absence (Mijic et al., 2017). It has also been shown that in BRCA2-deficient cells, stalled forks accumulated phosphorylated and ubiquitylated RPA which was dependent on RFWD3 E3 ligase activity and SMARCAL1 fork remodelling activity (Duan et al., 2020). The disruption of normal RPA and RAD51 dynamics following loss of ZUP1 DUB activity, as demonstrated in this chapter, may therefore similarly result in reversed fork vulnerability to nucleolytic degradation.

To elucidate the basis for excess ssDNA generation in ZUP1 KO cells in response to MMC damage, a future avenue of research could be to conduct a targeted siRNA or CRISPR-based screen of fork reversal factors, helicases, and nucleases that may be aberrantly regulated in ZUP1's absence. The native BrdU assay could be used as a readout to determine if the knockout of any factor can reverse the excessive ssDNA

observed in ZUP1 KO cells, which would suggest a regulatory role for ZUP1 in the functioning of that factor.

5

Genome-wide CRISPR screen identifies genetic interactors of ZUP1

Contents

5.1. Introduction

The work presented in this thesis thus far demonstrates that loss of ZUP1 has important consequences for the dynamics of RPA and RAD51 at challenged replication forks, which results in hypersensitivity to genotoxic agents that impose fork stalling lesions. These results relied on hypothesis-driven experimentation stemming from the initial finding of genotoxin sensitivity and RPA hyperphosphorylation in ZUP1 KO cells. While these data have generated some important observations of the phenotypic defects of ZUP1 KO cells, their targeted approach has not addressed the full scope of possible pathways and genetic interactors of ZUP1 in response to genotoxic insult. In this chapter I now turn to pooled genome-wide CRISPR-Cas9 KO screening to comprehensively assess the set of genes that confer sensitivity or resistance to MMC treated cells in ZUP1's absence to identify the molecular pathways that function redundantly to respond to and repair ICL lesions. Genome-wide screening provides a powerful, unbiased approach to assess ZUP1's chemogenetic interactors in response to MMC, which generates an important resource for hypothesis generation and future research.

Multiple genome-scale CRISPR-Cas9 KO libraries have been designed for use in pooled screens in human cells including the GeCKOv2, Brunello, Sabatini, Yusa, and TKOv3 libraries (Doench et al., 2016; Hart et al., 2017; Sanjana et al., 2014; Tzelepis et al.,

2016; Wang et al., 2015). These libraries differ in their targeting scope, number of sgRNAs used to target each gene, and the vector components that encode each library (Table 7). Given the labour and resource intensive nature of CRISPR screening there is often a trade-off between the efficiency and feasibility of a screen, and the targeting of each gene with many individual sgRNAs to yield statistically robust data. Newer generation libraries such as the Brunello and TKOv3 libraries use sequence-optimised sgRNAs based on functional validation and benchmarking against previous libraries to reduce the number of guides required to still allow robust identification of hit genes (Sanson et al., 2018). The process for sequence optimisation of the TKOv3 is described in section 1.4.3 of the introduction. The functional validation of the sequence optimised TKOv3 library found that the ability to identify essential genes was enhanced by only <5% when more than four sgRNAs were used per gene (Hart et al., 2017). Additionally, a meta-analysis of previous CRISPR screen data found that the use of more than two experimental replicates only marginally increased the discovery rate of core essential genes (Hart et al., 2017). The TKOv3 library was therefore chosen to perform the CRISPR screen in this chapter since:

1. It is a one-component system and allows targeting of genes with a single lentiviral transduction.
2. It is one of the most efficient libraries and only requires four sgRNAs per gene for robust hit identification.
3. It has been widely adopted and well validated in previous studies for the identification of synergistic and suppressor genetic interactors.

Table 7. Characteristics of commonly used human genome-wide CRISPR KO libraries

library	GeCKOv2	Brunello	Sabatini	Yusa	TKOv3
# of vectors	2	1 or 2	1	2	1
target scope	coding and noncoding	coding	coding	coding	coding
# genes targeted	20,914	19,114	18,663	18,009	18,056
sgRNAs per gene	6	4	10	5	4
total sgRNAs	122,411	76,441	187,535	90,709	71,090

The screen performed as part of this thesis was designed to identify genes whose KO either confers sensitivity or resistance to MMC. This design relies on the concept of synergistic and suppressor interactors whereby the KO of a hit gene in ZUP1 KO cells exposed to MMC confers a selective disadvantage or advantage respectively, but the targeting of the gene alone in a WT background does not significantly impact cell viability. The screen was therefore conducted as two parallel pooled CRISPR KO dropout screens in U2OS WT and ZUP1 KO cells. A key consideration of dropout screening is that the library coverage (i.e. the number of cells bearing a copy of each unique sgRNA in the library) should be maintained at a sufficiently high level to allow for statistically robust identification of depleted or enriched guides. A minimum coverage of 200x to 500x is therefore usually recommended and has generated robust results in previous dropout screens (Colic et al., 2019; Doench, 2018).

The ability of CRISPR screens to identify genes that confer sensitivity or resistance to a drug relies on the quantification of the abundance of integrated lentiviral sgRNA vectors using NGS. This in turn necessitates the use of robust bioinformatics tools to statistically analyse the representation of individual guides and determine their fold-change relative to non-targeting control sgRNAs and compare treatment conditions to identify hit genes. In this chapter, I used the widely adopted model-based analysis of

genome-wide CRISPR/Cas9 knockout (MaGECK) algorithm to determine sgRNA read counts from the different timepoints and treatment conditions (Li et al., 2014). I then used the DrugZ algorithm, which has been specifically designed to identify synergistic and suppressor chemogenetic interactions from CRISPR screens, to calculate normalised fold-change scores (normZ) for each gene between MMC-treated and untreated conditions (Colic et al., 2019). These algorithms therefore allow the robust and well-validated identification of synergistic and suppressor interactors.

To date there have been relatively few CRISPR screens conducted to assess the cellular response to MMC. A CRISPR-Cas9 based screen using a focused library targeting 365 DDR-associated genes identified 35 genes whose loss sensitised 293A cells to MMC, with genes mainly functioning in the FA and HR pathways (Su et al., 2020). A genome-wide CRISPR-Cas9 resistance screen utilising the GeCKO library was also reported, which demonstrated a synthetic viable interaction between BLM helicase and FANCC of the FA core complex in response to MMC (Moder et al., 2017). To my knowledge the only study reporting a genome-wide CRISPR-Cas9 dropout screen in response to MMC is the Schubert *et al.* study which used the TKOv3 library in RPE1 cells to identify SCAI as a factor important for the error-free repair of MMC-induced ICL lesions (Schubert et al., 2022). Notably, MMC was not included in the Olivieri *et al.* study of 31 genome-scale CRISPR screens that sought to define a comprehensive genetic map of the response to DNA damage in RPE1 cells (Olivieri et al., 2020). The genome-wide screen presented here therefore constitutes an important contribution to our understanding of the cellular response to MMC-induced damage in aneuploid U2OS cells and identifies novel chemogenetic interactors of ZUP1 that mediate the response to ICL lesions.

5.2. Results

5.2.1. Design of genome-wide CRISPR-Cas9 MMC dropout screen

Based on the data from Chapter 3, a genome-wide CRISPR-Cas9 dropout screen was designed to assess the function of ZUP1 in the repair of MMC-induced DNA damage in an unbiased manner. The goal of the screen was to determine the chemogenetic interactors of ZUP1 that confer either sensitivity or resistance to MMC. Two parallel screens were performed in U2OS WT and ZUP1 KO cells using the TKOv3 sgRNA lentiviral library (Figure 27). WT and ZUP1 KO cells were split into treatment groups in which cells were either left untreated or treated with a lethal dose of MMC that killed 20% of cells (i.e., the LD20 dose), which was determined empirically for each cell line. Each treatment condition was performed as a technical replicate, which has previously been shown to allow statistically robust identification of hit genes (Colic et al., 2019). Cells were cultured for 12 days after the addition of MMC with passaging and replenishment of drug containing media performed every 3 days. At the screen endpoint genomic DNA was extracted from cells and NGS sequencing libraries prepared via two sequential PCR steps. Samples were sequenced using a NovaSeq 6000 and read count values were generated for each gene using the MAGeCK Count algorithm. NormZ scores for each gene were then computed using the DrugZ algorithm, which reflect the fold change in treated cells relative to their untreated counterparts.

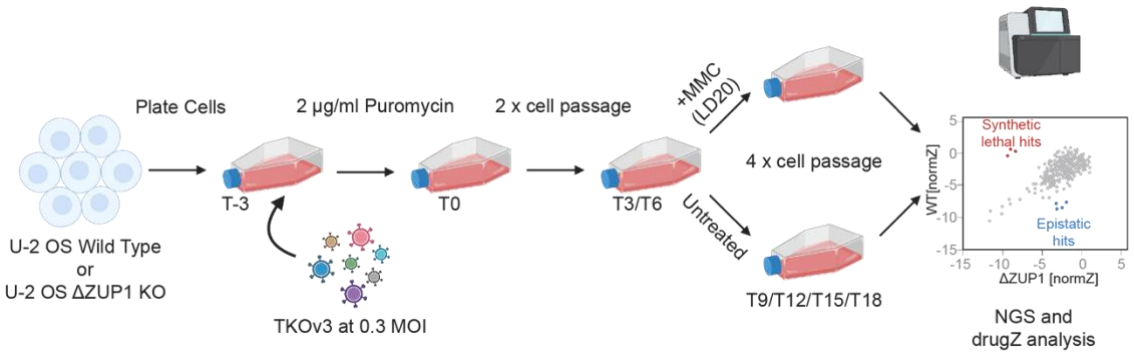

Figure 27. Schematic design of genome-wide CRISPR-Cas9 dropout screen with MMC

U2OS WT and ZUP1 KO clone 38 cells were plated at the density required for ~422x library coverage. Lentiviral packaged human genome-wide CRISPR-Cas9 KO library (TKOv3) containing 70,948 guides (4 guides/gene) targeting 18,053 protein-coding genes as used to transduce cells as a MOI of 0.3. Positively sgRNA transduced cells were selected by puromycin and cells were allowed to recover for two passages. Each cell line was then split into treatment arms and treated with an LD20 dose of MMC, calculated individually for WT and KO cells, or left untreated with 2x technical replicates for each treatment arm. Cells were then cultured for a further 12 days with cell passage and drug replacement every 3 days. Genomic DNA was then extracted from samples and two rounds of PCR were performed to first amplify sgRNA cassettes and then attach Illumina sequencing primers. Next generation sequencing was then performed using an Illumina NovaSeq 6000 and sgRNA copy numbers calculated using the MAGeCK v0.5.9 algorithm. The DrugZ algorithm was then used to calculate normZ scores for WT and KO untreated and treated cells to determine synergistic hits. Figure created using BioRender.com.

5.2.2. Optimisation of parameters for genome-wide CRISPR-Cas9 screen

To ensure the successful execution of the CRISPR screen, I first optimised the relevant parameters presented in Figure 28. The tolerance of cells to Polybrene (hexadimethrine bromide) was determined using the resazurin fluorometric assay that monitors the reduction of the non-fluorescent blue dye resazurin to a red fluorescent product (resorufin) by the mitochondrial respiratory chain in cells (O'Brien et al., 2000). The fluorescence output is therefore directly proportional to the number of living cells and can be used as a proxy for cell viability. Polybrene is a cationic polymer that neutralises the charge repulsion on the cell surface and can be used to improve transduction efficiency of lentiviral virions. Polybrene can, however, be toxic to cells at higher concentrations so the highest concentration of 8 μg/ml resulting in no perturbation of cell viability was chosen for use in transduction of the TKOv3 library (Figure 28A).

The TKOv3 library is encoded using the lentiCRISPRv2 plasmid backbone which allows for selection of positively transduced cells via a puromycin resistance determinant. The sensitivity of un-transduced cells to puromycin was therefore empirically determined to identify the dose required to kill all cells that do not contain a copy of the TKOv3 plasmid. The lowest dose that resulted in complete cell death (2 μg/ml) was chosen (Figure 28B).

To ensure that each cell is infected with a single copy of the TKOv3 vector a low MOI of 0.3 was used for transduction of the lentiviral library. The MOI was titred using the resazurin cell viability assay on cells transduced with different volumes of TKOv3 packaged lentiviral particles and selected with 2 μg/ml puromycin. The proportion of

surviving cells at each concentration was plotted and linear regressions performed to interpolate the volume of virus required for 30% cell survival (Figure 28F).

The resazurin cell viability assay was also used to derive a preliminary estimate of the LD20 dose for MMC in U2OS WT and ZUP1 KO cells. Cells were plated in 12-well format and treated with the indicated dose of MMC in Figure 28C for 3 days when the fluorescence reading was taken. The linear portion of this dose response curve was plotted Figure 28D and a linear regression performed to extrapolate the MMC concentration resulting in 20% cell death. This provided a rough estimate of the LD20 dose as ~100 nM for ZUP1 KO cells and ~200 nM for WT cells. A dose-response experiment was additionally performed using cell confluence as a measure of cell viability as determined by plate imaging using an Incucyte live-cell imaging system. Cells were plated in 12-well plates and treated with the indicated concentration of MMC for 3 days at which point plates were then imaged, and confluence determined (Figure 28E). This experiment indicated that the estimated LD20 dose was substantially lower than that calculated using the resazurin assay. Interestingly the cell confluence experiment revealed a biphasic dose response curve whereby confluence initially drops off, but then plateaus before decreasing towards total cell death at the highest concentrations tested. This perhaps reflects a cytostatic effect of MMC at lower concentrations while a full cytotoxic effect is observed at higher concentrations.

The resazurin and cell confluency experiments produced a large discrepancy in LD20 estimates (~10–200 nM MMC) and could further be confounded by the difference in plate format of 12-well plates compared to the T175 flask format used in the full-scale screen. Additionally, it has been shown that cell viability can diminish over the treatment course of a drug with repeated passages (Olivieri and Durocher, 2021). For example, a drug causing 20% cell death at day 3 could result in 40% cell death by the screen endpoint at

day 12. The aim, therefore, was to identify the LD20 dose at the treatment endpoint. To obviate these factors, a serial passage dose-response experiment mimicking the treatment time course of the full-scale screen was performed using T175 flasks with a direct cell number readout measured using a haemocytometer. A dose range of 5–150 nM MMC was chosen to be tested as indicated in Figure 28G. These data revealed that cell viability did indeed tend to drop off over the course of the experiment, while the higher doses of 75 nM and 150 nM lead to almost complete cell death by day 6. This serial passage experiment revealed that the lowest dose tested (5 nM) was closest to an LD20 dose for both WT and ZUP1 KO cells with WT survival just above the LD20 and ZUP1 KO survival just below the LD20 level.

Taking these above parameters into account, a final pilot screen using TKOv3 transduced cells was performed to confirm the appropriate MMC dose (Figure 28). Single T175 flasks of WT cells were treated with either 10 or 15 nM MMC, while ZUP1 KO cells were treated with 2.5 or 5 nM MMC. Cells were passaged and counted every 3 days and the proportion of surviving cells was calculated relative to an untreated control flask of either WT or ZUP1 KO cells. These data identified 10 nM for WT and 2.5 nM for ZUP1 KO cells to be the dose resulting in 20% cell death of the respective cell lines by day 12 in TKOv3 transduced cells.

The full-scale screen was then carried out using the conditions determined above using a cell number to ensure that the coverage of the TKOv3 library was maintained at 422x throughout the screen. 100 million cells were therefore transduced for each cell line since 100,000,000 cells x 0.3 MOI = 30,000,000 cells, and 30,000,000 cells ÷ ~71,000 sgRNAs in the TKOv3 library = ~422x coverage. 30 million cells were replated at each passage to maintain the 422-fold library coverage. Cell pellets were collected at T0 to

allow determination of dropout of essential genes, and at T18 to identify genes that either confer a selective advantage or disadvantage.

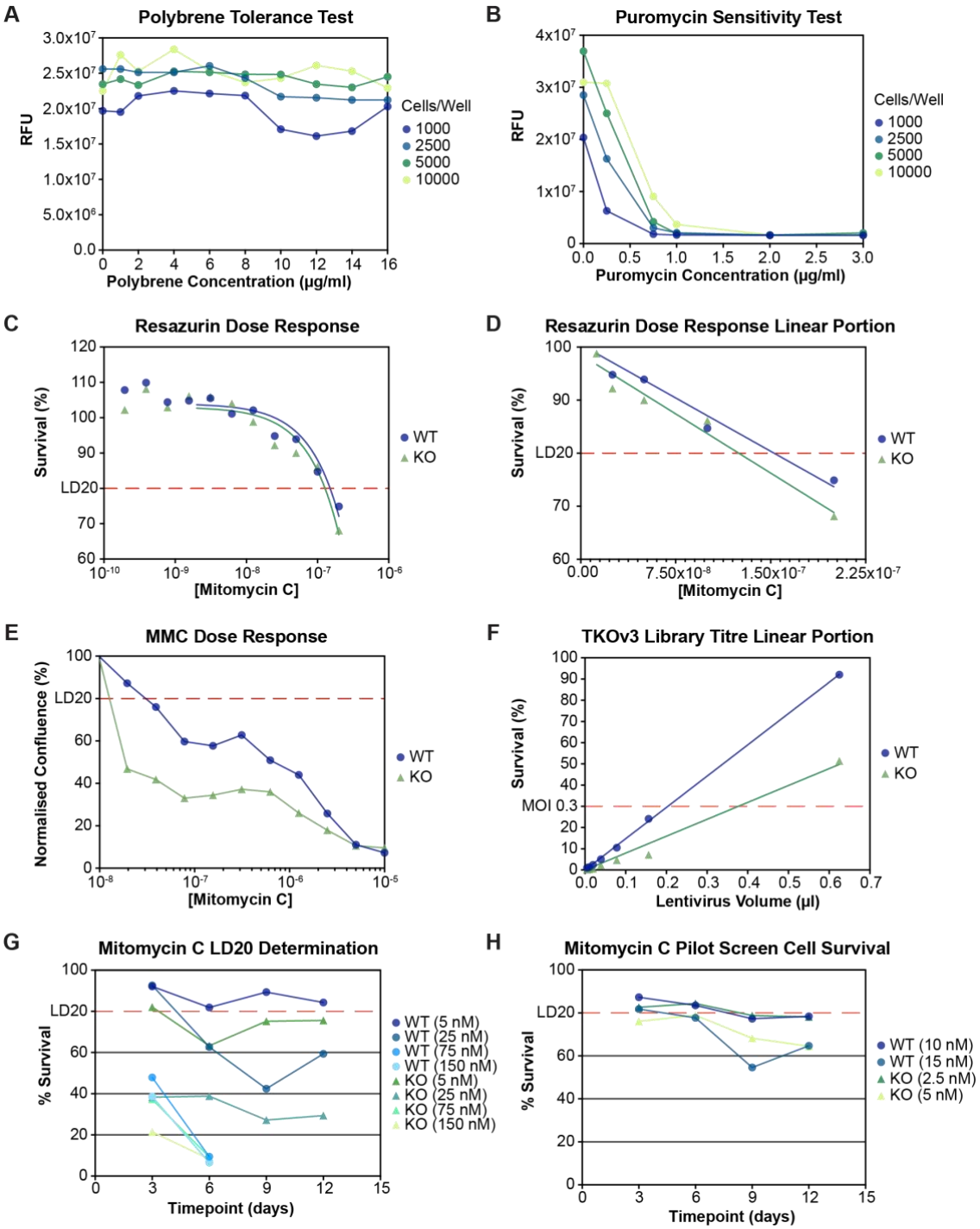

Figure 28. Optimisation of parameters for genome-wide CRISPR-Cas9 dropout screen

(A) The tolerance of cells to the indicated doses of polybrene was determined by quantifying cell viability using the resazurin fluorometric assay in 12-well plate format. 8 μg/ml polybrene was chosen as the dose for use TKOv3 library transduction as no observable impact on cell viability was noted at this concentration.

(B) Puromycin sensitivity was determined using the resazurin fluorometric assay in U2OS WT cells in 12-well plate format. 2 μg/ml was chosen as the lowest dose that resulted in complete cell death across all initial plating densities.

(C) MMC full dose response curves for U2OS WT and ZUP1 KO cells using the resazurin fluorometric assay. Cell survival was normalized against resazurin readings from untreated wells. The target LD20 dose is indicated by dotted red line.

(D) Linear portion of resazurin MMC dose response curve with linear curve fit regression applied. The target LD20 dose is indicated by dotted red line.

(E) MMC dose response using Incucyte confluency-based readout of cell viability. Cell survival was normalised to untreated cells.

(F) TKOv3 lentiviral library titre was performed using the resazurin fluorometric assay. U2OS WT and ZUP1 KO cells were transduced with the indicated volume of packaged lentivirus and cells were selected using 2 μg/ml puromycin. Trendlines represent linear regression used to interpolate the lentiviral volume required for 30% cell survival indicated with the red dotted line. TKOv3 library packing was performed by the Ebner lab.

(G) Full scale MMC dose response in T175 flask format using haemocytometer cell counting readout of cell survival. Untransduced U2OS WT and ZUP1 KO cells were cultured in the presence of the indicated MMC dose and cells counted and passaged at

3-day intervals. Percentage survival was normalized to an untreated control flask at each timepoint. Drug concentrations were discontinued if they resulted in greater cell death than required for a flask's seeding density.

(H) Pilot screen to identify appropriate drug concentration for use in full scale CRISPR screen. A single flask for each indicated treatment condition was transduced with TKOv3 lentiviral library and cultured according to the schematic for the full-scale screen in Figure 27. Cell numbers were calculated at each passage and the surviving fraction normalized to an untreated control at each timepoint.

5.2.3. Preparation of NGS library for genome-wide screen

NGS sequencing libraries were prepared from gDNA extracted from T0 and T18 cell pellets. Two sequential PCRs were performed to firstly amplify the TKOv3 sgRNA cassette from each cell and then attach i5 and i7 Illumina sequencing adapters to the 5′ and 3′ ends of the amplicon respectively. These reactions are referred to as PCR1 and PCR2 respectively below (Figure 29). PCR1 reactions were carried out in 96-well format using 3.5 µg of template gDNA per reaction, with the required number of reactions performed to amplify the total amount of gDNA extracted from each sample to maximise library coverage. To ensure this coverage was at least 422-fold the following calculation was performed to determine if all samples met the minimum requirement. Given the weight of a diploid human genome is ~6.5 pg and there are ~71,100 sgRNAs in the TKOv3 library then the amount of gRNA required for 1x library coverage is 0.46 µg. Therefore, for a 422x coverage 194 µg sample gDNA is required constituting 56 individual PCR1 reactions if each reaction requires 3.5 µg. All samples met this minimum requirement, but the entire sample was processed in each case to maximise coverage and improve statistical analysis of enriched or depleted guides. An analytic gel of PCR1 products showed an amplicon of the correct size for each sample and negative control PCR1 reactions without gDNA template revealed no off target or contaminant amplification (Figure 30A; water controls not shown). PCR2 reactions were then performed to attach Illumina sequencing adaptors as depicted schematically in Figure 29B**.** Forward primers were included as a pool of nine primers containing spacers of different lengths to create a stagger. This allows for greater sequence diversity in each NGS sequencing reaction resulting in increased sequencing fidelity. A unique reverse primer containing a DNA barcode was used for each separate sample to allow for read

deconvolution and identification of the relevant parental template following sequencing. PCR2 reactions successfully yielded an amplicon of correct size, but a smear and off target bands were observed as has been reported by previous groups for PCR2 reactions (Figure 30B). A gel extraction was therefore performed to isolate the band of correct size (211 bp) and a PCR clean-up column purification was run to remove any contaminating guanidine salt from the QG buffer used in the gel extraction. Samples were run on an analytic gel which confirmed the presence of a single band at 211 bp (Figure 30C). NanoDrop quantification of gel extracted samples before and after PCR clean-up also revealed that this step improved the A260/280 and A260/230 ratios to within the acceptable range, suggesting samples were of high quality and were not contaminated with protein or excess salts (i.e. 260/280 = 1.8-2.0, 260/230 > 2.00) (Table 8 and Table 9). Purified samples were then pooled and sequenced via NGS using a NovaSeq 6000 (Illumina).

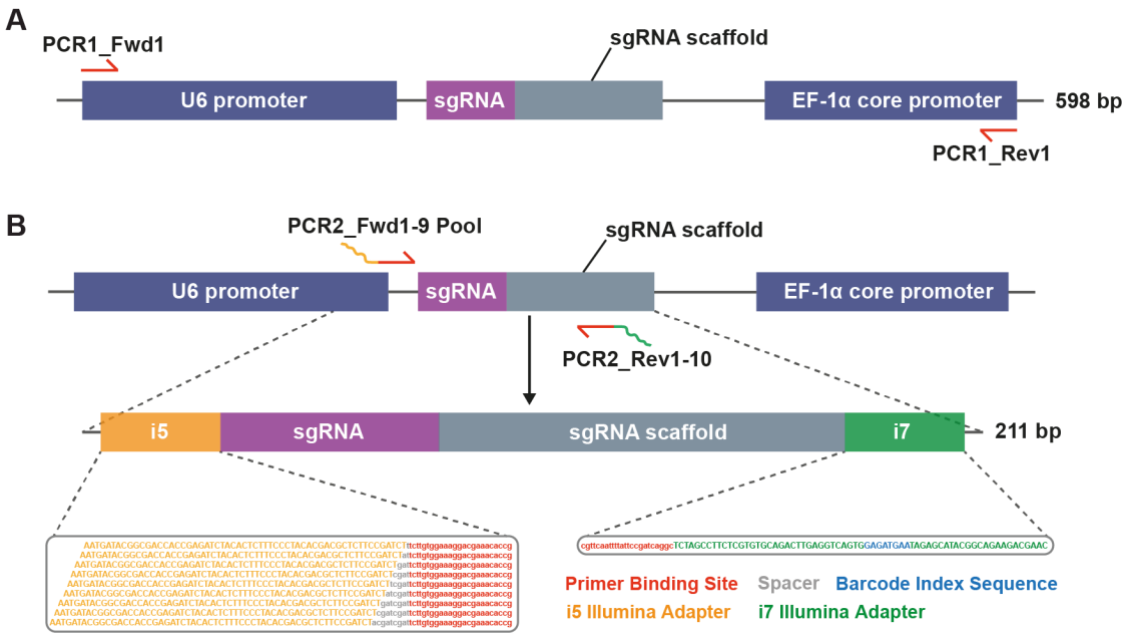

Figure 29. Schematic overview of NGS library preparation by PCR for CRISPR screen analysis

(A) Schematic of PCR1 reaction used to amplify integrated sgRNA cassettes. The TKOv3 library is based on the lentiCRISPRv2 backbone plasmid and forward and reverse primers are located in the promoter regions as depicted.

(B) Schematic of PCR2 reaction used to attach Illumina sequencing adapters to amplified sgRNA cassette templates. Forward primers were included as a pool of nine primers containing spacers of different lengths to create a stagger as shown. This allows for greater sequence diversity in each NGS sequencing reaction resulting in increased sequencing fidelity. A unique reverse primer containing a DNA barcode is used for each sample to allow for read deconvolution following sequencing.

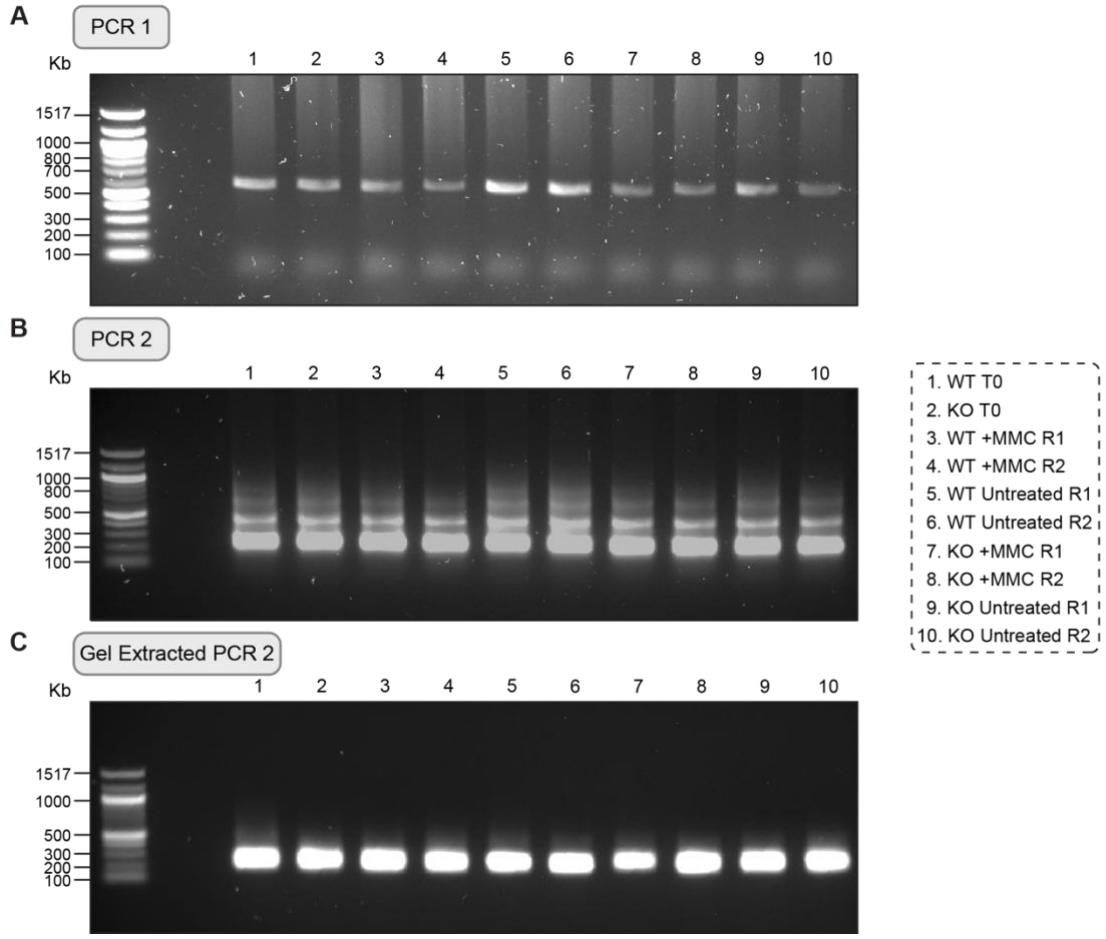

Figure 30. PCRs for generation of NGS library

(A) Agarose gel of PCR1 amplified sgRNA regions from CRISPR-Cas9 screen samples showing successful amplification of product at the expected 598 bp size.

(B) Agarose gel or PCR2 amplified product with main band corresponding expected 211 bp size for sgRNA region.

(C) Agarose gel of gel purified PCR2 showing isolation of 211 bp product corresponding to specific Illumina adaptor region.

Table 8. NanoDrop quantification of gel extracted PCR2 samples

Sample	Contents	Concentration (ng/µl)	260/280	260/230
1	WT T0	124.4	1.83	0.29
2	KO T0	196.9	1.85	0.36
3	WT +MMC R1	143.5	1.86	0.36
4	WT +MMC R2	108.9	1.86	0.24
5	WT Untreated R1	175.8	1.83	0.30
6	WT Untreated R2	145.6	1.85	0.37
7	KO +MMC R1	112.1	1.88	0.23
8	KO +MMC R2	144.3	1.89	0.32
9	KO Untreated R1	137.0	1.87	0.26
10	KO Untreated R2	142.0	1.87	0.29

Table 9. NanoDrop quantification of PCR clean-up purified NGS samples

Sample	Contents	Concentration (ng/µl)	260/280	260/230
1	WT T0	70.6	1.92	2.82
2	KO T0	167.8	1.89	2.49
3	WT +MMC R1	118.7	1.85	2.14
4	WT +MMC R2	79.8	1.94	2.12
5	WT Untreated R1	144.4	1.87	2.14
6	WT Untreated R2	123.1	1.86	2.14
7	KO +MMC R1	77.1	1.87	2.03
8	KO +MMC R2	113	1.86	2.13
9	KO Untreated R1	104.6	1.88	2.15
10	KO Untreated R2	112.2	1.87	2.08

5.2.4. Genome-wide CRISPR-Cas9 MMC sensitivity screen reveals putative synergistic and suppressor genetic interactors of ZUP1

Following the generation of read count matrices from NGS FASTQ output files using the MaGECK count algorithm, gene level depletion scores (normZ) were calculated for WT and ZUP1 KO cells using the drugZ algorithm. The ranked normZ scores for each gene are presented for each cell line individually, and in comparison, to one another in Figure 31. These data reveal the significant depletion (normZ <-3.0) of many factors in the FA pathway (FANCD2, RAD18, RFWD3, RTEL1, C17orf70/FAAP100), HR pathway (MCM8, MCM9), and NER pathway (ERCC5/XPG, ERCC8/CSA, GTF2H5) that are common to both WT and ZUP1 KO cells. FAN1 was also one of the most substantially depleted factors in WT cells while also showing moderate depletion in ZUP1 KO cells that did not quite reach the normZ cut-off score (normZ = -2.79). The identification of these factors validates the screening approach and demonstrates that it can successfully identify factors involved in ICL repair. Similar factors were also identified in a previous group's genome-wide sensitivity screen performed in RPE-1 $p53^{KO}$ cells which identified KEAP1 as the most significantly depleted gene as well as identifying the factor SCAI as a substantially depleted gene (Schubert et al., 2022). SCAI and KEAP1 were also the two most significantly depleted sgRNAs in both WT and ZUP1 KO cells in my screen and provides further confirmation of the screen's validity.

The enrichment of WT and ZUP1 KO cells transduced with sgRNA targeting NQO1 also validates the success of the screen as NQO1 encodes a two-electron reductase that reduces the prodrug form of MMC into active electrophilic metabolites that cause ICLs (Siegel et al., 1992). Knockout of the NQO1 gene therefore means MMC stays in its less

harmful parent compound form and is not able to cause substantial DNA damage, giving these cells a selective advantage and leading to their enrichment.

Excitingly, the comparison of normZ scores between WT and ZUP1 KO cell lines also revealed the presence of several outlier genes that were either depleted or enriched to a greater degree in the absence of ZUP1 (Figure 31C). These genes therefore potentially constitute synergistic and suppressor interactors of ZUP1 respectively. The most immediately interesting hit genes that were selected for further validation as part of this thesis are shown in bold in Figure 31**.** Hits were chosen for validation by two-colour competitive growth assay based on their high level of depletion or enrichment in ZUP1 KO cells relative to WT cells, as well as on a hypothesis driven basis. BRIP1/FANCJ was chosen as the most significantly depleted gene in ZUP1 KO cells that wasn't also represented in the top depleted genes (normZ <-3.0) in WT cells. BRCA2 and HELQ also had normZ scores below -3.0 in ZUP1 KO but not WT cells and were additionally selected on a hypothesis-driven basis with the reasoning that they may function in a parallel pathway to protect excess ssDNA generation following MMC damage as presented in the previous chapter.

NEIL3 was chosen for further characterisation as ZUP1 KO cells targeted with sgNEIL3 were substantially enriched over their WT counterparts (normZ 1.95 vs -1.26 respectively). As described in the introduction, NEIL3 is a glycosylase that can cleave DNA ICLs to generate an AP site that is bypassed by the action of error prone TLS polymerases (Semlow et al., 2016). Alternatively, the phosphodiester bonds that surround an ICL can be cleaved by FA complex proteins generating a DSB that is repaired via HR and allowing for higher fidelity repair. The protein TRAIP was demonstrated to regulate the pathway choice between NEIL3 and the FA complex by ubiquitylating the CMG replicative helicase when replication forks converge on an ICL,

with short Ub chains recruiting NEIL3 while longer chains led to unloading of CMG by p97/VCP which enables repair via the FA pathway (Figure 3) (Wu et al., 2019). The HMCES protein was shown to be recruited to replication forks via an interaction with PCNA and to 'shield' AP sites by forming a DPC which protects lesions from the action of error prone TLS polymerases and endonucleases (Mohni et al., 2019). Interestingly, it was found that siRNA knockdown of the DUB USP1 which causes increased PCNA ubiquitylation led to inhibition of HMCES recruitment to damaged DNA (Mohni et al., 2019). The Gibbs-Seymour lab has demonstrated that PCNA ubiquitylation is consistently elevated following DNA damage in ZUP1 KO cells (I.G.-S. personal communication; unpublished). It is possible, therefore, that HMCES recruitment to sites of DNA damage is impaired in ZUP1 KO cells. An interesting hypothesis, therefore, is that ZUP1 promotes pathway choice away from NEIL3 towards the FA pathway. Loss of ZUP1 then results in increased use of the NEIL3 glycosylase, but since PCNA ubiquitylation is higher in ZUP1 KO cells HMCES recruitment is decreased, and its AP site protective function is potentially diminished resulting in a deleterious unprotected NEIL3-induced AP site. Consequently, KO of NEIL3 in ZUP1 KO cells could shift the pathway choice back in favour of the FA complex and provide a selective advantage to cells leading to their accumulation. This hypothesis, however, remains highly speculative and will require substantial future research to clarify, but does provide a proof of concept for the utility of the genome-wide screen performed as part of this thesis to inform the investigation of future targets.

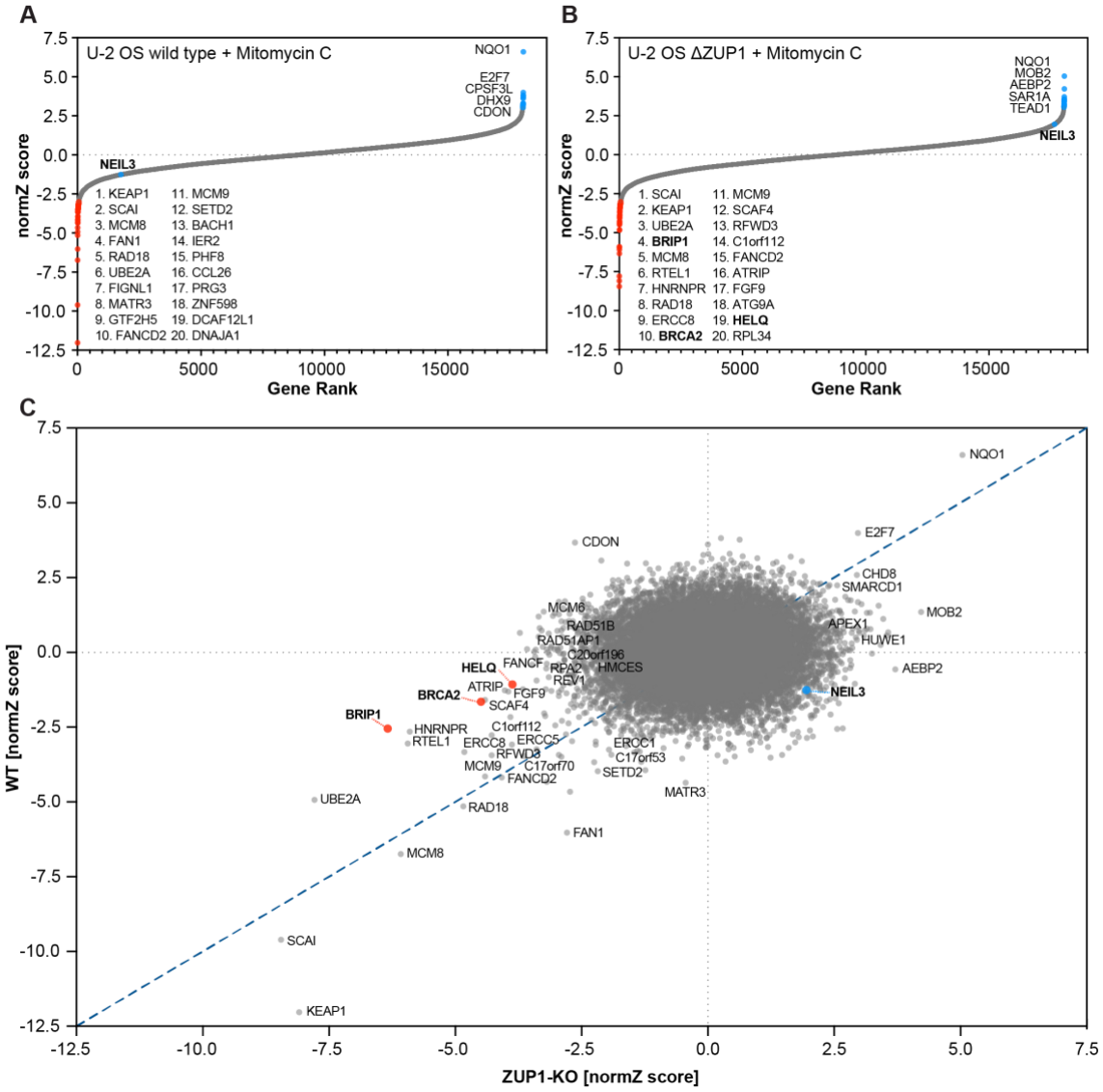

Figure 31. Results of genome-wide CRISPR-Cas9 MMC sensitivity dropout screen

(A) Plot of normZ score vs. gene rank from screen in U2OS WT cells. NormZ scores were calculated using the DrugZ algorithm. The top sensitising genes are labelled with red data points with the top 20 most significant hits named in rank order. The top suppressor genes are labelled with blue data points. Data is representative of n=2 technical replicates.

(B) Plot of normZ score vs. gene rank from screen in U2OS ZUP1 KO cells with data presented as in A. Data is representative of n=2 technical replicates.

(C) Plot of normZ scores for U2OS WT vs ZUP1 KO cells treated with MMC calculated using the drugZ algorithm. A gene's normZ score reflects the fold change in abundance of all four sgRNAs for a given gene in MMC treated cells relative to untreated cells with a lower score indicating greater sensitivity to MMC. Genes lying close to the blue dotted line (x=y) are those that are equally depleted or enriched in WT and ZUP1 KO cells. Synergistic genes are ones whose normZ scores skew more negatively in ZUP1 KO cells than in WT cells and are located further from the central blue line. BRIP1/FANCJ, BRCA2 and HELQ (highlighted in bold with red data points) were selected for further validation as potential synergistic interactors of interest. Suppressor genes on the other hand are ones that result in increased cell viability and skew more positively in ZUP1 KO cells relative to WT cells. NEIL3 (highlighted in bold with blue data point) was selected for further validation as a possible suppressor gene of interest. Data is representative of n=2 technical replicates. The cell culture for the CRISPR screen was performed by me and Sneha Anand of the Ebner lab.

5.2.5. Gene ontology enrichment analysis reveals depletion of specific networks in ZUP1 KO cells

Fourteen of the most significantly depleted gene hits (normZ <-3.0) identified were shared between MMC sensitivity screens performed in U2OS WT and ZUP1 KO cells. There were 54 and 56 genes identified with a normZ <-3.0 for WT and ZUP1 KO respectively (Figure 32A). This indicates that a substantial portion of the top hits from each screen were unique to their respective cell line, suggesting the possibility of identifying specific pathway involvement in ZUP1's absence. GO enrichment analysis of the most significantly depleted gene hits (normZ <-3.0) performed using the PANTHER database revealed the biological pathways implicated in response to MMC-induced DNA damage (Figure 32). The GO term with most substantial fold-enrichment in both WT and ZUP1 KO cells was ICL repair, which is consistent with response to MMC and provides further validation of the screens utility in specifically identifying pathways required for MMC-induced DNA damage. Other GO terms, centred on the cellular response to DNA damage, were commonly enriched in WT and KO cells (i.e. nucleotide excision repair, recombinational repair, DNA repair, nucleotide excision repair). Intriguingly, GO analysis revealed some terms that were specifically enriched in ZUP1 KO cells suggesting a possible redundant function in that pathway. Specifically, GO terms for DNA duplex unwinding, DNA geometric change, and DNA conformation change were found in the top 20 most enriched GO terms for the top hits (normZ <-3.0) in ZUP1 KO cells, but were not found in enriched GO terms for WT cells. The genes represented by these terms were MCM8, MCM9, HELQ, BRIP1/FANCJ, RAD54L, and RTEL with HELQ, BRIP1/FANCJ and RAD54L uniquely found in the top depleted genes

in ZUP1 KO cells. These findings therefore provide an intimation of cellular processes in which ZUP1 functions in response to MMC-induced DNA damage.

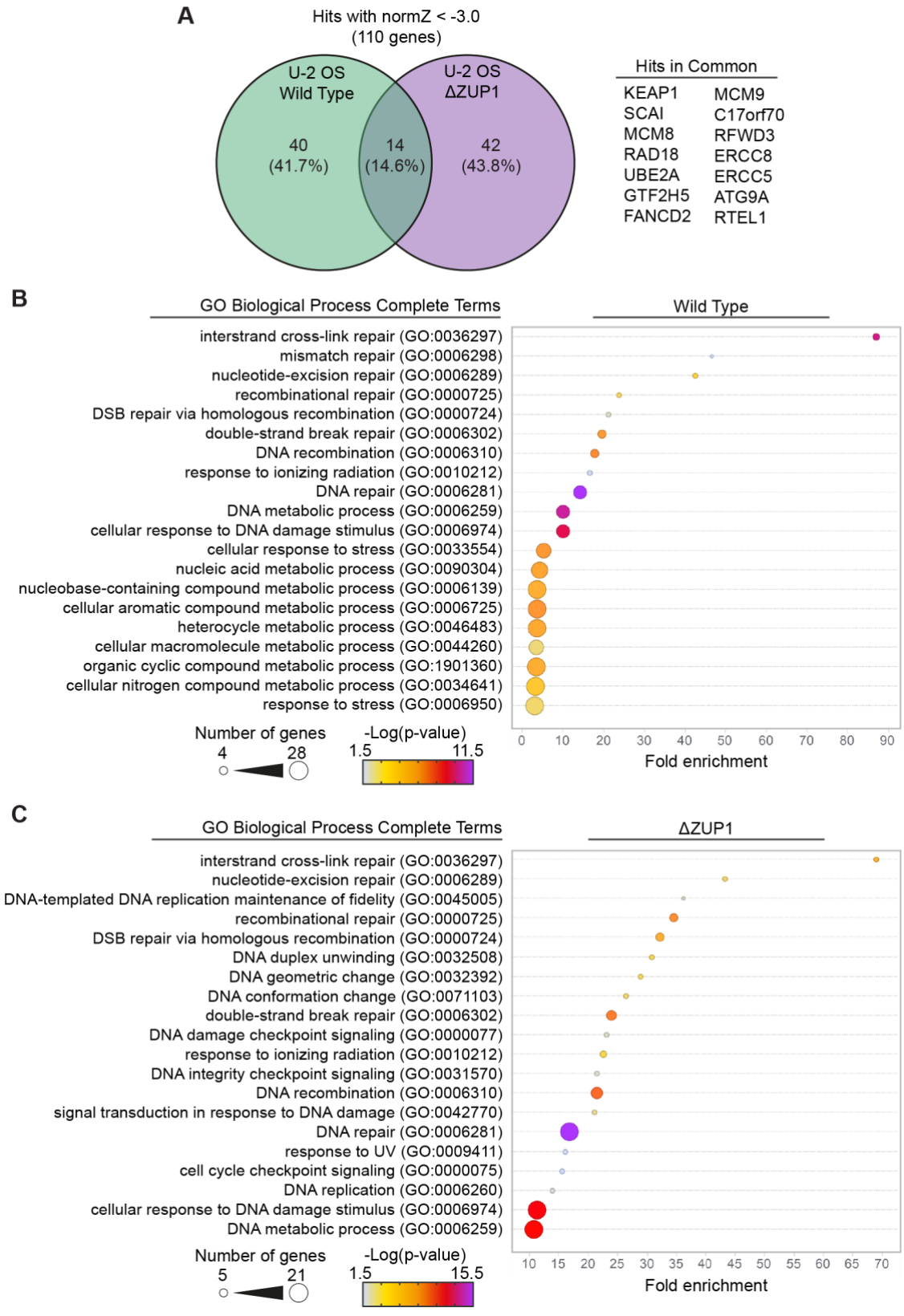

Figure 32. Gene ontology enrichment analysis of genome-wide CRISPR-Cas9 MMC sensitivity screen hits

(A) Venn diagram of top hits (normZ score < -3.0) in U2OS WT and ZUP1 KO cells.

(B) GO enrichment analysis of the top hits (normZ score < -3.0) depleted in U2OS WT cells in the MMC genome-wide sensitivity screen. The top 20 significantly enriched GO terms using the Biological Process Complete annotation data set are shown. GO analysis was performed using the PANTHER (version 17.0) overrepresentation test using Fisher's Exact test with Bonferroni correction for multiple testing. Value along the x-axis indicates the fold enrichment relative to the whole genome reference set of genes. Circle size indicates the number of hit genes represented in each GO term. Colour scale represents negative log of p-value. DSB, double-strand break; GO, gene ontology.

(C) GO enrichment analysis of the top hits (normZ score < -3.0) depleted in U2OS ZUP1 KO cells calculated as described above for WT cells.

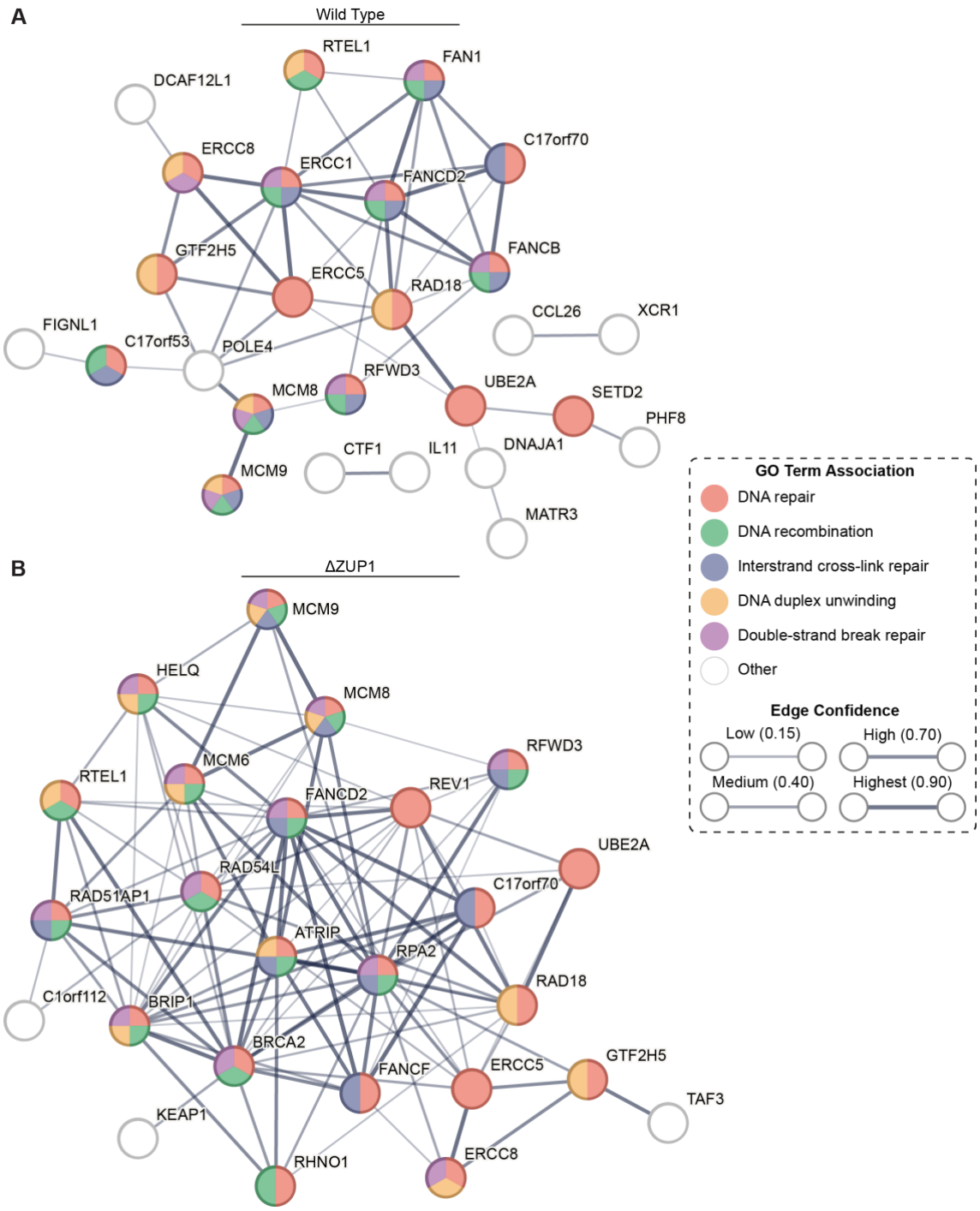
A
Wild Type
RTEL1
FAN1
DCAF12L1
C17orf70
ERCC8
ERCC1
FANCD2
GTF2H5
FANCB
ERCC5
RAD18
CCL26
XCR1
FIGNL1
C17orf53
POLE4
RFWD3
MCM8
UBE2A
SETD2
PHF8
CTF1
IL11
DNAJA1
MCM9
MATR3
B
ΔZUP1
MCM9
HELQ
MCM8
RFWD3
MCM6
RTEL1
FANCD2
REV1
UBE2A
RAD54L
C17orf70
RAD51AP1
ATRIP
RPA2
RAD18
C1orf112
BRIP1
BRCA2
FANCF
ERCC5
GTF2H5
TAF3
KEAP1
RHNO1
ERCC8
GO Term Association
DNA repair
DNA recombination
Interstrand cross-link repair
DNA duplex unwinding
Double-strand break repair
Other
Edge Confidence
Low (0.15)
High (0.70)
Medium (0.40)
Highest (0.90)

Figure 33. Network analysis of genome-wide CRISPR-Cas9 MMC sensitivity screen hits

(A) STRING network analysis of interactions between highly depleted hits (normZ <-3.0) from U2OS WT MMC sensitivity screen. Nodes are coloured by selected high confidence biological process GO (strength > 1.00; FDR $<1x10^{-9}$). Connection edges represent protein-protein associations (not necessarily direct physical binding) and the thickness of the connection indicate the strength of evidence associated with a particular interaction.

(B) As in panel A but for highly depleted hits (normZ <-3.0) from U2OS ZUP1 KO MMC sensitivity screen.

5.2.6. Two-colour competitive growth assay validation of CRISPR screen hits

Selected hits from the CRISPR screen were chosen for validation by two-colour competitive growth assay as described above in section 5.2.4. This assay measures the proliferation of a population of cells targeted with a GOI-specific sgRNA coupled to GFP expression relative to a control population of cells targeting with a non-targeting control sgRNA coupled to mCherry expression (Figure 34). HELQ, BRCA2 and FANJ/BRIP1 were chosen as putative synergistic interactors of ZUP1, while NEIL3 was chosen as a potential mediator of resistance to MMC. Independent sgRNAs targeting these factors were designed that were distinct from those used in the TKOv3 library. An EV control was also used to compare the effects of MMC treatment in WT and ZUP1 KO cells. Clonal U2OS WT and ZUP1 KO cells stably expressing Cas9 were generated for use in two-colour assays as described in the methods section 2.19. Clones expressing similar Cas9 protein levels were selected for WT and ZUP1 KO cells (Figure 35A). These clones were then used to perform competitive growth assays with the sgRNA constructs described above.

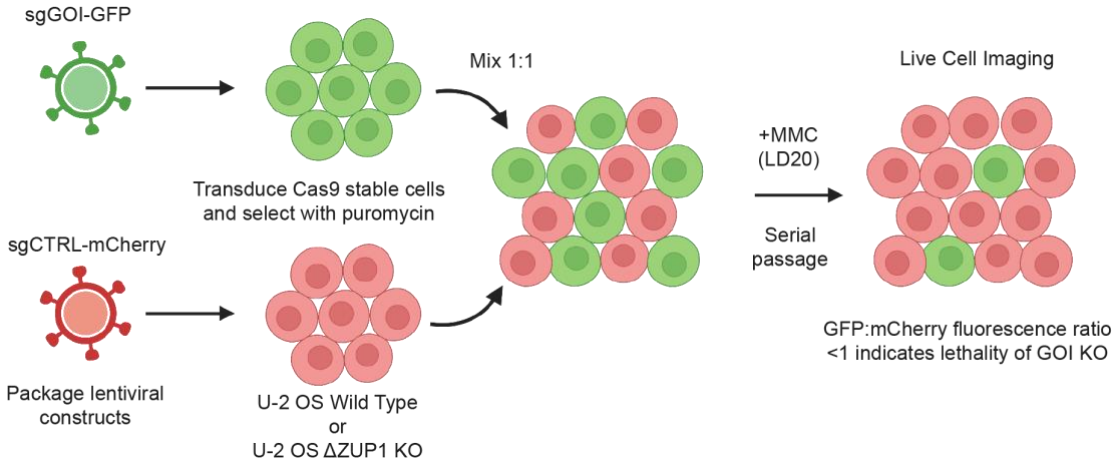

Figure 34. Schematic design of two-colour competitive growth assay

Schematic workflow of two-colour competitive growth assay for CRISPR screen hit validation. U2OS WT or ZUP1 KO cells stably expressing Cas9 were transduced with a lentiviral vector expressing an sgRNA targeting a GOI together with EGFP, or a control sgRNA targeting lacZ coupled with mCherry. Transduced cells were selected with puromycin and then EGFP and mCherry expressing cells were mixed in a 1:1 ratio. Cells were then treated with an LD20 dose of MMC or left untreated and imaged over time to quantify the proportion of EGFP and mCherry expressing cells. Figure created using BioRender.com.

These data revealed that U2OS WT and ZUP1 KO cells transduced with EV GFP constructs displayed broadly similar patterns in response to MMC treatment. Both cell lines showed a decreased GFP:mCherry fluorescence ratio at most timepoints in response to MMC treatment as expected. Fluorescence ratios were, however, relatively stable from day 3 to day 18 with a slight decrease over time. This is contrasted to cells targeted with sgBRIP1-GFP constructs which showed a marked decrease in GFP:mCherry fluorescence ratios over time in untreated conditions, indicating that KO of the BRIP1/FANCJ gene leads to loss of cell viability. Additionally, in response to MMC both WT and ZUP1 KO showed a strong loss of viability with almost all targeted cells outcompeted by non-targeting lacZ-mCherry control cells by the experimental endpoint. This validates BRIP1/FANCJ as a top hit in response to MMC. However, there was no apparent additive effect on cell viability when BRIP1/FANCJ was knocked out in the ZUP1 KO background relative to WT. Further work is therefore required to understand whether BRIP1/FANCJ is a true synergistic interactor of ZUP1.

In contrast, two-colour competitive growth assays for HELQ and BRCA2 provide support for a synergistic interaction with ZUP1. For untreated cells targeted with HELQ and BRCA2 sgRNAs the GFP:mCherry ratio also substantially decreased over time suggesting a deficit in cell viability under unchallenged conditions. Notably, however, cells targeted with either sgHELQ or sgBRCA2 showed an additional loss of viability when targeted in ZUP1 KO cells relative to WT cells when treated with MMC. While these data constitute a single biological repeat performed as a technical duplicate and should be treated as a proof-of-concept at this stage, they nevertheless lend support to the notion that HELQ and BRCA2 are *bona fide* synergistic interactors of ZUP1.

Competitive growth assays were also used to test the hypothesis that loss of NEIL3 confers resistance to MMC in ZUP1 KO cells. Knockout of NEIL3 in WT cells had no

major impact on cell viability, while in ZUP1 KO cells it led to a gradual decrease in GFP:mCherry ratios over time. Interestingly, no additional loss of viability was seen in either background when treated with MMC as was observed for EV control cells. Knockout of NEIL3, however, did not confer a selective advantage to ZUP1 KO relative to WT cells. It remains unconfirmed, therefore, whether targeting NEIL3 mediates resistance in ZUP1's absence in response to MMC. Additionally, NEIL3 was selected on a hypothesis driven basis rather than it being one of the most significantly enriched hits which highlights the necessity for rigorous hit validation following CRISPR screens. It should also be noted that the experimental set up of this CRISPR screen is more suited to identifying sensitising interactions due to the use of an LD20 dose of MMC. In future it would be useful to instead conduct a resistance screen with an LD80 dose of MMC to more robustly identify genes whose loss confers resistance in ZUP1 KO cells.

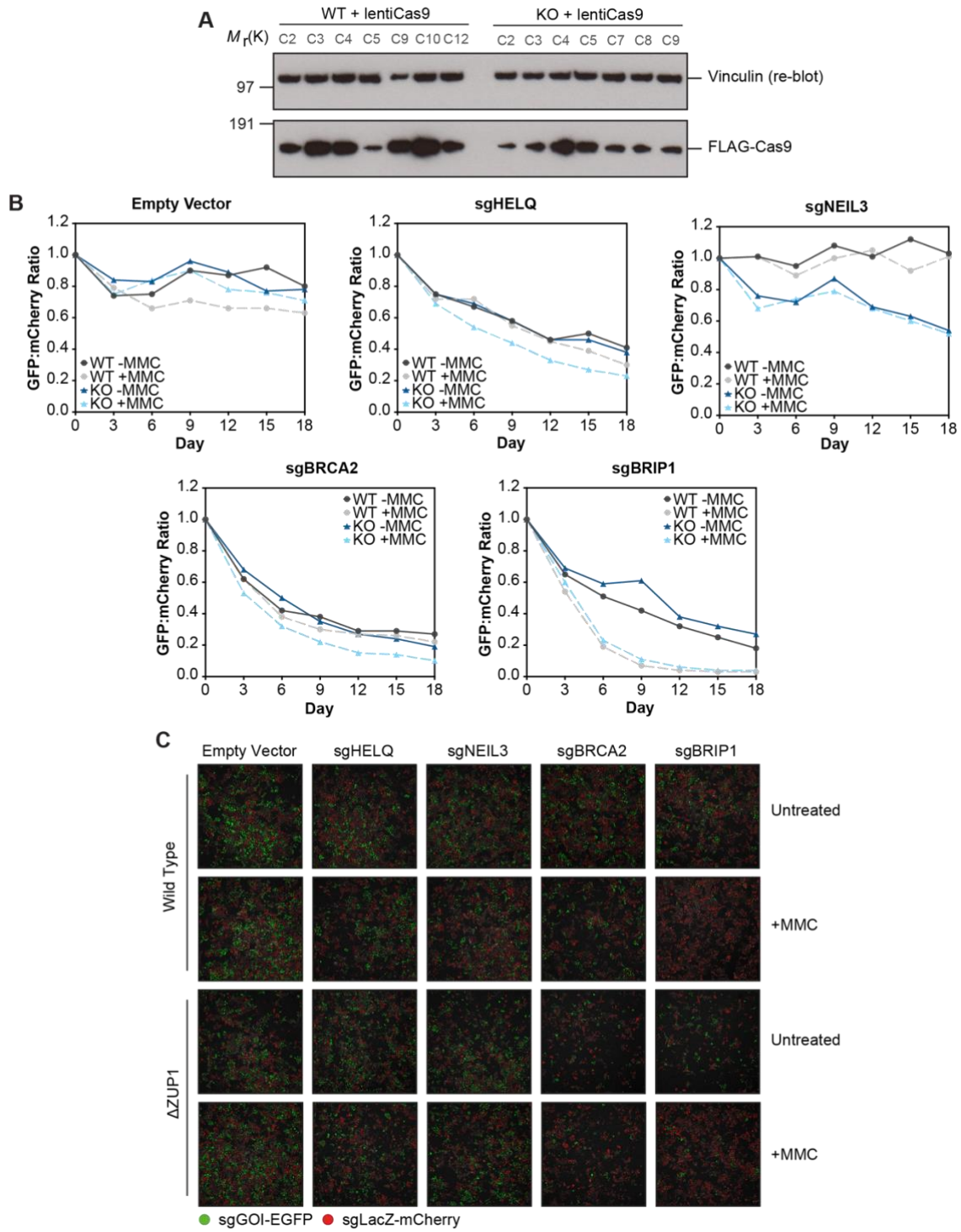
A
WT + lentiCas9
KO + lentiCas9
M_r(K)
C2 C3 C4 C5 C9 C10 C12
C2 C3 C4 C5 C7 C8 C9
97
191
Vinculin (re-blot)
FLAG-Cas9
B
Empty Vector
sgHELQ
sgNEIL3
sgBRCA2
sgBRIP1
GFP:mCherry Ratio
Day
WT -MMC
WT +MMC
KO -MMC
KO +MMC
C
Empty Vector
sgHELQ
sgNEIL3
sgBRCA2
sgBRIP1
Wild Type
ΔZUP1
Untreated
+MMC
sgGOI-EGFP
sgLacZ-mCherry

Figure 35. Two-colour competitive growth assay results

(A) Immunoblot to show generation of stable Cas9 expressing clonal cell lines in a U2OS WT of ZUP1 KO background. WT clone 4 and KO clone 5 were chosen to perform the two-colour competitive growth assay since they expressed Cas9 to a similar extent.

(B) Two-colour competitive growth assay results with indicated sgRNAs targeting GOI from the genome-wide CRISPR-Cas9 screen. The fluorescence ratio was normalized against the ratio of GFP:mCherry positive cells at day 0. The data is representative of a single biological replicate performed using 2x technical replicate wells.

(C) Representative widefield fluorescence microscopy images showing GFP and mCherry positive expressing cells. The number of positive cells in each case was calculated using an Olympus ScanR analysis pipeline.

5.3. Discussion

5.3.1. Summary of results

In this chapter I carried out parallel pooled genome-wide CRISPR-Cas9 dropout screens in U2OS WT and ZUP1 KO cell lines to identify genes whose depletion specifically confers sensitivity or resistance to MMC-induced ICL lesions in the absence of ZUP1. The aim of this approach was to identify the set of synergistic and suppressor genetic interactors of ZUP1 to deepen our knowledge of the potential DNA repair pathway(s) that ZUP1 functions parallel to. I have demonstrated that the screens performed in U2OS WT and ZUP1 KO cells were successfully able to identify hit genes from the FA, NER, and HR pathways that have previously been well validated for the repair of MMC-induced ICLs (Su et al., 2020). Excitingly, I additionally uncovered genes that were substantially more depleted or enriched in ZUP1 KO cells relative to WT and thus constitute putative synergistic or suppressor chemogenetic interactors of ZUP1 in response to MMC damage. I also carried out proof-of-concept validation by two-colour competitive growth assay of three selected synergistic hits (BRIP1/FANCJ, BRCA2, HELQ) and one suppressor hit (NEIL3). The results of this validation supports the notion that BRCA2 and HELQ are synergistic interactors of ZUP1, but did not show a synergistic or suppressor effect for independently designed sgRNAs targeting BRIP1/FANCJ or NEIL3 respectively. While the BRIP1/FANCJ synergistic interaction with ZUP1 was not confirmed by the two-colour competitive growth assay performed in this chapter, it would be useful to validate this interaction further using additional independently designed sgRNAs. BRIP1/FANCJ has been shown to suppress the formation of ssDNA gaps following replication stress and thereby confer resistance to PARPi. While resistant to PARPi, FANCJ KO cells were still seen to be sensitive to

cisplatin, MMC, and camptothecin (Cong et al., 2021). It would therefore be interesting to investigate whether depletion of BRIP1/FANCJ suppresses the excess formation of ssDNA in ZUP1 KO cells and determine if this depletion reverses the hypersensitivity of ZUP1 KO cells to PARPi shown in chapter 3. It should also be noted that the identification of false positives from CRISPR screens has been reported in previous studies and highlights the importance of complementary validation of hits as I have performed via two-colour competitive growth assay (Bock et al., 2022).

An additional aspect of my screen that should be considered is that the U2OS cell line in which it was performed is wild type for the tumour suppressor p53 (Oshima et al., 2007). CRISPR-Cas9 genome editing has been shown to induce a p53-mediated DNA damage apoptotic response that reduces the sensitivity of screens and impacts the ability to identify significant hits (Bowden et al., 2020; Haapaniemi et al., 2018). Although previous CRISPR screens conducted in parallel p53 WT and p53 KO cell lines demonstrated that robust screen performance could be achieved in p53 WT cells given optimal screen design, it will be important in future to validate hits from my screen in a p53 null background such as $p53^{KO}$ RPE1 cells.

5.3.2. Hyper ssDNA generation in ZUP1 KO cells promotes dependency on DNA processing enzymes

A major finding of this chapter is the synergistic chemogenetic interaction between BRCA2 and HELQ, and ZUP1 in response to MMC-induced DNA damage. Interestingly, these two genes have functions in processing ssDNA intermediates during ICL repair and suggest that loss of ZUP1 creates a dependency on ssDNA processing enzymes that leads to synergistic sensitivity when both are lost.

5.3.2.1. BRCA2 and ZUP1 synergistic genetic interaction

As noted in the previous chapter, BRCA2 confers an important replication fork protective function by promoting stable RAD51 nucleofilament formation that limits excessive nucleolytic degradation (Mijic et al., 2017). In BRCA2 proficient cells, stalled and reversed forks undergo controlled resection by MRE11, CtIP, DNA2, and EXO1 nucleases to promote HR repair and fork restart (Thangavel et al., 2015). When BRCA2 is absent, however, extensive uncontrolled resection occurs at reversed forks that can lead to their collapse and result in DSB formation (Lemacon et al., 2017). Interestingly it was reported that inactivation of the fork remodelling translocases SMARCAL1, HLTF, and ZRANB3 in BRCA-deficient cells restores replication fork stability and prevents excessive nucleolytic degradation (Taglialatela et al., 2017). A recent paper has also demonstrated that RFWD3-mediated ubiquitylation of PCNA promotes the recruitment of ZRANB3 to stalled replication forks to facilitate their remodelling and shown that in BRCA2 deficient cells RFWD3 is epistatic with ZRANB3 and restores fork stability when lost (Moore et al., 2023). Since we have shown in the Gibbs-Seymour lab that PCNA ubiquitylation is elevated in ZUP1 KO cells, this may lead to excess ZRANB3 recruitment leading to the increased generation of reversed fork structures that are susceptible to nucleolytic attack. In support of this, unpublished data from a collaborating group has shown using DNA fiber assays that ZUP1 KO cells exhibit a fork degradation phenotype which, notably, is rescued when ZRANB3 is depleted (I.G.-S. personal communication; unpublished). This nucleolytic degradation may therefore be exacerbated in BRCA2 deficient cells leading to the observed synergistic effect between ZUP1 and BRCA2. A potential counter argument to this is a recent study utilising BRCA2 separation of function mutants in which regions corresponding to its fork protection or HR repair are

separately ablated to show that sensitivity to cisplatin and olaparib depends on HR proficiency rather than fork protection proficiency (Lim et al., 2023). In contrast, another study compared BARD1 mutants with intact HR but deficient fork protection to BRCA1 mutants with impaired HR and fork protection, and showed similar sensitivity between the two to MMC, but less significant sensitivity of the BARD1 mutant to Olaparib (Billing et al., 2018). It will be important in future, therefore, to confirm whether ZUP1 sensitivity to different genotoxins is mediated by a fork protection or HR repair defect.

Interestingly, the FAN1 nuclease has also been reported to be recruited to ubiquitylated PCNA following replication fork stalling and to limit DNA synthesis and promote fork stability by a mechanism that is independent of BRCA2 (Porro et al., 2017). Intriguingly, in my CRISPR screen sgRNAs targeting FAN1 were substantially more depleted in WT cells (normZ = -6.03) compared to ZUP1 KO cells (normZ = -2.79), possibly indicating an epistatic interaction with ZUP1 (Figure 31). It would therefore be interesting to investigate this interaction further to validate whether FAN1 and ZUP1 are true epistatic interactors with regard to MMC sensitivity, ssDNA generation, and fork degradation.

5.3.2.2. HELQ and ZUP1 synergistic genetic interaction

The second putative ZUP1 synergistic interaction that I discovered in this thesis is with the HELQ helicase. As described in introductory section 1.1.8.6, HELQ possesses 3' to 5' helicase activity and a ssDNA strand annealing function that promotes repair of ICL lesions by SSA and MMEJ. It has been shown to be recruited to damage sites via RPA and then displace RPA to promote the annealing of complementary sequences to facilitate repair (Jenkins et al., 2021). HELQ also has recently been shown to possess ssDNA annealing functionality that promotes HR and is important for ICL repair

(Anand et al., 2022). The finding in this chapter that concomitant loss of HELQ and ZUP1 exacerbates MMC sensitivity suggests that ZUP1 functions in a parallel pathway to HELQ. Notably, HELQ deficiency leads to some of the same phenotypic consequences as ZUP1 KO, with genetic perturbation of the *HELQ* gene in cells leading to the persistence of RAD51 foci following ICLs induced by MMC (Adelman et al., 2013; Anand et al., 2022). It is possible that HELQ strand annealing activity therefore limits excessive ssDNA at ICL lesions sites. It is plausible, then, that ZUP1 functions in a parallel pathway to limit excessive ssDNA at challenged replication forks and it will be important in future to define ZUP1's complement of functionally interacting proteins that mediate this fork protection capability.

The Durocher lab has previously reported a synergistic interaction between HROB (C17orf53) and HELQ in response to cisplatin-induced ICLs (Hustedt et al., 2019). This study suggested that HROB acts to recruit the MCM8–MCM9 helicase complex to promote D-loop bubble migration during the DNA synthesis step of HR repair, and speculated that HELQ may also promote bubble migration via its 3' to 5' helicase activity. Interestingly, the study also reported that double HROB and HELQ KOs were still viable and retained residual HR activity, indicating the presence of additional pathways that support DNA synthesis during HR. Notably, while a synergistic interaction was seen between ZUP1 and HELQ in my CRISPR screen data, there was no additional sensitivity observed for cells targeted with sgRNA against C17or53/HROB (normZ = -1.91 and -3.42 for KO and WT cells respectively) or MCM8 (normZ = -6.08 and -6.74 respectively) or MCM9 (normZ = -4.41 and -4.15 respectively). These findings therefore leave open the possibility that ZUP1 functions in an epistatic manner to HROB–MCM8–MCM9.

In trying to understand the genetic interaction between ZUP1 and BRCA2 described above, it may be instructive to consider the synthetic lethal interaction between the WRN

helicase and cells with an MMR deficiency (Behan et al., 2019). Deficient MMR leads to microsatellite instability characterised by largescale expansion of nucleotide repeats that distort the secondary structure of DNA and stall replication forks. In these cells, WRN unwinds and processes the secondary structure formations at microsatellite regions to promote physiological DNA transactions (Chan et al., 2019). However, when WRN is lost these structures are susceptible to nucleolytic attack by the MUS81 nuclease that leads to chromosome shattering and cell death (van Wietmarschen et al., 2020). In the future, it will therefore be important to investigate whether aberrant nucleolytic processing occurs by nucleases such as MUS81 in double ZUP1 KOs with loss of the DNA processing factors identified here such as HELQ and BRIP/FANCJ.

5.3.3. Possible reasons why ZUP1 targeting sgRNAs are not depleted in screen performed in WT cells

An aspect of my CRISPR screen data that should be addressed is why ZUP1 targeting sgRNAs are not significantly depleted from the screen performed in WT cells. The normZ score for ZUP1 from the screen performed in WT cells was -0.73, indicative of a mild depletion, but not in line with the hypersensitivity to MMC I have demonstrated for ZUP1 KO cells in Chapter 3. ZUP1 was also not found to be significantly depleted in the previously reported genome-wide CRISPR-Cas9 MMC sensitivity screen that utilised the TKOv3 library (Schubert et al., 2022). A potential explanation for this is that the ZUP1 sgRNAs used in TKOv3 library may not all result in full KO of the ZUP1 protein. The four ZUP1-specific TKOv3 library guides target exon 2, 3, 4, and 7 respectively which would mean that only the sgRNA targeting exon 4 is common to all predicted isoforms as shown in Figure 9 of Chapter 3. The presence of hypomorphic KOs may therefore mean that the true ICL repair dysfunction of ZUP1 KO cells is not revealed

by the guides used in the TKOv3 library. The lack of dropout of ZUP1 in my and previous genome-wide CRISPR screens highlights an important limitation that must be considered for genome-scale CRISPR KO libraries. The design of sgRNAs for these libraries often follows a heuristic approach with rules governing their design such as: 40-70% GC content, no off-target hits with up to two mismatches in sgRNA sequence, no common restriction site sequences, no common SNPs in PAM sequence. In the case of the TKOv3 library this was coupled with a 'sequence score' to identify optimised sequences based on sgRNAs used in previous screens (Hart et al., 2017). While in general this approach yields a specific and robust sgRNA library, it lacks functional characterisation for each sgRNA selected so may not yield complete KO for less well characterised proteins such as ZUP1. I have shown that KO of ZUP1 required extensive empirical determination of the best sgRNA targeting strategy to yield a complete KO of the mRNA and protein due to the presence of additional splice variants, which would not have been achieved by a purely rational design approach using existing genomics databases. To investigate the lack of dropout of TKOv3 guides in future, a two-colour competitive growth assay could be conducted to compare WT cells targeted with the ZUP1 specific sgRNAs from the TKOv3 library with cells targeted with the guides designed as part of this thesis.

5.3.4. Conclusion

In conclusion, this chapter presents the successful use of genome-wide CRISPR screening to identify HELQ and BRCA2 as synergistic interactors of ZUP1 in response to MMC-induced ICL lesions. Coupled with the finding in Chapter 4 that ZUP1 loss results in aberrant generation of ssDNA following MMC-induced damage and consequent disruption of RPA and RAD51 dynamics this data positions ZUP1 as an

important player in the cellular response to replication-coupled DNA damage. The CRISPR screen data I generated also constitutes a valuable resource to deepen our understanding of ICL repair and may inform the design of therapeutic targeting strategies in future by exploiting the novel genetic vulnerabilities I have uncovered.

It will also be important to expand the scope of lesion types that are investigated to determine if the basis for hypersensitivity to the genotoxins tested in Chapter 3 is due to excess formation of ssDNA gaps as observed for MMC treated cells. This will be particularly interesting in the context of the striking sensitivity I observed for ZUP1 KO cells to PARPis given the recent paradigm that is merging that ssDNA gap generation underlies the sensitivity of cells to PARP inhibitors (Cong et al., 2021). Moreover, given the synergistic interaction between ZUP1 and BRCA2 identified in this chapter, it would be useful to create single and double CRISPR-Cas9 knockout cell lines of these genes to analyse epistasis with regard to ssDNA gap generation following PARPi treatment. This could be done in the karyotypically normal RPE-1 $p53^{KO}$ background that has recently been generated by the Gibbs-Seymour lab to determine whether hypersensitivity to genotoxins extends past the aneuploid U2OS background used to generate knockout in this study (I.G.-S. personal communication).

6

Discussion

Contents

6.1. Summary of results

The aim of my thesis was to deepen our understanding of the cellular role of the recently discovered DUB ZUP1. This intriguing protein constitutes a novel class of enzyme which, to date, has a poorly characterised role in the DDR. Prior to this thesis ZUP1 was characterised as having specific DUB activity against long K63-linked Ub chains, it was shown to be recruited to sites of DNA damage, and RNAi-mediated ZUP1 depleted cells were shown to have elevated levels of endogenous DNA damage and to be sensitive to a limited selection of genotoxic agents (Haahr et al., 2018; Hermanns et al., 2018; Hewings et al., 2018; Kwasna et al., 2018). The Gibbs-Seymour lab have subsequently shown that ZUP1 interacts directly with the major ssDNA-binding protein in cells, the RPA complex, and that its K63-linked DUB activity is greatly enhanced upon binding (Foster et al., 2023). Moreover, unpublished data from the lab has demonstrated that in ZUP1 KO cells PCNA polyubiquitylation levels are elevated following MMC treatment (I.G.-S. personal communication; unpublished). However, it remained unclear which DNA repair pathway(s) ZUP1 functioned in and a detailed investigation of the consequences of permanent ZUP1 loss in cells had not been performed, limiting our mechanistic understanding of its function.

In Chapter 3, I generated the first reported full monoclonal U2OS CRISPR-Cas9 ZUP1 knockout cell lines and used a semiquantitative RT-PCR approach to investigate ZUP1 isoform expression to develop an sgRNA targeting strategy to yield loss of all predicted splice variants. I then utilised these cells to reveal that in the absence of ZUP1 cells are hypersensitive to genotoxic agents that cause replication-coupled DNA damage, i.e. agents that cause ICLs, DPCs, or DPC-like lesions, as well as unscheduled origin firing. I also demonstrated that ZUP1 functions downstream, or parallel to, CHK1

and FANCD2 activation and that RPA2 is hyperphosphorylated following ICL lesion damage. These novel phenotypes in ZUP1 KO cells could also be rescued in initial complementation assays with re-expression of ZUP1 WT cDNA, although more work is required to extend this observation. In Chapter 4, using QIBC I discovered that ZUP1 is required to limit ssDNA formation following MMC-induced damage and that RPA and RAD51 accumulate on chromatin in the absence of ZUP1. I also utilised a small molecule inhibitor of the p97/VCP 'segregase' which suggests that ZUP1 may function in an epistatic manner to p97/VCP to promote the removal of RPA from chromatin following MMC-induced damage. I also surprisingly found that knockdown of the E3 ligase RFWD3 in ZUP1 KO cells leads to a synergistic effect on RPA phosphorylation following DNA damage. Together, these findings have provided the first insight into the mechanistic steps at which ZUP1 might function during ICL repair, while further work is required to establish the precise molecular basis for ZUP1's activity in cells. Finally, in Chapter 5, I performed the first genome-wide CRISPR-Cas9 screens to reveal the gene products required for survival in ZUP1 KO cells. These results suggest that ZUP1 KO cells rely on several DNA processing enzymes, TLS factors, and HR factors for survival, indicating that the elevated ssDNA produced in ZUP1 KO cells creates a dependency on these factors. Excitingly, some of these might be therapeutically actionable, for example, the synergistic interaction I identified between BRCA2 and ZUP1 could constitute a novel cancer cell vulnerability that could be exploited by targeting ZUP1 in BRCA2-deficient cancers.

6.2. Model of ZUP1 function in replication-coupled DNA repair

Taken together the results presented in this thesis suggest a role for ZUP1 in the response to replication-coupled DNA damage via a mechanism, or mechanisms, that limit the generation of ssDNA and/or promotes the timely removal of the RPA complex and RAD51 from chromatin. Based on these results I present a hypothetical model of ZUP1 function in replication-coupled DNA repair that details possible roles for ZUP1 in specific pathway steps, as described below. The sections below correspond to the numbered boxes in Figure 36.

6.2.1. ZUP1 may function in RPA phosphorylation ubiquitylation feedforward loop

A first hypothesis for ZUP1's role in replication-coupled DNA repair is that it may regulate the proposed feedforward loop that drives RPA ubiquitylation and phosphorylation described in section 1.3.2 of the Introduction. In this model ubiquitylation of RPA by PRP19 or RFWD3 promotes the recruitment of ATR through its obligate binding partner ATRIP, presumably via an interaction with K63-linked Ub chains on RPA (Marechal et al., 2014). This facilitates phosphorylation of RPA which in turn enhances the recruitment of PRP19 leading to repeated cycles of ubiquitylation and phosphorylation (Dubois et al., 2017). The finding in Chapter 3 of this thesis that RPA2 is hyperphosphorylated in ZUP1 KO cells following MMC damage may therefore suggest that ZUP1 plays a role in regulating the feedforward ubiquitylation phosphorylation loop by limiting RPA ubiquitylation. This is supported by evidence showing that the RPA complex is modified with K63-linked Ub chains in ZUP1 siRNA-

mediated knockdown cells (Hewings et al., 2018). ZUP1 may therefore prevent recruitment and hyperactivation of the ATR-ATRIP complex, limiting RPA complex phosphorylation. As a counter argument against this, I did not observe hyperphosphorylated CHK1 in ZUP1 KO cells in response to MMC damage, suggesting there is not a general hyperactivation of ATR-ATRIP. Analysis of ATR-ATRIP foci is technically challenging, and unfortunately several antibodies failed to detect ATRIP foci. Thus, endogenous tagging or cDNA-mediated over-expression would be required to monitor ATR-ATRIP foci in WT vs ZUP1 KO cells to assess if there is increased chromatin loading of the complex. It's also possible that the proposed feedforward loop is not robust as a model, and that RPA ubiquitylation has a different function. Indeed, chromatin mass spectrometry (CHROMASS) experiments using ICL substrates did not identify PRP19 as a major interactor of damaged chromatin (Gallina et al., 2021; Raschle et al., 2015). Moreover, central to this model, ATR-ATRIP or an interacting partner of the complex needs the ability to bind K63-linked Ub chains. However, evidence for this is currently lacking, and cryo-EM structures of the ATR-ATRIP complex do not reveal an obvious ubiquitin binding motif within the complex (Rao et al., 2018). Whilst the precise role for RPA ubiquitylation and phosphorylation requires further research to be confirmed, it is possible that the dynamics of these PTMs are important for the timely removal of RPA from ssDNA to promote HR repair as proposed by the Inano *et al*. study (Inano et al., 2017).

6.2.2. ZUP1 may regulate replication fork repriming

A second hypothesis, given the excess ssDNA generated in ZUP1 KO cells following MMC-induced ICL lesions, could be that ZUP1 activity may regulate fork repriming by PRIMPOL. PRIMPOL is recruited to sites of replication stress via an interaction through

RPA, so ZUP1 could impact its recruitment by regulating RPA chromatin binding dynamics (Guilliam et al., 2017). Therefore, loss of ZUP1 could lead to unrestrained repriming activity and accumulation of ssDNA gaps which could account for the excess ssDNA and concomitant chromatin-bound RPA2 and RAD51, as shown in Chapter 4. Depletion of PRIMPOL in ZUP1 KO cells would be the next step to assess this hypothesis. Alternatively, replication fork repriming by PRIMPOL has been shown to compete with fork reversal so an opposite explanation is that an increase in fork reversal occurs in the absence of ZUP1, which may reduce repriming activity but generate an excess of reversed fork structures which are susceptible to nucleolytic attack, as discussed below (Quinet et al., 2021). This is supported by the unpublished data from our collaborating group that shows that ZUP1 KO cells exhibit a fork degradation phenotype (I.G.-S. personal communication; unpublished).

6.2.3. ZUP1 may regulate replication fork reversal

A compelling hypothesis is that ZUP1 may regulate the recruitment of the fork remodelling enzyme ZRANB3 by counteracting PCNA K63-linked polyubiquitylation. This mechanism would ensure that excessive reversed fork structures are limited, which may therefore prevent nucleolytic attack. As detailed in discussion section 5.3.2.1 of Chapter 5 this hypothesis may also account for the synergistic interaction of ZUP1 and BRCA2 which provides a protective function to reversed forks, which may consequently be prone to nucleolytic attack when absent. Given the unpublished fork degradation phenotype in ZUP1 KO cells and its rescue by loss of ZRANB3, an important follow-up experiment would be to use the DNA fiber assay to additionally investigate replication fork dynamics in ZUP1 KO cells following loss or SMARCAL1, HLTF, and PRIMPOL to determine if this effect is mediated specifically by ZRANB3. The DNA fiber assay

permits the microscopic visualisation of replication forks at single-molecule resolution by pulse labelling nascent DNA through the incorporation of the thymidine analogues 5-iodo-2′-deoxyuridine (IdU) and 5-chloro-2′-deoxyuridine (CldU) which can be immunostained in different colour channels (Quinet et al., 2017a). By sequentially labelling DNA with IdU and CldU with an intervening genotoxin treatment, the dynamics of forks in response to replication stress can be monitored. This assay will be key to distinguish between the hypotheses detailed here and investigate ZUP1 regulation of fork reversal, repriming, or TLS.

6.2.4. ZUP1 may regulate TLS

ZUP1 may alternatively play a role in the regulation of TLS polymerase or associated factor recruitment by counteracting RFWD3-mediated ubiquitylation at stalled forks. The precise PCNA Ub linkage type that promotes TLS requires further investigation as it has classically been thought that PCNA monoubiquitylation promotes TLS, while polyubiquitylation promotes TS (Mirsanaye et al., 2021). Whilst there is good evidence for this mechanism in yeast, this model has recently been questioned by evidence demonstrating the importance of RFWD3-mediated PCNA polyubiquitylation in *Xenopus* extracts and human cells, with RFWD3 loss causing a TLS defect when a model substrate containing a DNA-protein crosslinks is replicated in *Xenopus* extracts (Gallina et al., 2021). It will therefore be important in the future to investigate if there is a TLS defect in ZUP1 KO cells. One could envisage that hyper PCNA polyubiquitination in ZUP1 KO cells might either impair usage of the correct TLS polymerase by blocking access to the lesion and/or may prolong retention of TLS polymerases, preventing bypass across the lesion and subsequent gap filling. If this were the case, then perhaps PRIMPOL re-primes synthesis, causing a ssDNA gap as described above. Genetic

abrogation of the TLS polymerases in ZUP1 KO cells, either alone or together with PRIMPOL depletion, could therefore be used to start to unravel these potential hypotheses.

6.2.5. ZUP1 may regulate TS

By limiting PCNA polyubiquitylation ZUP1 could also play a role in regulating the TS repair pathway. TS has been cast as an error-free fork restart mechanism as it involves copying genetic information from an in-tact strand and does not require error-prone TLS polymerases. A technique such as REPAIR-Seq could therefore be utilised in future to map the sequence outcomes of targeted DSBs in WT and ZUP1 KO cells to determine if ZUP1 alters the fidelity of repair and therefore provide an insight into which pathway is utilised (Hussmann et al., 2021).

6.2.6. ZUP1 may promote timely removal of RPA and RAD51

A final hypothesis is that ZUP1 may play a role in regulating HR repair by regulating DNA end resection or by promoting the timely removal of ubiquitylated RPA from ssDNA. This latter function has been proposed to be reliant on p97/VCP-mediated extraction from chromatin (Inano et al., 2017). I have shown that there is no additive effect on RPA chromatin loading with p97i treatment in ZUP1 KO cells, which suggests a possible epistatic interaction between ZUP1 and p97/VCP. Although a simplistic model would suggest that RPA polyubiquitylation promotes chromatin-extraction by p97/VCP and therefore ZUP1 would limit extraction, it may be that more complex branched or mixed chain architectures are involved and ZUP1 DUB activity does not merely function as a binary negative regulator. Alternatively, the timing of deubiquitylation may be important for efficient RPA removal and HR progression. Given ZUP1's potential impact

on HR efficiency, another critical area for future experiments will be to functionally assess the impact of ZUP1 loss on DDR pathway choice using reporter assays for specific repair pathways. Fluorescent reporter constructs have been designed for the main pathways of DSB repair (NHEJ, HR, SSA, MMEJ) whereby a disrupted fluorescent protein sequence is reconstituted if a specific repair pathway is used by cells (van de Kooij and van Attikum, 2021). The reporter constructs for these pathways could therefore be transfected into WT and ZUP1 KO cells and the fluorescence output measured to determine the efficiency of each repair pathway and whether it is impacted by loss of ZUP1.

Overall, the data presented in this thesis significantly advances our understanding of ZUP1 in the DDR and forms the foundation for future approaches to further delineate the mechanisms of its functions in cells.

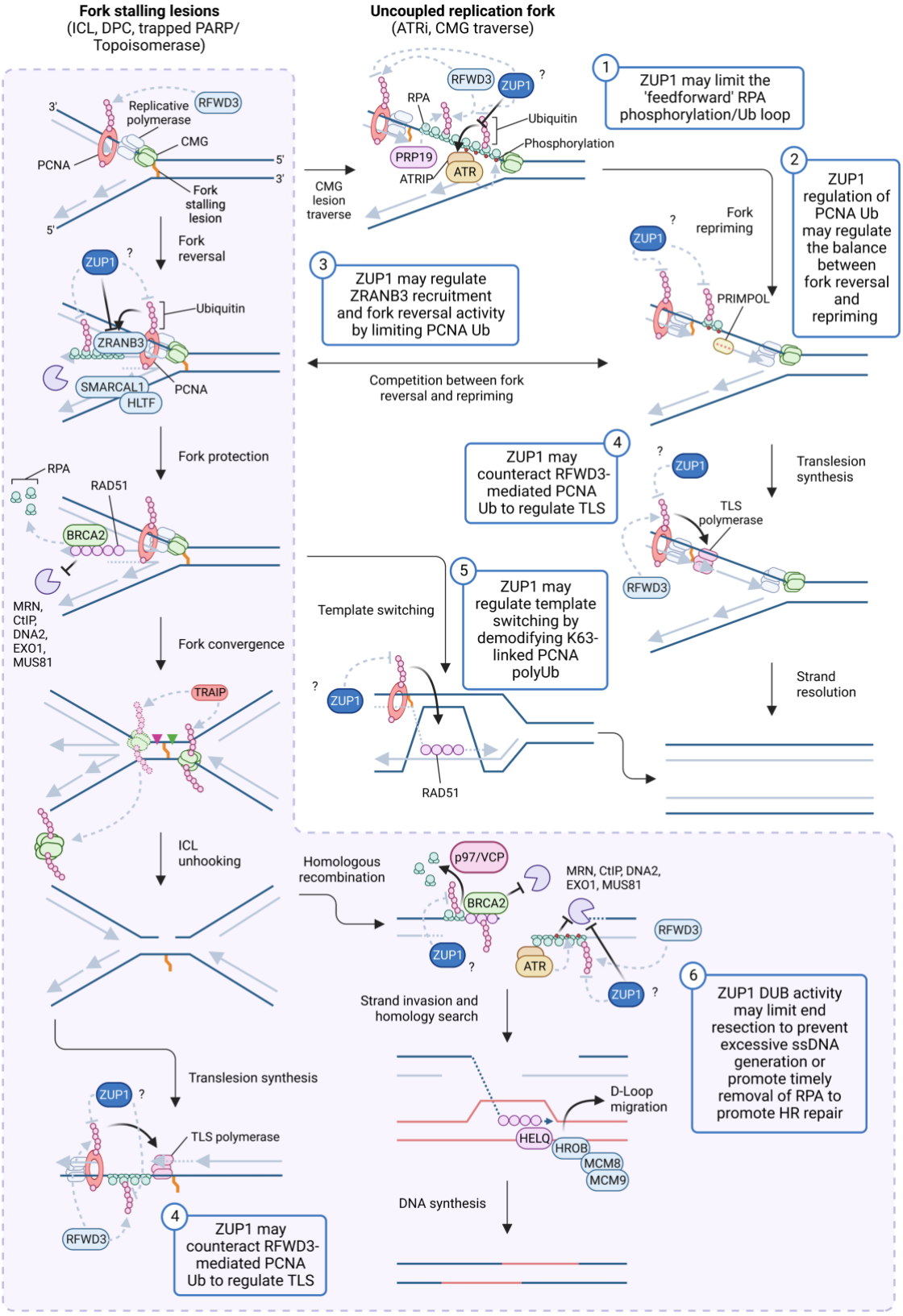
Fork stalling lesions
(ICL, DPC, trapped PARP/ Topoisomerase)
Uncoupled replication fork
(ATRi, CMG traverse)
Replicative polymerase
RFWD3
CMG
PCNA
Fork stalling lesion
Fork reversal
ZUP1
Ubiquitin
ZRANB3
SMARCAL1
HLTF
PCNA
Fork protection
RPA
RAD51
BRCA2
MRN, CtIP, DNA2, EXO1, MUS81
Fork convergence
TRAIP
ICL unhooking
Translesion synthesis
TLS polymerase
RFWD3
4
ZUP1 may counteract RFWD3-mediated PCNA Ub to regulate TLS
CMG lesion traverse
RPA
Ubiquitin
Phosphorylation
PRP19
ATRIP
ATR
1
ZUP1 may limit the 'feedforward' RPA phosphorylation/Ub loop
2
ZUP1 regulation of PCNA Ub may regulate the balance between fork reversal and repriming
Fork repriming
PRIMPOL
3
ZUP1 may regulate ZRANB3 recruitment and fork reversal activity by limiting PCNA Ub
Competition between fork reversal and repriming
Translesion synthesis
TLS polymerase
Template switching
5
ZUP1 may regulate template switching by demodifying K63-linked PCNA polyUb
Strand resolution
Homologous recombination
p97/VCP
BRCA2
MRN, CtIP, DNA2, EXO1, MUS81
Strand invasion and homology search
D-Loop migration
HELQ
HROB
MCM8
MCM9
DNA synthesis
6
ZUP1 DUB activity may limit end resection to prevent excessive ssDNA generation or promote timely removal of RPA to promote HR repair

Figure 36. Model for ZUP1 function in replication-coupled DNA damage repair

Figure depicts potential steps in which ZUP1 may play a role in the repair of replication-associated DNA damage. The pathways depicted represent some of the key factors but do not show all steps and factors involved. The pathway contained in the purple box broadly corresponds to the steps of the FA pathway of ICL repair while the other steps pictured correspond to other steps in the response to fork uncoupling lesions in which ZUP1 may function. The numbered blue boxes suggest steps in which ZUP1 activity may play a role based on the data produced in this thesis. Figure created using BioRender.com

References

1. Acharya, S., T. Wilson, S. Gradia, M.F. Kane, S. Guerrette, G.T. Marsischky, R. Kolodner, and R. Fishel. (1996). hMSH2 forms specific mispair-binding complexes with hMSH3 and hMSH6. *Proc Natl Acad Sci U S A*. 93:13629-13634.
2. Adam, S., S.E. Rossi, N. Moatti, M. De Marco Zompit, Y. Xue, T.F. Ng, A. Alvarez-Quilon, J. Desjardins, V. Bhaskaran, G. Martino, D. Setiaputra, S.M. Noordermeer, T.K. Ohsumi, N. Hustedt, R.K. Szilard, N. Chaudhary, M. Munro, A. Veloso, H. Melo, S.Y. Yin, R. Papp, J.T.F. Young, M. Zinda, M. Stucki, and D. Durocher. (2021). The CIP2A-TOPBP1 axis safeguards chromosome stability and is a synthetic lethal target for BRCA-mutated cancer. *Nat Cancer*. 2:1357-1371.
3. Adamson, B., A. Smogorzewska, F.D. Sigoillot, R.W. King, and S.J. Elledge. (2012). A genome-wide homologous recombination screen identifies the RNA-binding protein RBMX as a component of the DNA-damage response. *Nat Cell Biol*. 14:318-328.
4. Adelman, C.A., R.L. Lolo, N.J. Birkbak, O. Murina, K. Matsuzaki, Z. Horejsi, K. Parmar, V. Borel, J.M. Skehel, G. Stamp, A. D'Andrea, A.A. Sartori, C. Swanton, and S.J. Boulton. (2013). HELQ promotes RAD51 paralogue-dependent repair to avert germ cell loss and tumorigenesis. *Nature*. 502:381-384.
5. Ahel, I., U. Rass, S.F. El-Khamisy, S. Katyal, P.M. Clements, P.J. McKinnon, K.W. Caldecott, and S.C. West. (2006). The neurodegenerative disease protein aprataxin resolves abortive DNA ligation intermediates. *Nature*. 443:713-716.
6. Ahnesorg, P., P. Smith, and S.P. Jackson. (2006). XLF interacts with the XRCC4-DNA ligase IV complex to promote DNA nonhomologous end-joining. *Cell*. 124:301-313.
7. Al-Minawi, A.Z., N. Saleh-Gohari, and T. Helleday. (2008). The ERCC1/XPF endonuclease is required for efficient single-strand annealing and gene conversion in mammalian cells. *Nucleic Acids Res*. 36:1-9.
8. Alcon, P., S. Shakeel, Z.A. Chen, J. Rappsilber, K.J. Patel, and L.A. Passmore. (2020). FANCD2-FANCI is a clamp stabilized on DNA by monoubiquitination of FANCD2 during DNA repair. *Nat Struct Mol Biol*. 27:240-248.
9. Alpi, A.F., P.E. Pace, M.M. Babu, and K.J. Patel. (2008). Mechanistic insight into site-restricted monoubiquitination of FANCD2 by Ube2t, FANCL, and FANCI. *Mol Cell*. 32:767-777.
10. Alvarez-Quilon, A., J.L. Wojtaszek, M.C. Mathieu, T. Patel, C.D. Appel, N. Hustedt, S.E. Rossi, B.D. Wallace, D. Setiaputra, S. Adam, Y. Ohashi, H. Melo, T. Cho, C. Gervais, I.M. Munoz, E. Grazzini, J.T.F. Young, J. Rouse, M. Zinda, R.S. Williams, and D. Durocher. (2020). Endogenous DNA 3' blocks are vulnerabilities for BRCA1 and BRCA2 deficiency and are reversed by the APE2 nuclease. *Mol Cell*. 78:1152-1165 e1158.
11. Amunugama, R., S. Willcox, R.A. Wu, U.B. Abdullah, A.H. El-Sagheer, T. Brown, P.J. McHugh, J.D. Griffith, and J.C. Walter. (2018). Replication fork reversal during DNA interstrand crosslink repair requires CMG unloading. *Cell Rep*. 23:3419-3428.
12. Anand, R., E. Buechelmaier, O. Belan, M. Newton, A. Vancevska, A. Kaczmarczyk, T. Takaki, D.S. Rueda, S.N. Powell, and S.J. Boulton. (2022). HELQ is a dual-function DSB repair enzyme modulated by RPA and RAD51. *Nature*. 601:268-273.

13. Anantha, R.W., V.M. Vassin, and J.A. Borowiec. (2007). Sequential and synergistic modification of human RPA stimulates chromosomal DNA repair. *J Biol Chem*. 282:35910-35923.

14. Arana, M.E., M. Seki, R.D. Wood, I.B. Rogozin, and T.A. Kunkel. (2008). Low-fidelity DNA synthesis by human DNA polymerase theta. *Nucleic Acids Res*. 36:3847-3856.

15. Aregger, M., M. Chandrashekhar, A.H.Y. Tong, K. Chan, and J. Moffat. (2019). Pooled lentiviral CRISPR-Cas9 screens for functional genomics in mammalian cells. *Methods Mol Biol*. 1869:169-188.

16. Ashley, A.K., M. Shrivastav, J. Nie, C. Amerin, K. Troksa, J.G. Glanzer, S. Liu, S.O. Opiyo, D.D. Dimitrova, P. Le, B. Sishc, S.M. Bailey, G.G. Oakley, and J.A. Nickoloff. (2014). DNA-PK phosphorylation of RPA32 Ser4/Ser8 regulates replication stress checkpoint activation, fork restart, homologous recombination and mitotic catastrophe. *DNA Repair (Amst)*. 21:131-139.

17. Audebert, M., B. Salles, and P. Calsou. (2004). Involvement of poly(ADP-ribose) polymerase-1 and XRCC1/DNA ligase III in an alternative route for DNA double-strand breaks rejoining. *J Biol Chem*. 279:55117-55126.

18. Awwad, S.W., A. Serrano-Benitez, J.C. Thomas, V. Gupta, and S.P. Jackson. (2023). Revolutionizing DNA repair research and cancer therapy with CRISPR-Cas screens. *Nat Rev Mol Cell Biol*.

19. Bai, G., C. Kermi, H. Stoy, C.J. Schiltz, J. Bacal, A.M. Zaino, M.K. Hadden, B.F. Eichman, M. Lopes, and K.A. Cimprich. (2020). HLTF promotes fork reversal, limiting replication stress resistance and preventing multiple mechanisms of unrestrained DNA synthesis. *Mol Cell*. 78:1237-1251 e1237.

20. Balmus, G., A.C. Barros, P.W. Wijnhoven, C. Lescale, H.L. Hasse, K. Boroviak, C. le Sage, B. Doe, A.O. Speak, A. Galli, M. Jacobsen, L. Deriano, D.J. Adams, A.N. Blackford, and S.P. Jackson. (2016). Synthetic lethality between PAXX and XLF in mammalian development. *Genes Dev*. 30:2152-2157.

21. Balmus, G., D. Pilger, J. Coates, M. Demir, M. Sczaniecka-Clift, A.C. Barros, M. Woods, B. Fu, F. Yang, E. Chen, M. Ostermaier, T. Stankovic, H. Ponstingl, M. Herzog, K. Yusa, F.M. Martinez, S.T. Durant, Y. Galanty, P. Beli, D.J. Adams, A. Bradley, E. Metzakopian, J.V. Forment, and S.P. Jackson. (2019). ATM orchestrates the DNA-damage response to counter toxic non-homologous end-joining at broken replication forks. *Nat Commun*. 10:87.

22. Barker, S., M. Weinfeld, and D. Murray. (2005). DNA-protein crosslinks: their induction, repair, and biological consequences. *Mutat Res*. 589:111-135.

23. Barrangou, R., C. Fremaux, H. Deveau, M. Richards, P. Boyaval, S. Moineau, D.A. Romero, and P. Horvath. (2007). CRISPR provides acquired resistance against viruses in prokaryotes. *Science*. 315:1709-1712.

24. Bass, T.E., J.W. Luzwick, G. Kavanaugh, C. Carroll, H. Dungrawala, G.G. Glick, M.D. Feldkamp, R. Putney, W.J. Chazin, and D. Cortez. (2016). ETAA1 acts at stalled replication forks to maintain genome integrity. *Nat Cell Biol*. 18:1185-1195.

25. Beard, W.A., J.K. Horton, R. Prasad, and S.H. Wilson. (2019). Eukaryotic base excision repair: New approaches shine light on mechanism. *Annu Rev Biochem*. 88:137-162.

26. Becker, J.R., G. Clifford, C. Bonnet, A. Groth, M.D. Wilson, and J.R. Chapman. (2021). BARD1 reads H2A lysine 15 ubiquitination to direct homologous recombination. *Nature*. 596:433-437.

27. Behan, F.M., F. Iorio, G. Picco, E. Goncalves, C.M. Beaver, G. Migliardi, R. Santos, Y. Rao, F. Sassi, M. Pinnelli, R. Ansari, S. Harper, D.A. Jackson, R. McRae, R. Pooley, P. Wilkinson, D. van der Meer, D. Dow, C. Buser-Doepner, A. Bertotti, L. Trusolino, E.A.

Stronach, J. Saez-Rodriguez, K. Yusa, and M.J. Garnett. (2019). Prioritization of cancer therapeutic targets using CRISPR-Cas9 screens. *Nature*. 568:511-516.

28. Bennardo, N., A. Cheng, N. Huang, and J.M. Stark. (2008). Alternative-NHEJ is a mechanistically distinct pathway of mammalian chromosome break repair. *PLoS Genet*. 4:e1000110.

29. Benson, F.E., A. Stasiak, and S.C. West. (1994). Purification and characterization of the human Rad51 protein, an analogue of E. coli RecA. *EMBO J*. 13:5764-5771.

30. Berti, M., D. Cortez, and M. Lopes. (2020). The plasticity of DNA replication forks in response to clinically relevant genotoxic stress. *Nat Rev Mol Cell Biol*. 21:633-651.

31. Berti, M., A. Ray Chaudhuri, S. Thangavel, S. Gomathinayagam, S. Kenig, M. Vujanovic, F. Odreman, T. Glatter, S. Graziano, R. Mendoza-Maldonado, F. Marino, B. Lucic, V. Biasin, M. Gstaiger, R. Aebersold, J.M. Sidorova, R.J. Monnat, Jr., M. Lopes, and A. Vindigni. (2013). Human RECQ1 promotes restart of replication forks reversed by DNA topoisomerase I inhibition. *Nat Struct Mol Biol*. 20:347-354.

32. Betermier, M., P. Bertrand, and B.S. Lopez. (2014). Is non-homologous end-joining really an inherently error-prone process? *PLoS Genet*. 10:e1004086.

33. Beucher, A., J. Birraux, L. Tchouandong, O. Barton, A. Shibata, S. Conrad, A.A. Goodarzi, A. Krempler, P.A. Jeggo, and M. Lobrich. (2009). ATM and Artemis promote homologous recombination of radiation-induced DNA double-strand breaks in G2. *EMBO J*. 28:3413-3427.

34. Bhargava, R., D.O. Onyango, and J.M. Stark. (2016). Regulation of single-strand annealing and its role in genome maintenance. *Trends Genet*. 32:566-575.

35. Bhat, K.P., R. Betous, and D. Cortez. (2015). High-affinity DNA-binding domains of replication protein A (RPA) direct SMARCAL1-dependent replication fork remodeling. *J Biol Chem*. 290:4110-4117.

36. Bhat, K.P., and D. Cortez. (2018). RPA and RAD51: fork reversal, fork protection, and genome stability. *Nat Struct Mol Biol*. 25:446-453.

37. Bianchi, J., S.G. Rudd, S.K. Jozwiakowski, L.J. Bailey, V. Soura, E. Taylor, I. Stevanovic, A.J. Green, T.H. Stracker, H.D. Lindsay, and A.J. Doherty. (2013). PrimPol bypasses UV photoproducts during eukaryotic chromosomal DNA replication. *Mol Cell*. 52:566-573.

38. Billing, D., M. Horiguchi, F. Wu-Baer, A. Taglialatela, G. Leuzzi, S.A. Nanez, W. Jiang, S. Zha, M. Szabolcs, C.S. Lin, A. Ciccia, and R. Baer. (2018). The BRCT domains of the BRCA1 and BARD1 tumor suppressors differentially regulate homology-directed repair and stalled fork protection. *Mol Cell*. 72:127-139 e128.

39. Bizard, A.H., and I.D. Hickson. (2014). The dissolution of double Holliday junctions. *Cold Spring Harb Perspect Biol*. 6:a016477.

40. Blackford, A.N., and M. Stucki. (2020). How cells respond to DNA breaks in mitosis. *Trends Biochem Sci*. 45:321-331.

41. Block, W.D., Y. Yu, and S.P. Lees-Miller. (2004). Phosphatidyl inositol 3-kinase-like serine/threonine protein kinases (PIKKs) are required for DNA damage-induced phosphorylation of the 32 kDa subunit of replication protein A at threonine 21. *Nucleic Acids Res*. 32:997-1005.

42. Bock, C., P. Datlinger, F. Chardon, M.A. Coelho, M.T.B. Dong, K.A. Lawson, T. Lu, L. Maroc, T.M. Norman, B.A. Song, G. Stanley, S.D. Chen, M. Garnett, W. Li, J. Moffat, L.S. Qi, R.S. Shapiro, J. Shendure, J.S. Weissman, and X.W. Zhuang. (2022). High-content CRISPR screening. *Nature Reviews Methods Primers*. 2.

43. Bodapati, S., T.P. Daley, X. Lin, J. Zou, and L.S. Qi. (2020). A benchmark of algorithms for the analysis of pooled CRISPR screens. *Genome Biol*. 21:62.

44. Boettcher, M., and M.T. McManus. (2015). Choosing the right tool for the job: RNAi, TALEN, or CRISPR. *Mol Cell*. 58:575-585.

45. Bondeson, D.P., Z. Mullin-Bernstein, S. Oliver, T.A. Skipper, T.C. Atack, N. Bick, M. Ching, A.A. Guirguis, J. Kwon, C. Langan, D. Millson, B.R. Paolella, K. Tran, S.J. Wie, F. Vazquez, Z. Tothova, T.R. Golub, W.R. Sellers, and A. Ianari. (2022). Systematic profiling of conditional degron tag technologies for target validation studies. *Nat Commun*. 13:5495.

46. Botuyan, M.V., J. Lee, I.M. Ward, J.E. Kim, J.R. Thompson, J. Chen, and G. Mer. (2006). Structural basis for the methylation state-specific recognition of histone H4-K20 by 53BP1 and Crb2 in DNA repair. *Cell*. 127:1361-1373.

47. Boutros, M., and J. Ahringer. (2008). The art and design of genetic screens: RNA interference. *Nat Rev Genet*. 9:554-566.

48. Boutros, R., C. Dozier, and B. Ducommun. (2006). The when and wheres of CDC25 phosphatases. *Curr Opin Cell Biol*. 18:185-191.

49. Bowden, A.R., D.A. Morales-Juarez, M. Sczaniecka-Clift, M.M. Agudo, N. Lukashchuk, J.C. Thomas, and S.P. Jackson. (2020). Parallel CRISPR-Cas9 screens clarify impacts of p53 on screen performance. *Elife*. 9.

50. Branzei, D., and B. Szakal. (2016). DNA damage tolerance by recombination: Molecular pathways and DNA structures. *DNA Repair (Amst)*. 44:68-75.

51. Breslin, C., and K.W. Caldecott. (2009). DNA 3'-phosphatase activity is critical for rapid global rates of single-strand break repair following oxidative stress. *Mol Cell Biol*. 29:4653-4662.

52. Breslin, C., P. Hornyak, A. Ridley, S.L. Rulten, H. Hanzlikova, A.W. Oliver, and K.W. Caldecott. (2015). The XRCC1 phosphate-binding pocket binds poly (ADP-ribose) and is required for XRCC1 function. *Nucleic Acids Res*. 43:6934-6944.

53. Brown, E.J., and D. Baltimore. (2000). ATR disruption leads to chromosomal fragmentation and early embryonic lethality. *Genes Dev*. 14:397-402.

54. Budzowska, M., T.G. Graham, A. Sobeck, S. Waga, and J.C. Walter. (2015). Regulation of the Rev1-pol zeta complex during bypass of a DNA interstrand cross-link. *EMBO J*. 34:1971-1985.

55. Byrne, B.M., and G.G. Oakley. (2019). Replication protein A, the laxative that keeps DNA regular: The importance of RPA phosphorylation in maintaining genome stability. *Semin Cell Dev Biol*. 86:112-120.

56. Byun, T.S., M. Pacek, M.C. Yee, J.C. Walter, and K.A. Cimprich. (2005). Functional uncoupling of MCM helicase and DNA polymerase activities activates the ATR-dependent checkpoint. *Genes Dev*. 19:1040-1052.

57. Caldecott, K.W. (2008). Single-strand break repair and genetic disease. *Nat Rev Genet*. 9:619-631.

58. Caldecott, K.W. (2014). DNA single-strand break repair. *Exp Cell Res*. 329:2-8.

59. Caldecott, K.W. (2020). Mammalian DNA base excision repair: Dancing in the moonlight. *DNA Repair (Amst)*. 93:102921.

60. Caldecott, K.W. (2022). DNA single-strand break repair and human genetic disease. *Trends Cell Biol*. 32:733-745.

61. Cappelli, E., R. Taylor, M. Cevasco, A. Abbondandolo, K. Caldecott, and G. Frosina. (1997). Involvement of XRCC1 and DNA ligase III gene products in DNA base excision repair. *J Biol Chem*. 272:23970-23975.

62. Carley, A.C., M. Jalan, S. Subramanyam, R. Roy, G.E.O. Borgstahl, and S.N. Powell. (2022). Replication protein A phosphorylation facilitates RAD52-dependent homologous recombination in BRCA-deficient cells. *Mol Cell Biol*. 42:e0052421.

63. Carroll, D. (2011). Genome engineering with zinc-finger nucleases. *Genetics*. 188:773-782.

64. Carvajal-Garcia, J., J.E. Cho, P. Carvajal-Garcia, W. Feng, R.D. Wood, J. Sekelsky, G.P. Gupta, S.A. Roberts, and D.A. Ramsden. (2020). Mechanistic basis for microhomology identification and genome scarring by polymerase theta. *Proc Natl Acad Sci U S A*. 117:8476-8485.

65. Ceccaldi, R., P. Sarangi, and A.D. D'Andrea. (2016). The Fanconi anaemia pathway: new players and new functions. *Nat Rev Mol Cell Biol*. 17:337-349.

66. Cejka, P., and L.S. Symington. (2021). DNA End Resection: Mechanism and Control. *Annu Rev Genet*. 55:285-307.

67. Champoux, J.J. (2001). DNA topoisomerases: structure, function, and mechanism. *Annu Rev Biochem*. 70:369-413.

68. Chan, E.M., T. Shibue, J.M. McFarland, B. Gaeta, M. Ghandi, N. Dumont, A. Gonzalez, J.S. McPartlan, T. Li, Y. Zhang, J. Bin Liu, J.B. Lazaro, P. Gu, C.G. Piett, A. Apffel, S.O. Ali, R. Deasy, P. Keskula, R.W.S. Ng, E.A. Roberts, E. Reznichenko, L. Leung, M. Alimova, M. Schenone, M. Islam, Y.E. Maruvka, Y. Liu, J. Roper, S. Raghavan, M. Giannakis, Y.Y. Tseng, Z.D. Nagel, A. D'Andrea, D.E. Root, J.S. Boehm, G. Getz, S. Chang, T.R. Golub, A. Tsherniak, F. Vazquez, and A.J. Bass. (2019). WRN helicase is a synthetic lethal target in microsatellite unstable cancers. *Nature*. 568:551-556.

69. Chanut, P., S. Britton, J. Coates, S.P. Jackson, and P. Calsou. (2016). Coordinated nuclease activities counteract Ku at single-ended DNA double-strand breaks. *Nat Commun*. 7:12889.

70. Chen, C.C., W. Feng, P.X. Lim, E.M. Kass, and M. Jasin. (2018). Homology-directed repair and the role of BRCA1, BRCA2, and related proteins in genome integrity and cancer. *Annu Rev Cancer Biol*. 2:313-336.

71. Chen, S.H., N.L. Chan, and T.S. Hsieh. (2013). New mechanistic and functional insights into DNA topoisomerases. *Annu Rev Biochem*. 82:139-170.

72. Chen, X., Y. Velmurugu, G. Zheng, B. Park, Y. Shim, Y. Kim, L. Liu, B. Van Houten, C. He, A. Ansari, and J.H. Min. (2015). Kinetic gating mechanism of DNA damage recognition by Rad4/XPC. *Nat Commun*. 6:5849.

73. Chen, Z.J., and L.J. Sun. (2009). Nonproteolytic functions of ubiquitin in cell signaling. *Mol Cell*. 33:275-286.

74. Chiu, R.K., J. Brun, C. Ramaekers, J. Theys, L. Weng, P. Lambin, D.A. Gray, and B.G. Wouters. (2006). Lysine 63-polyubiquitination guards against translesion synthesis-induced mutations. *PLoS Genet*. 2:e116.

75. Choe, K.N., and G.L. Moldovan. (2017). Forging ahead through darkness: PCNA, still the principal conductor at the replication fork. *Mol Cell*. 65:380-392.

76. Chung, W.H., Z. Zhu, A. Papusha, A. Malkova, and G. Ira. (2010). Defective resection at DNA double-strand breaks leads to de novo telomere formation and enhances gene targeting. *PLoS Genet*. 6:e1000948.

77. Chvalova, K., V. Brabec, and J. Kasparkova. (2007). Mechanism of the formation of DNA-protein cross-links by antitumor cisplatin. *Nucleic Acids Res*. 35:1812-1821.

78. Ciccia, A., and S.J. Elledge. (2010). The DNA damage response: making it safe to play with knives. *Mol Cell*. 40:179-204.

79. Ciccia, A., A.V. Nimonkar, Y. Hu, I. Hajdu, Y.J. Achar, L. Izhar, S.A. Petit, B. Adamson, J.C. Yoon, S.C. Kowalczykowski, D.M. Livingston, L. Haracska, and S.J. Elledge. (2012). Polyubiquitinated PCNA recruits the ZRANB3 translocase to maintain genomic integrity after replication stress. *Mol Cell*. 47:396-409.

80. Clague, M.J., S. Urbe, and D. Komander. (2019). Breaking the chains: deubiquitylating enzyme specificity begets function. *Nat Rev Mol Cell Biol*. 20:338-352.

81. Clausen, A.R., S. Zhang, P.M. Burgers, M.Y. Lee, and T.A. Kunkel. (2013). Ribonucleotide incorporation, proofreading and bypass by human DNA polymerase delta. *DNA Repair (Amst)*. 12:121-127.

82. Colic, M., G. Wang, M. Zimmermann, K. Mascall, M. McLaughlin, L. Bertolet, W.F. Lenoir, J. Moffat, S. Angers, D. Durocher, and T. Hart. (2019). Identifying chemogenetic interactions from CRISPR screens with drugZ. *Genome Med*. 11:52.

83. Concordet, J.P., and M. Haeussler. (2018). CRISPOR: intuitive guide selection for CRISPR/Cas9 genome editing experiments and screens. *Nucleic Acids Res*. 46:W242-W245.

84. Cong, K., M. Peng, A.N. Kousholt, W.T.C. Lee, S. Lee, S. Nayak, J. Krais, P.S. VanderVere-Carozza, K.S. Pawelczak, J. Calvo, N.J. Panzarino, J.J. Turchi, N. Johnson, J. Jonkers, E. Rothenberg, and S.B. Cantor. (2021). Replication gaps are a key determinant of PARP inhibitor synthetic lethality with BRCA deficiency. *Mol Cell*. 81:3128-3144 e3127.

85. Cong, L., F.A. Ran, D. Cox, S. Lin, R. Barretto, N. Habib, P.D. Hsu, X. Wu, W. Jiang, L.A. Marraffini, and F. Zhang. (2013). Multiplex genome engineering using CRISPR/Cas systems. *Science*. 339:819-823.

86. Cortes Ledesma, F., S.F. El Khamisy, M.C. Zuma, K. Osborn, and K.W. Caldecott. (2009). A human 5'-tyrosyl DNA phosphodiesterase that repairs topoisomerase-mediated DNA damage. *Nature*. 461:674-678.

87. Cortez, D. (2019). Replication-Coupled DNA Repair. *Mol Cell*. 74:866-876.

88. Couch, F.B., C.E. Bansbach, R. Driscoll, J.W. Luzwick, G.G. Glick, R. Betous, C.M. Carroll, S.Y. Jung, J. Qin, K.A. Cimprich, and D. Cortez. (2013). ATR phosphorylates SMARCAL1 to prevent replication fork collapse. *Genes Dev*. 27:1610-1623.

89. Critchlow, S.E., R.P. Bowater, and S.P. Jackson. (1997). Mammalian DNA double-strand break repair protein XRCC4 interacts with DNA ligase IV. *Curr Biol*. 7:588-598.

90. Cunningham, F., J.E. Allen, J. Allen, J. Alvarez-Jarreta, M.R. Amode, I.M. Armean, O. Austine-Orimoloye, A.G. Azov, I. Barnes, R. Bennett, A. Berry, J. Bhai, A. Bignell, K. Billis, S. Boddu, L. Brooks, M. Charkhchi, C. Cummins, L. Da Rin Fioretto, C. Davidson, K. Dodiya, S. Donaldson, B. El Houdaigui, T. El Naboulsi, R. Fatima, C.G. Giron, T. Genez, J.G. Martinez, C. Guijarro-Clarke, A. Gymer, M. Hardy, Z. Hollis, T. Hourlier, T. Hunt, T. Juettemann, V. Kaikala, M. Kay, I. Lavidas, T. Le, D. Lemos, J.C. Marugan, S. Mohanan, A. Mushtaq, M. Naven, D.N. Ogeh, A. Parker, A. Parton, M. Perry, I. Pilizota, I. Prosovetskaia, M.P. Sakthivel, A.I.A. Salam, B.M. Schmitt, H. Schuilenburg, D. Sheppard, J.G. Perez-Silva, W. Stark, E. Steed, K. Sutinen, R. Sukumaran, D. Sumathipala, M.M. Suner, M. Szpak, A. Thormann, F.F. Tricomi, D. Urbina-Gomez, A. Veidenberg, T.A. Walsh, B. Walts, N. Willhoft, A. Winterbottom, E. Wass, M. Chakiachvili, B. Flint, A. Frankish, S. Giorgetti, L. Haggerty, S.E. Hunt, I.I. GR, J.E. Loveland, F.J. Martin, B. Moore, J.M. Mudge, M. Muffato, E. Perry, M. Ruffier, J. Tate, D. Thybert, S.J. Trevanion, S. Dyer, P.W. Harrison, K.L. Howe, A.D. Yates, D.R. Zerbino, and P. Flicek. (2022). Ensembl 2022. *Nucleic Acids Res*. 50:D988-D995.

91. Curtin, N.J. (2012). DNA repair dysregulation from cancer driver to therapeutic target. *Nat Rev Cancer*. 12:801-817.

92. Cybulla, E., and A. Vindigni. (2023). Leveraging the replication stress response to optimize cancer therapy. *Nat Rev Cancer*. 23:6-24.

93. D'Angiolella, V., V. Donato, F.M. Forrester, Y.T. Jeong, C. Pellacani, Y. Kudo, A. Saraf, L. Florens, M.P. Washburn, and M. Pagano. (2012). Cyclin F-mediated degradation of ribonucleotide reductase M2 controls genome integrity and DNA repair. *Cell*. 149:1023-1034.

94. Dantuma, N.P., and H. van Attikum. (2016). Spatiotemporal regulation of posttranslational modifications in the DNA damage response. *EMBO J*. 35:6-23.

95. Davidovic, L., M. Vodenicharov, E.B. Affar, and G.G. Poirier. (2001). Importance of poly(ADP-ribose) glycohydrolase in the control of poly(ADP-ribose) metabolism. *Exp Cell Res*. 268:7-13.

96. Davies, A.A., D. Huttner, Y. Daigaku, S. Chen, and H.D. Ulrich. (2008). Activation of ubiquitin-dependent DNA damage bypass is mediated by replication protein a. *Mol Cell*. 29:625-636.

97. de Laat, W.L., E. Appeldoorn, K. Sugasawa, E. Weterings, N.G. Jaspers, and J.H. Hoeijmakers. (1998). DNA-binding polarity of human replication protein A positions nucleases in nucleotide excision repair. *Genes Dev*. 12:2598-2609.

98. De Marco Zompit, M., M.T. Esteban, C. Mooser, S. Adam, S.E. Rossi, A. Jeanrenaud, P.A. Leimbacher, D. Fink, A.K. Shorrocks, A.N. Blackford, D. Durocher, and M. Stucki. (2022). The CIP2A-TOPBP1 complex safeguards chromosomal stability during mitosis. *Nat Commun*. 13:4143.

99. de Murcia, G., A. Huletsky, D. Lamarre, A. Gaudreau, J. Pouyet, M. Daune, and G.G. Poirier. (1986). Modulation of chromatin superstructure induced by poly(ADP-ribose) synthesis and degradation. *J Biol Chem*. 261:7011-7017.

100. Deans, A.J., and S.C. West. (2009). FANCM connects the genome instability disorders Bloom's Syndrome and Fanconi Anemia. *Mol Cell*. 36:943-953.

101. Deans, A.J., and S.C. West. (2011). DNA interstrand crosslink repair and cancer. *Nat Rev Cancer*. 11:467-480.

102. Deem, A., A. Keszthelyi, T. Blackgrove, A. Vayl, B. Coffey, R. Mathur, A. Chabes, and A. Malkova. (2011). Break-induced replication is highly inaccurate. *PLoS Biol*. 9:e1000594.

103. Delacroix, S., J.M. Wagner, M. Kobayashi, K. Yamamoto, and L.M. Karnitz. (2007). The Rad9-Hus1-Rad1 (9-1-1) clamp activates checkpoint signaling via TopBP1. *Genes Dev*. 21:1472-1477.

104. Demin, A.A., K. Hirota, M. Tsuda, M. Adamowicz, R. Hailstone, J. Brazina, W. Gittens, I. Kalasova, Z. Shao, S. Zha, H. Sasanuma, H. Hanzlikova, S. Takeda, and K.W. Caldecott. (2021). XRCC1 prevents toxic PARP1 trapping during DNA base excision repair. *Mol Cell*. 81:3018-3030 e3015.

105. Demple, B., and L. Harrison. (1994). Repair of oxidative damage to DNA: enzymology and biology. *Annu Rev Biochem*. 63:915-948.

106. Deng, S.K., H. Chen, and L.S. Symington. (2015). Replication protein A prevents promiscuous annealing between short sequence homologies: Implications for genome integrity. *Bioessays*. 37:305-313.

107. Deshpande, R.A., J.H. Lee, S. Arora, and T.T. Paull. (2016). Nbs1 converts the human Mre11/Rad50 nuclease complex into an endo/exonuclease machine specific for protein-DNA adducts. *Mol Cell*. 64:593-606.

108. Dewar, J.M., E. Low, M. Mann, M. Raschle, and J.C. Walter. (2017). CRL2(Lrr1) promotes unloading of the vertebrate replisome from chromatin during replication termination. *Genes Dev*. 31:275-290.

109. Din, S., S.J. Brill, M.P. Fairman, and B. Stillman. (1990). Cell-cycle-regulated phosphorylation of DNA replication factor A from human and yeast cells. *Genes Dev*. 4:968-977.

110. Dobbs, T.A., J.A. Tainer, and S.P. Lees-Miller. (2010). A structural model for regulation of NHEJ by DNA-PKcs autophosphorylation. *DNA Repair (Amst)*. 9:1307-1314.

111. Doench, J.G. (2018). Am I ready for CRISPR? A user's guide to genetic screens. *Nat Rev Genet*. 19:67-80.

112. Doench, J.G., N. Fusi, M. Sullender, M. Hegde, E.W. Vaimberg, K.F. Donovan, I. Smith, Z. Tothova, C. Wilen, R. Orchard, H.W. Virgin, J. Listgarten, and D.E. Root. (2016). Optimized sgRNA design to maximize activity and minimize off-target effects of CRISPR-Cas9. *Nat Biotechnol*. 34:184-191.

113. Doil, C., N. Mailand, S. Bekker-Jensen, P. Menard, D.H. Larsen, R. Pepperkok, J. Ellenberg, S. Panier, D. Durocher, J. Bartek, J. Lukas, and C. Lukas. (2009). RNF168 binds and amplifies ubiquitin conjugates on damaged chromosomes to allow accumulation of repair proteins. *Cell*. 136:435-446.

114. Doudna, J.A., and E. Charpentier. (2014). Genome editing. The new frontier of genome engineering with CRISPR-Cas9. *Science*. 346:1258096.

115. Duan, H., S. Mansour, R. Reed, M.K. Gillis, B. Parent, B. Liu, Z. Sztupinszki, N. Birkbak, Z. Szallasi, A.E.H. Elia, J.E. Garber, and S. Pathania. (2020). E3 ligase RFWD3 is a novel modulator of stalled fork stability in BRCA2-deficient cells. *J Cell Biol*. 219.

116. Dubois, J.C., M. Yates, A. Gaudreau-Lapierre, G. Clement, L. Cappadocia, L. Gaudreau, L. Zou, and A. Marechal. (2017). A phosphorylation-and-ubiquitylation circuitry driving ATR activation and homologous recombination. *Nucleic Acids Res*. 45:8859-8872.

117. Duckett, D.R., A.I. Murchie, S. Diekmann, E. von Kitzing, B. Kemper, and D.M. Lilley. (1988). The structure of the Holliday junction, and its resolution. *Cell*. 55:79-89.

118. Dupre, A., L. Boyer-Chatenet, and J. Gautier. (2006). Two-step activation of ATM by DNA and the Mre11-Rad50-Nbs1 complex. *Nat Struct Mol Biol*. 13:451-457.

119. Duxin, J.P., J.M. Dewar, H. Yardimci, and J.C. Walter. (2014). Repair of a DNA-protein crosslink by replication-coupled proteolysis. *Cell*. 159:346-357.

120. Dykxhoorn, D.M., C.D. Novina, and P.A. Sharp. (2003). Killing the messenger: short RNAs that silence gene expression. *Nat Rev Mol Cell Biol*. 4:457-467.

121. Eggler, A.L., R.B. Inman, and M.M. Cox. (2002). The Rad51-dependent pairing of long DNA substrates is stabilized by replication protein A. *J Biol Chem*. 277:39280-39288.

122. Eisemann, T., and J.M. Pascal. (2020). Poly(ADP-ribose) polymerase enzymes and the maintenance of genome integrity. *Cell Mol Life Sci*. 77:19-33.

123. El-Khamisy, S.F., M. Masutani, H. Suzuki, and K.W. Caldecott. (2003). A requirement for PARP-1 for the assembly or stability of XRCC1 nuclear foci at sites of oxidative DNA damage. *Nucleic Acids Res*. 31:5526-5533.

124. Elia, A.E., D.C. Wang, N.A. Willis, A.P. Boardman, I. Hajdu, R.O. Adeyemi, E. Lowry, S.P. Gygi, R. Scully, and S.J. Elledge. (2015). RFWD3-dependent ubiquitination of RPA regulates repair at stalled replication forks. *Mol Cell*. 60:280-293.

125. Fan, L., A.S. Arvai, P.K. Cooper, S. Iwai, F. Hanaoka, and J.A. Tainer. (2006). Conserved XPB core structure and motifs for DNA unwinding: implications for pathway selection of transcription or excision repair. *Mol Cell*. 22:27-37.

126. Fanning, E., V. Klimovich, and A.R. Nager. (2006). A dynamic model for replication protein A (RPA) function in DNA processing pathways. *Nucleic Acids Res*. 34:4126-4137.

127. Feeney, L., I.M. Munoz, C. Lachaud, R. Toth, P.L. Appleton, D. Schindler, and J. Rouse. (2017). RPA-mediated recruitment of the E3 ligase RFWD3 is vital for interstrand crosslink repair and human health. *Mol Cell*. 66:610-621 e614.

128. Feng, J., T. Wakeman, S. Yong, X. Wu, S. Kornbluth, and X.F. Wang. (2009). Protein phosphatase 2A-dependent dephosphorylation of replication protein A is required for the repair of DNA breaks induced by replication stress. *Mol Cell Biol*. 29:5696-5709.

129. Foster, B., M. Attwood, K. Chong, M. Drake, R. Gilroy, M. Fournier, and I. Gibbs-Seymour. (2023). The RPA complex orchestrates K63-linked deubiquitination via ZUP1. *bioRxiv*:2023.2001.2027.525918.

130. Fousteri, M., and L.H. Mullenders. (2008). Transcription-coupled nucleotide excision repair in mammalian cells: molecular mechanisms and biological effects. *Cell Res*. 18:73-84.

131. Fradet-Turcotte, A., M.D. Canny, C. Escribano-Diaz, A. Orthwein, C.C. Leung, H. Huang, M.C. Landry, J. Kitevski-LeBlanc, S.M. Noordermeer, F. Sicheri, and D. Durocher. (2013). 53BP1 is a reader of the DNA-damage-induced H2A Lys 15 ubiquitin mark. *Nature*. 499:50-54.

132. Fragkos, M., O. Ganier, P. Coulombe, and M. Mechali. (2015). DNA replication origin activation in space and time. *Nat Rev Mol Cell Biol*. 16:360-374.

133. Franken, N.A., H.M. Rodermond, J. Stap, J. Haveman, and C. van Bree. (2006). Clonogenic assay of cells in vitro. *Nat Protoc*. 1:2315-2319.

134. French, M.E., C.F. Koehler, and T. Hunter. (2021). Emerging functions of branched ubiquitin chains. *Cell Discov*. 7:6.

135. Fu, Y.V., H. Yardimci, D.T. Long, T.V. Ho, A. Guainazzi, V.P. Bermudez, J. Hurwitz, A. van Oijen, O.D. Scharer, and J.C. Walter. (2011). Selective bypass of a lagging strand roadblock by the eukaryotic replicative DNA helicase. *Cell*. 146:931-941.

136. Fugger, K., M. Mistrik, K.J. Neelsen, Q. Yao, R. Zellweger, A.N. Kousholt, P. Haahr, W.K. Chu, J. Bartek, M. Lopes, I.D. Hickson, and C.S. Sorensen. (2015). FBH1 catalyzes regression of stalled replication forks. *Cell Rep*. 10:1749-1757.

137. Fullbright, G., H.B. Rycenga, J.D. Gruber, and D.T. Long. (2016). p97 promotes a conserved mechanism of helicase unloading during DNA cross-link repair. *Mol Cell Biol*. 36:2983-2994.

138. Gaillard, H., T. Garcia-Muse, and A. Aguilera. (2015). Replication stress and cancer. *Nat Rev Cancer*. 15:276-289.

139. Gaj, T., C.A. Gersbach, and C.F. Barbas, 3rd. (2013). ZFN, TALEN, and CRISPR/Cas-based methods for genome engineering. *Trends Biotechnol*. 31:397-405.

140. Gallina, I., I.A. Hendriks, S. Hoffmann, N.B. Larsen, J. Johansen, C.S. Colding-Christensen, L. Schubert, S. Selles-Baiget, Z. Fabian, U. Kuhbacher, A.O. Gao, M. Raschle, S. Rasmussen, M.L. Nielsen, N. Mailand, and J.P. Duxin. (2021). The ubiquitin ligase RFWD3 is required for translesion DNA synthesis. *Mol Cell*. 81:442-458 e449.

141. Gao, R., M.J. Schellenberg, S.Y. Huang, M. Abdelmalak, C. Marchand, K.C. Nitiss, J.L. Nitiss, R.S. Williams, and Y. Pommier. (2014). Proteolytic degradation of topoisomerase II (Top2) enables the processing of Top2.DNA and Top2.RNA covalent complexes by tyrosyl-DNA-phosphodiesterase 2 (TDP2). *J Biol Chem*. 289:17960-17969.

142. Gatti, M., R. Imhof, Q. Huang, M. Baudis, and M. Altmeyer. (2020). The ubiquitin ligase TRIP12 limits PARP1 trapping and constrains PARP inhibitor efficiency. *Cell Rep.* 32:107985.

143. Ge, X.Q., and J.J. Blow. (2010). Chk1 inhibits replication factory activation but allows dormant origin firing in existing factories. *J Cell Biol.* 191:1285-1297.

144. Giannattasio, M., K. Zwicky, C. Follonier, M. Foiani, M. Lopes, and D. Branzei. (2014). Visualization of recombination-mediated damage bypass by template switching. *Nat Struct Mol Biol.* 21:884-892.

145. Gibson, B.A., and W.L. Kraus. (2012). New insights into the molecular and cellular functions of poly(ADP-ribose) and PARPs. *Nat Rev Mol Cell Biol.* 13:411-424.

146. Gibson, B.A., Y. Zhang, H. Jiang, K.M. Hussey, J.H. Shrimp, H. Lin, F. Schwede, Y. Yu, and W.L. Kraus. (2016). Chemical genetic discovery of PARP targets reveals a role for PARP-1 in transcription elongation. *Science.* 353:45-50.

147. Gomez-Herreros, F., R. Romero-Granados, Z. Zeng, A. Alvarez-Quilon, C. Quintero, L. Ju, L. Umans, L. Vermeire, D. Huylebroeck, K.W. Caldecott, and F. Cortes-Ledesma. (2013). TDP2-dependent non-homologous end-joining protects against topoisomerase II-induced DNA breaks and genome instability in cells and in vivo. *PLoS Genet.* 9:e1003226.

148. Gong, Z., and J. Chen. (2011). E3 ligase RFWD3 participates in replication checkpoint control. *J Biol Chem.* 286:22308-22313.

149. Gonzalez-Acosta, D., E. Blanco-Romero, P. Ubieto-Capella, K. Mutreja, S. Miguez, S. Llanos, F. Garcia, J. Munoz, L. Blanco, M. Lopes, and J. Mendez. (2021). PrimPol-mediated repriming facilitates replication traverse of DNA interstrand crosslinks. *EMBO J.* 40:e106355.

150. Gradia, S., S. Acharya, and R. Fishel. (1997). The human mismatch recognition complex hMSH2-hMSH6 functions as a novel molecular switch. *Cell.* 91:995-1005.

151. Grafstrom, R.C., A.J. Fornace, Jr., H. Autrup, J.F. Lechner, and C.C. Harris. (1983). Formaldehyde damage to DNA and inhibition of DNA repair in human bronchial cells. *Science.* 220:216-218.

152. Graham, T.G., J.C. Walter, and J.J. Loparo. (2016). Two-stage synapsis of DNA ends during non-homologous end joining. *Mol Cell.* 61:850-858.

153. Gravel, S., J.R. Chapman, C. Magill, and S.P. Jackson. (2008). DNA helicases Sgs1 and BLM promote DNA double-strand break resection. *Genes Dev.* 22:2767-2772.

154. Grawunder, U., M. Wilm, X. Wu, P. Kulesza, T.E. Wilson, M. Mann, and M.R. Lieber. (1997). Activity of DNA ligase IV stimulated by complex formation with XRCC4 protein in mammalian cells. *Nature.* 388:492-495.

155. Groelly, F.J., M. Fawkes, R.A. Dagg, A.N. Blackford, and M. Tarsounas. (2023). Targeting DNA damage response pathways in cancer. *Nat Rev Cancer.* 23:78-94.

156. Grou, C.P., M.P. Pinto, A.V. Mendes, P. Domingues, and J.E. Azevedo. (2015). The de novo synthesis of ubiquitin: identification of deubiquitinases acting on ubiquitin precursors. *Sci Rep.* 5:12836.

157. Grundy, G.J., L.M. Polo, Z. Zeng, S.L. Rulten, N.C. Hoch, P. Paomephan, Y. Xu, S.M. Sweet, A.W. Thorne, A.W. Oliver, S.J. Matthews, L.H. Pearl, and K.W. Caldecott. (2016). PARP3 is a sensor of nicked nucleosomes and monoribosylates histone H2B(Glu2). *Nat Commun.* 7:12404.

158. Guilliam, T.A., N.C. Brissett, A. Ehlinger, B.A. Keen, P. Kolesar, E.M. Taylor, L.J. Bailey, H.D. Lindsay, W.J. Chazin, and A.J. Doherty. (2017). Molecular basis for PrimPol recruitment to replication forks by RPA. *Nat Commun.* 8:15222.

159. Guo, C., A. Kumagai, K. Schlacher, A. Shevchenko, A. Shevchenko, and W.G. Dunphy. (2015). Interaction of Chk1 with Treslin negatively regulates the initiation of chromosomal DNA replication. *Mol Cell*. 57:492-505.

160. Haahr, P., N. Borgermann, X. Guo, D. Typas, D. Achuthankutty, S. Hoffmann, R. Shearer, T.K. Sixma, and N. Mailand. (2018). ZUFSP deubiquitylates K63-linked polyubiquitin chains to promote genome stability. *Mol Cell*. 70:165-174 e166.

161. Haahr, P., S. Hoffmann, M.A. Tollenaere, T. Ho, L.I. Toledo, M. Mann, S. Bekker-Jensen, M. Raschle, and N. Mailand. (2016). Activation of the ATR kinase by the RPA-binding protein ETAA1. *Nat Cell Biol*. 18:1196-1207.

162. Haapaniemi, E., S. Botla, J. Persson, B. Schmierer, and J. Taipale. (2018). CRISPR-Cas9 genome editing induces a p53-mediated DNA damage response. *Nat Med*. 24:927-930.

163. Hammel, M., Y. Yu, B.L. Mahaney, B. Cai, R. Ye, B.M. Phipps, R.P. Rambo, G.L. Hura, M. Pelikan, S. So, R.M. Abolfath, D.J. Chen, S.P. Lees-Miller, and J.A. Tainer. (2010). Ku and DNA-dependent protein kinase dynamic conformations and assembly regulate DNA binding and the initial non-homologous end joining complex. *J Biol Chem*. 285:1414-1423.

164. Hanahan, D., and R.A. Weinberg. (2011). Hallmarks of cancer: the next generation. *Cell*. 144:646-674.

165. Hart, T., M. Chandrashekhar, M. Aregger, Z. Steinhart, K.R. Brown, G. MacLeod, M. Mis, M. Zimmermann, A. Fradet-Turcotte, S. Sun, P. Mero, P. Dirks, S. Sidhu, F.P. Roth, O.S. Rissland, D. Durocher, S. Angers, and J. Moffat. (2015). High-resolution CRISPR screens reveal fitness genes and genotype-specific cancer liabilities. *Cell*. 163:1515-1526.

166. Hart, T., A.H.Y. Tong, K. Chan, J. Van Leeuwen, A. Seetharaman, M. Aregger, M. Chandrashekhar, N. Hustedt, S. Seth, A. Noonan, A. Habsid, O. Sizova, L. Nedyalkova, R. Climie, L. Tworzyanski, K. Lawson, M.A. Sartori, S. Alibeh, D. Tieu, S. Masud, P. Mero, A. Weiss, K.R. Brown, M. Usaj, M. Billmann, M. Rahman, M. Constanzo, C.L. Myers, B.J. Andrews, C. Boone, D. Durocher, and J. Moffat. (2017). Evaluation and design of genome-wide CRISPR/SpCas9 knockout screens. *G3 (Bethesda)*. 7:2719-2727.

167. Harvey, S.L., A. Charlet, W. Haas, S.P. Gygi, and D.R. Kellogg. (2005). Cdk1-dependent regulation of the mitotic inhibitor Wee1. *Cell*. 122:407-420.

168. He, L., R. Lever, A. Cubbon, M. Tehseen, T. Jenkins, A.O. Nottingham, A. Horton, H. Betts, M. Fisher, S.M. Hamdan, P. Soultanas, and E.L. Bolt. (2023). Interaction of human HelQ with DNA polymerase delta halts DNA synthesis and stimulates DNA single-strand annealing. *Nucleic Acids Res*. 51:1740-1749.

169. He, P., and W. Yang. (2018). Template and primer requirements for DNA Pol theta-mediated end joining. *Proc Natl Acad Sci U S A*. 115:7747-7752.

170. Hegde, M.L., T.K. Hazra, and S. Mitra. (2008). Early steps in the DNA base excision/single-strand interruption repair pathway in mammalian cells. *Cell Res*. 18:27-47.

171. Hermanns, T., C. Pichlo, I. Woiwode, K. Klopffleisch, K.F. Witting, H. Ovaa, U. Baumann, and K. Hofmann. (2018). A family of unconventional deubiquitinases with modular chain specificity determinants. *Nat Commun*. 9:799.

172. Hewings, D.S., J. Heideker, T.P. Ma, A.P. AhYoung, F. El Oualid, A. Amore, G.T. Costakes, D. Kirchhofer, B. Brasher, T. Pillow, N. Popovych, T. Maurer, C. Schwerdtfeger, W.F. Forrest, K. Yu, J. Flygare, M. Bogyo, and I.E. Wertz. (2018). Reactive-site-centric chemoproteomics identifies a distinct class of deubiquitinase enzymes. *Nat Commun*. 9:1162.

173. Heyer, W.D., K.T. Ehmsen, and J. Liu. (2010). Regulation of homologous recombination in eukaryotes. *Annu Rev Genet*. 44:113-139.

174. Ho, E.L., and M.S. Satoh. (2003). Repair of single-strand DNA interruptions by redundant pathways and its implication in cellular sensitivity to DNA-damaging agents. *Nucleic Acids Res*. 31:7032-7040.

175. Hoa, N.N., T. Shimizu, Z.W. Zhou, Z.Q. Wang, R.A. Deshpande, T.T. Paull, S. Akter, M. Tsuda, R. Furuta, K. Tsutsui, S. Takeda, and H. Sasanuma. (2016). Mre11 is essential for the removal of lethal topoisomerase 2 covalent cleavage complexes. *Mol Cell*. 64:580-592.

176. Hoege, C., B. Pfander, G.L. Moldovan, G. Pyrowolakis, and S. Jentsch. (2002). RAD6-dependent DNA repair is linked to modification of PCNA by ubiquitin and SUMO. *Nature*. 419:135-141.

177. Hoeijmakers, J.H. (2009). DNA damage, aging, and cancer. *N Engl J Med*. 361:1475-1485.

178. Hogg, M., M. Seki, R.D. Wood, S. Doublie, and S.S. Wallace. (2011). Lesion bypass activity of DNA polymerase theta (POLQ) is an intrinsic property of the pol domain and depends on unique sequence inserts. *J Mol Biol*. 405:642-652.

179. Hopkins, T.A., Y. Shi, L.E. Rodriguez, L.R. Solomon, C.K. Donawho, E.L. DiGiammarino, S.C. Panchal, J.L. Wilsbacher, W. Gao, A.M. Olson, D.F. Stolarik, D.J. Osterling, E.F. Johnson, and D. Maag. (2015). Mechanistic dissection of PARP1 trapping and the impact on in vivo tolerability and efficacy of PARP inhibitors. *Mol Cancer Res*. 13:1465-1477.

180. Howard, S.M., D.A. Yanez, and J.M. Stark. (2015). DNA damage response factors from diverse pathways, including DNA crosslink repair, mediate alternative end joining. *PLoS Genet*. 11:e1004943.

181. Hozak, P., and P.R. Cook. (1994). Replication factories. *Trends Cell Biol*. 4:48-52.

182. Hsu, P.D., E.S. Lander, and F. Zhang. (2014). Development and applications of CRISPR-Cas9 for genome engineering. *Cell*. 157:1262-1278.

183. Huang, H., L. Zhu, B.R. Reid, G.P. Drobny, and P.B. Hopkins. (1995). Solution structure of a cisplatin-induced DNA interstrand cross-link. *Science*. 270:1842-1845.

184. Huang, J., S. Liu, M.A. Bellani, A.K. Thazhathveetil, C. Ling, J.P. de Winter, Y. Wang, W. Wang, and M.M. Seidman. (2013). The DNA translocase FANCM/MHF promotes replication traverse of DNA interstrand crosslinks. *Mol Cell*. 52:434-446.

185. Huang, T.T., S.M. Nijman, K.D. Mirchandani, P.J. Galardy, M.A. Cohn, W. Haas, S.P. Gygi, H.L. Ploegh, R. Bernards, and A.D. D'Andrea. (2006). Regulation of monoubiquitinated PCNA by DUB autocleavage. *Nat Cell Biol*. 8:339-347.

186. Huertas, P., and S.P. Jackson. (2009). Human CtIP mediates cell cycle control of DNA end resection and double strand break repair. *J Biol Chem*. 284:9558-9565.

187. Hussmann, J.A., J. Ling, P. Ravisankar, J. Yan, A. Cirincione, A. Xu, D. Simpson, D. Yang, A. Bothmer, C. Cotta-Ramusino, J.S. Weissman, and B. Adamson. (2021). Mapping the genetic landscape of DNA double-strand break repair. *Cell*. 184:5653-5669 e5625.

188. Hustedt, N., Y. Saito, M. Zimmermann, A. Alvarez-Quilon, D. Setiaputra, S. Adam, A. McEwan, J.Y. Yuan, M. Olivieri, Y. Zhao, M.T. Kanemaki, A. Jurisicova, and D. Durocher. (2019). Control of homologous recombination by the HROB-MCM8-MCM9 pathway. *Genes Dev*. 33:1397-1415.

189. Huttner, D., and H.D. Ulrich. (2008). Cooperation of replication protein A with the ubiquitin ligase Rad18 in DNA damage bypass. *Cell Cycle*. 7:3629-3633.

190. Inano, S., K. Sato, Y. Katsuki, W. Kobayashi, H. Tanaka, K. Nakajima, S. Nakada, H. Miyoshi, K. Knies, A. Takaori-Kondo, D. Schindler, M. Ishiai, H. Kurumizaka, and M. Takata. (2017). RFWD3-mediated ubiquitination promotes timely removal of both RPA and RAD51 from DNA damage sites to facilitate homologous recombination. *Mol Cell*. 66:622-634 e628.

191. Jackson, A.L., S.R. Bartz, J. Schelter, S.V. Kobayashi, J. Burchard, M. Mao, B. Li, G. Cavet, and P.S. Linsley. (2003). Expression profiling reveals off-target gene regulation by RNAi. *Nat Biotechnol*. 21:635-637.

192. Jaishree, T.N., G.A. van der Marel, J.H. van Boom, and A.H. Wang. (1993). Structural influence of RNA incorporation in DNA: quantitative nuclear magnetic resonance refinement of d(CG)r(CG)d(CG) and d(CG)r(C)d(TAGCG). *Biochemistry*. 32:4903-4911.

193. Jenkins, T., S.J. Northall, D. Ptchelkine, R. Lever, A. Cubbon, H. Betts, V. Taresco, C.D.O. Cooper, P.J. McHugh, P. Soultanas, and E.L. Bolt. (2021). The HelQ human DNA repair helicase utilizes a PWI-like domain for DNA loading through interaction with RPA, triggering DNA unwinding by the HelQ helicase core. *NAR Cancer*. 3:zcaa043.

194. Jensen, R.B., A. Carreira, and S.C. Kowalczykowski. (2010). Purified human BRCA2 stimulates RAD51-mediated recombination. *Nature*. 467:678-683.

195. Jiang, W., J.L. Crowe, X. Liu, S. Nakajima, Y. Wang, C. Li, B.J. Lee, R.L. Dubois, C. Liu, X. Yu, L. Lan, and S. Zha. (2015). Differential phosphorylation of DNA-PKcs regulates the interplay between end-processing and end-ligation during nonhomologous end-joining. *Mol Cell*. 58:172-185.

196. Jinek, M., K. Chylinski, I. Fonfara, M. Hauer, J.A. Doudna, and E. Charpentier. (2012). A programmable dual-RNA-guided DNA endonuclease in adaptive bacterial immunity. *Science*. 337:816-821.

197. Johnson, R.D., and M. Jasin. (2000). Sister chromatid gene conversion is a prominent double-strand break repair pathway in mammalian cells. *EMBO J*. 19:3398-3407.

198. Joung, J.K., and J.D. Sander. (2013). TALENs: a widely applicable technology for targeted genome editing. *Nat Rev Mol Cell Biol*. 14:49-55.

199. Kadyk, L.C., and L.H. Hartwell. (1992). Sister chromatids are preferred over homologs as substrates for recombinational repair in Saccharomyces cerevisiae. *Genetics*. 132:387-402.

200. Kadyrov, F.A., L. Dzantiev, N. Constantin, and P. Modrich. (2006). Endonucleolytic function of MutLalpha in human mismatch repair. *Cell*. 126:297-308.

201. Kais, Z., B. Rondinelli, A. Holmes, C. O'Leary, D. Kozono, A.D. D'Andrea, and R. Ceccaldi. (2016). FANCD2 maintains fork stability in BRCA1/2-deficient tumors and promotes alternative end-joining DNA repair. *Cell Rep*. 15:2488-2499.

202. Kalasova, I., R. Hailstone, J. Bublitz, J. Bogantes, W. Hofmann, A. Leal, H. Hanzlikova, and K.W. Caldecott. (2020). Pathological mutations in PNKP trigger defects in DNA single-strand break repair but not DNA double-strand break repair. *Nucleic Acids Res*. 48:6672-6684.

203. Kamp, J.A., B. Lemmens, R.J. Romeijn, S.C. Changoer, R. van Schendel, and M. Tijsterman. (2021). Helicase Q promotes homology-driven DNA double-strand break repair and prevents tandem duplications. *Nat Commun*. 12:7126.

204. Kang, S.G., H. Chung, Y.D. Yoo, J.G. Lee, Y.I. Choi, and Y.S. Yu. (2001). Mechanism of growth inhibitory effect of Mitomycin-C on cultured human retinal pigment epithelial cells: Apoptosis and cell cycle arrest. *Curr Eye Res*. 22:174-181.

205. Kanu, N., T. Zhang, R.A. Burrell, A. Chakraborty, J. Cronshaw, C. DaCosta, E. Gronroos, H.N. Pemberton, E. Anderton, L. Gonzalez, S. Sabbioneda, H.D. Ulrich, C. Swanton, and A. Behrens. (2016). RAD18, WRNIP1 and ATMIN promote ATM signalling in response to replication stress. *Oncogene*. 35:4009-4019.

206. Kapor, S., V. Cokic, and J.F. Santibanez. (2021). Mechanisms of hydroxyurea-induced cellular senescence: An oxidative stress connection? *Oxid Med Cell Longev*. 2021:7753857.

207. Karanam, K., R. Kafri, A. Loewer, and G. Lahav. (2012). Quantitative live cell imaging reveals a gradual shift between DNA repair mechanisms and a maximal use of HR in mid S phase. *Mol Cell*. 47:320-329.

208. Kashammer, L., J.H. Saathoff, K. Lammens, F. Gut, J. Bartho, A. Alt, B. Kessler, and K.P. Hopfner. (2019). Mechanism of DNA end sensing and processing by the Mre11-Rad50 complex. *Mol Cell*. 76:382-394 e386.

209. Katsuno, Y., A. Suzuki, K. Sugimura, K. Okumura, D.H. Zineldeen, M. Shimada, H. Niida, T. Mizuno, F. Hanaoka, and M. Nakanishi. (2009). Cyclin A-Cdk1 regulates the origin firing program in mammalian cells. *Proc Natl Acad Sci U S A*. 106:3184-3189.

210. Kellner, V., and B. Luke. (2020). Molecular and physiological consequences of faulty eukaryotic ribonucleotide excision repair. *EMBO J*. 39:e102309.

211. Kelsall, I.R. (2022). Non-lysine ubiquitylation: Doing things differently. *Front Mol Biosci*. 9:1008175.

212. Khan, A.A., D. Betel, M.L. Miller, C. Sander, C.S. Leslie, and D.S. Marks. (2009). Transfection of small RNAs globally perturbs gene regulation by endogenous microRNAs. *Nat Biotechnol*. 27:549-555.

213. Kile, A.C., D.A. Chavez, J. Bacal, S. Eldirany, D.M. Korzhnev, I. Bezsonova, B.F. Eichman, and K.A. Cimprich. (2015). HLTF's ancient HIRAN domain binds 3' DNA ends to drive replication fork reversal. *Mol Cell*. 58:1090-1100.

214. Kim, C., B.F. Paulus, and M.S. Wold. (1994). Interactions of human replication protein A with oligonucleotides. *Biochemistry*. 33:14197-14206.

215. Klein Douwel, D., R.A. Boonen, D.T. Long, A.A. Szypowska, M. Raschle, J.C. Walter, and P. Knipscheer. (2014). XPF-ERCC1 acts in unhooking DNA interstrand crosslinks in cooperation with FANCD2 and FANCP/SLX4. *Mol Cell*. 54:460-471.

216. Klein, H.L. (2017). Genome instabilities arising from ribonucleotides in DNA. *DNA Repair (Amst)*. 56:26-32.

217. Klungland, A., and T. Lindahl. (1997). Second pathway for completion of human DNA base excision-repair: reconstitution with purified proteins and requirement for DNase IV (FEN1). *EMBO J*. 16:3341-3348.

218. Knies, K., S. Inano, M.J. Ramirez, M. Ishiai, J. Surralles, M. Takata, and D. Schindler. (2017). Biallelic mutations in the ubiquitin ligase RFWD3 cause Fanconi anemia. *J Clin Invest*. 127:3013-3027.

219. Kojima, Y., Y. Machida, S. Palani, T.R. Caulfield, E.S. Radisky, S.H. Kaufmann, and Y.J. Machida. (2020). FAM111A protects replication forks from protein obstacles via its trypsin-like domain. *Nat Commun*. 11:1318.

220. Kolinjivadi, A.M., V. Sannino, A. De Antoni, K. Zadorozhny, M. Kilkenny, H. Techer, G. Baldi, R. Shen, A. Ciccia, L. Pellegrini, L. Krejci, and V. Costanzo. (2017). SMARCAL1-mediated fork reversal triggers MRE11-dependent degradation of nascent DNA in the absence of BRCA2 and stable RAD51 nucleofilaments. *Mol Cell*. 67:867-881 e867.

221. Komander, D., and M. Rape. (2012). The ubiquitin code. *Annu Rev Biochem*. 81:203-229.

222. Kottemann, M.C., and A. Smogorzewska. (2013). Fanconi anaemia and the repair of watson and crick DNA crosslinks. *Nature*. 493:356-363.

223. Krais, J.J., Y. Wang, P. Patel, J. Basu, A.J. Bernhardy, and N. Johnson. (2021). RNF168-mediated localization of BARD1 recruits the BRCA1-PALB2 complex to DNA damage. *Nat Commun*. 12:5016.

224. Krijger, P.H., K.Y. Lee, N. Wit, P.C. van den Berk, X. Wu, H.P. Roest, A. Maas, H. Ding, J.H. Hoeijmakers, K. Myung, and H. Jacobs. (2011). HLTF and SHPRH are not essential for PCNA polyubiquitination, survival and somatic hypermutation: existence of an alternative E3 ligase. *DNA Repair (Amst)*. 10:438-444.

225. Krokan, H.E., and M. Bjoras. (2013). Base excision repair. *Cold Spring Harb Perspect Biol*. 5:a012583.

226. Kuhbacher, U., and J.P. Duxin. (2020). How to fix DNA-protein crosslinks. *DNA Repair (Amst)*. 94:102924.

227. Kumagai, A., J. Lee, H.Y. Yoo, and W.G. Dunphy. (2006). TopBP1 activates the ATR-ATRIP complex. *Cell*. 124:943-955.

228. Kunkel, T.A. (1993). Nucleotide repeats. Slippery DNA and diseases. *Nature*. 365:207-208.

229. Kunkel, T.A. (2009). Evolving views of DNA replication (in)fidelity. *Cold Spring Harb Symp Quant Biol*. 74:91-101.

230. Kunkel, T.A., and D.A. Erie. (2015). Eukaryotic mismatch repair in relation to DNA replication. *Annu Rev Genet*. 49:291-313.

231. Kwasna, D., S.A. Abdul Rehman, J. Natarajan, S. Matthews, R. Madden, V. De Cesare, S. Weidlich, S. Virdee, I. Ahel, I. Gibbs-Seymour, and Y. Kulathu. (2018). Discovery and characterization of ZUFSP/ZUP1, a distinct deubiquitinase class important for genome stability. *Mol Cell*. 70:150-164 e156.

232. Labun, K., T.G. Montague, M. Krause, Y.N. Torres Cleuren, H. Tjeldnes, and E. Valen. (2019). CHOPCHOP v3: expanding the CRISPR web toolbox beyond genome editing. *Nucleic Acids Res*. 47:W171-W174.

233. Lai, Y., M. Zhu, W. Wu, N. Rokutanda, Y. Togashi, W. Liang, and T. Ohta. (2019). HERC2 regulates RPA2 by mediating ATR-induced Ser33 phosphorylation and ubiquitin-dependent degradation. *Sci Rep*. 9:14257.

234. Larsen, N.B., A.O. Gao, J.L. Sparks, I. Gallina, R.A. Wu, M. Mann, M. Raschle, J.C. Walter, and J.P. Duxin. (2019). Replication-coupled DNA-protein crosslink repair by SPRTN and the proteasome in xenopus egg extracts. *Mol Cell*. 73:574-588 e577.

235. Layer, J.V., L. Debaize, A. Van Scoyk, N.C. House, A.J. Brown, Y. Liu, K.E. Stevenson, M. Hemann, S.A. Roberts, B.D. Price, D.M. Weinstock, and T.A. Day. (2020). Polymerase delta promotes chromosomal rearrangements and imprecise double-strand break repair. *Proc Natl Acad Sci U S A*. 117:27566-27577.

236. Lee, D.H., Y. Pan, S. Kanner, P. Sung, J.A. Borowiec, and D. Chowdhury. (2010). A PP4 phosphatase complex dephosphorylates RPA2 to facilitate DNA repair via homologous recombination. *Nat Struct Mol Biol*. 17:365-372.

237. Lee, J., A. Kumagai, and W.G. Dunphy. (2001). Positive regulation of Wee1 by Chk1 and 14-3-3 proteins. *Mol Biol Cell*. 12:551-563.

238. Lee, J.H., and T.T. Paull. (2004). Direct activation of the ATM protein kinase by the Mre11/Rad50/Nbs1 complex. *Science*. 304:93-96.

239. Leimbacher, P.A., S.E. Jones, A.K. Shorrocks, M. de Marco Zompit, M. Day, J. Blaauwendraad, D. Bundschuh, S. Bonham, R. Fischer, D. Fink, B.M. Kessler, A.W. Oliver, L.H. Pearl, A.N. Blackford, and M. Stucki. (2019). MDC1 interacts with TOPBP1 to maintain chromosomal stability during mitosis. *Mol Cell*. 74:571-583 e578.

240. Lemacon, D., J. Jackson, A. Quinet, J.R. Brickner, S. Li, S. Yazinski, Z. You, G. Ira, L. Zou, N. Mosammaparast, and A. Vindigni. (2017). MRE11 and EXO1 nucleases degrade reversed forks and elicit MUS81-dependent fork rescue in BRCA2-deficient cells. *Nat Commun*. 8:860.

241. Lemonidis, K., M.L. Rennie, C. Arkinson, V.K. Chaugule, M. Clarke, J. Streetley, and H. Walden. (2023). Structural and biochemical basis of interdependent FANCI-FANCD2 ubiquitination. *EMBO J.* 42:e111898.

242. Lescale, C., H. Lenden Hasse, A.N. Blackford, G. Balmus, J.J. Bianchi, W. Yu, L. Bacoccina, A. Jarade, C. Clouin, R. Sivapalan, B. Reina-San-Martin, S.P. Jackson, and L. Deriano. (2016). Specific roles of XRCC4 paralogs PAXX and XLF during V(D)J recombination. *Cell Rep.* 16:2967-2979.

243. Leuzzi, G., V. Marabitti, P. Pichierri, and A. Franchitto. (2016). WRNIP1 protects stalled forks from degradation and promotes fork restart after replication stress. *EMBO J.* 35:1437-1451.

244. Li, G.M., and P. Modrich. (1995). Restoration of mismatch repair to nuclear extracts of H6 colorectal tumor cells by a heterodimer of human MutL homologs. *Proc Natl Acad Sci U S A.* 92:1950-1954.

245. Li, W., H. Xu, T. Xiao, L. Cong, M.I. Love, F. Zhang, R.A. Irizarry, J.S. Liu, M. Brown, and X.S. Liu. (2014). MAGeCK enables robust identification of essential genes from genome-scale CRISPR/Cas9 knockout screens. *Genome Biol.* 15:554.

246. Lim, P.X., M. Zaman, and M. Jasin. (2023). BRCA2 promotes genomic integrity and therapy resistance primarily through its role in homology-directed repair. *bioRxiv.*

247. Lin, C.P., Y. Ban, Y.L. Lyu, S.D. Desai, and L.F. Liu. (2008). A ubiquitin-proteasome pathway for the repair of topoisomerase I-DNA covalent complexes. *J Biol Chem.* 283:21074-21083.

248. Lin, F.L., K. Sperle, and N. Sternberg. (1984). Model for homologous recombination during transfer of DNA into mouse l-cells - role for DNA ends in the recombination process. *Molecular and Cellular Biology.* 4:1020-1034.

249. Lindahl, T. (1993). Instability and decay of the primary structure of DNA. *Nature.* 362:709-715.

250. Lipkin, S.M., V. Wang, R. Jacoby, S. Banerjee-Basu, A.D. Baxevanis, H.T. Lynch, R.M. Elliott, and F.S. Collins. (2000). MLH3: a DNA mismatch repair gene associated with mammalian microsatellite instability. *Nat Genet.* 24:27-35.

251. Liu, C., J. Wu, S.C. Paudyal, Z. You, and X. Yu. (2013). CHFR is important for the first wave of ubiquitination at DNA damage sites. *Nucleic Acids Res.* 41:1698-1710.

252. Liu, H., S. Takeda, R. Kumar, T.D. Westergard, E.J. Brown, T.K. Pandita, E.H. Cheng, and J.J. Hsieh. (2010). Phosphorylation of MLL by ATR is required for execution of mammalian S-phase checkpoint. *Nature.* 467:343-346.

253. Liu, J.C.Y., U. Kuhbacher, N.B. Larsen, N. Borgermann, D.H. Garvanska, I.A. Hendriks, L. Ackermann, P. Haahr, I. Gallina, C. Guerillon, E. Branigan, R.T. Hay, Y. Azuma, M.L. Nielsen, J.P. Duxin, and N. Mailand. (2021). Mechanism and function of DNA replication-independent DNA-protein crosslink repair via the SUMO-RNF4 pathway. *EMBO J.* 40:e107413.

254. Liu, L.F., S.D. Desai, T.K. Li, Y. Mao, M. Sun, and S.P. Sim. (2000a). Mechanism of action of camptothecin. *Ann N Y Acad Sci.* 922:1-10.

255. Liu, Q., S. Guntuku, X.-S. Cui, S. Matsuoka, D. Cortez, K. Tamai, G. Luo, S. Carattini-Rivera, F. DeMayo, A. Bradley, L.A. Donehower, and S.J. Elledge. (2000b). Chk1 is an essential kinase that is regulated by Atr and required for the G2/M DNA damage checkpoint. *Genes & Development.* 14:1448-1459.

256. Liu, S., J. Chu, N. Yucer, M. Leng, S.Y. Wang, B.P. Chen, W.N. Hittelman, and Y. Wang. (2011). RING finger and WD repeat domain 3 (RFWD3) associates with replication protein

A (RPA) and facilitates RPA-mediated DNA damage response. *J Biol Chem*. 286:22314-22322.

257. Liu, S., S.O. Opiyo, K. Manthey, J.G. Glanzer, A.K. Ashley, C. Amerin, K. Troksa, M. Shrivastav, J.A. Nickoloff, and G.G. Oakley. (2012). Distinct roles for DNA-PK, ATM and ATR in RPA phosphorylation and checkpoint activation in response to replication stress. *Nucleic Acids Res*. 40:10780-10794.

258. Long, D.T., M. Raschle, V. Joukov, and J.C. Walter. (2011). Mechanism of RAD51-dependent DNA interstrand cross-link repair. *Science*. 333:84-87.

259. Longerich, S., J. San Filippo, D. Liu, and P. Sung. (2009). FANCI binds branched DNA and is monoubiquitinated by UBE2T-FANCL. *J Biol Chem*. 284:23182-23186.

260. Longley, M.J., A.J. Pierce, and P. Modrich. (1997). DNA polymerase delta is required for human mismatch repair in vitro. *J Biol Chem*. 272:10917-10921.

261. Lord, C.J., and A. Ashworth. (2017). PARP inhibitors: Synthetic lethality in the clinic. *Science*. 355:1152-1158.

262. MacLeod, G., N. Rajakulendran, and S. Angers. (2022). Identification of drug resistance mechanisms using genome-wide CRISPR-Cas9 screens. *Methods Mol Biol*. 2535:141-156.

263. Mahaney, B.L., K. Meek, and S.P. Lees-Miller. (2009). Repair of ionizing radiation-induced DNA double-strand breaks by non-homologous end-joining. *Biochem J*. 417:639-650.

264. Mailand, N., J. Falck, C. Lukas, R.G. Syljuasen, M. Welcker, J. Bartek, and J. Lukas. (2000). Rapid destruction of human Cdc25A in response to DNA damage. *Science*. 288:1425-1429.

265. Makarova, K.S., N.V. Grishin, S.A. Shabalina, Y.I. Wolf, and E.V. Koonin. (2006). A putative RNA-interference-based immune system in prokaryotes: computational analysis of the predicted enzymatic machinery, functional analogies with eukaryotic RNAi, and hypothetical mechanisms of action. *Biol Direct*. 1:7.

266. Mali, P., L. Yang, K.M. Esvelt, J. Aach, M. Guell, J.E. DiCarlo, J.E. Norville, and G.M. Church. (2013). RNA-guided human genome engineering via Cas9. *Science*. 339:823-826.

267. Mansour, W.Y., T. Rhein, and J. Dahm-Daphi. (2010). The alternative end-joining pathway for repair of DNA double-strand breaks requires PARP1 but is not dependent upon microhomologies. *Nucleic Acids Res*. 38:6065-6077.

268. Marechal, A., J.M. Li, X.Y. Ji, C.S. Wu, S.A. Yazinski, H.D. Nguyen, S. Liu, A.E. Jimenez, J. Jin, and L. Zou. (2014). PRP19 transforms into a sensor of RPA-ssDNA after DNA damage and drives ATR activation via a ubiquitin-mediated circuitry. *Mol Cell*. 53:235-246.

269. Marechal, A., and L. Zou. (2015). RPA-coated single-stranded DNA as a platform for post-translational modifications in the DNA damage response. *Cell Res*. 25:9-23.

270. Marteijn, J.A., H. Lans, W. Vermeulen, and J.H. Hoeijmakers. (2014). Understanding nucleotide excision repair and its roles in cancer and ageing. *Nat Rev Mol Cell Biol*. 15:465-481.

271. Martin, M. (2011). Cutadapt removes adapter sequences from high-throughput sequencing reads. *EMBnet.journal*. 17:10-12.

272. Masani, S., L. Han, K. Meek, and K. Yu. (2016). Redundant function of DNA ligase 1 and 3 in alternative end-joining during immunoglobulin class switch recombination. *Proc Natl Acad Sci U S A*. 113:1261-1266.

273. Maslov, A.Y., M. Lee, M. Gundry, S. Gravina, N. Strogonova, C. Tazearslan, A. Bendebury, Y. Suh, and J. Vijg. (2012). 5-aza-2'-deoxycytidine-induced genome rearrangements are mediated by DNMT1. *Oncogene*. 31:5172-5179.

274. Mateos-Gomez, P.A., T. Kent, S.K. Deng, S. McDevitt, E. Kashkina, T.M. Hoang, R.T. Pomerantz, and A. Sfeir. (2017). The helicase domain of Poltheta counteracts RPA to promote alt-NHEJ. *Nat Struct Mol Biol*. 24:1116-1123.

275. Mathieu, N., N. Kaczmarek, P. Ruthemann, A. Luch, and H. Naegeli. (2013). DNA quality control by a lesion sensor pocket of the xeroderma pigmentosum group D helicase subunit of TFIIH. *Curr Biol*. 23:204-212.

276. Matsumoto, Y., and K. Kim. (1995). Excision of deoxyribose phosphate residues by DNA polymerase beta during DNA repair. *Science*. 269:699-702.

277. Matveeva, E.A., Q.M.H. Al-Tinawi, E.C. Rouchka, and Y.N. Fondufe-Mittendorf. (2019). Coupling of PARP1-mediated chromatin structural changes to transcriptional RNA polymerase II elongation and cotranscriptional splicing. *Epigenetics Chromatin*. 12:15.

278. McVey, M., M. Adams, E. Staeva-Vieira, and J.J. Sekelsky. (2004). Evidence for multiple cycles of strand invasion during repair of double-strand gaps in Drosophila. *Genetics*. 167:699-705.

279. McVey, M., V.Y. Khodaverdian, D. Meyer, P.G. Cerqueira, and W.D. Heyer. (2016). Eukaryotic DNA polymerases in homologous recombination. *Annu Rev Genet*. 50:393-421.

280. Mehta, K.P.M., V. Thada, R. Zhao, A. Krishnamoorthy, M. Leser, K. Lindsey Rose, and D. Cortez. (2022). CHK1 phosphorylates PRIMPOL to promote replication stress tolerance. *Sci Adv*. 8:eabm0314.

281. Metzakopian, E., A. Strong, V. Iyer, A. Hodgkins, K. Tzelepis, L. Antunes, M.J. Friedrich, Q. Kang, T. Davidson, J. Lamberth, C. Hoffmann, G.D. Davis, G.S. Vassiliou, W.C. Skarnes, and A. Bradley. (2017). Enhancing the genome editing toolbox: genome wide CRISPR arrayed libraries. *Sci Rep*. 7:2244.

282. Mi, H., A. Muruganujan, D. Ebert, X. Huang, and P.D. Thomas. (2019). PANTHER version 14: more genomes, a new PANTHER GO-slim and improvements in enrichment analysis tools. *Nucleic Acids Res*. 47:D419-D426.

283. Mijic, S., R. Zellweger, N. Chappidi, M. Berti, K. Jacobs, K. Mutreja, S. Ursich, A. Ray Chaudhuri, A. Nussenzweig, P. Janscak, and M. Lopes. (2017). Replication fork reversal triggers fork degradation in BRCA2-defective cells. *Nat Commun*. 8:859.

284. Mimitou, E.P., and L.S. Symington. (2008). Sae2, Exo1 and Sgs1 collaborate in DNA double-strand break processing. *Nature*. 455:770-774.

285. Mine-Hattab, J., and R. Rothstein. (2012). Increased chromosome mobility facilitates homology search during recombination. *Nat Cell Biol*. 14:510-517.

286. Mirman, Z., N.K. Sasi, A. King, J.R. Chapman, and T. de Lange. (2022). 53BP1-shieldin-dependent DSB processing in BRCA1-deficient cells requires CST-Polalpha-primase fill-in synthesis. *Nat Cell Biol*. 24:51-61.

287. Mirsanaye, A.S., D. Typas, and N. Mailand. (2021). Ubiquitylation at stressed replication forks: Mechanisms and functions. *Trends Cell Biol*. 31:584-597.

288. Moder, M., G. Velimezi, M. Owusu, A. Mazouzi, M. Wiedner, J. Ferreira da Silva, L. Robinson-Garcia, F. Schischlik, R. Slavkovsky, R. Kralovics, M. Schuster, C. Bock, T. Ideker, S.P. Jackson, J. Menche, and J.I. Loizou. (2017). Parallel genome-wide screens identify synthetic viable interactions between the BLM helicase complex and Fanconi anemia. *Nat Commun*. 8:1238.

289. Mohni, K.N., S.R. Wessel, R. Zhao, A.C. Wojciechowski, J.W. Luzwick, H. Layden, B.F. Eichman, P.S. Thompson, K.P.M. Mehta, and D. Cortez. (2019). HMCES maintains genome integrity by shielding abasic sites in single-strand DNA. *Cell*. 176:144-153 e113.

290. Moore, C.E., S.E. Yalcindag, H. Czeladko, R. Ravindranathan, Y. Wijesekara Hanthi, J.C. Levy, V. Sannino, D. Schindler, A. Ciccia, V. Costanzo, and A.E.H. Elia. (2023). RFWD3 promotes ZRANB3 recruitment to regulate the remodeling of stalled replication forks. *J Cell Biol*. 222.

291. Motegi, A., H.J. Liaw, K.Y. Lee, H.P. Roest, A. Maas, X. Wu, H. Moinova, S.D. Markowitz, H. Ding, J.H. Hoeijmakers, and K. Myung. (2008). Polyubiquitination of proliferating cell nuclear antigen by HLTF and SHPRH prevents genomic instability from stalled replication forks. *Proc Natl Acad Sci U S A*. 105:12411-12416.

292. Motycka, T.A., T. Bessho, S.M. Post, P. Sung, and A.E. Tomkinson. (2004). Physical and functional interaction between the XPF/ERCC1 endonuclease and hRad52. *J Biol Chem*. 279:13634-13639.

293. Mouron, S., S. Rodriguez-Acebes, M.I. Martinez-Jimenez, S. Garcia-Gomez, S. Chocron, L. Blanco, and J. Mendez. (2013). Repriming of DNA synthesis at stalled replication forks by human PrimPol. *Nat Struct Mol Biol*. 20:1383-1389.

294. Muniandy, P.A., J. Liu, A. Majumdar, S.T. Liu, and M.M. Seidman. (2010). DNA interstrand crosslink repair in mammalian cells: step by step. *Crit Rev Biochem Mol Biol*. 45:23-49.

295. Murai, J., S.Y. Huang, B.B. Das, A. Renaud, Y. Zhang, J.H. Doroshow, J. Ji, S. Takeda, and Y. Pommier. (2012). Trapping of PARP1 and PARP2 by clinical PARP inhibitors. *Cancer Res*. 72:5588-5599.

296. Murphy, A.K., M. Fitzgerald, T. Ro, J.H. Kim, A.I. Rabinowitsch, D. Chowdhury, C.L. Schildkraut, and J.A. Borowiec. (2014). Phosphorylated RPA recruits PALB2 to stalled DNA replication forks to facilitate fork recovery. *J Cell Biol*. 206:493-507.

297. Nakamura, K., G. Saredi, J.R. Becker, B.M. Foster, N.V. Nguyen, T.E. Beyer, L.C. Cesa, P.A. Faull, S. Lukauskas, T. Frimurer, J.R. Chapman, T. Bartke, and A. Groth. (2019). H4K20me0 recognition by BRCA1-BARD1 directs homologous recombination to sister chromatids. *Nat Cell Biol*. 21:311-318.

298. Nakazawa, Y., Y. Hara, Y. Oka, O. Komine, D. van den Heuvel, C. Guo, Y. Daigaku, M. Isono, Y. He, M. Shimada, K. Kato, N. Jia, S. Hashimoto, Y. Kotani, Y. Miyoshi, M. Tanaka, A. Sobue, N. Mitsutake, T. Suganami, A. Masuda, K. Ohno, S. Nakada, T. Mashimo, K. Yamanaka, M.S. Luijsterburg, and T. Ogi. (2020). Ubiquitination of DNA damage-stalled RNAPII promotes transcription-coupled repair. *Cell*. 180:1228-1244 e1224.

299. Nambiar, T.S., L. Baudrier, P. Billon, and A. Ciccia. (2022). CRISPR-based genome editing through the lens of DNA repair. *Mol Cell*. 82:348-388.

300. Neale, M.J., J. Pan, and S. Keeney. (2005). Endonucleolytic processing of covalent protein-linked DNA double-strand breaks. *Nature*. 436:1053-1057.

301. Neelsen, K.J., and M. Lopes. (2015). Replication fork reversal in eukaryotes: from dead end to dynamic response. *Nat Rev Mol Cell Biol*. 16:207-220.

302. Nick McElhinny, S.A., D. Kumar, A.B. Clark, D.L. Watt, B.E. Watts, E.B. Lundstrom, E. Johansson, A. Chabes, and T.A. Kunkel. (2010a). Genome instability due to ribonucleotide incorporation into DNA. *Nat Chem Biol*. 6:774-781.

303. Nick McElhinny, S.A., B.E. Watts, D. Kumar, D.L. Watt, E.B. Lundstrom, P.M. Burgers, E. Johansson, A. Chabes, and T.A. Kunkel. (2010b). Abundant ribonucleotide incorporation into DNA by yeast replicative polymerases. *Proc Natl Acad Sci U S A*. 107:4949-4954.

304. Nijman, S.M., T.T. Huang, A.M. Dirac, T.R. Brummelkamp, R.M. Kerkhoven, A.D. D'Andrea, and R. Bernards. (2005). The deubiquitinating enzyme USP1 regulates the Fanconi anemia pathway. *Mol Cell*. 17:331-339.

305. Nimonkar, A.V., J. Genschel, E. Kinoshita, P. Polaczek, J.L. Campbell, C. Wyman, P. Modrich, and S.C. Kowalczykowski. (2011). BLM-DNA2-RPA-MRN and EXO1-BLM-RPA-MRN constitute two DNA end resection machineries for human DNA break repair. *Genes Dev*. 25:350-362.

306. Nitiss, J.L. (2009). Targeting DNA topoisomerase II in cancer chemotherapy. *Nat Rev Cancer*. 9:338-350.

307. Noordermeer, S.M., S. Adam, D. Setiaputra, M. Barazas, S.J. Pettitt, A.K. Ling, M. Olivieri, A. Alvarez-Quilon, N. Moatti, M. Zimmermann, S. Annunziato, D.B. Krastev, F. Song, I. Brandsma, J. Frankum, R. Brough, A. Sherker, S. Landry, R.K. Szilard, M.M. Munro, A. McEwan, T. Goullet de Rugy, Z.Y. Lin, T. Hart, J. Moffat, A.C. Gingras, A. Martin, H. van Attikum, J. Jonkers, C.J. Lord, S. Rottenberg, and D. Durocher. (2018). The shieldin complex mediates 53BP1-dependent DNA repair. *Nature*. 560:117-121.

308. O'Brien, J., I. Wilson, T. Orton, and F. Pognan. (2000). Investigation of the Alamar Blue (resazurin) fluorescent dye for the assessment of mammalian cell cytotoxicity. *Eur J Biochem*. 267:5421-5426.

309. O'Brien, P.J., A.G. Siraki, and N. Shangari. (2005). Aldehyde sources, metabolism, molecular toxicity mechanisms, and possible effects on human health. *Crit Rev Toxicol*. 35:609-662.

310. O'Leary, N.A., M.W. Wright, J.R. Brister, S. Ciufo, D. Haddad, R. McVeigh, B. Rajput, B. Robbertse, B. Smith-White, D. Ako-Adjei, A. Astashyn, A. Badretdin, Y. Bao, O. Blinkova, V. Brover, V. Chetvernin, J. Choi, E. Cox, O. Ermolaeva, C.M. Farrell, T. Goldfarb, T. Gupta, D. Haft, E. Hatcher, W. Hlavina, V.S. Joardar, V.K. Kodali, W. Li, D. Maglott, P. Masterson, K.M. McGarvey, M.R. Murphy, K. O'Neill, S. Pujar, S.H. Rangwala, D. Rausch, L.D. Riddick, C. Schoch, A. Shkeda, S.S. Storz, H. Sun, F. Thibaud-Nissen, I. Tolstoy, R.E. Tully, A.R. Vatsan, C. Wallin, D. Webb, W. Wu, M.J. Landrum, A. Kimchi, T. Tatusova, M. DiCuccio, P. Kitts, T.D. Murphy, and K.D. Pruitt. (2016). Reference sequence (RefSeq) database at NCBI: current status, taxonomic expansion, and functional annotation. *Nucleic Acids Res*. 44:D733-745.

311. O'Neil, N.J., M.L. Bailey, and P. Hieter. (2017). Synthetic lethality and cancer. *Nat Rev Genet*. 18:613-623.

312. Obayashi, Y., R. Fujikane, S. Morita, Y. Uechi, A. Hiraki, and M. Hidaka. (2021). Suppression of TopBP1 function increases the efficacy of chemotherapeutic treatments by enhancing the induction of apoptosis. *Oral Science International*. 18:209-216.

313. Ochi, T., A.N. Blackford, J. Coates, S. Jhujh, S. Mehmood, N. Tamura, J. Travers, Q. Wu, V.M. Draviam, C.V. Robinson, T.L. Blundell, and S.P. Jackson. (2015). DNA repair. PAXX, a paralog of XRCC4 and XLF, interacts with Ku to promote DNA double-strand break repair. *Science*. 347:185-188.

314. Oestergaard, V.H., F. Langevin, H.J. Kuiken, P. Pace, W. Niedzwiedz, L.J. Simpson, M. Ohzeki, M. Takata, J.E. Sale, and K.J. Patel. (2007). Deubiquitination of FANCD2 is required for DNA crosslink repair. *Mol Cell*. 28:798-809.

315. Ogi, T., S. Limsirichaikul, R.M. Overmeer, M. Volker, K. Takenaka, R. Cloney, Y. Nakazawa, A. Niimi, Y. Miki, N.G. Jaspers, L.H. Mullenders, S. Yamashita, M.I. Fousteri, and A.R. Lehmann. (2010). Three DNA polymerases, recruited by different mechanisms, carry out NER repair synthesis in human cells. *Mol Cell*. 37:714-727.

316. Oh, E., D. Akopian, and M. Rape. (2018). Principles of ubiquitin-dependent signaling. *Annu Rev Cell Dev Biol*. 34:137-162.

317. Olivieri, M., T. Cho, A. Alvarez-Quilon, K. Li, M.J. Schellenberg, M. Zimmermann, N. Hustedt, S.E. Rossi, S. Adam, H. Melo, A.M. Heijink, G. Sastre-Moreno, N. Moatti, R.K. Szilard, A. McEwan, A.K. Ling, A. Serrano-Benitez, T. Ubhi, S. Feng, J. Pawling, I.

Delgado-Sainz, M.W. Ferguson, J.W. Dennis, G.W. Brown, F. Cortes-Ledesma, R.S. Williams, A. Martin, D. Xu, and D. Durocher. (2020). A genetic map of the response to dna damage in human cells. *Cell*. 182:481-496 e421.

318. Olivieri, M., and D. Durocher. (2021). Genome-scale chemogenomic CRISPR screens in human cells using the TKOv3 library. *STAR Protoc*. 2:100321.

319. Olson, E., C.J. Nievera, V. Klimovich, E. Fanning, and X. Wu. (2006). RPA2 is a direct downstream target for ATR to regulate the S-phase checkpoint. *J Biol Chem*. 281:39517-39533.

320. Oshima, Y., Y. Sasaki, H. Negishi, M. Idogawa, M. Toyota, T. Yamashita, T. Wada, S. Nagoya, S. Kawaguchi, T. Yamashita, and T. Tokino. (2007). Antitumor effect of adenovirus-mediated p53 family gene transfer on osteosarcoma cell lines. *Cancer Biol Ther*. 6:1058-1066.

321. Paes Dias, M., V. Tripathi, I. van der Heijden, K. Cong, E.M. Manolika, J. Bhin, E. Gogola, P. Galanos, S. Annunziato, C. Lieftink, M. Andujar-Sanchez, S. Chakrabarty, G.C.M. Smith, M. van de Ven, R.L. Beijersbergen, J. Bartkova, S. Rottenberg, S. Cantor, J. Bartek, A. Ray Chaudhuri, and J. Jonkers. (2021). Loss of nuclear DNA ligase III reverts PARP inhibitor resistance in BRCA1/53BP1 double-deficient cells by exposing ssDNA gaps. *Mol Cell*. 81:4692-4708 e4699.

322. Paiano, J., N. Zolnerowich, W. Wu, R. Pavani, C. Wang, H. Li, L. Zheng, B. Shen, B.P. Sleckman, B.R. Chen, and A. Nussenzweig. (2021). Role of 53BP1 in end protection and DNA synthesis at DNA breaks. *Genes Dev*. 35:1356-1367.

323. Palombo, F., I. Iaccarino, E. Nakajima, M. Ikejima, T. Shimada, and J. Jiricny. (1996). hMutSbeta, a heterodimer of hMSH2 and hMSH3, binds to insertion/deletion loops in DNA. *Curr Biol*. 6:1181-1184.

324. Panzarino, N.J., J.J. Krais, K. Cong, M. Peng, M. Mosqueda, S.U. Nayak, S.M. Bond, J.A. Calvo, M.B. Doshi, M. Bere, J. Ou, B. Deng, L.J. Zhu, N. Johnson, and S.B. Cantor. (2021). Replication gaps underlie BRCA deficiency and therapy response. *Cancer Res*. 81:1388-1397.

325. Parsons, J.L., Dianova, II, and G.L. Dianov. (2004). APE1 is the major 3'-phosphoglycolate activity in human cell extracts. *Nucleic Acids Res*. 32:3531-3536.

326. Pascal, J.M., and T. Ellenberger. (2015). The rise and fall of poly(ADP-ribose): An enzymatic perspective. *DNA Repair (Amst)*. 32:10-16.

327. Plo, I., Z.Y. Liao, J.M. Barcelo, G. Kohlhagen, K.W. Caldecott, M. Weinfeld, and Y. Pommier. (2003). Association of XRCC1 and tyrosyl DNA phosphodiesterase (Tdp1) for the repair of topoisomerase I-mediated DNA lesions. *DNA Repair (Amst)*. 2:1087-1100.

328. Pluciennik, A., L. Dzantiev, R.R. Iyer, N. Constantin, F.A. Kadyrov, and P. Modrich. (2010). PCNA function in the activation and strand direction of MutLalpha endonuclease in mismatch repair. *Proc Natl Acad Sci U S A*. 107:16066-16071.

329. Pommier, Y. (2006). Topoisomerase I inhibitors: camptothecins and beyond. *Nat Rev Cancer*. 6:789-802.

330. Pommier, Y., S.Y. Huang, R. Gao, B.B. Das, J. Murai, and C. Marchand. (2014). Tyrosyl-DNA-phosphodiesterases (TDP1 and TDP2). *DNA Repair (Amst)*. 19:114-129.

331. Pommier, Y., Y. Sun, S.N. Huang, and J.L. Nitiss. (2016). Roles of eukaryotic topoisomerases in transcription, replication and genomic stability. *Nat Rev Mol Cell Biol*. 17:703-721.

332. Porro, A., M. Berti, J. Pizzolato, S. Bologna, S. Kaden, A. Saxer, Y. Ma, K. Nagasawa, A.A. Sartori, and J. Jiricny. (2017). FAN1 interaction with ubiquitylated PCNA alleviates

replication stress and preserves genomic integrity independently of BRCA2. *Nat Commun*. 8:1073.

333. Pourquier, P., L.M. Ueng, G. Kohlhagen, A. Mazumder, M. Gupta, K.W. Kohn, and Y. Pommier. (1997). Effects of uracil incorporation, DNA mismatches, and abasic sites on cleavage and religation activities of mammalian topoisomerase I. *J Biol Chem*. 272:7792-7796.

334. Prasad, R., W.A. Beard, P.R. Strauss, and S.H. Wilson. (1998). Human DNA polymerase beta deoxyribose phosphate lyase. Substrate specificity and catalytic mechanism. *J Biol Chem*. 273:15263-15270.

335. Price, N.E., K.M. Johnson, J. Wang, M.I. Fekry, Y. Wang, and K.S. Gates. (2014). Interstrand DNA-DNA cross-link formation between adenine residues and abasic sites in duplex DNA. *J Am Chem Soc*. 136:3483-3490.

336. Qiu, S., G. Jiang, L. Cao, and J. Huang. (2021). Replication fork reversal and protection. *Front Cell Dev Biol*. 9:670392.

337. Quinet, A., D. Carvajal-Maldonado, D. Lemacon, and A. Vindigni. (2017a). DNA fiber analysis: Mind the gap! *Methods Enzymol*. 591:55-82.

338. Quinet, A., D. Lemacon, and A. Vindigni. (2017b). Replication fork reversal: Players and guardians. *Mol Cell*. 68:830-833.

339. Quinet, A., S. Tirman, E. Cybulla, A. Meroni, and A. Vindigni. (2021). To skip or not to skip: choosing repriming to tolerate DNA damage. *Mol Cell*. 81:649-658.

340. Quinet, A., S. Tirman, J. Jackson, S. Svikovic, D. Lemacon, D. Carvajal-Maldonado, D. Gonzalez-Acosta, A.T. Vessoni, E. Cybulla, M. Wood, S. Tavis, L.F.Z. Batista, J. Mendez, J.E. Sale, and A. Vindigni. (2020). PRIMPOL-mediated adaptive response suppresses replication fork reversal in BRCA-deficient cells. *Mol Cell*. 77:461-474 e469.

341. Rack, J.G.M., L. Palazzo, and I. Ahel. (2020). (ADP-ribosyl)hydrolases: structure, function, and biology. *Genes Dev*. 34:263-284.

342. Rahighi, S., and I. Dikic. (2012). Selectivity of the ubiquitin-binding modules. *FEBS Lett*. 586:2705-2710.

343. Ramsden, D.A., J. Carvajal-Garcia, and G.P. Gupta. (2022). Mechanism, cellular functions and cancer roles of polymerase-theta-mediated DNA end joining. *Nat Rev Mol Cell Biol*. 23:125-140.

344. Ran, F.A., P.D. Hsu, J. Wright, V. Agarwala, D.A. Scott, and F. Zhang. (2013). Genome engineering using the CRISPR-Cas9 system. *Nat Protoc*. 8:2281-2308.

345. Rao, Q., M. Liu, Y. Tian, Z. Wu, Y. Hao, L. Song, Z. Qin, C. Ding, H.W. Wang, J. Wang, and Y. Xu. (2018). Cryo-EM structure of human ATR-ATRIP complex. *Cell Res*. 28:143-156.

346. Raschle, M., G. Smeenk, R.K. Hansen, T. Temu, Y. Oka, M.Y. Hein, N. Nagaraj, D.T. Long, J.C. Walter, K. Hofmann, Z. Storchova, J. Cox, S. Bekker-Jensen, N. Mailand, and M. Mann. (2015). DNA repair. Proteomics reveals dynamic assembly of repair complexes during bypass of DNA cross-links. *Science*. 348:1253671.

347. Rass, U., S.A. Compton, J. Matos, M.R. Singleton, S.C. Ip, M.G. Blanco, J.D. Griffith, and S.C. West. (2010). Mechanism of Holliday junction resolution by the human GEN1 protein. *Genes Dev*. 24:1559-1569.

348. Ray Chaudhuri, A., and A. Nussenzweig. (2017). The multifaceted roles of PARP1 in DNA repair and chromatin remodelling. *Nat Rev Mol Cell Biol*. 18:610-621.

349. Rehman, F.L., C.J. Lord, and A. Ashworth. (2010). Synthetic lethal approaches to breast cancer therapy. *Nat Rev Clin Oncol*. 7:718-724.

350. Reinking, H.K., H.S. Kang, M.J. Gotz, H.Y. Li, A. Kieser, S. Zhao, A.C. Acampora, P. Weickert, E. Fessler, L.T. Jae, M. Sattler, and J. Stingele. (2020). DNA structure-specific cleavage of DNA-protein crosslinks by the SPRTN protease. *Mol Cell*. 80:102-113 e106.

351. Renkawitz, J., C.A. Lademann, and S. Jentsch. (2014). Mechanisms and principles of homology search during recombination. *Nat Rev Mol Cell Biol*. 15:369-383.

352. Rothkamm, K., S. Barnard, J. Moquet, M. Ellender, Z. Rana, and S. Burdak-Rothkamm. (2015). DNA damage foci: Meaning and significance. *Environ Mol Mutagen*. 56:491-504.

353. Roy, U., and O.D. Scharer. (2016). Involvement of translesion synthesis DNA polymerases in DNA interstrand crosslink repair. *DNA Repair (Amst)*. 44:33-41.

354. Saini, N., S. Ramakrishnan, R. Elango, S. Ayyar, Y. Zhang, A. Deem, G. Ira, J.E. Haber, K.S. Lobachev, and A. Malkova. (2013). Migrating bubble during break-induced replication drives conservative DNA synthesis. *Nature*. 502:389-392.

355. Sakofsky, C.J., and A. Malkova. (2017). Break induced replication in eukaryotes: mechanisms, functions, and consequences. *Crit Rev Biochem Mol Biol*. 52:395-413.

356. Saldivar, J.C., D. Cortez, and K.A. Cimprich. (2017). The essential kinase ATR: ensuring faithful duplication of a challenging genome. *Nat Rev Mol Cell Biol*. 18:622-636.

357. Sale, J.E. (2012). Competition, collaboration and coordination – determining how cells bypass DNA damage. *J Cell Sci*. 125:1633-1643.

358. Sale, J.E. (2013). Translesion DNA synthesis and mutagenesis in eukaryotes. *Cold Spring Harb Perspect Biol*. 5:a012708.

359. San Filippo, J., P. Sung, and H. Klein. (2008). Mechanism of eukaryotic homologous recombination. *Annu Rev Biochem*. 77:229-257.

360. Sanjana, N.E., O. Shalem, and F. Zhang. (2014). Improved vectors and genome-wide libraries for CRISPR screening. *Nat Methods*. 11:783-784.

361. Sanson, K.R., R.E. Hanna, M. Hegde, K.F. Donovan, C. Strand, M.E. Sullender, E.W. Vaimberg, A. Goodale, D.E. Root, F. Piccioni, and J.G. Doench. (2018). Optimized libraries for CRISPR-Cas9 genetic screens with multiple modalities. *Nat Commun*. 9:5416.

362. Sarbajna, S., D. Davies, and S.C. West. (2014). Roles of SLX1-SLX4, MUS81-EME1, and GEN1 in avoiding genome instability and mitotic catastrophe. *Genes Dev*. 28:1124-1136.

363. Sartori, A.A., C. Lukas, J. Coates, M. Mistrik, S. Fu, J. Bartek, R. Baer, J. Lukas, and S.P. Jackson. (2007). Human CtIP promotes DNA end resection. *Nature*. 450:509-514.

364. Saxena, S., and L. Zou. (2022). Hallmarks of DNA replication stress. *Mol Cell*. 82:2298-2314.

365. Scharer, O.D. (2013). Nucleotide excision repair in eukaryotes. *Cold Spring Harb Perspect Biol*. 5:a012609.

366. Schellenberg, M.J., J.A. Lieberman, A. Herrero-Ruiz, L.R. Butler, J.G. Williams, A.M. Munoz-Cabello, G.A. Mueller, R.E. London, F. Cortes-Ledesma, and R.S. Williams. (2017). ZATT (ZNF451)-mediated resolution of topoisomerase 2 DNA-protein cross-links. *Science*. 357:1412-1416.

367. Schlacher, K., N. Christ, N. Siaud, A. Egashira, H. Wu, and M. Jasin. (2011). Double-strand break repair-independent role for BRCA2 in blocking stalled replication fork degradation by MRE11. *Cell*. 145:529-542.

368. Schonenberger, F., A. Deutzmann, E. Ferrando-May, and D. Merhof. (2015). Discrimination of cell cycle phases in PCNA-immunolabeled cells. *BMC Bioinformatics*. 16:180.

369. Schubert, L., I.A. Hendriks, E.P.T. Hertz, W. Wu, S. Selles-Baiget, S. Hoffmann, K.S. Viswalingam, I. Gallina, S. Pentakota, B. Benedict, J. Johansen, K. Apelt, M.S. Luijsterburg, S. Rasmussen, M. Lisby, Y. Liu, M.L. Nielsen, N. Mailand, and J.P. Duxin. (2022). SCAI promotes error-free repair of DNA interstrand crosslinks via the Fanconi anemia pathway. *EMBO Rep*. 23:e53639.

370. Scully, R., A. Panday, R. Elango, and N.A. Willis. (2019). DNA double-strand break repair-pathway choice in somatic mammalian cells. *Nat Rev Mol Cell Biol*. 20:698-714.

371. Sekiguchi, J., and S. Shuman. (1997). Site-specific ribonuclease activity of eukaryotic DNA topoisomerase I. *Mol Cell*. 1:89-97.

372. Semlow, D.R., and J.C. Walter. (2021). Mechanisms of vertebrate DNA interstrand cross-link repair. *Annu Rev Biochem*. 90:107-135.

373. Semlow, D.R., J. Zhang, M. Budzowska, A.C. Drohat, and J.C. Walter. (2016). Replication-dependent unhooking of DNA interstrand cross-links by the NEIL3 glycosylase. *Cell*. 167:498-511 e414.

374. Sfeir, A., and L.S. Symington. (2015). Microhomology-mediated end joining: A back-up survival mechanism or dedicated pathway? *Trends Biochem Sci*. 40:701-714.

375. Shalem, O., N.E. Sanjana, E. Hartenian, X. Shi, D.A. Scott, T. Mikkelson, D. Heckl, B.L. Ebert, D.E. Root, J.G. Doench, and F. Zhang. (2014). Genome-scale CRISPR-Cas9 knockout screening in human cells. *Science*. 343:84-87.

376. Shell, S.M., E.K. Hawkins, M.S. Tsai, A.S. Hlaing, C.J. Rizzo, and W.J. Chazin. (2013). Xeroderma pigmentosum complementation group C protein (XPC) serves as a general sensor of damaged DNA. *DNA Repair (Amst)*. 12:947-953.

377. Shrivastav, M., L.P. De Haro, and J.A. Nickoloff. (2008). Regulation of DNA double-strand break repair pathway choice. *Cell Res*. 18:134-147.

378. Shukla, V., L. Halabelian, S. Balagere, D. Samaniego-Castruita, D.E. Feldman, C.H. Arrowsmith, A. Rao, and L. Aravind. (2020). HMCES functions in the alternative end-joining pathway of the DNA DSB repair during class switch recombination in B cells. *Mol Cell*. 77:384-394 e384.

379. Siegel, D., H. Beall, C. Senekowitsch, M. Kasai, H. Arai, N.W. Gibson, and D. Ross. (1992). Bioreductive activation of mitomycin C by DT-diaphorase. *Biochemistry*. 31:7879-7885.

380. Sijacki, T., P. Alcon, Z.A. Chen, S.H. McLaughlin, S. Shakeel, J. Rappsilber, and L.A. Passmore. (2022). The DNA-damage kinase ATR activates the FANCD2-FANCI clamp by priming it for ubiquitination. *Nat Struct Mol Biol*. 29:881-890.

381. Simsek, D., E. Brunet, S.Y. Wong, S. Katyal, Y. Gao, P.J. McKinnon, J. Lou, L. Zhang, J. Li, E.J. Rebar, P.D. Gregory, M.C. Holmes, and M. Jasin. (2011). DNA ligase III promotes alternative nonhomologous end-joining during chromosomal translocation formation. *PLoS Genet*. 7:e1002080.

382. Smith, C.E., B. Llorente, and L.S. Symington. (2007). Template switching during break-induced replication. *Nature*. 447:102-105.

383. Sneeden, J.L., S.M. Grossi, I. Tappin, J. Hurwitz, and W.D. Heyer. (2013). Reconstitution of recombination-associated DNA synthesis with human proteins. *Nucleic Acids Res*. 41:4913-4925.

384. Song, L., and Z.Q. Luo. (2019). Post-translational regulation of ubiquitin signaling. *J Cell Biol*. 218:1776-1786.

385. Soniat, M.M., L.R. Myler, H.C. Kuo, T.T. Paull, and I.J. Finkelstein. (2019). RPA phosphorylation inhibits DNA resection. *Mol Cell*. 75:145-153 e145.

386. Sonneville, R., R. Bhowmick, S. Hoffmann, N. Mailand, I.D. Hickson, and K. Labib. (2019). TRAIP drives replisome disassembly and mitotic DNA repair synthesis at sites of incomplete DNA replication. *Elife*. 8.

387. Sparks, J.L., and P.M. Burgers. (2015). Error-free and mutagenic processing of topoisomerase 1-provoked damage at genomic ribonucleotides. *EMBO J*. 34:1259-1269.

388. Sparks, J.L., G. Chistol, A.O. Gao, M. Raschle, N.B. Larsen, M. Mann, J.P. Duxin, and J.C. Walter. (2019). The CMG helicase bypasses DNA-protein cross-links to facilitate their repair. *Cell*. 176:167-181 e121.

389. Sparks, J.L., H. Chon, S.M. Cerritelli, T.A. Kunkel, E. Johansson, R.J. Crouch, and P.M. Burgers. (2012). RNase H2-initiated ribonucleotide excision repair. *Mol Cell*. 47:980-986.

390. Stephan, H., C. Concannon, E. Kremmer, M.P. Carty, and H.P. Nasheuer. (2009). Ionizing radiation-dependent and independent phosphorylation of the 32-kDa subunit of replication protein A during mitosis. *Nucleic Acids Res*. 37:6028-6041.

391. Stingele, J., R. Bellelli, and S.J. Boulton. (2017). Mechanisms of DNA-protein crosslink repair. *Nat Rev Mol Cell Biol*. 18:563-573.

392. Stingele, J., and S. Jentsch. (2015). DNA-protein crosslink repair. *Nat Rev Mol Cell Biol*. 16:455-460.

393. Sturzenegger, A., K. Burdova, R. Kanagaraj, M. Levikova, C. Pinto, P. Cejka, and P. Janscak. (2014). DNA2 cooperates with the WRN and BLM RecQ helicases to mediate long-range DNA end resection in human cells. *J Biol Chem*. 289:27314-27326.

394. Su, D., X. Feng, M. Colic, Y. Wang, C. Zhang, C. Wang, M. Tang, T. Hart, and J. Chen. (2020). CRISPR/CAS9-based DNA damage response screens reveal gene-drug interactions. *DNA Repair (Amst)*. 87:102803.

395. Sugasawa, K., Y. Okuda, M. Saijo, R. Nishi, N. Matsuda, G. Chu, T. Mori, S. Iwai, K. Tanaka, K. Tanaka, and F. Hanaoka. (2005). UV-induced ubiquitylation of XPC protein mediated by UV-DDB-ubiquitin ligase complex. *Cell*. 121:387-400.

396. Sugawara, N., G. Ira, and J.E. Haber. (2000). DNA length dependence of the single-strand annealing pathway and the role of Saccharomyces cerevisiae RAD59 in double-strand break repair. *Mol Cell Biol*. 20:5300-5309.

397. Sun, Y., L.M. Miller Jenkins, Y.P. Su, K.C. Nitiss, J.L. Nitiss, and Y. Pommier. (2020a). A conserved SUMO pathway repairs topoisomerase DNA-protein cross-links by engaging ubiquitin-mediated proteasomal degradation. *Sci Adv*. 6.

398. Sun, Y., L.K. Saha, S. Saha, U. Jo, and Y. Pommier. (2020b). Debulking of topoisomerase DNA-protein crosslinks (TOP-DPC) by the proteasome, non-proteasomal and non-proteolytic pathways. *DNA Repair (Amst)*. 94:102926.

399. Sung, P., and H. Klein. (2006). Mechanism of homologous recombination: Mediators and helicases take on regulatory functions. *Nat Rev Mol Cell Biol*. 7:739-750.

400. Swatek, K.N., and D. Komander. (2016). Ubiquitin modifications. *Cell Res*. 26:399-422.

401. Sy, S.M., M.S. Huen, and J. Chen. (2009). PALB2 is an integral component of the BRCA complex required for homologous recombination repair. *Proc Natl Acad Sci U S A*. 106:7155-7160.

402. Symington, L.S. (2016). Mechanism and regulation of DNA end resection in eukaryotes. *Crit Rev Biochem Mol Biol*. 51:195-212.

403. Szklarczyk, D., A.L. Gable, D. Lyon, A. Junge, S. Wyder, J. Huerta-Cepas, M. Simonovic, N.T. Doncheva, J.H. Morris, P. Bork, L.J. Jensen, and C.V. Mering. (2019). STRING v11:

protein-protein association networks with increased coverage, supporting functional discovery in genome-wide experimental datasets. *Nucleic Acids Res*. 47:D607-D613.

404. Taglialatela, A., S. Alvarez, G. Leuzzi, V. Sannino, L. Ranjha, J.W. Huang, C. Madubata, R. Anand, B. Levy, R. Rabadan, P. Cejka, V. Costanzo, and A. Ciccia. (2017). Restoration of replication fork stability in BRCA1- and BRCA2-deficient cells by inactivation of SNF2-family fork remodelers. *Mol Cell*. 68:414-430 e418.

405. Taglialatela, A., G. Leuzzi, V. Sannino, R. Cuella-Martin, J.W. Huang, F. Wu-Baer, R. Baer, V. Costanzo, and A. Ciccia. (2021). REV1-Polzeta maintains the viability of homologous recombination-deficient cancer cells through mutagenic repair of PRIMPOL-dependent ssDNA gaps. *Mol Cell*. 81:4008-4025 e4007.

406. Takata, K., S. Reh, J. Tomida, M.D. Person, and R.D. Wood. (2013). Human DNA helicase HELQ participates in DNA interstrand crosslink tolerance with ATR and RAD51 paralogs. *Nat Commun*. 4:2338.

407. Takata, M., M.S. Sasaki, E. Sonoda, C. Morrison, M. Hashimoto, H. Utsumi, Y. Yamaguchi-Iwai, A. Shinohara, and S. Takeda. (1998). Homologous recombination and non-homologous end-joining pathways of DNA double-strand break repair have overlapping roles in the maintenance of chromosomal integrity in vertebrate cells. *EMBO J*. 17:5497-5508.

408. Tarsounas, M., and P. Sung. (2020). The antitumorigenic roles of BRCA1-BARD1 in DNA repair and replication. *Nat Rev Mol Cell Biol*. 21:284-299.

409. Taylor, M.R.G., and J.T.P. Yeeles. (2019). Dynamics of replication fork progression following helicase-polymerase uncoupling in eukaryotes. *J Mol Biol*. 431:2040-2049.

410. Thangavel, S., M. Berti, M. Levikova, C. Pinto, S. Gomathinayagam, M. Vujanovic, R. Zellweger, H. Moore, E.H. Lee, E.A. Hendrickson, P. Cejka, S. Stewart, M. Lopes, and A. Vindigni. (2015). DNA2 drives processing and restart of reversed replication forks in human cells. *J Cell Biol*. 208:545-562.

411. Thierry-Mieg, D., and J. Thierry-Mieg. (2006). AceView: a comprehensive cDNA-supported gene and transcripts annotation. *Genome Biol*. 7 Suppl 1:S12 11-14.

412. Thorslund, T., M.J. McIlwraith, S.A. Compton, S. Lekomtsev, M. Petronczki, J.D. Griffith, and S.C. West. (2010). The breast cancer tumor suppressor BRCA2 promotes the specific targeting of RAD51 to single-stranded DNA. *Nat Struct Mol Biol*. 17:1263-1265.

413. Tirman, S., A. Quinet, M. Wood, A. Meroni, E. Cybulla, J. Jackson, S. Pegoraro, A. Simoneau, L. Zou, and A. Vindigni. (2021). Temporally distinct post-replicative repair mechanisms fill PRIMPOL-dependent ssDNA gaps in human cells. *Mol Cell*. 81:4026-4040 e4028.

414. Toledo, L., K.J. Neelsen, and J. Lukas. (2017). Replication Catastrophe: When a Checkpoint Fails because of Exhaustion. *Mol Cell*. 66:735-749.

415. Toledo, L.I., M. Altmeyer, M.B. Rask, C. Lukas, D.H. Larsen, L.K. Povlsen, S. Bekker-Jensen, N. Mailand, J. Bartek, and J. Lukas. (2013). ATR prohibits replication catastrophe by preventing global exhaustion of RPA. *Cell*. 155:1088-1103.

416. Tounekti, O., A. Kenani, N. Foray, S. Orlowski, and L.M. Mir. (2001). The ratio of single- to double-strand DNA breaks and their absolute values determine cell death pathway. *Br J Cancer*. 84:1272-1279.

417. Tran, P.T., N. Erdeniz, L.S. Symington, and R.M. Liskay. (2004). EXO1 – A multi-tasking eukaryotic nuclease. *DNA Repair (Amst)*. 3:1549-1559.

418. Traut, T.W. (1994). Physiological concentrations of purines and pyrimidines. *Mol Cell Biochem*. 140:1-22.

419. Trenner, A., and A.A. Sartori. (2019). Harnessing DNA double-strand break repair for cancer treatment. *Front Oncol.* 9:1388.

420. Truong, L.N., Y. Li, L.Z. Shi, P.Y. Hwang, J. He, H. Wang, N. Razavian, M.W. Berns, and X. Wu. (2013). Microhomology-mediated End Joining and Homologous Recombination share the initial end resection step to repair DNA double-strand breaks in mammalian cells. *Proc Natl Acad Sci U S A.* 110:7720-7725.

421. Tsherniak, A., F. Vazquez, P.G. Montgomery, B.A. Weir, G. Kryukov, G.S. Cowley, S. Gill, W.F. Harrington, S. Pantel, J.M. Krill-Burger, R.M. Meyers, L. Ali, A. Goodale, Y. Lee, G. Jiang, J. Hsiao, W.F.J. Gerath, S. Howell, E. Merkel, M. Ghandi, L.A. Garraway, D.E. Root, T.R. Golub, J.S. Boehm, and W.C. Hahn. (2017). Defining a cancer dependency map. *Cell.* 170:564-576 e516.

422. Tsodikov, O.V., D. Ivanov, B. Orelli, L. Staresincic, I. Shoshani, R. Oberman, O.D. Scharer, G. Wagner, and T. Ellenberger. (2007). Structural basis for the recruitment of ERCC1-XPF to nucleotide excision repair complexes by XPA. *EMBO J.* 26:4768-4776.

423. Tzelepis, K., H. Koike-Yusa, E. De Braekeleer, Y. Li, E. Metzakopian, O.M. Dovey, A. Mupo, V. Grinkevich, M. Li, M. Mazan, M. Gozdecka, S. Ohnishi, J. Cooper, M. Patel, T. McKerrell, B. Chen, A.F. Domingues, P. Gallipoli, S. Teichmann, H. Ponstingl, U. McDermott, J. Saez-Rodriguez, B.J.P. Huntly, F. Iorio, C. Pina, G.S. Vassiliou, and K. Yusa. (2016). A CRISPR Dropout Screen Identifies Genetic Vulnerabilities and Therapeutic Targets in Acute Myeloid Leukemia. *Cell Rep.* 17:1193-1205.

424. Vallerga, M.B., S.F. Mansilla, M.B. Federico, A.P. Bertolin, and V. Gottifredi. (2015). Rad51 recombinase prevents Mre11 nuclease-dependent degradation and excessive PrimPol-mediated elongation of nascent DNA after UV irradiation. *Proc Natl Acad Sci U S A.* 112:E6624-6633.

425. van de Kooij, B., and H. van Attikum. (2021). Genomic reporter constructs to monitor pathway-specific repair of DNA double-strand breaks. *Front Genet.* 12:809832.

426. van den Heuvel, D., Y. van der Weegen, D.E.C. Boer, T. Ogi, and M.S. Luijsterburg. (2021). Transcription-coupled DNA repair: From mechanism to human disorder. *Trends Cell Biol.* 31:359-371.

427. van der Weegen, Y., H. Golan-Berman, T.E.T. Mevissen, K. Apelt, R. Gonzalez-Prieto, J. Goedhart, E.E. Heilbrun, A.C.O. Vertegaal, D. van den Heuvel, J.C. Walter, S. Adar, and M.S. Luijsterburg. (2020). The cooperative action of CSB, CSA, and UVSSA target TFIIH to DNA damage-stalled RNA polymerase II. *Nat Commun.* 11:2104.

428. Van Dyck, E., A.Z. Stasiak, A. Stasiak, and S.C. West. (1999). Binding of double-strand breaks in DNA by human Rad52 protein. *Nature.* 398:728-731.

429. van Twest, S., V.J. Murphy, C. Hodson, W. Tan, P. Swuec, J.J. O'Rourke, J. Heierhorst, W. Crismani, and A.J. Deans. (2017). Mechanism of ubiquitination and deubiquitination in the Fanconi anemia pathway. *Mol Cell.* 65:247-259.

430. van Wietmarschen, N., S. Sridharan, W.J. Nathan, A. Tubbs, E.M. Chan, E. Callen, W. Wu, F. Belinky, V. Tripathi, N. Wong, K. Foster, J. Noorbakhsh, K. Garimella, A. Cruz-Migoni, J.A. Sommers, Y. Huang, A.A. Borah, J.T. Smith, J. Kalfon, N. Kesten, K. Fugger, R.L. Walker, E. Dolzhenko, M.A. Eberle, B.E. Hayward, K. Usdin, C.H. Freudenreich, R.M. Brosh, Jr., S.C. West, P.J. McHugh, P.S. Meltzer, A.J. Bass, and A. Nussenzweig. (2020). Repeat expansions confer WRN dependence in microsatellite-unstable cancers. *Nature.* 586:292-298.

431. Vassin, V.M., M.S. Wold, and J.A. Borowiec. (2004). Replication protein A (RPA) phosphorylation prevents RPA association with replication centers. *Mol Cell Biol.* 24:1930-1943.

432. Vermeulen, W., and M. Fousteri. (2013). Mammalian transcription-coupled excision repair. *Cold Spring Harb Perspect Biol*. 5:a012625.

433. Vizeacoumar, F.J., R. Arnold, F.S. Vizeacoumar, M. Chandrashekhar, A. Buzina, J.T. Young, J.H. Kwan, A. Sayad, P. Mero, S. Lawo, H. Tanaka, K.R. Brown, A. Baryshnikova, A.B. Mak, Y. Fedyshyn, Y. Wang, G.C. Brito, D. Kasimer, T. Makhnevych, T. Ketela, A. Datti, M. Babu, A. Emili, L. Pelletier, J. Wrana, Z. Wainberg, P.M. Kim, R. Rottapel, C.A. O'Brien, B. Andrews, C. Boone, and J. Moffat. (2013). A negative genetic interaction map in isogenic cancer cell lines reveals cancer cell vulnerabilities. *Mol Syst Biol*. 9:696.

434. Vu, T.V., S. Das, C.C. Nguyen, J. Kim, and J.Y. Kim. (2022). Single-strand annealing: Molecular mechanisms and potential applications in CRISPR-Cas-based precision genome editing. *Biotechnol J*. 17:e2100413.

435. Vujanovic, M., J. Krietsch, M.C. Raso, N. Terraneo, R. Zellweger, J.A. Schmid, A. Taglialatela, J.W. Huang, C.L. Holland, K. Zwicky, R. Herrador, H. Jacobs, D. Cortez, A. Ciccia, L. Penengo, and M. Lopes. (2017). Replication fork slowing and reversal upon DNA damage require PCNA polyubiquitination and ZRANB3 DNA translocase activity. *Mol Cell*. 67:882-890 e885.

436. Walker, J.R., R.A. Corpina, and J. Goldberg. (2001). Structure of the Ku heterodimer bound to DNA and its implications for double-strand break repair. *Nature*. 412:607-614.

437. Walton, R.T., K.A. Christie, M.N. Whittaker, and B.P. Kleinstiver. (2020). Unconstrained genome targeting with near-PAMless engineered CRISPR-Cas9 variants. *Science*. 368:290-296.

438. Wang, F., Y. Zhao, Y. Hao, and Z. Tan. (2008). Identification of low-abundance alternatively spliced mRNA variants by exon exclusive reverse transcriptase polymerase chain reaction. *Anal Biochem*. 383:307-310.

439. Wang, H., L.Z. Shi, C.C. Wong, X. Han, P.Y. Hwang, L.N. Truong, Q. Zhu, Z. Shao, D.J. Chen, M.W. Berns, J.R. Yates, 3rd, L. Chen, and X. Wu. (2013). The interaction of CtIP and Nbs1 connects CDK and ATM to regulate HR-mediated double-strand break repair. *PLoS Genet*. 9:e1003277.

440. Wang, M., W. Wu, W. Wu, B. Rosidi, L. Zhang, H. Wang, and G. Iliakis. (2006). PARP-1 and Ku compete for repair of DNA double strand breaks by distinct NHEJ pathways. *Nucleic Acids Res*. 34:6170-6182.

441. Wang, R., S. Wang, A. Dhar, C. Peralta, and N.P. Pavletich. (2020). DNA clamp function of the monoubiquitinated Fanconi anaemia ID complex. *Nature*. 580:278-282.

442. Wang, S., R. Wang, C. Peralta, A. Yaseen, and N.P. Pavletich. (2021). Structure of the FA core ubiquitin ligase closing the ID clamp on DNA. *Nat Struct Mol Biol*. 28:300-309.

443. Wang, T., K. Birsoy, N.W. Hughes, K.M. Krupczak, Y. Post, J.J. Wei, E.S. Lander, and D.M. Sabatini. (2015). Identification and characterization of essential genes in the human genome. *Science*. 350:1096-1101.

444. Wardlaw, C.P., A.M. Carr, and A.W. Oliver. (2014). TopBP1: A BRCT-scaffold protein functioning in multiple cellular pathways. *DNA Repair (Amst)*. 22:165-174.

445. Waters, L.S., B.K. Minesinger, M.E. Wiltrout, S. D'Souza, R.V. Woodruff, and G.C. Walker. (2009). Eukaryotic translesion polymerases and their roles and regulation in DNA damage tolerance. *Microbiol Mol Biol Rev*. 73:134-154.

446. Weickert, P., and J. Stingele. (2022). DNA-protein crosslinks and their resolution. *Annu Rev Biochem*. 91:157-181.

447. West, S.C. (2003). Molecular views of recombination proteins and their control. *Nat Rev Mol Cell Biol*. 4:435-445.

448. West, S.C., M.G. Blanco, Y.W. Chan, J. Matos, S. Sarbajna, and H.D. Wyatt. (2015). Resolution of recombination intermediates: Mechanisms and regulation. *Cold Spring Harb Symp Quant Biol.* 80:103-109.

449. Whitehouse, C.J., R.M. Taylor, A. Thistlethwaite, H. Zhang, F. Karimi-Busheri, D.D. Lasko, M. Weinfeld, and K.W. Caldecott. (2001). XRCC1 stimulates human polynucleotide kinase activity at damaged DNA termini and accelerates DNA single-strand break repair. *Cell.* 104:107-117.

450. Williams, J.S., D.J. Smith, L. Marjavaara, S.A. Lujan, A. Chabes, and T.A. Kunkel. (2013). Topoisomerase 1-mediated removal of ribonucleotides from nascent leading-strand DNA. *Mol Cell.* 49:1010-1015.

451. Willis, N.A., R.L. Frock, F. Menghi, E.E. Duffey, A. Panday, V. Camacho, E.P. Hasty, E.T. Liu, F.W. Alt, and R. Scully. (2017). Mechanism of tandem duplication formation in BRCA1-mutant cells. *Nature.* 551:590-595.

452. Wojtaszek, J.L., N. Chatterjee, J. Najeeb, A. Ramos, M. Lee, K. Bian, J.Y. Xue, B.A. Fenton, H. Park, D. Li, M.T. Hemann, J. Hong, G.C. Walker, and P. Zhou. (2019). A small molecule targeting mutagenic translesion synthesis improves chemotherapy. *Cell.* 178:152-159 e111.

453. Wold, M.S. (1997). Replication protein A: a heterotrimeric, single-stranded DNA-binding protein required for eukaryotic DNA metabolism. *Annu Rev Biochem.* 66:61-92.

454. Wright, W.D., and W.D. Heyer. (2014). Rad54 functions as a heteroduplex DNA pump modulated by its DNA substrates and Rad51 during D loop formation. *Mol Cell.* 53:420-432.

455. Wu, L., and I.D. Hickson. (2003). The Bloom's syndrome helicase suppresses crossing over during homologous recombination. *Nature.* 426:870-874.

456. Wu, R.A., D.R. Semlow, A.N. Kamimae-Lanning, O.V. Kochenova, G. Chistol, M.R. Hodskinson, R. Amunugama, J.L. Sparks, M. Wang, L. Deng, C.A. Mimoso, E. Low, K.J. Patel, and J.C. Walter. (2019). TRAIP is a master regulator of DNA interstrand crosslink repair. *Nature.* 567:267-272.

457. Wu, Y., N. Kantake, T. Sugiyama, and S.C. Kowalczykowski. (2008). Rad51 protein controls Rad52-mediated DNA annealing. *J Biol Chem.* 283:14883-14892.

458. Wyatt, D.W., W. Feng, M.P. Conlin, M.J. Yousefzadeh, S.A. Roberts, P. Mieczkowski, R.D. Wood, G.P. Gupta, and D.A. Ramsden. (2016). Essential roles for polymerase theta-mediated end joining in the repair of chromosome breaks. *Mol Cell.* 63:662-673.

459. Wyatt, H.D., S. Sarbajna, J. Matos, and S.C. West. (2013). Coordinated actions of SLX1-SLX4 and MUS81-EME1 for Holliday junction resolution in human cells. *Mol Cell.* 52:234-247.

460. Xie, A., A. Kwok, and R. Scully. (2009). Role of mammalian Mre11 in classical and alternative nonhomologous end joining. *Nat Struct Mol Biol.* 16:814-818.

461. Yaneva, D., J.L. Sparks, M. Donsbach, S. Zhao, P. Weickert, R. Bezalel-Buch, J. Stingele, and J.C. Walter. (2023). The FANCJ helicase unfolds DNA-protein crosslinks to promote their repair. *Mol Cell.* 83:43-56 e10.

462. Yates, M., and A. Marechal. (2018). Ubiquitylation at the fork: Making and breaking chains to complete DNA replication. *Int J Mol Sci.* 19:2909-2909.

463. Yau, R., and M. Rape. (2016). The increasing complexity of the ubiquitin code. *Nat Cell Biol.* 18:579-586.

464. Yekezare, M., B. Gomez-Gonzalez, and J.F. Diffley. (2013). Controlling DNA replication origins in response to DNA damage - inhibit globally, activate locally. *J Cell Sci.* 126:1297-1306.

465. Yi, C., and C. He. (2013). DNA repair by reversal of DNA damage. *Cold Spring Harb Perspect Biol.* 5:a012575.

466. Yin, Y., W.T.C. Lee, D. Gupta, H. Xue, P. Tonzi, J.A. Borowiec, T.T. Huang, M. Modesti, and E. Rothenberg. (2021). A basal-level activity of ATR links replication fork surveillance and stress response. *Mol Cell.* 81:4243-4257 e4246.

467. Yokoi, M., C. Masutani, T. Maekawa, K. Sugasawa, Y. Ohkuma, and F. Hanaoka. (2000). The xeroderma pigmentosum group C protein complex XPC-HR23B plays an important role in the recruitment of transcription factor IIH to damaged DNA. *J Biol Chem.* 275:9870-9875.

468. Zahn, K.E., A.M. Averill, P. Aller, R.D. Wood, and S. Doublie. (2015). Human DNA polymerase theta grasps the primer terminus to mediate DNA repair. *Nat Struct Mol Biol.* 22:304-311.

469. Zellweger, R., D. Dalcher, K. Mutreja, M. Berti, J.A. Schmid, R. Herrador, A. Vindigni, and M. Lopes. (2015). Rad51-mediated replication fork reversal is a global response to genotoxic treatments in human cells. *J Cell Biol.* 208:563-579.

470. Zeman, M.K., and K.A. Cimprich. (2014). Causes and consequences of replication stress. *Nat Cell Biol.* 16:2-9.

471. Zhang, F., J. Ma, J. Wu, L. Ye, H. Cai, B. Xia, and X. Yu. (2009). PALB2 links BRCA1 and BRCA2 in the DNA-damage response. *Curr Biol.* 19:524-529.

472. Zhang, H., C.J. Koch, C.A. Wallen, and K.T. Wheeler. (1995). Radiation-induced DNA damage in tumors and normal tissues. III. Oxygen dependence of the formation of strand breaks and DNA-protein crosslinks. *Radiat Res.* 142:163-168.

473. Zhang, J., J.M. Dewar, M. Budzowska, A. Motnenko, M.A. Cohn, and J.C. Walter. (2015). DNA interstrand cross-link repair requires replication-fork convergence. *Nat Struct Mol Biol.* 22:242-247.

474. Zhao, B., E. Rothenberg, D.A. Ramsden, and M.R. Lieber. (2020). The molecular basis and disease relevance of non-homologous DNA end joining. *Nat Rev Mol Cell Biol.* 21:765-781.

475. Zhao, H., J.L. Watkins, and H. Piwnica-Worms. (2002). Disruption of the checkpoint kinase 1/cell division cycle 25A pathway abrogates ionizing radiation-induced S and G2 checkpoints. *Proc Natl Acad Sci U S A.* 99:14795-14800.

476. Zhao, W., J.B. Steinfeld, F. Liang, X. Chen, D.G. Maranon, C. Jian Ma, Y. Kwon, T. Rao, W. Wang, C. Sheng, X. Song, Y. Deng, J. Jimenez-Sainz, L. Lu, R.B. Jensen, Y. Xiong, G.M. Kupfer, C. Wiese, E.C. Greene, and P. Sung. (2017). BRCA1-BARD1 promotes RAD51-mediated homologous DNA pairing. *Nature.* 550:360-365.

477. Zhao, W., S. Vaithiyalingam, J. San Filippo, D.G. Maranon, J. Jimenez-Sainz, G.V. Fontenay, Y. Kwon, S.G. Leung, L. Lu, R.B. Jensen, W.J. Chazin, C. Wiese, and P. Sung. (2015). Promotion of BRCA2-dependent homologous recombination by DSS1 via RPA targeting and DNA mimicry. *Mol Cell.* 59:176-187.

478. Zhu, Z., W.H. Chung, E.Y. Shim, S.E. Lee, and G. Ira. (2008). Sgs1 helicase and two nucleases Dna2 and Exo1 resect DNA double-strand break ends. *Cell.* 134:981-994.

479. Zimmermann, M., O. Murina, M.A.M. Reijns, A. Agathanggelou, R. Challis, Z. Tarnauskaite, M. Muir, A. Fluteau, M. Aregger, A. McEwan, W. Yuan, M. Clarke, M.B. Lambros, S. Paneesha, P. Moss, M. Chandrashekhar, S. Angers, J. Moffat, V.G. Brunton, T. Hart, J. de Bono, T. Stankovic, A.P. Jackson, and D. Durocher. (2018). CRISPR screens identify genomic ribonucleotides as a source of PARP-trapping lesions. *Nature.* 559:285-289.

480. Zong, W., Y. Gong, W. Sun, T. Li, and Z.Q. Wang. (2022). PARP1: Liaison of chromatin remodeling and transcription. *Cancers (Basel)*. 14:4162.

481. Zou, L., and S.J. Elledge. (2003). Sensing DNA damage through ATRIP recognition of RPA-ssDNA complexes. *Science*. 300:1542-1548.

Appendices

Appendix A. Primary antibodies

Antibody	Species	Clonality	Dilution WB	Dilution IF	Source	RRID	Identifier
ZUP1	Mouse	Monoclonal	1:750	n/a	DC Biosciences	n/a	Custom from DCB-GTA-1972 project
ZUP1	Rabbit	Polyclonal	1:1,000	n/a	Cambridge Bioscience	AB_10960887	HPA044426
Vinculin-HRP	Mouse	Monoclonal	1:10,000	n/a	Santa Cruz Biotechnology	AB_1131294	sc-73614-HRP
RPA2 (pT21)	Rabbit	Monoclonal	1:5,000	1:500	Abcam	AB_10860648	ab109394
RPA2 (pS4/8)	Rabbit	Polyclonal	1:5,000	1:500	Cambridge Bioscience	AB_210547	A300-245A
RPA2 (pS33)	Rabbit	Polyclonal	1:5,000	1:2,000	Cambridge Bioscience	AB_2180847	A300-246A
FANCD2	Rabbit	Polyclonal	1:1,000	n/a	Novus Biologicals	AB_10002867	NB100-182
CHK1	Mouse	Monoclonal	1:1,000	n/a	Cell Signaling Technology	AB_2080320	2360S
pCHK1 (S317)	Rabbit	Monoclonal	1:1,000	n/a	Cell Signaling Technology	AB_2783865	12302S
FLAG-HRP	Mouse	Monoclonal	1:10,000	n/a	Sigma-Aldrich (Merck)	AB_439702	A8592
RPA2	Mouse	Monoclonal	n/a	1:500	Abcam	AB_302873	ab2175
PCNA	Rabbit	Polyclonal	n/a	1:500	Abcam	AB_444313	ab18197
MCM3	Mouse	Monoclonal	n/a	1:500	Santa Cruz Biotechnology	n/a	sc-390480
RAD51	Rabbit	Monoclonal	n/a	1:500	Abcam	AB_2722613	ab133534
RPA1	Rabbit	Monoclonal	n/a	1:1,000	Abcam	AB_1603759	ab79398
BrdU	Mouse	Monoclonal	n/a	1:200	GE Healthcare	AB_2314032	GERPN202

Appendix B. Secondary antibodies

Antibody	Species	Clonality	Dilution IB	Dilution IF	Source	RRID	Identifier
Anti-mouse HRP	Donkey	Polyclonal	1:2,000	n/a	Jackson ImmunoResearch	AB_2340770	715-035-150-JIR
Anti-rabbit HRP	Donkey	Polyclonal	1:2,000	n/a	Jackson ImmunoResearch	AB_10015282	711-035-152-JIR
Anti-mouse Alexa Fluor 488	Donkey	Polyclonal	n/a	1:500	Thermo Fisher Scientific	AB_141607	A21202
Anti-rabbit Alexa Fluor 488	Donkey	Polyclonal	n/a	1:500	Thermo Fisher Scientific	AB_2535792	A21206
Anti-mouse Alexa Fluor 555	Donkey	Polyclonal	n/a	1:500	Thermo Fisher Scientific	AB_2536180	A31570
Anti-rabbit Alexa Fluor 555	Donkey	Polyclonal	n/a	1:500	Thermo Fisher Scientific	AB_162543	A31572

Appendix C. Chemicals, peptides, and recombinant proteins

Reagent or resource	Source	Identifier
Dulbecco's Modified Eagle Medium	Gibco	31966047
Fetal Bovine Serum	Gibco	10270106
TrypLE Express Enzyme (1X), phenol red	Gibco	12605010
Opti-MEM Reduced Serum Medium	Gibco	51985026
TransIT-LT1 Transfection Reagent	Mirus	MIR 2300
Puromycin Dihydrochloride (10 mg/ml)	Gibco	A1113803
FastDigest BbsI (BpiI)	Thermo Fisher Scientific	10569110
FastDigest BsmBI (Esp3I)	Thermo Fisher Scientific	10620301
Hygromycin B (50 mg/mL)	Thermo Fisher Scientific	10687010
UltraPure 1M Tris-HCI, pH 8.0	Thermo Fisher Scientific	15568025
Triton X-100	Sigma-Aldrich (Merck)	T8787
Dithiothreitol (DTT)	Thermo Fisher Scientific	10578170

Reagent or resource	Source	Identifier
Protease Inhibitor Cocktail	Sigma-Aldrich (Merck)	P2714
Sodium Orthovanadate	Sigma-Aldrich (Merck)	S6508
N-Ethylmaleimide (NEM)	Sigma-Aldrich (Merck)	E1271
Sodium fluoride (NaF)	Sigma-Aldrich (Merck)	201154
β-Glycerophosphate	Sigma-Aldrich (Merck)	G9422
Benzonase Nuclease	Sigma-Aldrich (Merck)	E1014-5KU
NuPAGE LDS Sample Buffer (4X)	Thermo Fisher Scientific	NP0008
NuPAGE 4-12% Bis-Tris Midi Protein Gels, 26-well	Thermo Fisher Scientific	WG1403BOX
NuPAGE 8% Bis-Tris Midi Protein Gels, 26-well	Thermo Fisher Scientific	WG1003BOX
NuPAGE MOPS SDS Running Buffer (20X)	Thermo Fisher Scientific	NP0001
Trans-Blot Turbo Midi Nitrocellulose Transfer Packs	Bio-Rad	1704159
Trans-Blot Turbo Midi PVDF Transfer Packs	Bio-Rad	1704157
TWEEN 20	Sigma-Aldrich (Merck)	P1379
Clarity Western ECL Substrate	Bio-Rad	1705061
Pierce ECL Western Blotting Substrate	Thermo Fisher Scientific	32209
Amersham Hyperfilm ECL	GE Healthcare	28-9068-37
ReBlot Plus Strong Antibody Stripping Solution, 10x	Sigma-Aldrich (Merck)	2504
QuickExtract DNA Extraction Solution	Lucigen	QE09050
Q5 High-Fidelity 2X Master Mix	New England Biolabs	M0492L
SuperScript IV First-Strand Synthesis System with ezDNase Enzyme	Thermo Fisher Scientific	18091150
UltraPure Agarose	Thermo Fisher Scientific	16500100
cis-Diammineplatinum(II) dichloride (cisplatin)	Sigma-Aldrich (Merck)	P4394
Pierce 16% Formaldehyde (w/v), Methanol-free	Thermo Fisher Scientific	28906
MMC from Streptomyces caespitosus	Sigma-Aldrich (Merck)	M4287
Olaparib	Enzo Life Sciences	LKT-O4402-M005
Talazoparib	Selleck Chemicals	S7048

Reagent or resource	**Source**	**Identifier**
Hydroxyurea	Sigma-Aldrich (Merck)	H8627
Topotecan hydrochloride	Tocris	4562/50
AZD6738 (ATRi)	ApexBio	B6007
NMS-873 (p97i)	Selleck Chemicals	S7285
Crystal Violet	Sigma-Aldrich (Merck)	C0775
Blasticidin S HCl (10 mg/mL)	Thermo Fisher Scientific	A1113903
MOWIOL 4-88 Reagent	Sigma-Aldrich (Merck)	475904
5-Bromo-2′-deoxyuridine (BrdU)	Sigma-Aldrich (Merck)	B9285
Lipofectamine RNAiMAX Transfection Reagent	Thermo Fisher Scientific	13778075
NEBuilder HiFi DNA Assembly Master Mix	New England Biolabs	E2621S
Gateway LR Clonase II Enzyme Mix	Thermo Fisher Scientific	11791020
Wizard Genomic DNA Purification Kit	Promega	A1120
PureLink RNase A	Thermo Fisher Scientific	12091021
NEBNext Ultra II Q5 Master Mix	New England Biolabs	M0544

Appendix D. Experimental models

Reagent or resource	Source	Identifier
U2OS	ATCC	HTB-96
U2OS ZUP1 KO	This study	n/a
U2OS pLenti-PGK-Hygro EV	This study	n/a
U2OS pLenti-PGK-Hygro ZUP1 WT	This study	n/a
U2OS ZUP1 KO pLenti-PGK-Hygro EV	This study	n/a
U2OS ZUP1 KO pLenti-PGK-Hygro ZUP1 WT	This study	n/a
U2OS ZUP1 KO pLenti-PGK-Hygro ZUP1 C360R	This study	n/a
U2OS ZUP1 KO pLenti-PGK-Hygro ZUP1 Δα2/3	This study	n/a
U2OS lentiCas9-Blast	This study	n/a
U2OS ZUP1 KO lentiCas9-Blast	This study	n/a
HEK293T	ATCC	CRL-3216

Appendix E. Oligonucleotides

Reagent or resource	Source	Identifier
TOPBP1 (SMARTpool: ON-TARGETplus)	Horizon Discovery	L-012358-00-0005
ETAA1 (SMARTpool: ON-TARGETplus)	Horizon Discovery	L-021193-01-0005
RFWD3 (SMARTpool: ON-TARGETplus)	Horizon Discovery	L-017095-00-0005
CTRL (ON-TARGETplus Non-targeting Control Pool)	Horizon Discovery	D-001810-10-20

Appendix F. Primer sequences

Reagent or resource	Sequence
sgZUP1_Ex2_1	TCCAGCCTGACCGAAATAAA
sgZUP1_Ex6_2	AACAGTTGTACTTTATGTGC
sgZUP1_Ex6_3	TATGTACTCGGGGAACTTTA
ZUP1_Ex6_FWD_1	ATTGGGAGCAAATTGATTAAGACTG
ZUP1_Ex6_REV_1	GCCCCCTGAGGATCAAAAC
ZUP1_Ex6_REV_2	CAGATGACAAGTTCAGAGTACTAG
ZUP1_Ex6_Seq_FWD	CTTGGACTGTAGTAACAAGC
ZUP1_Ex2_FWD_1	AATCCAGCGTTAAAGACCAAGT
ZUP1_Ex2_REV_1	GAGTCCAGGACAGTCCAGATGC
ZUP1_Ex2_Cleavage_1	ACCTGACTAAAGATAGTACTTTAAAACATGAAcc
ZUP1_Ex3_Cleavage_1	CCTATGTGTGGGCTCATATGTACAAATTACCAcc
ZUP1_Ex7_Cleavage_1	TCTATGATTGAAGATGCATGGAAGGAAGGTTTcc
ZUP1_Ex1_FWD_1	TCAGTCATCAGGCCAGGAGA
ZUP1_Ex6_REV_3	ACCACAACCCCAACCTTTGT
sgHELQ	TTATCTCTTACCTTCGAGC
sgNEIL3	ATGGATCAGAACGTATTGCC
sgBRCA2	GTCTACCTGACCAATCGATG
sgBRIP1	AGTTACCGACTACCTCAGGA
sgLacZ	CCCGAATCTCTATCGTGCGG
lentiGuide-Puro_FWD	tcctggaccgACCGAGTACAAGCCCACG
lentiGuide-Puro_REV	tagaaccggtGGTGGCCGTACGTCACGA
GFP-NLS-P2A_FWD	tacggccaccACCGGTTCTAGAGCGCTG
GFP-NLS-P2A_REV	tgtactcggtCGGTCCAGGATTCTCTTCG
mCherry-NLS-P2A_FWD	tacggccaccACCGGTTCTAGAGCGCTG
mCherry-NLS-P2A_REV	tgtactcggtCGGTCCAGGATTCTCTTCG

Reagent or resource	Sequence
PCR1_LCV2_FWD	GAGGGCCTATTTCCCATGATTC
PCR1_LCV2_REV	GTTGCGAAAAAGAACGTTCACGG
PCR2_FWD_01	AATGATACGGCGACCACCGAGATCTACACTCTTTCCCTACACG ACGCTCTTCCGATCTttcttgtggaaaggacgaaacaccg
PCR2_FWD_02	AATGATACGGCGACCACCGAGATCTACACTCTTTCCCTACACG ACGCTCTTCCGATCTattcttgtggaaaggacgaaacaccg
PCR2_FWD_03	AATGATACGGCGACCACCGAGATCTACACTCTTTCCCTACACG ACGCTCTTCCGATCTgattcttgtggaaaggacgaaacaccg
PCR2_FWD_04	AATGATACGGCGACCACCGAGATCTACACTCTTTCCCTACACG ACGCTCTTCCGATCTcgattcttgtggaaaggacgaaacaccg
PCR2_FWD_05	AATGATACGGCGACCACCGAGATCTACACTCTTTCCCTACACG ACGCTCTTCCGATCTtcgattcttgtggaaaggacgaaacaccg
PCR2_FWD_06	AATGATACGGCGACCACCGAGATCTACACTCTTTCCCTACACG ACGCTCTTCCGATCTatcgattcttgtggaaaggacgaaacaccg
PCR2_FWD_07	AATGATACGGCGACCACCGAGATCTACACTCTTTCCCTACACG ACGCTCTTCCGATCTgatcgattcttgtggaaaggacgaaacaccg
PCR2_FWD_08	AATGATACGGCGACCACCGAGATCTACACTCTTTCCCTACACG ACGCTCTTCCGATCTcgatcgattcttgtggaaaggacgaaacaccg
PCR2_FWD_09	AATGATACGGCGACCACCGAGATCTACACTCTTTCCCTACACG ACGCTCTTCCGATCTacgatcgattcttgtggaaaggacgaaacaccg
PCR2_REV_01	CAAGCAGAAGACGGCATACGAGATAAGTAGAGGTGACTGGA GTTCAGACGTGTGCTCTTCCGATCTcggactagccttattttaacttgc
PCR2_REV_02	CAAGCAGAAGACGGCATACGAGATACACGATCGTGACTGGAG TTCAGACGTGTGCTCTTCCGATCTcggactagccttattttaacttgc
PCR2_REV_03	CAAGCAGAAGACGGCATACGAGATCGCGCGGTGTGACTGGAG TTCAGACGTGTGCTCTTCCGATCTcggactagccttattttaacttgc
PCR2_REV_05	CAAGCAGAAGACGGCATACGAGATCGTTACCAGTGACTGGAG TTCAGACGTGTGCTCTTCCGATCTcggactagccttattttaacttgc

Reagent or resource	Sequence
PCR2_REV_06	CAAGCAGAAGACGGCATACGAGATTCCTTGGTGTGACTGGAG TTCAGACGTGTGCTCTTCCGATCTcggactagccttattttaacttgc
PCR2_REV_07	CAAGCAGAAGACGGCATACGAGATAACGCATTGTGACTGGAG TTCAGACGTGTGCTCTTCCGATCTcggactagccttattttaacttgc
PCR2_REV_08	CAAGCAGAAGACGGCATACGAGATACAGGTATGTGACTGGAG TTCAGACGTGTGCTCTTCCGATCTcggactagccttattttaacttgc
PCR2_REV_09	CAAGCAGAAGACGGCATACGAGATAGGTAAGGGTGACTGGA GTTCAGACGTGTGCTCTTCCGATCTcggactagccttattttaacttgc
PCR2_REV_12	CAAGCAGAAGACGGCATACGAGATAGGTCGCAGTGACTGGAG TTCAGACGTGTGCTCTTCCGATCTcggactagccttattttaacttgc
PCR2_REV_13	CAAGCAGAAGACGGCATACGAGATTTACGCACGTGACTGGAG TTCAGACGTGTGCTCTTCCGATCTcggactagccttattttaacttgc

Appendix G. Recombinant DNA

Reagent or resource	Source	Identifier
pSpCas9(BB)-2A-Puro (PX459) V2.0	Addgene	62988
PX459 sgZUP1_Exon 2_#1	This study	n/a
PX459 sgZUP1_Exon 6_#2	This study	n/a
PX459 sgZUP1_Exon 6_#3	This study	n/a
pMD2.G	Addgene	12259
psPAX2	Addgene	12260
pLenti-PGK-Hygro_ZUP1	This study	n/a
pLenti-PGK-Hygro_ZUP1(C360R)	This study	n/a
pLenti-PGK-Hygro_ZUP1(Δα2/3)	This study	n/a
lentiCas9-Blast	Addgene	52962
pKLV2-U6gRNA5(gGFP)-PGKBFP2AGFP-W	Addgene	67980
lentiGuide-Puro	Addgene	52963
lentiGuide-Puro-EGFP-NLS	This study	n/a
lentiGuide-Puro-mCherry-NLS	This study	n/a
lentiGuide-Puro-EGFP-NLS_sgHELQ	This study	n/a
lentiGuide-Puro-EGFP-NLS_sgNEIL3	This study	n/a
lentiGuide-Puro-EGFP-NLS_sgBRCA2	This study	n/a
lentiGuide-Puro-EGFP-NLS_sgBRIP1	This study	n/a
lentiGuide-Puro-mCherry-NLS_sgLacZ	This study	n/a
LCV2::TKOv3	Addgene	90294

Appendix H. Software and algorithms

Reagent or resource	Source	URL
Image Lab Software V6.1	Bio-Rad	https://www.bio-rad.com/en-uk/product/image-lab-software?ID=KRE6P5E8Z
ICE	Synthego	https://ice.synthego.com/#/
CHOPCHOP	Valen Lab	https://chopchop.cbu.uib.no
CRISPOR	Haeussler Lab	http://crispor.tefor.net
CRISPick	Broad Institute	https://portals.broadinstitute.org/gppx/crispick/public
Prism v9.5.1	Graphpad	https://www.graphpad.com/scientific-software/prism/
TIBCO Spotfire v12.2.0	TIBCO	https://www.tibco.com/products/tibco-spotfire
ScanR Acquisition Software 3.2.0	Olympus Lifesciences	https://www.olympus-lifescience.com/en/microscopes/inverted/scanr/
ScanR Image Analysis Software 3.2.0	Olympus Lifesciences	https://www.olympus-lifescience.com/en/microscopes/inverted/scanr/
Cutadapt v4.1	Marcel Martin	https://cutadapt.readthedocs.io/en/stable/
MAGeCK v0.5.9	Li Lab	https://sourceforge.net/p/mageck/wiki/Home/
DrugZ	Hart Lab	https://github.com/hart-lab/drugz
PANTHER v17.0	Gene Ontology	http://geneontology.org
STRINGdb v11.5	String Consortium	https://string-db.org
Adobe Illustrator v27.2	Adobe	https://www.adobe.com/uk/products/illustrator/
Adobe Photoshop v24.1.1	Adobe	https://www.adobe.com/uk/products/photoshop/